TECHNISCHE UNIVERSITÄT MÜNCHEN

Physik-Department

Fachgebiet Physik weicher Materie

Orthogonally switchable block copolymers

Natalya Vishnevetskaya

Vollständiger Abdruck der von der Fakultät für Physik der Technischen Universität München zur Erlangung des akademischen Grades eines

Doktors der Naturwissenschaften (Dr. rer. nat.)

genehmigten Dissertation.

Vorsitzender:	Univ.-Prof. Dr. Martin Zacharias
Prüfer der Dissertation:	1. Univ.-Prof. Dr. Christine M. Papadakis
	2. Univ.-Prof. Dr. Katharina Krischer

Die Dissertation wurde am 22.05.2017 bei der Technischen Universität München eingereicht und durch die Fakultät für Physik am 04.09.2017 angenommen.

Preface

The present research was conducted under the supervision of Professor Dr. Christine M. Papadakis in the Soft Matter Physics Group at the Physics Department, Technical University of Munich.

The project described herein has been developed in collaboration with Professor Dr. André Laschewsky (Institute of Chemistry, University of Potsdam and Fraunhofer Institute for Applied Polymer Research, Potsdam-Golm, Germany) and with Professor Dr. Peter Müller-Buschbaum (Chair of Functional Materials, Physics Department, Technical University of Munich). The synthesis of thermoresponsive polymers investigated in this work and their introductory characterization were held by Dr. Viet Hildebrand (Institute of Chemistry, University of Potsdam).

Small-angle neutron scattering (SANS) experiments presented in the present work were performed at the instrument D11 at the Institute Laue-Langevin (ILL, Grenoble, France) and at the instrument KWS-1 operated by JCSN at the Heinz Maier-Leibniz Zentrum (MLZ, Garching, Germany). Experiments were carried out with the support from the instrument scientists: Dr. Isabelle Grillo (D11) and Dr. Zhenyu Di (KWS-1).

Dynamic light scattering (DLS) measurements were carried out using a Zetasizer Nano ZS (Malvern) laser particle size analyzer at the Institute of Macromolecular Chemistry (Prague, Czech Republic).

Abstract

Thermoresponsive polymers are receiving increasing attention in various fields of application due to their tunable properties. In this dissertation, the focus is on the behavior of twofold thermoresponsive diblock copolymers, consisting of a zwitterionic polysulfobetaine and a nonionic thermoresponsive blocks, in solution. We investigate the self-assembled structures in dependence on temperature and electrolyte content, using small-angle neutron scattering as the main method.

Zusammenfassung

Thermoresponsive Polymere sind auf Grund ihrer kontrollierbaren Eigenschaften von Interesse für verschiedene Anwendungsbereiche. Ziel dieser Arbeit ist es, Lösungen zweifach thermoresponsiver Diblockcopolymere, die aus einem zwitterionischen Polysulfobetainblock und einem nichtionischen thermoresponsiven Block bestehen, hinsichtlich des Phasenverhaltens und der Selbstassemblierung in Abhängigkeit von Temperatur und Elektrolytgehalt mit Neutronenkleinwinkelstreuung als Hauptmethode zu untersuchen.

List of abbreviations and symbols

BC	block copolymer
CP_{LCST}	a LCST-type cloud point
CP_{UCST}	an UCST-type cloud point
DLS	dynamic light scattering
LCST	lower critical solution temperature
NMR	nuclear magnetic resonance
OZ	Ornstein-Zernike
PNIPAM	poly(*N*-isopropylacrylamide)
PNIPMAM	poly(*N*-isopropylmethacrylamide)
PSB	polysulfobetaine
PSBP	poly(4-((3-methacrylamidopropyl)dimethylammonio)butane-1-sulfonate)
PSPP	poly(3-((3-methacrylamidopropyl)dimethylammonio)propane-1-sulfonate)
RAFT	reversible addition-fragmentation chain transfer
SANS	small-angle neutron scattering
SAXS	small-angle X-ray scattering
SLD	scattering length density
UCST	upper critical solution temperature
UV-vis	ultraviolet-visible

b	Kuhn length of flexible cylinders
C	scaling factor of the solvation term
d_0	average distance between the charged domains
I_P	scaling factor of the Porod term
Ioz	scaling factor of the OZ structure factor
I_G	scaling factor of the Guinier term
L	contour length of flexible cylinders
m	solvation Porod exponent
p	polydispersity of the micellar radius
p_{core}	polydispersity of the core radius of the core-shell structure
r_{avg}	average sphere radius
R_{avg}	average cylinder radius
R_g	radius of gyration
r_{mic}	micellar radius of the core-shell structure
r_{core}	core radius of the core-shell structure
R_{HS}	hard-sphere radius
α	Porod exponent
η	hard-sphere volume fraction
ξ_{OZ}	correlation length from the OZ structure factor
ξ_{solv}	correlation length from the polyelectrolyte peak model

Contents

1. Introduction

Core-shell micelles in aqueous solution are of interest for encapsulation, transport and release of substances, which are not water-soluble. Traditionally, they have been prepared by self-assembly of amphiphilic diblock copolymers featuring a hydrophilic and a hydrophobic block.[1-3] Such diblock copolymers typically form (star-like) micelles with the hydrophobic block forming the (usually considered as water-free) core and the hydrophilic block forming the shell, which is swollen by water. The micellar size and shape can be tuned by the absolute as well as the relative block lengths, while the micellar dynamics are controlled by the hydrophobicity and the length of the hydrophobic block as well as by its glass transition temperature.[4-6] Additional functionality can be obtained by rendering one of the blocks responsive.[7-11] If, for instance, the hydrophilic block is made thermoresponsive, the amphiphilic character and the ability for self-assembly can be turned "on" and "off" by changing the temperature. Upon a thermal stimulus, the shell block may become water-insoluble and collapses, thus enabling, e.g. control of phase separation or viscosity.

Thermoresponsive polymer solubility transitions can be basically divided in two types: lower critical solution temperature (LCST) behavior and upper critical solution temperature (UCST) behavior. Although intuitively, one would expect that polymers become more soluble in a solvent at higher temperatures, there are in fact very few polymers that exhibit a UCST-type phase separation in water.[12] The vast majority of fundamental studies on thermo-responsive systems address polymers that show a LCST in water.[13,14] Nevertheless, UCST-type polymers can be analogously exploited for their thermoresponsive behavior.[15-18]

UCST- and LCST-based thermoresponsiveness can be combined in diblock copolymers. This gives rise to so-called "schizophrenic"[19,20] self-assembly, enabling to invert the roles of the respective blocks for forming the micellar core and shell (Figure 1.1).[21-28] The micelles provide microdomains and surfaces of different character, which can be controlled by a simple thermal stimulus. Depending on the relative positions of the UCST- and LCST-type transitions, the block copolymer passes through a molecularly dissolved or an insoluble intermediate regime. Such systems are advantageous for a number of applications, especially in the biomedical domain, e.g., for induced gelling or for triggering the release of hydrophobic solubilizates.[8,29]

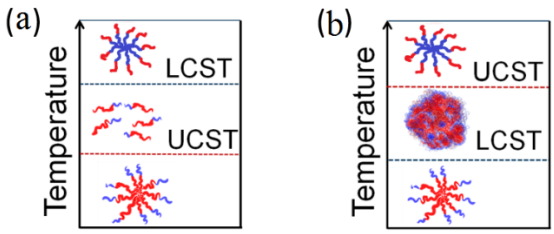

Figure 1.1: Schematic "schizophrenic" micellar self-assembly of a doubly thermoresponsive block copolymer showing $CP_{UCST} < CP_{LCST}$ (a) and $CP_{UCST} > CP_{LCST}$ (b). Red and blue dashed lines indicate the UCST-type and LCST-type transitions, respectively.

So far, only a limited number of such block copolymers have been described due to the limited choice of UCST-type segments currently available. Polysulfobetaines (PSB) are one of the most studied UCST-type polymers, they provide chemically and structurally well-defined polymers which are well-suited as model systems. Moreover, recent detailed studies of the UCST behavior of the permanently zwitterionic PSB showed that it depends sensitively on the molar mass and even more on the type and concentration of added low molar mass electrolytes.[30-32] The ion sensitivity of the UCST of PSB, when copolymerized with nonionic thermoresponsive polymer with LCST behavior of type II, which depends only rather weakly on molar mass and concentration,[13] enables a controlled variation of the UCST-type transition without an effect on the LCST-type transition. Which, in turn, allows controlling the width of the intermediate regime between the UCST- and LCST-type transitions and the relative position of the transitions (Figure 1.1).

The motivation of this thesis is to study the aggregation behavior of twofold thermoresponsive diblock copolymers consisting of a zwitterionic polysulfobetaine block featuring UCST behavior and a nonionic thermoresponsive block featuring LCST behavior in aqueous solution in dependence on temperature and electrolyte content. By varying the architecture of the diblock copolymers, namely the nature of a nonionic thermoresponsive block and a zwitterionic polysulfobetaine block as well as the ratio of the blocks lengths, we aim to investigate their influence on the self-assembly in aqueous solution and mutual interactions. The particular interest is on the possible switch of the relative positions of UCST- and LCST-type transitions by the variation of the architecture of the diblock copolymers and/or by addition of electrolyte to the polymer solution. We will investigate the aggregation behavior of the diblock copolymers in salt-free solution and in solutions with salt additives using turbidimetry to map the phase behavior and to locate the cloud points and

small-angle neutron scattering (SANS) to elucidate the mesoscopic structures in detail. The overall behavior will be approved by means of dynamic light scattering (DLS) in backscattering geometry. Small-angle X-ray scattering (SAXS) will be used to investigate the stability during heating/cooling cycles.

2. Background

This chapter gives a brief overview of the polymer behavior in solution and amphiphilic self-assembly phenomena in general and thermally induced self-organization with a particular focus on the "schizophrenic" micellization.

2.1. Polymers in solution

The word (poly)-(mer) means (many)-(parts) and refers to molecules consisting of many elementary units, called monomers.[33] Monomers are structural repeating units of a polymer that are connected to each other by covalent bonds. Polymer solutions can be obtained by dissolving a polymer in a solvent. The dissolution of a polymer into a thermodynamically compatible solvent is a stepwise process, which include solvent diffusion and chain disentanglement:[34] First, the solvent molecules penetrate and swell the polymer. Secondly, the solvated polymer molecules create a gel. Finally, the gel breaks up, and the molecules are dispersed into a true solution. Not all polymers can form a true solution in solvent.

The general phase behavior of the polymer-solvent mixtures has been described by Flory-Huggins theory, based on the principles of thermodynamics.[35,36] The behavior of a polymer in solution depends both on the polymer and solvent properties. Flory-Huggins' mathematical model implies disregard small thermal composition fluctuations as in the mean field theory. The result is an equation for the change of the Gibbs free energy of mixing, ΔG_m, which reads as:

$$\Delta G_m = \Delta H_m - T\Delta S_m , \tag{2.1}$$

where ΔH_m is the enthalpy of mixing, $\Delta H_m = RT\chi_{12}\varphi_1\varphi_2$, R is the universal gas constant and χ_{12} is the interaction parameter, which take into account the energy of interdispersing polymer and solvent molecules. ΔS_m is the entropy of mixing, T is the absolute temperature, and $\Delta S_m = -R(\varphi_1 ln\varphi_1 + \frac{\varphi_2}{N} ln\varphi_2)$. Thus, the right-hand side is a function of the number of moles and volume fraction of solvent, φ_1, and polymer, φ_2.($\varphi_1 + \varphi_2 \equiv 1$). Thus, the Gibbs free energy takes the following form:

$$\Delta G_m = RT(n_1 \ln\varphi_1 + n_2 \ln\varphi_2 + \chi_{12}\varphi_1\varphi_2). \tag{2.2}$$

Mixing takes place when the change of the Gibbs free energy is negative. The entropy of mixing is given by the number of possible configurations of the polymer chains; its change is very small for polymer-solvent systems, especially at low concentrations of a high molecular weight polymer. Thus, the sign of the change of the Gibbs free energy determines the enthalpy term, which characterizes the interaction between two molecules, e.g. polymer-polymer, polymer-solvent or solvent-solvent interactions.

To describe the enthalpy of mixing, the solubility parameter has been developed by Hildebrand:[37]

$$\frac{\Delta H_m}{V} = (\delta_1 - \delta_2)^2 \Phi_1 \Phi_2 . \tag{2.3}$$

δ_i is the solubility parameter, Φ_i is the volume fraction of *i*th constituent in the mixture, and V is the volume of the mixture. The difference in solubility parameters must be small to obtain miscibility over the entire volume fraction range. Thus, the value of the interaction parameter is given by:

$$\chi_{12} = \frac{V(\delta_1 - \delta_2)^2}{RT} . \tag{2.4}$$

The change in the interactions upon mixing (or enthalpy of mixing) governs the miscibility. Empirically, the temperature dependence of the Flory interaction parameter is often written as the sum of two terms, referred to the 'entropic part', A, and the 'enthalpic' part, B/T:

$$\chi_{12} = A + \frac{B}{T} . \tag{2.5}$$

In practice, there are a number of confounding factors to the Flory-Huggins theory. When the entropy of mixing for polymer-solvent systems is not small enough, the simple Flory-Huggins approach would be not sufficient. There are several aspects, which this simple form of the interaction parameter proposed by Flory-Huggins, does not take into account, e.g. molecular weight polydispersity or compressibility and thermal expansions effects.

The polymer solubility depends on the solvent quality, the polymer concentrations, its molecular weight, polydispersity and perhaps other values, including the solution temperature. The solvent quality is related to the balance between the enthalpy and entropy of mixing.[38] When they are in balance, the energetic part of two-body interactions exactly

cancels the entropic part and the interaction parameter $\chi = ½$. In this case, the solution is in so-called θ-conditions and at the θ–temperature and chains behave as "ideal". As the parameter χ is lowered, the polymer "likes" the solvent more and the chains are expanded. As the parameter χ is increased, the polymer "likes" the solvent less, and phase separation occurs. The solubility properties of a polymer can be changed either by changing the temperature or by changing the mixing ratio of a good solvent to a poor solvent.

The dimension of the real chain is different from that of the ideal chain of the same contour length, for instance, due to the excluded volume, which corresponds to the interaction between segments.[13,39] Excluded volume interaction cause a polymer coil expansion and mixing with solvent molecules in a good solvent, and the polymer coil shrinkage with formation of a very compact structure that excludes all solvent in a poor solvent.[40,41] The polymer chains extension is limited by the C-C covalent bonds and the entropy of the coil. The excluded volume effect can be described in terms of the total internal energy of the segmental interactions, U, expanded as a power series of the segment density ρ:

$$U = VkT(\rho^2 A_2 + \rho^3 A_3 + ...), \tag{2.6}$$

where A_2 is the second virial coefficient of the expansion, which is a measure of the solvent-mediated polymer-polymer interactions. A_2 accounts for the pair interaction between the repeating units of the chain and solvent molecules, it is the characteristic of the interaction potential between the segments and in general depends on the temperature.[13] A_2 =0 in the Θ-state of a polymer solution, $T = T_\Theta$, when there is no interaction between the repeating units and the polymer chains are in an ideal Gaussian coil conformation.

The mean-field theory predicts the collapse of a single linear polymer chain from expanded coil to a rather dense globule, the coil-to-globule transition, in organic solvents.[42] The solubility of a polymer characterized by the short-range van der Waals interactions: the stronger the interactions, the more thermodynamically poor the solvent and the lower the polymer solubility ($A_2 < 0$). An ideal polymer chain of infinite molecular weight undergoes the transition at T_Θ, whether, a real polymer chain of finite molecular weight at lower temperature, $T < T_\Theta$.[43]

2.2. Thermoresponsive polymers

All polymers in solution are sensitive to temperature changes, which cause a change in the polymer chain conformation. In contrast, the so-called thermoresponsive polymers undergo dramatic changes of their properties in response to small changes of temperature and defined as a subclass of stimuli-sensitive polymeric systems (often referred to as "smart materials").[14,44,45] Thermoresponsive polymers have been widely studied, as the variation of temperature is easy to realize. Nowadays, there are a large number of reviews on thermoresponsive polymers, most of the research focused on water-soluble systems, which are of great interest for potential applications in e.g. chromatography,[46-48] smart surfaces,[49-51] or biomedical applications including drug or gene delivery and tissue engineering.[52-55] A common characteristic feature of thermoresponsive polymers is the presence of a hydrophobic group, such as a methyl, ethyl or propyl groups.[56] These polymers possess two critical parameters, i.e. lower critical solution temperature (LCST) and upper critical solution temperature (UCST).

The solubility of thermosensitive polymers in aqueous solutions depends on the hydrophobic-hydrophilic balance. The strength of polymer-polymer (hydrophobic interactions) and polymer-solvent interactions (hydrogen bonding) depends on the solution temperature.[13] Small temperature changes around the critical temperature induce the new adjustments of the hydrophobic and hydrophilic interactions between the polymeric chains and the aqueous media and cause a significant conformation change, namely a transition between expanded (coil) and compacted (globule) chain conformations. This coil-globule collapse transition of the macromolecules at the phase separation temperature is reversible and is the common feature in all these thermoresponsive polymers.[57] The collapsed chains form compact globules which subsequently aggregate, causing turbidity.[58]

2.2.1. Upper and lower critical solution temperature

Sketch of the possible phase diagrams is shown in Figure 2.1, where the temperature changes, affecting the quality of the solvent for a given polymer, indicated with the coexistence or binoidal curve shown on the temperature-composition plane. Thus, the coexistence curve corresponds to the temperature at which the coil-globule transition takes place. Below the coexistence or binoidal curve, the phase separation occurs for polymer solutions with UCST behavior, which is the most common case for the polymer in organic solvent (Figure 2.1a).

The apex of the coexistence curve (the critical point) is referred to as the UCST and specified by the critical temperature and the critical composition. The UCST is below the *Θ*-temperature, which corresponds to zero excluded volume and indicated by the dashed line. In the case of an UCST-type phase transition, the excluded volume increases together with the temperature and the value of the second virial coefficient changes from negative to positive across T_Θ during heating. At high temperatures, the polymer chains are in an expanded well-hydrated state, the polymer solution is uniform and therefore transparent.[17] At temperatures lower than the critical point, the system has a miscibility gap: the polymer chains are in a dehydrated, collapsed state, they form compact globules, which subsequently aggregate and precipitate in solution, and this lead to the phase separation.[39]

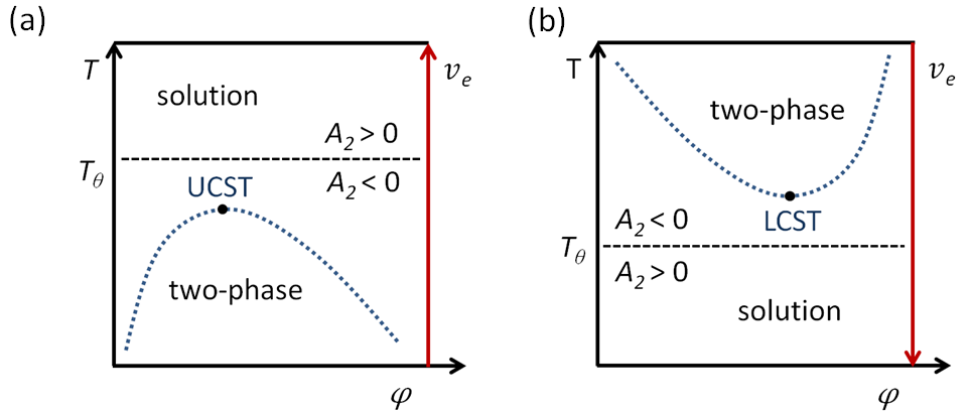

Figure 2.1: Sketch of possible phase diagrams for polymers exhibiting either (a) UCST-type or (b) LCST-type phase behavior. *T* is the temperature, φ is the polymer volume fraction, T_Θ is the *Θ*-temperature, and A_2 is the second virial coefficient value. The black dashed line indicates the T_Θ level. The blue dotted line indicates the coexistence or binoidal curve. The critical point is at the apex/bottom of the coexistence curve; it is specified by the critical temperature (UCST/LCST) and the critical composition.

UCST behavior is mainly observed in organic and water/organic solvent mixtures,[59-61] where interpolymer interactions are getting weak upon heating. Some few polymers, mostly ionic, have been reported to possess UCST in water, such as: poly(acrylic acid) (PAA), but only at high ionic strength,[62] poly(sulfobetaine),[15,63,64] and poly(6-(acryloxyloxy-methyl)uracil).[65] Among the nonionic, water-soluble polymers with UCST behavior have been reported such polymers as: poly(ethyleneoxide), poly(vinylmethylether), hydrophobically modified poly(vinyl alcohol), poly(*N*-acryloyl glycinamide), ureido-derivatized polymers and poly(hydroxyethyl methacrylate).[18] These polymers usually have a pair of interactive sites

that cause the polymers to be insoluble at lower temperatures due to intramolecular and intermolecular interactions (such as hydrogen bonding and electrostatic attraction), which can be disrupted at higher temperatures due to intensified molecular motion within the polymer chains, resulting in a hydrated polymer.[66] Such polymers typically are very sensitive to ionic contaminations. UCST-type polymers reported so far are mostly limited to structures with zwitterions[15] or hydrogen bond donor/acceptor groups.[12]

Most of the reported thermo-sensitive polymers in aqueous solutions exhibit another type of phase behavior, namely LCST: The chains are well-hydrated by water molecules at low temperatures and exhibit an expanded conformation, whereas, above the transition temperature, they collapse along with a partial release of the water molecules, forming, when applicable, new intra- and interchain H-bonds.[13] LCST behavior is "inverted" compared to UCST (Figure 2.1b) and characterized by reverse dependence of the temperature, the value of the second virial coefficient and excluded volume, compared to the UCST-type phase diagram. Many thermoresponsive polymers with LCST behavior have been synthesized and studied, such as poly(*N*-isopropylacrylamide) (PNIPAM) and the corresponding derivative polymer, poly(*N*-vinylcaprolactam), poly(2-oxazoline)s, poly(2-oxazine)s, pyrrolidone-based polymers, oligo(ethylene glycol)-containing polymers etc.[13] All these polymers undergo fast phase transitions in aqueous solution: they are soluble below their LCST through their hydrogen bonding with water, but become dehydrated and insoluble when heated above the LCST.

2.3 Self-organization of amphiphilic block copolymers

Block copolymers contain two or more different homopolymer subunits linked by covalent bonds and thus combine their properties. Amphiphilic block copolymers contain both hydrophilic and hydrophobic segments, i.e. two blocks which are incompatible and interact very differently with their environment.[67] This phenomenon can induce microphase separation in aqueous media as well as in organic solvents, depending on the chemical nature and properties of the blocks. Virtually all biological processes take place in aqueous media, thus the self-assembly of amphiphilic block copolymers in aqueous solutions have attracted considerable interest. Two different types of water-soluble block copolymers are typically distinguished: amphiphilic block copolymers and double-hydrophilic block copolymers, which combining two different hydrophilic blocks.[22] The particular structure of double-hydrophilic block copolymers enables one of the blocks to undergo physical or chemical

transformations in aqueous solution which render them insoluble, while the copolymer stays in solution by virtue of the hydrophilicity of the other block. For the successive conversion of such a block from a hydrophilic into hydrophobic state, different stimuli are used, like change of pH, ionic strength, magnetic or electric field and temperature.[53] Thus stimuli-sensitive double-hydrophilic block copolymers include amphiphilic states.

Self-assembly of amphiphilic block copolymers in water into micellar morphologies is driven by a minimization of the free energy in the system through a limitation of energetically unfavorable interactions of the hydrophobic block with water.[57,67] The most common of these are the core-shell structures called micelles, where the outer hydrophilic polymer block assembles into a hydrated dense corona and prevents further aggregation of the hydrophobic collapsed block due to the repulsion between the hydrophilic groups.[68] Thus the copolymer stays in solution by virtue of the hydrophilicity of the other block. Micelle formation is a spontaneous self-assembly process at or above a specific concentration called the critical micelle concentration (CMC). Below the CMC, no micelles are present in the solution, only molecularly dissolved copolymer chains (unimers), while above the CMC, micelles are in thermodynamic equilibrium with the unimers. The CMC may be affected by the temperature, pressure and by the presence of other components in the system, e.g. electrolytes, alcohols, etc.[69]

Different morphologies accessible by self-assembly of amphiphilic block copolymers, such as spherical micelles, cylindrical micelles and bilayers or vesicles, are shown in Figure 2.2. The morphology depends on the stretching of the core forming blocks, the core-shell interfacial energy, and repulsion between the shell forming blocks. Changes in one of these three factors will result in thermodynamic instability and lead to rearrangement into thermodynamically more stable morphologies. The resulting morphology of micellar aggregates in solution of low molecular weight amphiphiles is determined by their intrinsic geometry, which can be predefined by the dimensionless packing parameter $p = v/a_s l_c$, where v is the volume occupied by the hydrophobic chains and l_c is their extended length, a_s is the equilibrium area occupied by an amphiphilic molecule at the micelle–water interface.[70] Packing parameter correspond to the interfacial curvature between the hydrophilic and the hydrophobic polymer block in the state of minimum interfacial energy, i.e. the hydrophilic headgroup on the side of the water interface and the hydrophobic tail on the other side. Generally, spherical micelles are formed when p ~1/3 and characterized by high curvature, i.e. when $a_s > v$ and the radius of the formed micelles does not exceed l_c.[71] With an interfacial

curvature decrease cylindrical micelles ($1/3 < p < 1/2$), bilayers or vesicles ($1/2 < p < 1$) are formed. Changes in both a_s as well as l_c depend on the amphiphile properties and solution conditions.

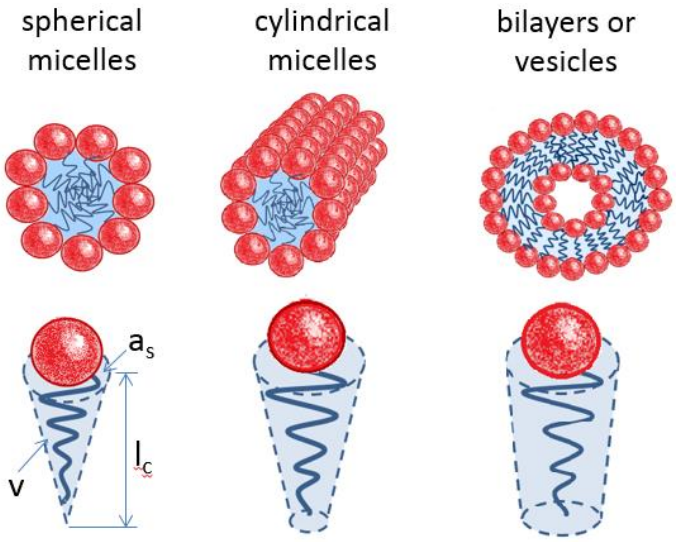

Figure 2.2: Schematic representation of possible micellar structures formed by amphiphilic block copolymers with head group area a_S, hydrophobic chain volume v and length l_c, together with the preferred aggregate morphologies. Modified from [71].

2.3.1. Different types of thermally induced self-organization

The use of water-soluble thermoresponsive block copolymers has opened a number of opportunities for smart behavior.[7,11] Studies on such block copolymers have been mostly limited to simple "on-off" systems, where the polymers undergo a transition from the molecularly dissolved state to the aggregated state or vice versa, exhibiting either a LCST or an UCST for one of the blocks (Figure 2.3a,b).

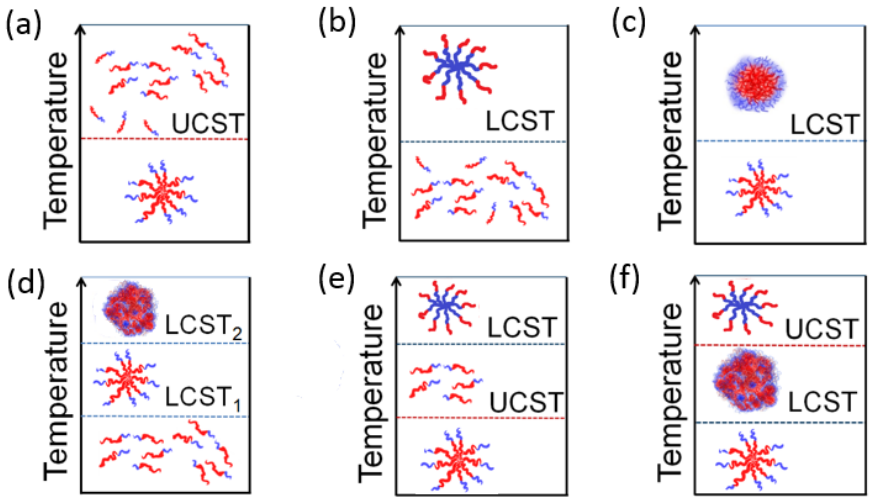

Figure 2.3: Schematic representation of different types of thermally induced self-organization: one-step transition from molecular to aggregated state via UCST (a) or via LCST (b) and transition from superstructure 1 to superstructure 2 via LCST (c); and twofold thermo-responsive block copolymers with two transitions: molecular state - superstructure 1 - macroscopic precipitation via two LCSTs (d), superstructure 1 – molecularly dispersed state - inverse superstructure 3 via two sequential UCST and LCST transition (e), superstructure 1 – macroscopic precipitation - inverse superstructure 3 via two sequential LCST and UCST transitions (f).

Also known, but much less studied are systems in which a direct transition between two different self-assembled superstructures takes place,[11,59] as well as complex responsive systems in which two thermal transitions proceed subsequently via two LCST-type transitions, e.g. transitions from the molecularly dispersed state to one superstructure and then to aggregation / macroscopic precipitation (Figure 2.3d).[7,72-76]

It seems particularly attractive to combine two different switching behaviors, namely UCST and LCST behavior, in order to obtain a structure inversion ("schizophrenic" behavior), namely inversion of micelle core and shell.[20,77] The transformation proceeds via an intermediate state, which may either, be insolubility or the molecularly dissolved state, depending on the relative positions of the two phase transitions (Figure 2.3e,f).[19,21,24,26,27,78-82]

2.3.2. “Schizophrenic” micellar systems

Armes and co-workers coined the term “schizophrenic” to describe micellization of block copolymers incorporating two or more responsive blocks which can form two distinct

structures in response to external stimuli (temperature, pH, salt, etc.).[19] Since the first report in 1998,[77] numerous examples of novel water-soluble diblock copolymers that exhibit so-called "schizophrenic" character have been reported: a number of systems with dual pH-responsive blocks,[83-86] dual thermoresponsive blocks,[12,22-24,28,87-89] dual salt responsive blocks,[25] a pH- and a temperature-responsive block,[66,90-95] and a pH- and a salt-responsive block.[19]

Temperature-controlled "schizophrenic" diblock copolymers requires the difference of solubility of the constituting blocks to form micellar structures with switchable core and shell.[20] The group of Laschewsky has been pioneers in the field of dual thermoresponsive block copolymers consisting of a zwitterionic UCST block, namely polysulfobetaine, and nonionic LCST block, first reports appeared already in 2002.[22,23] By consecutive reversible addition-fragmentation chain transfer (RAFT) polymerizations have been prepared poly(*N*-isopropylacrylamide)-*block*-poly(3-[*N*-(3-methacrylamido-propyl)-*N*,*N*-dimethyl] ammonio propanesulfonate) (PNIPAM-*b*-PSPP), which retained the capability of PNIPAM and PSPP blocks to undergo LCST-type and UCST-type transitions in water, respectively. The relationship between UCST and LCST always was: UCST (9 - 20 °C) < LCST (33 - 34 °C). The polymers were soluble in water at temperatures between UCST and LCST and formed micellar aggregates both at temperatures below UCST and above LCST (Figure 2.3e). The addition of salt (NaCl), led to screening of the charges of the PSPP block and a decrease of the UCST or even its disappearance at high salt concentration.[23] During the same year, was reported another diblock copolymer exhibiting both UCST- and LCST-type transitions, poly(sulfobetaine methacrylate)-*block*-poly(2-(*N*-morpholino) ethyl methacrylate) (PSBMA-*b*-PMEMA), which was prepared by group transfer polymerization followed by quaternarization.[87] PSBMA-*b*-PMEMA was soluble in water between UCST and LCST (between 20 and 50 °C), assigned to the PSBMA and the PMEMA blocks, respectively, and formed micelles below 20 °C and reverse micelles above 50 °C (Figure 2.3e). Later, Maeda et al. described thermoresponsive association of poly(3-dimethyl(methacryloyloxyethyl)ammonium propane sulfonate)-*block*-poly(N,N-diethylacrylamide), P(dMMAEAPS)-*b*-P(dEA), which exhibited the UCST-type transition around 12 °C, assigned to the zwitterionic sulfobetaine segment dMMAEAPS, and the LCST-type transition around 40 °C, assigned to dEA.[24] By infrared spectroscopy (IR) has been indicated the change of the segmental interaction of each block at each transition (Figure 2.3e). In recent past, Yoshimitsu et al. reported on a dual thermosensitive behavior

achieved in water using vinyl ether block copolymers with imidazolium salt side-chains (exhibiting an UCST behavior) and oxyethylene side-chains (exhibiting a LCST behavior).[12] UV-vis spectroscopy, dynamic light scattering (DLS), static light scattering (SLS), variable temperature proton nuclear magnetic resonance (^{1}H NMR) spectroscopy, and fluorescence measurements results revealed that the block copolymers undergo thermosensitive gel–sol–gel transition in water (Figure 2.3e), and formed micelles at lower temperatures and vesicles at higher temperatures. Latterly, Sun et al. described another example of dual thermoresponsive aggregation of "schizophrenic" copolymer.[89] The block copolymers poly[2-(dimethylamino)ethyl methacrylate]-*block*-poly-(sulfobetaine methacrylate), PDMAEMA-*b*-PSBMA, with various block ratios underwent UCST- and LCST-type transitions in aqueous solutions due to the properties of the PSBMA and PDMAEMA block, respectively. UV-vis spectroscopy and DLS results revealed that both the UCST and LCST of PDMAEMA-*b*-PSBMA were shifted to lower values with an increase of the DMAEMA/SBMA block ratios. Moreover, the UCST and LCST values were altered with the salt concentrations and pH due to the salt-sensitivity of PSBMA and pH-responsivity of PDMAEMA. Only a limited number of such block copolymers have been described. The difficulty of creating systems combining UCST and LCST behaviors lies in the limited choice of UCST-type segments currently available.

Recently, Zhang et al. reported that also uncharged UCST block copolymers could be used to prepare "schizophrenic" polymers.[96] Was reported the block copolymer consisting of a random copolymer of acrylamide and acrylonitrile (P(AAm-*co*-AN)) and a thermoresponsive poly(*N*,*N*-dimethylaminoethyl methacrylate) (PDMAEMA) block, and featuring a composition-tunable UCST and LCST behavior, respectively. Temperature dependent turbidimetry and DLS studies showed reversible dissolution and formation of micelles with a window of molecular dissolution between ca. 20 and 45 °C (Figure 2.3e). But the observed effects could result from a mere superposition of the individual polymer behaviors, as the UCST block is a mixture of copolymers, averaging over a range of different compositions. Käfer et al. reported on the double thermoresponsive behavior of block copolymers made from poly(ethylene glycol) (PEG) which was chemically coupled to a set of acrylamide-acrylonitrile (AM-AN) statistical copolymers.[97] Temperature-resolved turbidimetry and DLS indicated that, for some of these copolymers, a miscibility gap exists at intermediate temperatures (Figure 2.3e). Surprisingly, small changes of the composition of the AM-AN block did not only shifted the UCST transition markedly, but also the LCST transition in the

same direction (from 20 °C to 70 °C). In addition, the authors mention that they encountered difficulties due to the sensibility of the AN-AM copolymer against hydrolysis, yielding AN-AM-acrylic acid terpolymers. Interestingly, very similar block copolymers using a poly(ethylene glycol) having an average molecular weight of 6000 (PEG6000) only show UCST-type transitions, but no LCST-type ones.[98] Mäkinen et al. described thermosensitive ABC triblock terpolymers with different block lengths and block orders.[99] These featured a short PEO block, a PNIPAM block and a poly(*N*-acryloylglycinamide (PNAGA) block. Temperature-resolved ^{1}H-NMR, turbidimetry and DLS studies revealed "schizophrenic" behavior with a window of (at least close to) molecular dissolution between ca. 5-20 °C and 28-38 °C for some of the polymers (Figure 2.3e). In particular, the chemical structures presented are rather complex, thus preventing a clear interpretation of the aggregation forms and the switching behavior observed. Consequently, only few data are available on the diblock copolymers consisting of an uncharged UCST block and a LCST block, which allow up to now only limited inferences.

In the present work, the focus is on the twofold thermoresponsive diblock copolymers based on charged UCST-type monomers and nonionic LCST-type monomers. The aggregation behavior of such diblock copolymers can be controlled by both the temperature and the ionic strength of the solution. Decoupling of stimuli from each other improves not only the degree of precision and complexity of the system but promotes the simplicity of the application likewise.[95,100,101]

3. General idea of the thesis

The present work is devoted to studies of self-organization of twofold thermoresponsive polymers, which exhibit UCST and LCST switching behavior in aqueous solution. Up to now, most studies on thermoresponsive block copolymers exhibiting "schizophrenic" behavior have dealt with block copolymers which show two step sequential transitions via UCST- and LCST-type transitions and molecularly dissolved intermediate state, respectively (paragraph 2.3, Figure 2.3e). In this work, we investigate the diblock copolymers consisting of a zwitterionic polysulfobetaine block and a nonionic thermoresponsive block, which combine the UCST and LCST behaviors, respectively, of the constitutive homopolymers in aqueous solution, and offer numerous perspectives for the creation of switchable polymer systems: The diblock copolymers switch from micelles with a nonionic shell and a polysulfobetaine core at low temperatures to the reverse micelles at high temperatures via an intermediate state, which may either be the molecularly dissolved polymers (Figure 2.3e) or large aggregates/macroscopic precipitates (Figure 2.3f), depending on the relative positions of the UCST- and LCST-type transitions.

The detailed phase diagram depends on the block lengths and the chemical structures of the two blocks. For instance, the chemical structure of the spacer group separating the ammonium and the sulfonate groups in polysulfobetaine strongly affects the phase transition temperature.[32] Apart from the well-established zwitterionic polymers such as poly(3-((3-methacrylamidopropyl)dimethylammonio) propane-1-sulfonate) (PSPP) (Figure 3.1a), the closely related polymer poly(4-((3-methacrylamidopropyl) dimethylammonio)-butane-1-sulfonate) (PSBP) (Figure 3.1b), which exhibit higher UCST than PSPP of a comparable molar mass,[32,102] can be used. As the nonionic block, poly(*N*-isopropylacrylamide) (PNIPAM) (Figure 3.1c) has been chosen, which is a well known thermoresponsive polymer with LCST behavior, which exhibits a sharp collapse transition at ~32 °C.[103-106] Alternatively, the thermoresponsive PNIPAM block may be replaced by poly(*N*-isopropylmethacrylamide) (PNIPMAM) (Figure 3.1d). PNIPMAM is thermoresponsive as well, but with a higher LCST (~44 °C) than PNIPAM.[107-110] This way, the cloud points of the diblock copolymers in aqueous solution and their relative position may be tuned.

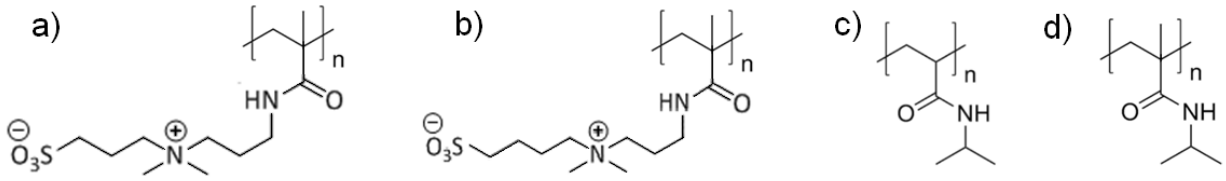

Figure 3.1: Chemical structures of the homopolymers under investigation: zwitterionic (a) PSPP and (b) PSBP, and nonionic (c) PNIPAM and (d) PNIPMAM. In PSBP, the spacer separating the ammonium group and the sulfonate group is extended by one methylene group compared to PSPP. PNIPMAM has an additional methyl group attached to the α-carbon of the repeat unit on the backbone compared to PNIPAM.

Moreover, the ion sensitivity of the cloud point of the zwitterionic block to both the ionic strength and the nature of the salt[30-32] offers the possibility to create orthogonally switchable systems where the transition from the core-shell micelles of one type to the opposite one ("schizophrenic" behavior) may proceed via precipitation or via the molecularly dissolved state, depending on two stimuli, namely temperature and electrolyte concentration, as depicted in Figure 3.2.

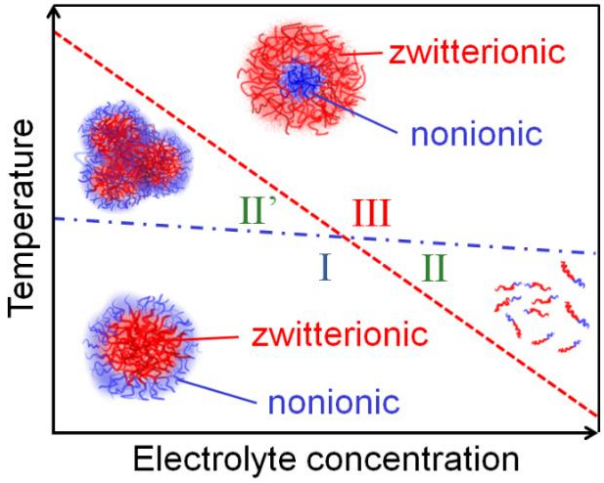

Figure 3.2: Phase behavior expected for a diblock copolymer combining a zwitterionic polysulfobetaine (red) and a nonionic thermoresponsive block (blue) in aqueous solution in dependence on temperature and electrolyte concentration: (I) at low temperatures, micelles with a nonionic shell and a polysulfobetaine core; in the intermediate temperature range, (II') large aggregates/macroscopic precipitates or (II) molecularly dissolved polymers; (III) at high temperatures, the reverse micelles with a nonionic core and a polysulfobetaine shell. The UCST-type transition of polysulfobetaine is depicted by the red dashed line and the LCST of

nonionic thermoresponsive block by the blue dash-dotted line. The UCST-type transition is expected to be more strongly dependent on electrolyte concentration than the LCST-type transition.[23]

Hereby, we aim to investigate the influence of the architecture of the twofold thermoresponsive diblock copolymers, namely the nature of a polysulfobetaine and a nonionic block and the composition of the diblock copolymers, i.e. the relative lengths of the blocks, on their self-assembly in aqueous solution in dependence on temperature and electrolyte concentration.

The structural characterization of "schizophrenic" block copolymers reported in the literature was mainly performed via ^{1}H NMR and laser light scattering (DLS and SLS) (see paragraph 2.3). These methods allow to determine only the micellar structure of polymers in solution with respect to the core and shell forming blocks, and the size of particles in solution. In the context of this thesis, small-angle neutron scattering (SANS) was chosen as the main method for structural characterization. SANS gives detailed and quantitative structural information on the size, inner structure (core-shell) and correlation of the micelles as well as their aggregates. We have combined SANS with turbidimetry to map the phase behavior and to locate the cloud points and dynamic light scattering (DLS) in backscattering geometry to confirm the overall behavior.

4. Systems under investigation

This chapter gives an overview of the polymers used in this study. Firstly, the polymers involved in the investigated twofold thermoresponsive diblock copolymers are described. Secondly, previous investigations of diblock copolymers analogous to those under investigations are highlighted.

4.1. Poly(*N*-isopropylacrylamide)

Poly(*N*-isopropylacrylamide) PNIPAM (Figure 3.1c) is by far the most studied thermo-responsive polymer with LCST behavior, it exhibits a sharp collapse transition at CP_{LCST} ~ 32 °C.[13,103-107,111] PNIPAM was first synthesized in 1956.[111] The first systematic study of the phase diagram of PNIPAM was reported by Heskins and Guillet in 1968.[112] The authors constructed the first phase diagram of PNIPAM in water by measuring the phase transition temperature as a function of PNIPAM concentration (Figure 4.1).

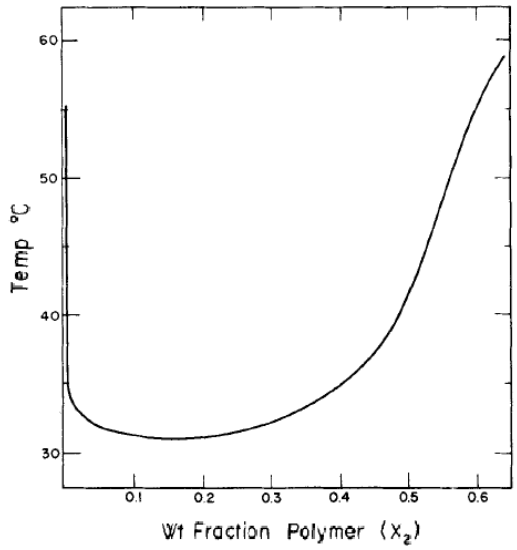

Figure 4.1: The phase diagram of PNIPAM reported by Heskins and Guillet in 1968 [112]

Later, several research groups investigated the mechanism of the phase separation of PNIPAM.[106,113-115] It was found that the absolute values and the phase boundaries strongly different from the first phase diagram, which is due to the influence of the many factors, such as: the molecular weight of the polymers, synthesis protocols, the external pressure, measurement issues and the detection of phase boundaries. Nevertheless, aqueous PNIPAM solutions refer to exhibit LCST behavior of type II, which depends only weakly on molar mass and concentration.[13,106,107,111,115] The versatility of PNIPAM systems include dilute

single chains, gels and brushes of terminally anchored chains, which make them suitable for a wide range of biotechnological applications.[106]

In solution, PNIPAM chains exhibit competing forces arising from the interactions of water with the hydrophilic amide groups and the hydrophobic isopropyl and backbone groups:[116-118] At temperatures lower than CP_{LCST}, the amide group (which offers two H-bond sites) forms hydrogen bonds with water and thus solubilize the polymer. Upon heating to above the CP_{LCST}, these hydrogen bonds break down and new bonds are formed between the polymer segments, thus most of the former bound water molecules are expelled. The dehydration of the PNIPAM chains results in an abrupt transition from a swollen to a collapsed or a globular conformation and induces the volume to shrink. This so-called coil-to-globule transition of individual PNIPAM chains is a reversible phenomenon with a heating–cooling hysteresis, which is related to the formation of additional hydrogen bonds between the polymer segments in the globule state that retard the swelling of the PNIPAM globule.[119-121]

Coil-to-globule collapse of PNIPAM in water has been described in detail by different models.[58,115,122,123] In 1978, T. Tanaka first reported on the thermally-induced volume phase transition of polyacrylamide gels. The transition can be explained in terms of mean-field theory based on the extension of Flory's formula for the free energy of gels, which predicts the existence of a critical point.[124] Later, the PNIPAM coil-to-globule transition was extensively studied.[107,125,126] In the mid-1990s, Wu et al. first stated that single PNIPAM chains in a dilute aqueous solution collapse into stable single-chain globules upon heating.[127] The authors described a four-stage coil-to-globule transition process for a single PNIPAM chain in water, which include the following stages: the chain contraction, crumpling, knotting, and collapsing.

Later, in a series of publications, F. Tanaka et al. introduced the cooperative model of the hydration of the PNIPAM chains in solution focused on sequential hydrogen bond formation between polymer chains and water molecules (or solvent molecules in general).[115,123,128,129] This model allows studying the interaction between polymer and solvent molecules and is capable to describe hydration process of PNIPAM from water molecules as well as from the mixed solvents of both water and any polar solvent (e.g. methanol). PNIPAM chains are not accessible to the water molecules with equal probability due to their rather bulky side chain, which contains polar and apolar parts and interacts mostly with the solvent molecules. The cooperative character is schematically represented in the figure 4.2: The water molecules

(blue circles) bind to an amide group on a side chain by hydrogen bond. The bound water causes a slight displacement of the isopropyl group on the side chain giving rise for the preferential formation of the second hydrogen bond on the neighboring position, thus forming sequences. The second bound water and the following ones each gain the additional energy when they are adsorbed at a position next an already occupied one. Thus, this cooperativity is of the nature to minimize the energy cost that a water molecule has to pay in order to find a position on the PNIPAM chain by the energy gain due to the small spatial displacement of the rather bulky side chain. The uneven hydration leads to a pearl-necklace conformation of the chain, since some parts of the chain are hydrated, whereas others are forming intermolecular bonds (blobs). When the chain is heated to above the CP_{LCST}, intramolecular hydrogen bonds become dominating. The detachment of one bound water molecule induces the easier detachment of the neighboring bound water molecule. The sequence is dehydrated, and bound water is released from the polymer chains, which results in the sharp collapse of the PNIPAM chain.

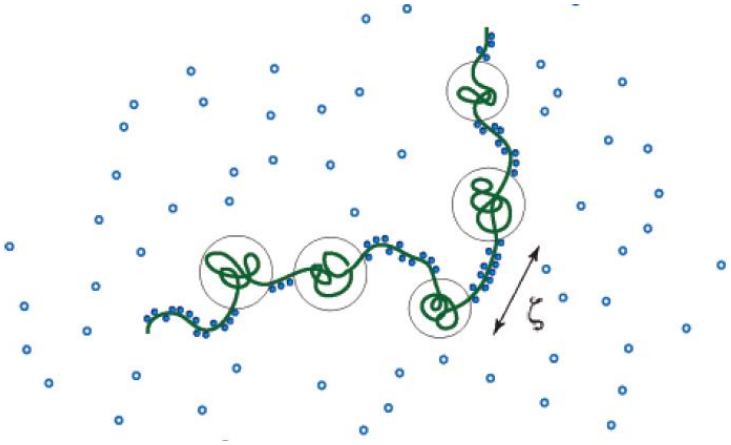

Figure 4.2: Schematic representation of the pearl-necklace conformation induced by the cooperative hydration of PNIPAM chains introduced by F. Tanaka et al.[115,123] Blue circles represent the water molecules. Cooperativity originates in the nearest-neighboring bound water molecules. The polymer chain consists of a sequences of hydrogen-bonded consecutive water molecules with length ξ. The random-coil parts (thin circles) are collapsed near CP_{LCST}.

The water molecules play an important role in the PNIPAM transition.[118] Below the LCST, they form water cages around the hydrophobic group and hydrogen bond bridges between isopropylamide groups, thus sustaining an extended conformation. Above the LCST, the dehydration of PNIPAM is indicated by a significant decrease in the hydration number, defined as the number of water molecules bound to each NIPAM monomer, which, in turn,

decreases with the PNIPAM concentration in aqueous solution and depends sensitively on PNIPAM architecture and topology.[130-133] Nevertheless, not all associated water molecules are liberated above the CP_{LCST}, and the aggregates formed by PNIPAM contain significant amount of water.

On a microscopic level, heating the aqueous solution to above the LCST changes the conformation of a flexible, linear PNIPAM chain from a swollen coil to a collapsed globule.[107,127,134] Above the LCST, the globules tend to associate and to form mesoglobules/aggregates, which attain diameters from tens to a few hundred nanometers.[135-137] Dissolved chains below the cloud point and dominating large aggregates above the cloud point were confirmed in the recent study by Meier-Koll et al. on the phase separation behavior in semidilute PNIPAM solution.[137] In dilute solution, PNIPAM chains are isolated and interact with each other only seldomly. In concentrated PNIPAM solution, interpenetration of the polymer molecules may cause formation of additional, intermolecular hydrogen bonds.

Changes of the molecular weight and hydrophobic/hydrophilic balance in PNIPAM aqueous solution can alter the transition behavior. Copolymerization of PNIPAM with hydrophilic or hydrophobic comonomers increases or decreases the LCST of PNIPAM, respectively.[138-140] The lower the molecular weight of polymers, the higher the effect of the end groups.[131,141,142] The change of the LCST depends not only on the level of hydrophobic/hydrophilic comonomer incorporation and on its chemical structure, but also on its position on the chain. Thus, the LCST of PNIPAM can be controlled by varying copolymer composition. The LCST behavior of PNIPAM can be extended to more complex architectures by addition of stimuli-responsive moieties to provide a phase transition of PNIPAM-based polymers in response to corresponding stimuli.[143] Such dual-responsive polymers are promising for a number of biomedical applications including drug delivery systems, cell culture substrates, and separation systems.[144-146]

We should stress here that the aim of this work is to study double-hydrophilic block copolymers including those composed from PNIPAM and polysulfobetaine blocks, the last ones are sensitive to the presence of electrolyte. Thus, one of the important aspects is the influence of salt on the transition of PNIPAM in the solution. Addition of salt to a rather high concentration, which is specific for each salt, in the solutions of PNIPAM[147] or PNIPAM-based copolymers[23,148,149] causes enhanced aggregation and shift of its LCST, typically to a

lower temperature. This LCST shift follows the so-called Hofmeister series, which is an empirical classification of ions in order of their ability to decrease ("salt-out") or increase the solubility ("salt-in") of proteins.[150] Ions are divided according to their ability to "salt-out" or "salt-in" effect into kosmotropic and chaotropic ions, respectively.[150,151] For instance, the transition temperatures of PNIPAM (1.4 wt. %) in 1 M NaCl and NaBr salt solutions (Br^- has slightly stronger chaotropic character than Cl^-) are found to be reduced to 20 °C and 25 °C, respectively.[152] In contrast to an earlier suggestion that anions play a critical role in the LCST conformational transition of PNIPAM,[153,154] Du et al. found that cations have stronger affinity with the polymer, whereas anions virtually have no association with the polymer.[147] Furthermore, the stronger the cation-anion interaction is, the more weakly the cation binds to the polymer, e.g. K^+ and Cl^- have a stronger association constant than Na^+ and I^-. In the present work, the polymer solutions will be investigated at low salt concentrations (< 0.005 M), which should not affect the LCST of PNIPAM.

4.2. Poly(*N*-isopropylmethacrylamide)

Some other *N*-substituted poly(acrylamides) and poly(methacrylamides) exhibit similar behaviors to PNIPAM in aqueous solution,[7] including poly(*N*-isopropylmethacrylamide) (PNIPMAM). PNIPMAM differs from PNIPAM by an additional methyl group attached to the α-carbon of the repeat unit on the backbone (Figure. 3.1c,d), which has a strong effect on the cloud point as well as on its dependence on ionic strength.[107,109,125,155-160] The LCST behavior of PNIPMAM was investigated by various kinds of methods including nuclear magnetic resonance (NMR) spectroscopy, differential scanning calorimetry (DSC), light scattering, neutron scattering, infrared (IR) spectroscopy and raman spectroscopy. One might expect the LCST of PNIPMAM in water solutions to be lower than the one of PNIPAM due to the presence of the hydrophobic methyl group on the backbone. However, the value mostly reported in the literature for PNIPMAM with molar masses in the range of 40,000 - 400,000 g mol^{-1} is around 44 °C, i.e. higher.[107-110] The origin of the counter-intuitive increase of CP_{LCST} for PNIPMAM compared to PNIPAM is still under discussion.[155,160,161] A possible explanation can be found in conformational reasons: The presence of a methyl group restricts the free rotation due to the change of the hydration water around the polymer chain.[160] Thus, the hydrophobic moieties cannot associate in the most favorable way, i.e. the intrachain collapse and interchain association of the polymer chain are restrained, giving rise to a counter-intuitively higher LCST. Djokpé et al. investigated turbidimetrically the cloud points

of dilute aqueous solutions of PNIPAM, PNIPMAM and their statistical copolymers.[110] The cloud points are independent of the total concentration of the solutions. Mixtures of the binary systems in water exhibit two cloud points, which are nearly the same as the cloud points of PNIPAM and PNIPMAM homopolymers.

PNIPMAM exhibits significantly weaker intermolecular interactions between the amide groups, and at temperatures below the LCST, PNIPMAM molecules form more expanded structures in solution than PNIPAM, although the hydrophobic interactions for PNIPMAM and PNIPAM are very similar.[161,162] At temperatures above the LCST, PNIPMAM forms more stable compact aggregates compared to PNIPAM, and the dissolution of PNIPMAM during the backward cooling requires overcoming a higher energy barrier due to polymer-polymer hydrogen bonding in the globular state and shows therefore a stronger hysteresis.[116,163] Moreover, the differences in the critical transition temperatures for the heating and cooling scans of PNIPMAM solution increase with polymer concentration.[110] Spěváček et al. indicated by means of ^{1}H NMR relaxation and IR spectroscopy methods that in PNIPMAM solutions a certain portion of water is bound in phase separated mesoglobules formed above the LCST and with time this bound water is slowly released.[164] IR spectra of PNIPMAM solution in H_2O indicate a two-steps character of the phase transition: during heating, the transition temperature of hydrophilic C=O groups is slightly higher than the transition temperature of hydrophobic CH_3 groups.

PNIPMAM seems to exhibit type II LCST behavior,[13] as PNIPAM, according to the weak molar mass and concentration dependencies reported.[107-110] Thus, PNIPMAM is a good candidate for creation of double hydrophilic block copolymers. For instance, Luo et al. have applied the double thermoresponsive block copolymer PNIPAM-*b*-PNIPMAM as the shell of a dendritic polymer H40.[165] Upon continuous heating through the LCSTs of PNIPAM and PNIPMAM, dendritic H40-PNIPAM-*b*-PNIMAM exhibits a two-stage thermoresponsive collapse (Figure 2.3d). Another example was reported by Jochum et al., they investigated the stimuli-responsive properties of a functional double thermoresponsive poly[(oligo(ethylene glycol) monomethyl ether methacrylate)-*block*-(*N*-isopropylmethacrylamide)] (POEGMA-*b*-PNIPMAM) block copolymer with a biotin end group on the PNIPMAM block, in order to control the biological binding ability of the system via external stimuli.[166] The double thermoresponsive POEGMA-*b*-PNIPMAM showed a temperature dependent multi-stage assembly behavior: completely soluble in water at temperatures below the LCST of both

blocks, micellar structures formed above the LCST of PNIPMAM but below the LCST of POEGMA, and precipitated from solution above the LCST of both blocks (Figure 2.3d).

In the present study, we selected PNIPMAM as an alternative nonionic thermoresponsive block for PNIPAM. We expect that its higher LCST, compared to the one of PNIPAM, will enlarge temperature window between CP_{UCST} and CP_{LCST}, in the solutions of the corresponding diblock copolymers with the zwitterionic polysulfobetaine block, compared to those with PNIPAM. We expect that the enlarged temperature window between CP_{UCST} and CP_{LCST} should also favor "schizophrenic" micellar self-assembly.

4.3. Polysulfobetaines

Polyzwitterions or synonymous polybetaines represent a special subclass of polyampholytes. Polyampholytes carry positive and negative charges on different monomer units, and charges can be randomly or alternately distributed along polymer chains.[167] Polyampholytes behave mostly either as polyanionic or as polycationic species. Polyzwitterions, in contrast, contain on the same monomer unit both positive and negative charged sites linked through covalent bonds, which are typically not electronically conjugated with each other. Thus, polyzwitterions are electrically neutral. The distribution of ionic groups within polyzwitterions may be different, by far the most widespread architecture of polyzwitterions is shown in Figure 4.3a.[168]

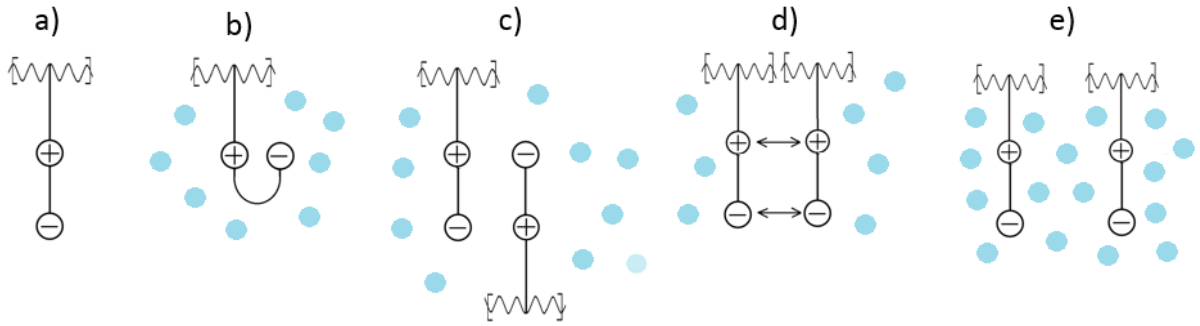

Figure 4.3: Schematic representation of the most widespread type of architecture of polyzwitterions (a) and interactions between zwitterionic groups in water solution and those with water molecules: attractive intra- (b) and interchain interactions (c), repulsive intermolecular interactions (d) and attractive water-polymer interactions (e). Water molecules are shown with blue circles. Modified from ref. [168]

4.3. Polysulfobetaines

The type of zwitterionic group determines the specific properties of polybetaines. Typically, for polybetaines, the positively charged functional group is a quaternary ammonium or phosphonium group and is thus permanently charged.[167,169] Depending on the chemical structure of the negatively charged functional group, polybetaines may be further subdivided: The anionic functionality may be a carboxylate (carbo or carboxybetaines), a sulfonate (sulfobetaines), a phosphate, phosphonate, or phosphinate (phosphobetaine), or can be enolate based, as in the dicyanoetheneolate derivatives. The most widespread subclasses of polybetains are polyphosphobetaines, polycarboxybetaines, and polysulfobetaines, the latter are chemically the most inert.[32,64,167,169]

The coexistence of the different charges in polybetaines applies to a broad range of physicochemical conditions, e.g., pH and ionic strength.[167] Polysulfobetaines, at which we will focus on in the present study, exhibit zwitterionic character over the broad pH window (typically 2–14 minimum).[32,170] The synthesis and phase behavior of polysulfobetaines have been thoroughly outlined.[16,64,167,171-173] In aqueous solution, they respond to changes in temperature and to the presence of electrolyte, which makes them particularly attractive from a fundamental point of view, as well as a practical one.

In salt-free conditions, polysulfobetaines are electrically neutral due to the formation of an inner salt by the ammonium cation and the sulfonate anion (Figure 4.3a).[64] Strong inter/intra-molecular interactions lead to a range of unique properties. Anionic sulphonate groups may interact with cationic quaternary ammonia groups in the same monomer chain (intragroup), or form a head-to-tail stacking with opposite charges in the same polymer (intrachain), or attract the neighboring zwitterionic polymers (interchain), the combination of all effects leads to ionically cross-linked networks (Figure 4.3b,c). Polysulfobetaines have the ability to exhibit a UCST in solution due to ionic interactions, i.e. mutual inter/intra-molecular attraction of the zwitterionic groups (Figure 4.3b,c), which dominate below a critical temperature, the CP_{UCST}. Above the CP_{UCST}, this attraction weakens and a balance between attractive and repulsive interactions is generated, which promotes water-solubility due to the attractive water-polymer interactions (Figure 4.3d,e). In addition to the frequently found UCST-behavior in aqueous media, polysulfobetaines are also of high interest for responsive systems in the biomedical field by virtue of their high biocompatibility.[173] Moreover, in combination with hydrophobic and hydrophilic fragments, polybetaines can form well-defined micelles,[167] which is of high interest in the present project.

Addition of electrolytes to aqueous solutions of polysulfobetaines leads to enhanced viscosity and solubility, showing so-called "antipolyelectrolyte behavior" (chain expansion).[24,172,174,175] In general, the "polyelectrolyte behavior" is characterized by a decrease of viscosity and solubility in aqueous solution in presence of simple electrolytes, whereas, the "non-polyelectrolyte behavior" demonstrates no change in viscosity in similar conditions. According to Flory's formalism, the phase diagrams (transition temperature versus the polymer volume fraction in a solvent) depend on the solvent quality.[30] Most studies report on effectively increasing solvent quality with salt addition, making polysulfobetaines more soluble, and therefore lowering the transition temperature:[30,176-178] The salt-induced phase transition of a polysulfobetaine solution is a consequence of a Coulomb screening effect. Increase of ionic strength breaks the intra-/intermolecular interactions, frees the zwitterionic functional groups in the side chains, and causing the polymer coil to swell with water. Thus, the Flory-Huggins interaction parameter becomes increasingly negative (that is, its absolute value becomes larger) and a macroscopic consequence of this is the decrease of the critical temperature (UCST), $T_c \propto 1/|\chi|$.[30]

Moreover, the solution properties of polysulfobetaines are determined by the nature and the concentration of the added salt.[30,31,63,150,152,176,178] Salamone et al. have investigated the critical salt concentration (CSC), i.e. the minimum salt concentration needed for solubilization, of the polysulfobetaines and the respective effect of the cation and the anion nature on the CSC value.[176] Often specific ion effects are more pronounced with anions than with cations. Anions increase the solubility of polysulfobetaines ("salting-in") and thus affect the CSC. The effect of anions on the CSC follows the Hofmeister series or lyotropic series ($ClO^{4-} > I^- > SCN^- > Br^- > NO_3^- > Cl^- > F^- \approx SO_4^{2-}$).[150,177,178] Salamone et al. also proposed the "site-binding"/"atmospheric-binding" phenomenon, which explains the improvement of water-solubility of polyelectrolytes by addition of salts.[176] "Site-binding" is a consequence of Coulombic interactions of the counterions with specific sites of the polyelectrolytes, it gives rise to the formation of ion pairs in which the counterions have no mobility. "Site-binding" ability predominates at low salt concentration and is followed by "atmospheric-binding" at higher salt concentration. The latter is governed by the large electrostatic field, which surrounds the polymer. Binding of (almost) fully hydrated counterions is a long-range interaction and will occur if the charged groups are large and the charge is highly delocalized. In "atmospheric-binding", the counterions do have mobility, and there will be on average a slightly higher concentration of these mobile counterions near the polyion than in the bulk of

the solution. Thus, an addition of simple salts improves the water-solubility of polysulfobetaines only once a threshold concentration of added salt has been reached, whereas below the threshold concentration, addition of salt can decrease their solubility.[30] Very few studies report on the effect of small salt additions (smaller than a threshold concentration or the minimal salt concentration needed for dissolution of the polysulfobetaine), which can be adverse to the solubility of polyzwitterions and cause an increase of the critical temperature.[30,31]

The salt effect on polysulfobetaines depends on attractive interactions of polysulfobetaines with themselves, which, in turn, depends on their chemical structure. In the present project, two permanently zwitterionic sulfobetaine polymers with different structure are employed: well-established zwitterionic polymer PSPP (Figure 3.1a) and the closely related polymer PSBP (Figure 3.1b). SPP is the most attractive sulfobetaine monomer for the creation of zwitterionic polymers due to the best combination of polymerizability, hydrophilicity, and resistance to hydrolysis, at present it is commercially available.[31] With the aim to modulate the accessible range of cloud points of PSPP, Hildebrandt et al. varied the hydrophilicity of the spacer group that separates the ammonium and the sulfonate moieties.[32] Thus, PSBP has been created, which has a spacer between the charged groups, which is extended by one methylene group compared to PSPP (Figure 3.1a,b). A rather complex influence of the spacer group on the hydrophilicity of the zwitterionic moiety result in an increase of the CP_{UCST} of PSBP, compared to the one of analogous PSPP with a comparable molar mass.[32,102]

The UCST behavior of PSPP and PSBP was recently studied in detail.[30-32] It depends sensitively on the molar mass, and even more on the type and concentration of added low molar mass electrolytes. The salt effects are complex and reveal an interesting difference for PSPP and PSBP:[31,32] At low salt concentrations, the CP_{UCST} of PSPP increases with the amount of added salt. It passes through a maximum, beyond which it continuously decreases. The strongest effects on its CP_{UCST} were typically found for chaotropic anions in agreement with the Hofmeister series,[150,152] increasing in the order $SO_4^{2-} < Cl^- < Br^-$. For instance, for NaBr, the maximum of the CP_{UCST} is found at about 0.004 M for PSPP solutions in D_2O.[31] In contrast, in aqueous solutions of PSBP, the CP_{UCST} decreases monotonously when sodium halides are added, but pass through a minimum in the case of added sulfates.[32] In addition, the phase transition temperatures of both PSPP and PSBP have been recently shown to be

significantly higher in heavy water, D_2O, than in normal water, H_2O.[31] The reasons for the strong H-D-effect are not clear at present.

When combining a polysulfobetaine block with a nonionic thermoresponseive block, the sensitivity to ionic strength of polysulfobetaines offers the possibility to create a system, which responds sensitively to both temperature changes and changes in the electrolyte type and concentration.[23]

4.4. Previous investigations of the systems under investigation

Combination of the UCST of the zwitterionic polymers with the LCST of PNIPAM displays an intriguing temperature induced self-assembly behavior into different types of polymeric aggregates in aqueous solution.[22-24,87,149,179,180] As mentioned earlier, the group of Laschewsky have been pioneers in the field of dual thermoresponsive block copolymers consisting of a charged UCST block and uncharged LCST block.[22,23] Using RAFT reactions, diblock copolymers of PSPP and PNIPAM with low to moderate molar masses (10,000 and 50,000 g mol^{-1}) were prepared, which retained the capability of PNIPAM and PSPP blocks to undergo a LCST or an UCST transition, respectively. The carried-out studies were performed mostly in H_2O at high dilution, and focused on proving the occurrence of two transitions with subsequent polymer aggregation using ^1H NMR, turbidimetric, viscometric and DLS studies.[22,23] The polymers were soluble in water at temperatures between UCST and LCST and formed micellar aggregates both at temperatures below UCST and above LCST. Interestingly, qualitative solubilization experiments suggested that the presumed micellar aggregates formed due to the collapse of the PNIPAM block at elevated temperatures exhibit core properties which are markedly different from the ones of the aggregates formed due to the collapse of the PSPP block at low temperatures. For instance, the latter were incapable of solubilizing a hydrophobic dye.[22] Moreover, the effect of salt (NaCl, NaBr) was demonstrated for a few selected concentrations of the diblock copolymers in water, which suppressed the UCST transition completely, while the LCST transition temperature was only reduced slightly.

Interesting results have been reported lately on the investigation of the statistical copolymers from NIPAM and zwitterionic sulfobetaine methacrylate (SBMA, 4-((3-(methacryloyloxy)propyl)dimethylammonio)butane-1-sulfonate) monomers.[149,179,180] For instance, Chang et al. showed by means of UV-visible spectrophotometry how the UCST and

LCST of the copolymer systems were affected by changing the molar percentage of the two monomers, ionic environment, and their mass concentrations.[179] Combing zwitterionic and thermoresponsive features, Obiweluozor et al. recently investigated the viscoelastic behavior of a zwitterionic copolymer of NIPAM, containing 10 mol% of SBMA, in aqueous solution as a function of ionic strength in the presence of different ions.[149] They demonstrated that zwitterions play an important role in slowing down the precipitation process at the LCST of PNIPAM in salt-free conditions and that the attractive interactions among the sulfobetaine chain could be effectively manipulated by the amount of low molecular weight ions, which, in turn, affect the LCST. Zhao et al. compared the statistical copolymer consisting of NIPAM monomers and different zwitterionic monomers, namely SBMA and carboxybetaine methacrylate (CBMA).[180] The authors showed that SBMA inhibits the thermo-sensitive and viscoelastic features of the corresponding copolymer system, causing a delayed LCST and weakened viscoelastic response, compared to the PNIPAM. In contrast, CBMA monomers in P(NIPAM-*co*-CBMA) copolymer acted as stronger ionic bridges to form elastic networks when compared with P(NIPAM-co-SBMA) copolymer. Thus, the structure of the zwitterionic segments play an important role in the self-assembly of copolymers with PNIPAM in aqueous solution.

4.5. The diblock copolymers under investigation

In the present work, we focus on the investigation of the aggregation behavior of the diblock copolymers consisting of a zwitterionic block, either PSPP or PSBP (Figure 3.1a,b) and a nonionic block, either PNIPAM or PNIPMAM (Figure 3.1c,d), in aqueous solution. The chemical structures of the diblock copolymers under investigation are shown in Figure 4.4. The details of the chosen design of the diblock copolymers see in chapters 6-8. All diblock copolymers were prepared by consecutive reversible addition-fragmentation chain transfer polymerization (RAFT) polymerizations by Dr. Viet Hildebrand (Institute of Chemistry, University of Potsdam, Potsdam-Golm, Germany). Different from the first "schizophrenic" block copolymers studied based on PSPP and PNIPAM, which were synthesized in the early days of the RAFT polymerization technology,[22] in the present study, the block sequence in the synthesis was chosen as PSPP-*b*-PNIPAM, in order to enhance the blocking efficiency.[181] The block sequence for all block copolymers in the present work was kept identical: namely PSPP-*b*-PNIPAM, PSPP-*b*-PNIPMAM, PSBP-*b*-PNIPAM and PSBP-*b*-PNIPMAM. A RAFT agent was chosen that is well-suited for polymerizing methacrylic monomers, and that

had been additionally labeled with a fluorescent dye via the R-group (Figure 4.4). This end-group label serves not only as a tracer, but also facilitates the a priori difficult molar mass analysis of amphiphilic and zwitterionic block copolymers.[31,32] Further details of the synthesis can be found elsewhere.[168] The polymers were characterized by ^{1}H nuclear magnetic resonance (NMR) and ultraviolet-visible (UV-vis) spectroscopy (Table 4.1).

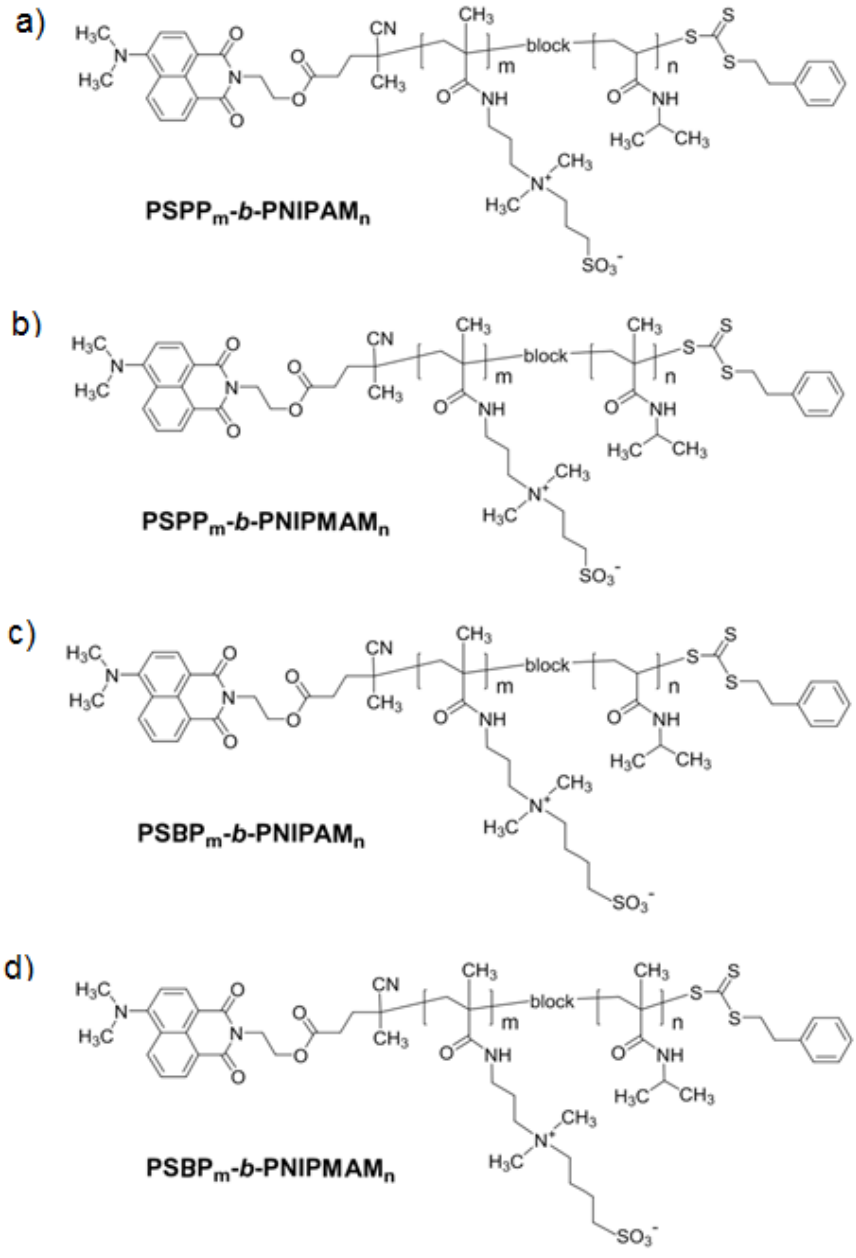

Figure 4.4: Chemical structures of the diblock copolymers under investigation, (a) PSPP$_m$-*b*-PNIPAM$_n$ (*m* = 430, *n* = 200), (b) PSPP$_m$-*b*-PNIPAM$_n$ (*m* = 498, *n* = 144), (c) PSBP$_m$-*b*-PNIPAM$_n$ (*m* = 78; *n* = 100) and (d) PSBP$_m$-*b*-PNIPAM$_n$ (*m* = 51, 78 or 243; *n* = 156, 115 or 103). Every macromolecule carries one naphthalimide chromophore moiety (the group on the left), which is the fluorescence label.

Table 4.1. Molecular characteristics of the polymers studied

Polymer	M_n [g mol^{-1}]		
	theoretically expected[a)]	via ^{1}H NMR[b)]	by end group analysis[c)]
$PSPP_{430}$[d)]	127,000	-	113,000
$PSPP_{498}$[d)]	146,200	-	185,000
$PSBP_{51}$[d)]	16,200	24,200	16,800
$PSBP_{78}$[d)]	24,500	29,700	29,900
$PSBP_{243}$[d)]	75,100	-	-
$PNIPMAM_{195}$	24,800	-	29,000
$PSPP_{430}$-*b*-$PNIPAM_{200}$	150,000	149,000	152,000
$PSPP_{498}$-*b*-$PNIPMAM_{144}$	164,500	160,000	210,000
$PSPP_{51}$-*b*-$PNIPMAM_{156}$	36,500	34,400	49,900
$PSBP_{78}$-*b*-$PNIPMAM_{115}$	39,100	35,700	45,700
$PSBP_{78}$-*b*-$PNIPAM_{100}$	35,800	37,600	46,100
$PSPP_{243}$-*b*-$PNIPMAM_{103}$	88,200	82,700	83,700

[a)]calculated from monomer conversion and molar ratios of monomer and CTA, [b)]calculated from the relative signal intensities of the ^{1}H NMR signals of the PSPP, PNIPAM and PNIPMAM blocks, assuming that the molar mass of the PSPP block is the same in the macroRAFT and in the block copolymer, [c)]based on the UV/Vis absorbance band at 442 nm of the R group, [d)]employed as macro CTA in the synthesis of the block copolymer.

4.5.1. Sample preparation

Polymer solutions were prepared in salt-free D_2O, in 0.002 M, 0.004 M NaBr or in 0.006 M NaCl in D_2O. The polymer concentrations were 2 - 50 g L^{-1} for turbidimetric measurements 10 g L^{-1} for DLS and 50 g L^{-1} for SANS. All polymer solutions were equilibrated for about 2 days in a thermoshaker at temperature, where they are expected to be molecularly dissolved: the diblock copolymers PSPP-*b*-PNIPAM, PSPP-*b*-PNIPMAM, PSBP-*b*-PNIPAM at 35 °C and PSBP-*b*-PNIPMAM at 40 °C. To avoid salt contaminations from cuvettes, the cuvettes were rinsed with organic solvents and D_2O in the final step before sample preparation.

5. Characterization methods

The self-assembly of diblock copolymers with different architecture in solutions is of interest in the present project. The behavior of the cloud points for the homo- and the diblock copolymers in salt-free solution and in the presence of electrolyte were determined using turbidimetry. In order to determine the size of formed particles in diblock copolymer solutions dynamic light scattering (DLS) measurements were performed. Internal structures in the polymer solutions, namely solutions of the diblock copolymers under investigation and the PNIPMAM homopolymer, were addressed by small-angle neutron scattering (SANS) measurements. In the present chapter, the main principles of the three above-mentioned methods are presented.

5.1. Turbidimetry

Turbidity is an expression of the optical property of a medium, which causes light to be scattered and absorbed rather than transmitted in straight lines through the sample.[182] Turbidity in a liquid is caused by the presence of finely divided suspended particles.

Turbidity can be defined by ultraviolet-visible spectroscopy (UV-vis) measurements: The emitted light from a source for the visible wavelengths passes through a medium and the resulting light is sensed by the measurement detector. UV-vis spectrometer measures the intensity of light passing through a sample (I), and compares it to the intensity of light before it passes through the sample (I_0). The ratio I/I_0 is called the transmission (T), and is usually expressed as a percentage. When measuring absorbance (A) in a UV-vis spectrometer, the transmission calculates using equation:

$$T,\% = 10^{-(A-2)}. \tag{5.1}$$

5.1.1. Instrument

The turbidimetry measurements were performed using a Varian Cary 50 UV−vis spectrometer from Varian Inc., Palo Alto, CA. It contains the basic parts of a spectrophotometer: a light source, a holder for the sample, a beam splitter to separate the different wavelengths of light, and dual Si diode detectors.[183] The radiation source is a Xenon flash lamp, owing to which the light beam is narrow and very intense with excellent noise

performance due to a small aperture. The instrument is equipped with a single cell Peltier thermostat for the temperature control.

5.2. Dynamic light scattering

Dynamic light scattering (DLS) is an important and one of the most popular experimental techniques, which is used to determine the size distribution profile of small particles in suspension of colloidal particles in solution, it allows particle sizing down to 1 nm diameter.[184-186] DLS is often used to monitor aggregation in polymer solutions. In this method, the sample in the cell is illuminated with monochromatic coherent laser light, and the light is scattered by fluctuations of the concentration of molecules, particles, or aggregates suspended in a sample solution and undergoing Brownian motion (Figure 5.1). The intensity fluctuations of the scattered light are recorded as a function of time and converted into electrical pulses, which are fed into a digital correlator. The rate of decay of the fluctuations of scattered light is indicative of the diffusion coefficient of the scattering species in the sample, which is lower for large particles and higher for small particles.

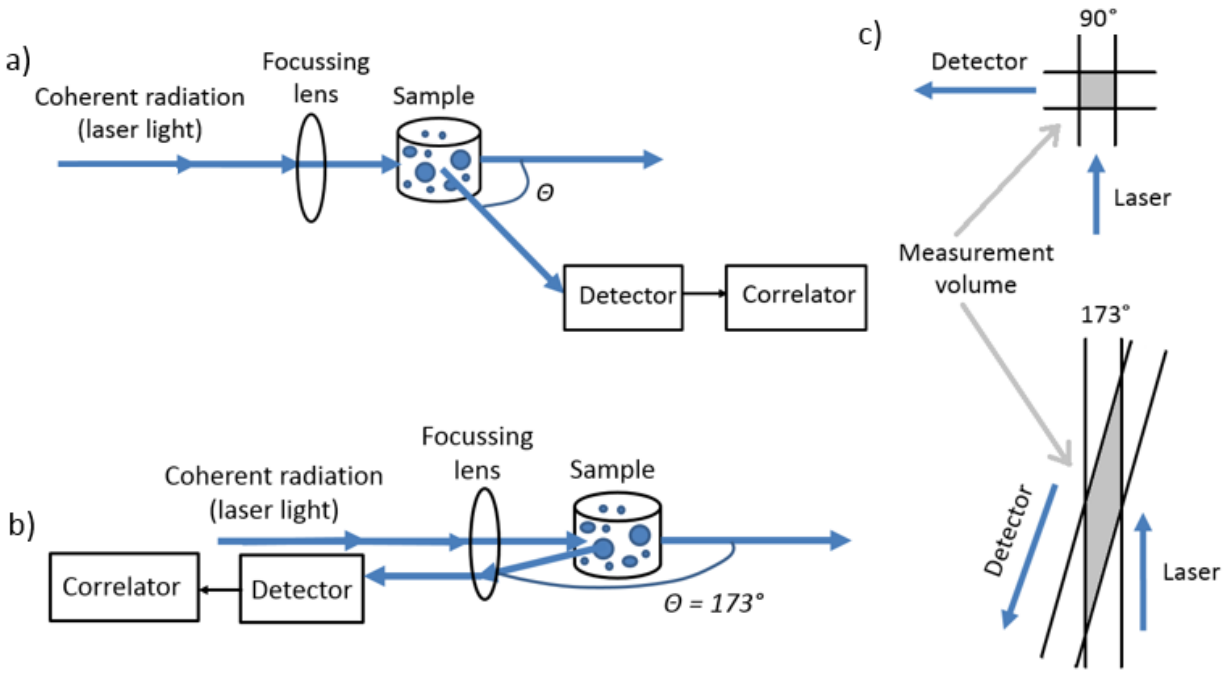

Figure 5.1: Schematic representation of: conventional, 90° dynamic light scattering instrument (a); and backscattering, 173° DLS instrument (b). Measurement volume at 90º and 173º.

In most instruments, a monochromatic coherent He-Ne, Ar or Kr ion lasers with a fixed wavelength are used as the light source, which converges to a waist of focus in the sample, by use of a focusing lens. Particles of different sizes scatter with different intensities in dependence of the scattering angle and photon detection at several scattering angles (multiangle DLS), for instance wide-angle light scattering setups covering approximately the range 20° - 180°, may provide a high quality analysis for polydisperse samples. In contrast, a conventional DLS instrument only detects the scattered light at one angle. For highly dilute solutions, almost transparent, the DLS instrument with detection of the scattered light signal at 90° (right angle, Figure 5.1a) is used, while for more concentrated solutions, and aggregated particles, the instrument with detector at 173° (backscattering angle, Figure 5.1b) is more applicable.[187] The DLS measurements with the right angle detection is successfully applied for analysis of sample solutions with concentration that gives the highest scattering light intensity, but below the concentration where multiple scattering effect starts to occur. Backscattering geometry of the DLS measurement with non-invasive backscatter (NIBS) system allows to reduce the multiple scattering effect, due to the minimization of the distance through the cuvette that light must travel from the scattering volume. Moreover, the measurement volume is increased by about 8-fold compared with a 90º instrument, with a corresponding increase in sensitivity (Figure 5.1c). In addition, by moving a focusing lens, through which pass both the incident and the scattered beams, between the laser and the sample, it is possible to shorten or to enlarge the measurement position within the cell. The shorter distance from the cell allows to reduce the distance that the light must travel through the sample within the cell and hence to minimize multiple scattering. The larger distance allows to minimize the effect of laser flare to increase the signal to noise ratio and to improve sensitivity, particularly to weakly scattering and dilute samples.

5.2.1. Data processing

Dynamic light scattering outputs the normalized time autocorrelation function, $G^{(2)}(\tau)$, of the scattered light intensity fluctuations, which directly related to the motion of particles in solution; it is generated from the intensity trace as follow:

$$G^{(2)}(\tau) = \frac{\langle I(t)\rangle\langle I(t+\tau)\rangle}{\langle I(t)\rangle^2}, \qquad (5.2)$$

where $\langle I(t)\rangle$ is the initial intensity for all starting times *t* and $\langle I(t+\tau)\rangle$ is the intensity after a delayed time τ.[188] After only a very short time interval, the correlation of the scattering intensity is high and the intensity is essentially unchanged. At longer time delays, the correlation between the scattered intensity of the initial and final states is decreases and the correlation function decays exponentially. When the intensity correlation is lost, the correlation functions reaches zero.

The intensity fluctuations are correlated with fluctuations in the electric field. The correlation function of the scattered electric field, $G^{(1)}(\tau)$, can be obtained using the Siegert relation:

$$G^{(2)}(\tau) = 1 + \beta\left[G^{(1)}(\tau)\right]^2, \tag{5.3}$$

where β is the coherence factor, which represents the degree of spatial coherence of the scattered light over the detector and is determined by the geometry of the instrument.

The correlation function for dilute suspensions of identical species in Brownian motion decays exponentially with decay rate Γ:

$$G^{(1)}(\tau) = e^{-\Gamma\tau}. \tag{5.4}$$

The decay rate Γ is the inverse of the correlation time τ and related to the transitional diffusion coefficient of the particle D_t as follow:

$$\Gamma = D_t q^2, \tag{5.5}$$

D_t may be derived at a single angle or at a range of angles depending on the momentum transfer *q*, given by:

$$q = \frac{4\pi n_0}{\lambda_0}\sin\frac{\theta}{2}, \tag{5.6}$$

where λ_0 is the incident laser light wavelength, n_0 the refractive index of the sample solution and θ is the scattering angle at which the detector is located with respect to the sample cell.

The size of non-interacting diffusing particles can be determined using the Stokes-Einstein relation, which links the diffusion coefficient of a molecule or particle with its radius:

$$D = \frac{k_B T}{6\pi\eta_0 R_H}, \tag{5.7}$$

where k_B is Boltzmann's constant, T is the absolute temperature and η_0 is the viscosity of the solution and R_H is the particles hydrodynamic radius.

In the case of polydisperse sample with two different particle sizes, the autocorrelation function is a sum of two exponential decays corresponding to each of the species in dilute suspension:

$$G^{(1)}(\tau) = A_1\left[e^{-\Gamma_1\tau}\right] + A_2\left[e^{-\Gamma_2\tau}\right], \tag{5.8}$$

where A_1 and A_2 are the amplitudes of the corresponding decay modes ($A_1 + A_2 = 1$), Γ_1 and Γ_2 are the inverse of the correlation times τ_1 and τ_2, respectively, and β_1 and β_2 are the corresponding stretching exponents which are characteristic of the breadth of the distribution of the relaxation times and assumes values in the interval [0, 1].[189]

For data evaluation, the DTS (Nano) software (Malvern) was used, which provides the hydrodynamic radius, R_h, and the fraction of each measured species.

5.2.2. Instrument

DLS measurements were carried out using a Zetasizer Nano ZS (Malvern) laser particle size analyzer, which is a high performance two angle size analyzer of particles and molecules in solution.[190] The laser particle size analyzer equipped with a 633 nm laser at an angle of 173° (backscattering detection). Non-invasive backscatter (NIB) system is used in Zetasizer Nano ZS, which provide the highest sensitivity simultaneously with the highest size and concentration range: a size measurement from 1 nm (hydrodynamic radius, R_h) to 1000 nm. It allows to measure small samples, minimum sample volume is 12 μL, and samples concentration from very low to high, i.e. from 0.1 ppm to 40% w/v. The instrument temperature range extends from 0 °C to 90 °C, with an additional option of measurements at 120 ºC. The Zetasizer software controls the optical unit as well as processing and presenting the measured data to give the size, fraction, molecular weight or zeta potential for the sample measured.

5.3. Small-angle neutron scattering

Small-angle neutron scattering (SANS) is one of the most powerful experimental methods to study the structure, the organization and the dynamics of particles or aggregates in a continuous medium. SANS uses elastic neutron scattering at small scattering angles which allow probing inhomogeneities at a mesoscopic scale, i.e. from the near atomic scale (1 nm) to the near micron scale (600 nm).[191]

The neutron was discovered by Chadwick in 1932. It has zero charge, a mass equivalent to 1839 electrons (1.67×10^{-27} kg), a spin of 1/2 and a magnetic moment of -1.9132 nuclear magnetons and a lifetime of 15 minutes (885.9 s).[192] SANS uses thermal neutrons having an average energy of motion (kinetic energy) corresponding to the average energy of the particles of the material they are permeating, in the 5 to 100 meV range ($\approx k_BT$, where k_B is Boltzmann's constant). The neutrons have the wavelengths of the order of 10^{-10} m (0.5–2 nm), which is comparable to atomic sizes and interatomic spacing. Neutrons are uncharged, their electric dipole moment is either zero or too small to measure, they interact with atomic nuclei and magnetic fields from unpaired electrons rather than via electrical forces. The interaction of neutrons with matter is weak, and the absorption of neutrons by most materials is correspondingly small. Neutron radiation is therefore very penetrating and causes negligible radiation damage. Moreover, neutrons are highly sensitive to the isotope composition, e.g. the interaction (absorption and scattering) of neutrons with hydrogen and deuterium is quite different from one another, which may provide high selective contrast between particles and matrix.[192] Furthermore, isotope substitution, e.g. partial deuteration of the components of a sample, is extremely useful with SANS through control of the scattering contrast. These major advantages of neutron scattering making SANS the most powerful analytical tool for investigating soft matter, particularly polymers, and obtaining detailed structural information.[193]

In this chapter, the principle of elastic small-angle neutron scattering will be discussed including the experimental aspects, the principle of the method the description of a SANS instrument and the data reduction. The later part is dedicated to data interpretation and analysis.

5.3.1. Scattering set-up and momentum transfer

The focus of the following section is on elastic small-angle neutron scattering. The following information was taken from the [194-196]

The schematic representation of a SANS experiment is presented in Figure 5.2. A well collimated neutron beam with wavelength λ (selected by a velocity selector) can be described by a planar monochromatic wave, the propagation equation can be written as:

$$\varphi(x,t) = \varphi_0 e^{-i(kt-\omega t)}, \tag{5.9}$$

$\omega = 2\pi / T$ is the pulsation frequency and k_i is the incident wave vector; the magnitude is $k = 2\pi / \lambda$. The high flux required for SANS measurements can only be achieved by using a large wavelength distribution, which is typically Δλ/λ = 10% - 20% (Δλ/λ - full width at half maximum value of the function describing the wavelength distribution). Most of the incident radiation is transmitted through the sample without any further interaction and some radiation might be absorbed. Only a certain fraction of the incident beam is interacting with the sample and is scattered at an angle $0° < \theta < 20°$. As the incident neutron beam arrives at an atom, the scattered atom gives rise to a scattered spherical wave. In SANS, only the elastic interaction between the neutron beam and the sample is considered, which implies no energy change and thus only spatial information is provided on the scattering system. The scattered neutrons change their direction, i.e. the direction of the scattering vector $\vec{k_s}$. The scatterers are detected by an area position-sensitive detector.

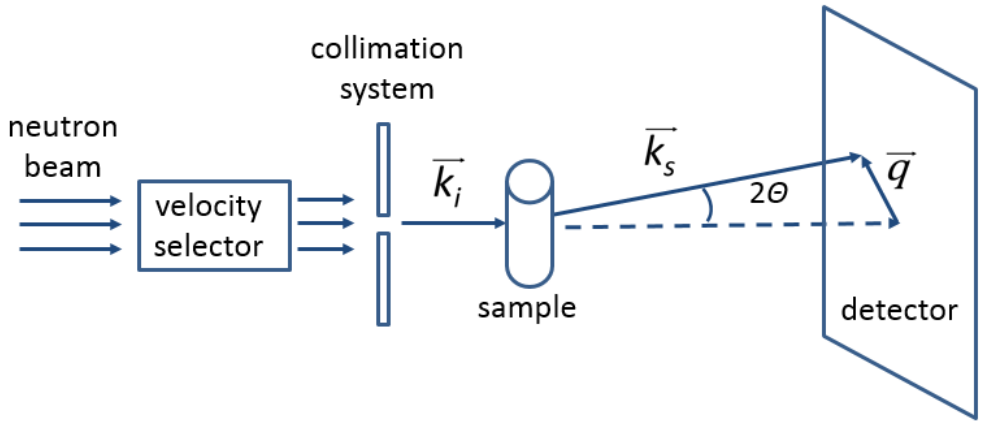

Figure 5.2: Schematic representation of a small-angle scattering experiment and of the scattering vector $\vec{q}$. Modified from Ref. [194]

In the SANS experiment, the scattered intensity is recorded as a function of scattering angle θ, the angle between $\overrightarrow{k_s}$ and $\overrightarrow{k_i}$ at a certain distance away from the sample. In order to compare results obtained at different wavelengths, detector distances and scattering angles, a more convenient parameter is the scattering vector (or wave vector or momentum transfer) which is the difference between incident and scattered wave vectors ($\vec{q} = \overrightarrow{k_s} - \overrightarrow{k_i}$). In the case of elastic scattering $|\overrightarrow{k_s}| = |\overrightarrow{k_i}|$. The momentum transfer q can be obtained using the relationship between θ and λ:

$$q = \frac{4\pi}{\lambda} sin\frac{\theta}{2}. \qquad (5.10)$$

5.3.2. Scattering cross-section

SANS experiment consists in comparing the incident intensity I_i with the scattered intensity I_s, measured at angle θ and a distance L on a detector area $A_{\text{det}} = \Delta\Omega \cdot L^2$, where $\Delta\Omega$ is the solid angle (Figure 5.3).[195] The ratio of both intensities is a measure of the scattering power of a sample, called the differential scattering cross-section of the sample per unit solid angle, $d\sigma/d\Omega$:

$$\frac{I \times L^2}{I_i} = \frac{d\sigma}{d\Omega}. \qquad (5.11)$$

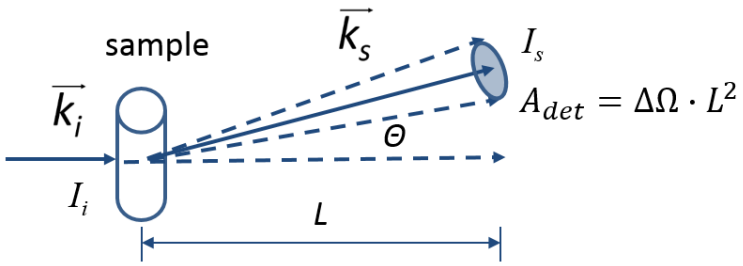

Figure 5.3: The geometry of a scattering experiment. Modified from Ref. [195]

Normalization to the unit sample volume (V) yields the differential scattering cross-section which represent the probability of incident neutrons scatterer being scattered out from the unit sample volume into the solid angle $\Delta\Omega$:

$$\frac{d\sigma}{d\Omega} \times \frac{1}{\mathrm{V}} = \frac{d\Sigma}{d\Omega} \ (\mathrm{cm}^{-1}). \qquad (5.12)$$

This cross-section is the sum of the coherent scattering and an angle-independent incoherent component, due to scattering from uncorrelated nuclei.[196] The incoherent scattering cross section represents neutrons emitted in all directions without interference, it is *q*-independent and does not contain information about structure; it is used for inelastic measurements probing molecular motions. Only the coherent scattering provides structural information (size and shape of the scattering entities) of the sample.

For an assembly of *N* atoms, the incident planar wave is interacting with the sample's atoms, which leads to interference of spherically symmetric waves. The length scales observed with SANS are much larger than interatomic distances. The amplitude scattered by the different particles, positions of which are not correlated at long range, can be written as:

$$A(\vec{q}) \propto \int_V \rho(\vec{r}_i) e^{-i\vec{q}\vec{r}_i} d\vec{r} \,. \tag{5.13}$$

$\rho(\vec{r}_i)$ is the scattering length density (SLD), which reads as:

$$\rho = \frac{\sum_i b^i}{V}, \tag{5.14}$$

where b^i is the scattering length of the relevant atom, characterizing the range of interaction, and *V* is the volume containing the *N* atoms. Considering solution of *n* polymer chains composed of *N* atoms each, the differential scattering cross-section of the sample reads as a function of momentum transfer *q*:

$$\frac{d\sigma}{d\Omega}(\vec{q}) = \frac{1}{N} \sum \sum b_i b_j e^{-\left[i\vec{q}(\vec{r}_i - \vec{r}_j)\right]}, \tag{5.15}$$

where the relative positions of only a pair of scatterers play a role. This equation can be rearranged, by the integration across the whole sample and taking into account eqn. 5.12, to:

$$\frac{d\Sigma}{d\Omega}(\vec{q}) \propto \frac{1}{V}(\rho_1 - \rho_2)^2 \int_V e^{-\left[i\vec{q}(\vec{r}_i - \vec{r}_j)\right]} d\vec{r}_i d\vec{r}_j, \tag{5.16}$$

where $(\rho_1 - \rho_2)$ is the difference of length scattering densities between scatterer and the medium, e.g. the polymer chain and the solvent, respectively.

5.3.3. Characterization of a system of particles

This coherent cross-section is related to properties of the material, an assembly of *N* particles, in terms of a form factor, *P(q)*, that represents the interference of neutron scattered from different parts of the same object, and a structure factor, *S(q)*, that represents the interference of neutrons scattered from different objects:

$$\frac{d\Sigma}{d\Omega}(q) = \frac{N}{V}(\rho_1 - \rho_2)^2 V_p^2 P(q) S(q). \quad (5.17)$$

For low concentrations of scatterers, the scattering intensity is governed primarily by the form factor and *S(q)* = 1; however, for higher concentrations, interparticle correlations become significant. The form factor describes the size and shape of the scattering objects and for many simple particle shapes can be evaluated analytically, whereas for complex biomolecules, for example, it has to be deduced or constructed from these.

In the case of an isotropic solution the azimuthal average is trivial for the structure factor:

$$S(q) = 1 + \frac{N}{V}\int_0^\infty 4\pi r^2 [g(r) - 1]\frac{\sin(qr)}{qr} dr, \quad (5.18)$$

where g(r) is the pair correlation function for the particles centers of mass $g(r) = e^{U(r)/k_B T}$ (*r* is a radial distance outward from the center of any scattering particle in the sample) and its natural logarithm is directly related to the potential energy function *U(r)* that describes the interparticle interaction.

5.3.4. Instruments

The SANS experiments presented in this work were performed at two different instruments, namely D11 at the Institute Laue-Langevin (ILL) in Grenoble, France, and KWS-1 at Heinz Maier-Leibnitz Zentrum (MLZ) operated by Jülich Centre for Neutron Science in Garching, Germany. The instruments description is based on the information taken from the refs. [197].

KWS-1 SANS instrument

KWS-1 is a high flux, high resolution SANS instrument (Figure 5.4) owing to its neutron velocity selector with $\Delta\lambda/\lambda$ = 10%, the wavelength resolution of the incoming neutron beam

controlled by a high-speed chopper. Accessible wavelengths of the incident neutrons vary from 0.45 to 4.2 nm. Neutron beam collimated in the 20 m-long collimation line, which is enclosed in a nonmagnetic evacuated chamber and consists of 18 carriages (a 1 m-long neutron guides of 50 × 50 mm cross section) and five active apertures positioned at 2, 4, 8, 14 and 20 m from the sample and used to define the source aperture for the corresponding collimation distances. The source aperture (square or rectangular shape) can be arbitrarily defined from 1 × 1 mm^2 up to 50 × 50 mm^2. MgF_2 focusing lenses enable an increase in the neutron flux and provide a wide q range. The covered *q* range of the KWS-1 instrument extends from 0.007 to 5 nm^{-1}. The signal is recorded by a large two-dimensional position-sensitive scintillation detector of Anger type with a 64 × 64 cm^2 area and a resolution of 6.25 mm. The beamstop 50 × 50 mm is fixed in the middle of detector, which has a small window for a ^{3}He counter allowing determining the intensity of the direct beam for transmission measurements. A larger 70 × 70 mm beamstop with analogous window, which can be moved in and out of the beam, is only utilized when the full neutron guide cross section is used. The detector can move along the tube as well as across the neutron beam, so that for each sample-to-detector distance the center of the detector can be precisely adjusted to the direct beam according to the neutron wavelength.

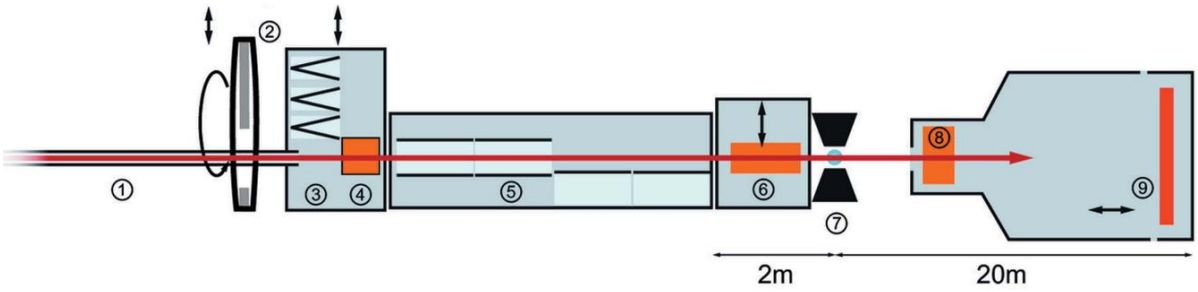

Figure 5.4: A schematic representation of the KWS-1 SANS diffractometer: (1) S-shaped neutron guide; (2) high-speed chopper; (3) polarizer changer; (4) radio-frequency spin flipper; (5) neutron guide sections (18 × 1 m); (6) MgF_2 focusing lenses; (7) sample position with hexapod for heavy loading; (8) ^{3}He analyzer with reversible polarization (to be implemented); (9) Anger-type scintillation detector. Adapted from ref. [197].

D11 SANS Instrument, ILL

D11 is a standard pinhole geometry instrument, designed for the study of large scale structures in soft matter systems, chemistry, biology, solid state physics and materials science. The operating principle is similar to that of a KWS-1 instrument, described above.

The polychromatic neutron beam is monochromated by a helical slot (ASTRIUM) velocity selector with $\Delta\lambda/\lambda$ = 9 % with accessible wavelengths range from 0.45 to 4 nm. The neutrons are collimated by a series of moveable glass guides controlled by computer. Guide sections are inserted into or removed from the beam depending on the incident beam divergence required. The sample zone, situated 40 m down-stream from the velocity selector. Neutrons scattered from the sample are detected by a ^{3}He gas detector with an area 128 × 128 cm^2 and a pixel size of 7.5 × 7.5 mm^2. The detector mounted on a moveable trolley within the evacuated detector tube and may be placed at any distance between 1.2 and 39 meters from the sample position, giving a total accessible momentum transfer range from 0.003 to 0.1 nm^{-1}.

5.3.5. Data Analysis

Data analyses of SANS experiments rely on fitting models, which help to extract structural information. The models used in fitting of the SANS curves in this work will be presented in this chapter.

5.3.5.1. Form factors

Self-assembly of amphiphilic block copolymers results in formation of stable aggregates or micelles, which can adopt a variety of shapes.[198] The form factors describing SANS curves from the solutions of the block copolymers under investigation consisting from interacting particles, namely spherical and cylindrical micelles, were used in this work.

Form factor of polydisperse, homogeneous spheres

The form factor that is based on the simplest model for scattering from a spherical homogeneous sphere and accounts for a continuous distribution of particle size, $P_{\text{sphere}}(q)$, is given by:[199]

$$P_{sphere}(q) = \left(\frac{4\pi}{3}\right)^2 N_0 (\Delta\rho)^2 \int_0^\infty f(r) r^6 F^2(q) dr, \qquad (5.19)$$

where N_0 is the total number of particles per unit volume. $\Delta\rho$ is the difference in scattering length density of the sphere and the solvent: $\Delta\rho = \rho_{sphere} - \rho_{solvent}$ (values used see below). *f(r)* is the normalized Schulz distribution:[200]

$$f(r) = (z+1)^{z+1} u^2 \frac{u \exp[-(z+1)u]}{\sigma_{avg} \Gamma(z+1)}. \quad (5.20)$$

$u = r / r_{avg}$, where r_{avg} denotes the average radius; $\Gamma(n)$ is the Gamma function and z is related to the polydispersity by $z = 1/(p^2 - 1)$. $p = \sigma / r_{avg}$, where σ^2 is the variance of the distribution. $F(q)$ is the scattering amplitude of a sphere having a radius r:

$$F(q) = \frac{3[\sin(qr) - qr\cos(qr)]}{(qr)^3}. \quad (5.21)$$

Figure 5.5 presents four examples of the form factor of polydisperse, homogeneous spheres with different radius and/or polydispersity, assuming in all four cases similar SLD values of the spheres and the solvent, as well as the volume fraction of the spheres in the solution, the change of which would alter only the value of the intensity value.

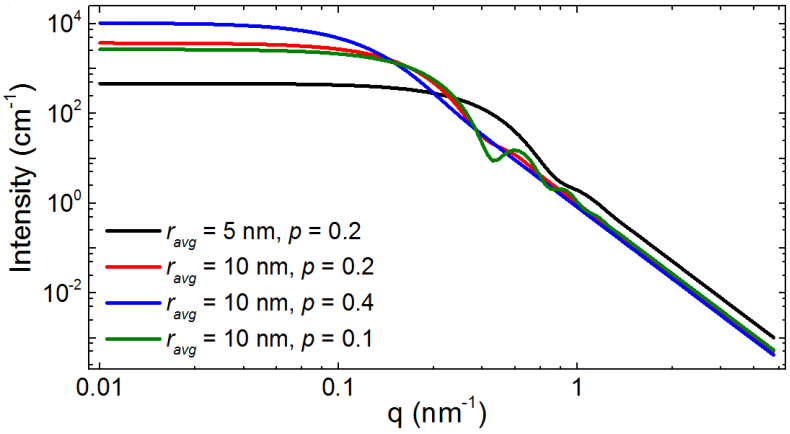

Figure 5.5: Form factor of polydisperse, homogeneous spheres. Different curves correspond to various values of the parameters as described in the graphs. In all cases the volume fraction of the spheres is 0.01 and the SLD values of the spheres and the solvent are ρ_{sphere} = 1.0 × 10^{-4} nm^{-2} and $\rho_{solvent}$ = 6.4 × 10^{-4} nm^{-2}, respectively.

Form factor for core-shell micelles

In a selective solvent, block copolymers tend to self-assemble into micelles. In aqueous solution, the amphiphilic property of block copolymers composed of hydrophilic and hydrophobic segments can cause formation of core-shell structures in which the hydrophobic core is insulated from the water by shell, the core and shell are characterized by different

density. For the solution of the block copolymer where density distribution of the micelles is assumed, the form factor of a core-shell particle, $P_{\text{core-shell}}(q)$, having a polydisperse core and a uniform shell thickness is used,[201,202] which reads:

$$P_{\text{core-shell}}(\text{q}) = \frac{1}{\langle \text{V}_{\text{mic}} \rangle} \int_0^\infty f(\text{r}_{\text{core}})\, F_{\text{core-shell}}{}^2(q)\, dr\,, \tag{5.22}$$

$$F_{\text{core-shell}}(\text{q}) = \frac{3V_{core}(\rho_{core} - \rho_{shell})\, j_1(qr_{core})}{qr_{core}} + \frac{3V_{mic}(\rho_{shell} - \rho_{solv})\, j_1(qr_{mic})}{qr_{mic}}, \tag{5.23}$$

where $j_1(x) = (\sin x - x\cos x)/x^2$ and the micellar radius, r_{mic}, is the sum of the core radius, r_{core}, and the shell thickness, t: $r_{mic} = r_{core} + t$. The form factor is normalized by the average micelle volume $\langle V_{mic} \rangle = 4\pi \langle r_{mic}{}^3 \rangle / 3$. The function $f(r_{core})$ is the normalized probability of finding a particle with a core radius between r_{core} and $r_{core} + dr$, and it accounts for the polydispersity of the cores according to a Schultz distribution (Eq. 5.20). The polydispersity of the core radius is $p_{core} = \sigma / r_{core}$.

Figure 5.6 shows four examples of the form factor of core-shell micelles with a polydisperse core for the various values of the core radius, polydispersity of the core and the shell thickness. The SLD values of the core, shell and solvent are identical in all four cases.

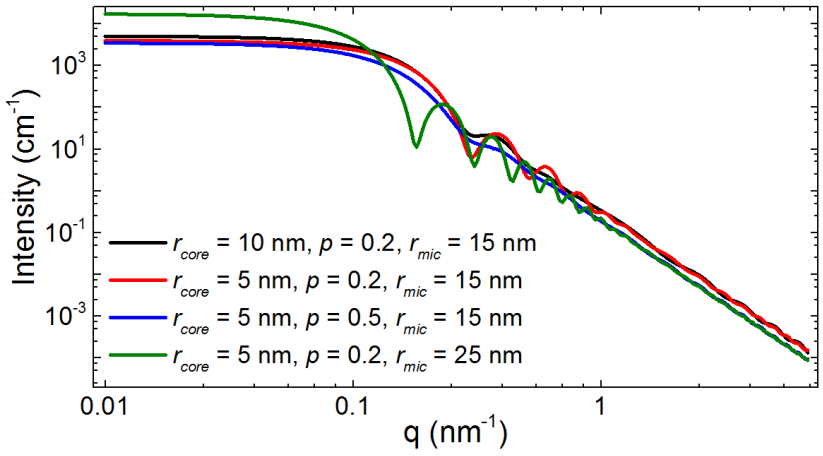

Figure 5.6: Examples of the form factor of core-shell micelles with a polydisperse core. Different lines represent the curves for different values of the parameters as described in the

graphs. In all cases the SLD values of the core, shell and solvent are $\rho_{core} = 5 \times 10^{-5}$ nm^{-2}, $\rho_{shell} = 1 \times 10^{-4}$ nm^{-2} and $\rho_{solvent} = 6.4 \times 10^{-4}$ nm^{-2}, respectively.

Form factor for flexible cylinder with polydispersity radius

One of the basic micellar morphologies is cylindrical micelles, which are often referred to as "worm-like", "rod-like" or even "thread-like" micelles.[203] This morphology less frequently observed, compared to spherical micelles. Such polymer-like micelles are typically composed of several amphiphilic molecules and are thus continuous in nature. A scattering function for semiflexible cylinders with disperse radii developed by Pedersen et al.[204] and then modified by Chen et al.[205] was employed.

The form factor for semiflexible chains of cross-sectional radius R_{avg}, contour length L, Kuhn length describing the local stiffness of the chain b, represented as the product of the cross-section form factor P_{CS},[205] scattering function of single semiflexible chain with excluded volume effects P_{WC}[204] and the difference in scattering length density of the cylinder and the solvent $\Delta\rho$:[206]

$$P_{FC}(q) = \Delta\rho^2 P_{CS}(q,R) S_{WC}(q,L,b). \tag{5.24}$$

The cross-section form factor P_{CS} of cylindrical chain can be approximated as follows:

$$P_{CS}(q,R_{avg}) = \left[\frac{2j_1(qR_{avg})}{qR_{avg}}\right]^2. \tag{5.25}$$

$$\begin{aligned} S_{WC}(q,L,b) &= \left[1 - w(qR_g)\right] S_{Debye}(q,L,b) + \\ & w(qR_g)\left[C_1(qR_g)^{-1/\nu} + C_2(qR_g)^{-2/\nu} + C_3(qR_g)^{-3/\nu}\right] \end{aligned} \tag{5.26}$$

$S_{Debye}(q,L,b)$ is the Debye function, or the scattering function of a flexible chain without excluded volume effects, given by:

$$S_{Debye}(q,L,b) = 2\left[\exp(-R_g^2 q^2) + R_g^2 q^2 - 1\right] / R_g^4 q^4 \tag{5.27}$$

R_g is the radius of gyration with excluded volume effects, and it is given by:

$$R_g = \left\langle R_g^2 \right\rangle^{1/2} = \alpha(n_b)^2 \left\langle R_g^2 \right\rangle_0, \tag{5.28}$$

where $n_b = L/b$ is the number of statistical segments of the chain and $\alpha(L/b)^2$ is the expansion factor which follows the following empirical expression:

$$\alpha(x)^2 = \left[1 + (x/3.12)^2 + (x/8.67)^3\right]^{0.17/3} \tag{5.29}$$

$\left\langle R_g^2 \right\rangle_0$ is the average of the square of the radius of gyration which reads as:

$$\left\langle R_g^2 \right\rangle_0 = \frac{Lb}{6}\left[1 - \frac{3}{2n_b} + \frac{3}{2n_b^2} - \frac{3}{4n_b^3}\left[1 - exp(-2n_b\right]\right]. \tag{5.30}$$

The function $w(qR_g)$ is an empirical crossover function chosen as:

$$w(x) = \left[1 + tanh((x - 1.52)/0.148)\right]/2. \tag{5.31}$$

Polydispersity is included by integrating the form factor over a Schulz distribution (Eq. 5.20) of cylinder radius:

$$P_{CS}(q, R_{avg}) = \int f(R) P_{CS}(q, R_{avg}) dR_{avg}. \tag{5.32}$$

The polydispersity of the radius of a cylinder is $p_d = 1/\sqrt{z+1}$.

In Figure 5.7 presented four examples of the form factor of flexible cylinders with polydisperse radius with the various values of the cylinder radius, polydispersity and the contour and Kuhn lengths. The SLD values of the cylinder and solvent are identical in all five cases.

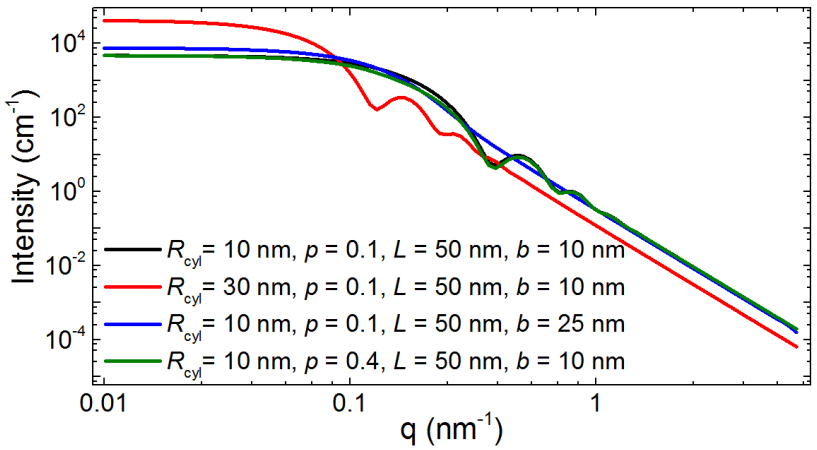

Figure 5.7: Examples of the form factor of flexible cylinders with polydisperse radius. Different lines represent the curves for different values of the parameters as described in the graphs. In all cases the SLD values of the cylinders and the solvent are $\rho_{cyl} = 1 \times 10^{-4}$ nm^{-2} and $\rho_{solvent} = 6.4 \times 10^{-4}$ nm^{-2}, respectively.

5.3.5.2. Hard-sphere structure factor

As mentioned above (section 5.3.3), the structure factor $S(q)$ of a system of interacting particles can be determined for a given interparticle interaction potential (Eq. 5.18). The most well-known approximation for $S(q)$ able to describe a system of interacting hard spheres is obtained by Percus and Yevick (PY),[207] which was used in the present work. This approximation is based on solution of the Ornstein-Zernike equation,[208] which describes how correlations between two particles are constructed from contributions of direct correlations between the two particles and of contributions mediated by the surrounding particles:[209]

$$h(r) = c(r) + \rho \int ds \cdot c(s) h(|r - s|), \tag{5.33}$$

where r and s are the magnitudes of the vectors r and s, $c(r)$ is the direct correlation function, $h(r)$ is the total correlation function given by:

$$h(r) = g(r) - 1. \tag{5.34}$$

$g(r)$ is the pair correlation function ($g(r) = e^{U(r)/k_B T}$).

The Percus-Yevick approximation uses the following relation in order to solve the Ornstein-Zernike integral equation:

$$c(r) = g(r)[1 - e^{-U(r)/k_B T}], \tag{5.35}$$

with the following hard-sphere interaction potential between particles:

$$U(r) = \begin{cases} 0 & \text{for } r > 2R_{HS} \\ \infty & \text{for } r < 2R_{HS} \end{cases} \tag{5.36}$$

Here R_{HS} is the hard-sphere radius, i.e. half the center-to-center distance between the particles. Solution to the Ornstein-Zernike equation is analytical and details could be found in [207]. The Percus-Yevick approximation is expressed as follows:

$$S_{HS}(q) = \frac{1}{1 + 24\eta G(2R_{HS}q)/2R_{HS}q}, \tag{5.37}$$

where η is the hard-sphere volume fraction, i.e. the fraction of micelles which are correlated, and

$$G(x) = \gamma \frac{\sin x - x\cos x}{x^2} + \delta \frac{2x\sin x + (2 - x^2)\cos x - 2}{x^3}$$

$$+ \varepsilon \frac{-x^4 \cos x + 4(3x^2 - 6\cos x + (x^3 - 6x)\sin x + 6)}{x^5}, \tag{5.38}$$

where $\gamma = (1 + 2\eta)^2/(1 - \eta)^4$, $\delta = -6\eta(1 + \eta/2)^2/(1 - \eta)^4$ and $\varepsilon = \gamma\eta/2$. (5.39)

Figure 5.8 shows three examples of the hard-sphere structure factor with the various values of the hard-sphere radius and polydispersity.

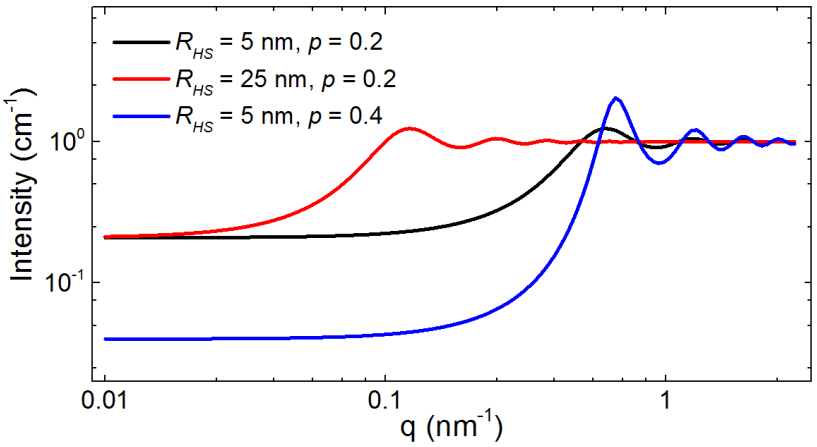

Figure 5.8: Examples of the hard-sphere structure factor. Different lines represent the curves for different values of the parameters as described in the graphs.

5.3.5.3. Porod law

Presence of large-scale particles in a polymer solution causes strong forward scattering, which dominates the signal, and the size of this particles cannot be resolved. The forward scattering can be approximated by a modified Porod term, which reads:[210]

$$I_{agg}(q) = \frac{I_P}{q^{\alpha}}, \qquad (5.40)$$

where I_P is a scaling factor. α is the Porod exponent, which characterizes the surface roughness of the aggregates: $\alpha = 4$ is obtained for particles with a smooth surface, whereas $\alpha < 4$ points to rough surfaces and $\alpha > 4$ to a concentration gradient near the aggregate surface.[211,212]

Figure 5.9 shows three examples of the Porod low with the various values of the Porod exponent.

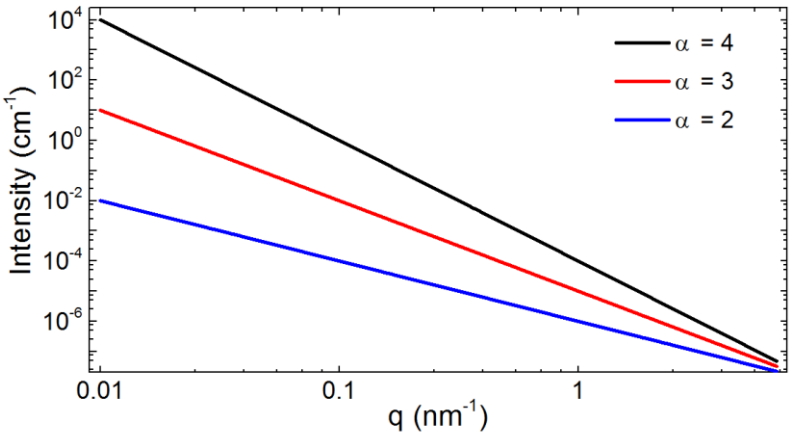

Figure 5.9: Examples of the Porod low. Different lines represent the curves for different values of the Porod exponent as described in the graphs.

5.3.5.4. Guinier law

In the case of nonlinear increase of the scattering intensity at low-q values the Guinier approximation was used for $I_{agg}(q)$, to describe the size of the aggregates:

$$I_{agg}(q) = I_G \exp\left(\frac{-q^2 R_g^2}{3}\right), \tag{5.41}$$

where I_G is a scaling factor and R_g the radius of gyration.

Figure 5.10 shows three examples of the Guinier low with the various values of the Porod exponent.

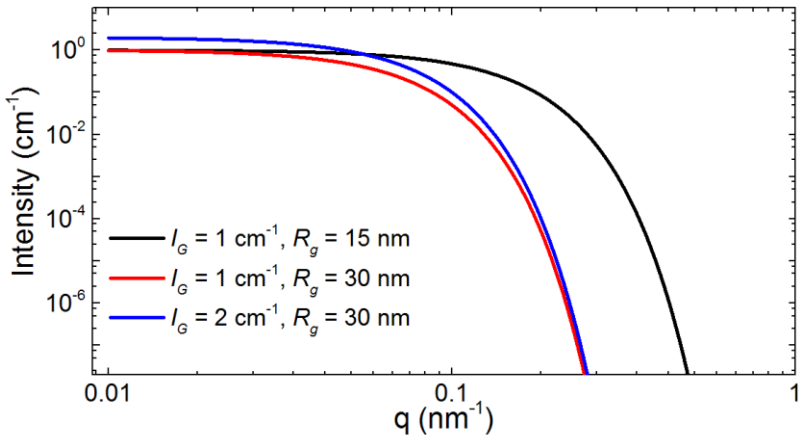

Figure 5.10: Examples of the Guinier low. Different lines represent the curves for different values of the radius of gyration R_g as described in the graphs.

5.3.5.5. Empirical models

The polyelectrolyte peak model (Solvation term)

So-called solvation term $I_{solv}(q)$ is used to describe the high-q scattering originates from the concentration fluctuations in semidilute polymer solutions and is governed by the solvation (hydration) of the polymer chains:[213]

$$I_{solv}(q) = CF_{solv}(q) . \tag{5.42}$$

The parameter C characterizes the solvation intensity, which reads:

$$C = A\frac{k_B T \Delta\rho^2}{K}, \tag{5.43}$$

where A is a scaling factor related to the volume fraction, K is the osmotic compressibility, $\Delta\rho^2$ is the contrast factor with ρ being the scattering length densities of the chains and the solvent, k_B is Boltzmann's constant, and T is the absolute temperature. $F(x)$ is the scaling function, which is given by a modified Ornstein–Zernike function:

$$F_{solv}(q) = \frac{1}{1 + \left(|q - q_0|\xi_{solv}\right)^m} . \tag{5.44}$$

m is the solvation Porod exponent. For non-charged polymers, m = 5/3 is expected for a polymer coil in a good solvent, while m = 2 corresponds to a Gaussian coil in a theta solvent.[214] ξ_{solv} is a correlation length or mesh size. q_0 is the peak position: if applicable, it corresponds to an average distance $d_0 = 2\pi/q_o$ between the charged domains. d_0 is finite for solutions of charged polymers and zero for neutral polymer solutions.

Figure 5.11 shows three examples of the Solvation term with the various values of the correlation length ξ_{solv}, the solvation Porod exponent m and an average distance between the charged domains d_0.

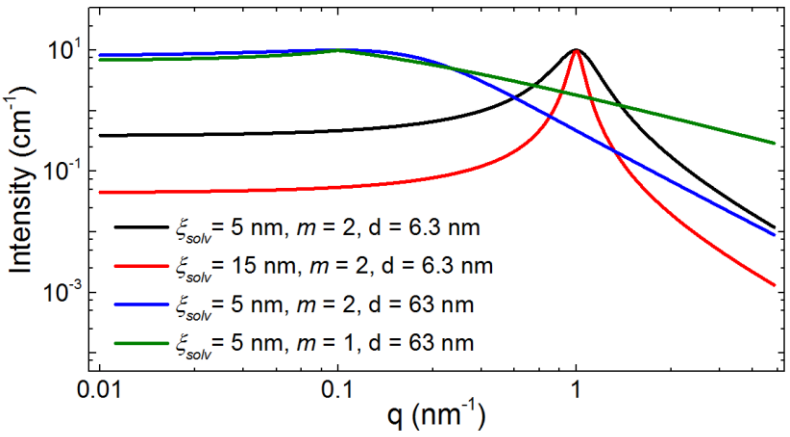

Figure 5.11: Examples of the Solvation term. Different lines represent the curves for different values of the parameters as described in the graphs.

Ornstein-Zernike approximation

The Ornstein-Zernike (OZ) term describes the concentration fluctuations in semidilute polymer solutions and the correlation length or mesh size ξ_{OZ}.[215] It reads:

$$I_{OZ}(q) = \frac{I_{OZ}}{1 + q^2 \xi_{OZ}^2}, \tag{5.45}$$

where I_{OZ} is the scaling factor.

Figure 5.12 shows three examples of the Ornstein-Zernike term with the various values of the correlation length ξ_{OZ} .

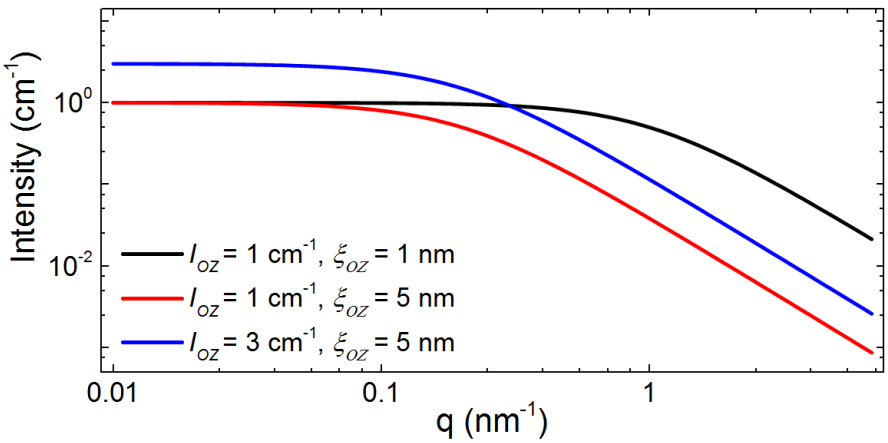

Figure 5.12: Examples of the Ornstein-Zernike term. Different lines represent the curves for different values of the correlation length ξ_{OZ} as described in the graphs.

6. “Schizophrenic” behavior of doubly thermoresponsive diblock copolymers

In this chapter, we aim to study the aggregation behavior in aqueous solution of the twofold thermoresponsive diblock copolymers consisting of a zwitterionic polysulfobetaine PSPP block, and a nonionic PNIPAM or PNIPMAM block, namely PSPP-*b*-PNIPAM and PSPP-*b*-PNIPMAM (Figure 4.4a,b). PSPP-*b*-PNIPAM has been designed to feature the minimum gap between the CP_{UCST} of the PSPP block and the CP_{LCST} of the PNIPAM block in aqueous solution. In particular, we speculated whether in such system the salting-in effect upon appropriate NaBr addition might result in an overlap of the two transition processes, i.e. regime II’ depicted in Figure 3.2 may be encountered. As the UCST of PSPP increases notably with molar mass,[31] a block copolymer with a relatively long PSPP block together with a shorter PNIPAM block has been synthesized, namely $PSPP_{430}$-*b*-$PNIPAM_{200}$. PSPP-*b*-PNIPMAM has been designed with the aim to enhance the tendency for microphase separation in solution compared to $PSPP_{432}$-*b*-$PNIPAM_{200}$ solution, by increasing the polarity difference between the zwitterionic and the nonionic block via the additional methyl group on the backbone of the nonionic block. The architecture of the PSPP-*b*-PNIPMAM block copolymer was chosen to be analogous to $PSPP_{432}$-*b*-$PNIPAM_{200}$, namely $PSPP_{498}$-*b*-$PNIPMAM_{144}$, in order to enable meaningful comparisons. We expect a large temperature window between CP_{UCST} and CP_{LCST}, i.e. presence of regime II in the system (Figure 3.2), due to a notably higher LCST transition of PNIPMAM compared to PNIPAM. The addition of low molar weight salt in the $PSPP_{498}$-*b*-$PNIPMAM_{144}$ solution may bring the two transition temperatures closer to each other.

The impact of the features of one block on the phase transition due to the aggregation of another one should be different in these two systems, i.e. stronger for $PSPP_{432}$-*b*-$PNIPAM_{200}$ and weaker for $PSPP_{498}$-*b*-$PNIPMAM_{144}$. This is expected to be reflected in “schizophrenic“ micellar self-assembly. Hereby, we aim to compare the behavior of $PSPP_{432}$-*b*-$PNIPAM_{200}$ and $PSPP_{498}$-*b*-$PNIPMAM_{144}$ in aqueous solution in order to investigate the influence of the architecture and the chemical nature of the individual blocks on the self-assembly of the diblock copolymers.

In the beginning of this chapter, we will discuss the characterization of the temperature-dependent aggregation behavior of the diblock copolymers in solution, including the behavior

of the cloud points for the homo- and the diblock copolymers in salt-free solution and in the presence of electrolyte, determined by means of turbidimetry. Then, we will turn to the discussion of the aggregation behavior of the diblock copolymers in solution explored by temperature-resolved DLS measurements, which were carried out to confirm the overall behavior. Subsequently, the detailed structural studies with SANS of the PNIPMAM homopolymer and the diblock copolymers in salt-free solution and in the presence of electrolyte will be presented. The details of sample preparation can be found in paragraph 4.5.1.

6.1. Experimental set-up

Turbidimetry. Cloud points were determined by turbidimetry using a Cary 50 UV-vis spectrometer (Varian Inc., Palo Alto, CA) equipped with a single cell Peltier thermostat for the temperature control. Quartz glass cells (Hellma Analytics) with a light path of 10 mm were used. The measurements were performed during heating form regime II (25 ºC in the $PSPP_{432}$-*b*-$PNIPAM_{200}$ solution; and 35 ºC for the $PSPP_{498}$-*b*-$PNIPMAM_{144}$ solution) to regime III above CP_{LCST} and cooling from regime II to regime I below CP_{UCST}. Transmittance measurements were performed at the wavelength of 500 nm during heating/cooling runs in steps of 0.5 °C with a thermal equilibration time of 5 min at each temperature. The data were normalized to the absorption of the solvent-filled cell, whose transmittance was set to 100%, i.e. zero absorption. The cloud points of the $PSPP_{430}$, $PSPP_{498}$ and $PNIPMAM_{195}$ homopolymers were determined at the wavelength of 800 nm during cooling/heating runs in steps of 0.1 °C with an equilibration time of 12 s at each temperature. The solutions were heated above the phase transition temperature and stirred prior measurement. The cloud points CP_{UCST} and CP_{LCST} were taken as the temperature where the normalized transmittance of the solution in the cooling and heating runs was reduced to 95 % of its maximum value.

Dynamic light scattering (DLS). Measurements were carried out using a Zetasizer Nano ZS (Malvern) laser particle size analyzer equipped with a 633 nm laser at an angle of 173° (backscattering detection). The maximum particle radius which can be resolved is 1000 nm. The $PSPP_{498}$-*b*-$PNIPAM_{144}$ and $PSPP_{430}$-*b*-$PNIPAM_{200}$ diblock copolymers were measured in salt-free D_2O. 0.5 mL of sample was mounted in a plastic microcuvette (Malvern). Measurements were performed during heating from 10 °C to 60 °C in steps of 5 °C and were repeated 3 times at each temperature. The equilibration time was chosen at 15 min and the measurement time at 3 min. For data evaluation, the DTS (Nano) software (Malvern) was

used, which provides the hydrodynamic radius, R_h, and the volume fraction of each species (1 or 2) for each of the 3 measurements. The results were averaged.

Small-angle neutron scattering (SANS). SANS experiments were performed at the instrument D11 at the Institut Laue-Langevin (ILL) in Grenoble, France. The incident neutrons had a wavelength λ = 6.0 Å with a spread of 9 %. A q-range from 0.002 to 0.52 Å^{-1} was covered. Samples were mounted in quartz glass cells (Hellma Analytics) with a neutron light path of 1 mm. At the end of each run, the sample transmission was measured. Boron carbide was used for measurement of the dark current, and H_2O for the detector sensitivity and calibration of the intensity. The scattered intensity curves were azimuthally averaged and corrected for background scattering from the solvent-filled cell and parasitic scattering with the software package LAMP.[216]

The homopolymer PNIPMAM$_{195}$ was measured in pure D_2O while heating from 22 °C to 50 °C in steps of 7-10 °C. The diblock copolymers PSPP$_{430}$-*b*-PNIPAM$_{200}$ and PSPP$_{498}$-*b*-PNIPMAM$_{144}$ were measured in pure D_2O and in 0.004 M NaBr in D_2O while heating from 15 °C to 49 / 59 °C in steps of 7-10 °C. Measurements were performed using a copper sample holder and an inner flow circuit, which was connected to a thermostat. After each temperature change, a thermal equilibration time of 15 min was applied. The measuring times were 40 min, 6 min and 5 min at the sample-detector distances (SDDs) of 34.00 m, 7.99 m and 1.20 m, respectively.

Modeling of the SANS curves. SANS curves of the homopolymer PNIPMAM solution and of the diblock copolymers PSPP$_{430}$-*b*-PNIPAM$_{200}$ and PSPP$_{498}$-*b*-PNIPMAM$_{144}$ solutions in regimes I and III were fitted via the model function:

$$I(q) = I_0 P(q) S_{HS}(q) + I_{agg}(q) + I_{OZ}(q) + I_{bkg} \tag{6.1}$$

I_0 is a scaling factor, $P(q)$ the form factor of the micelles, and $S_{HS}(q)$ the hard-sphere structure factor (Eqs. 5.37-39). $I_{OZ}(q)$ the Ornstein-Zernike term (Eq. 5.45), $I_{agg}(q)$ describes scattering from large aggregates modeled by the modified Porod law (Eq. 5.40), and I_{bkg} is the incoherent background. These contributions are described in detail in chapter 5. Different functions were used for $P(q)$, namely the form factor of polydisperse, homogeneous spheres (Eqs. 5.19-21), $P_{sphere}(q)$, for the curves from the PNIPMAM solution and in regime I of the diblock copolymers, or the form factor of polydisperse spherical particles with a core-shell structure (Eqs. 5.22-23), $P_{core\text{-}shell}(q)$, in regime III of the diblock copolymers. The form factor

of polydisperse, homogeneous spheres reveals the average radius r_{avg} with the polydispersity p modeled by the Schulz distribution, taking into account the difference in scattering length densities (SLD) of the sphere, ρ_{sphere}, and the solvent, $\rho_{solvent}$, (values used see below). The form factor of a polydisperse spherical core-shell particle having a polydisperse core and a uniform shell thickness, reveals the micellar radius, r_{mic}, which is the sum of the core radius, r_{core}, and the shell thickness, t: $r_{mic} = r_{core} + t$; the core polydispersity is again accounted for by the Schulz distribution. The differences in SLDs of the core and shell, $\rho_{core} - \rho_{shell}$, and the shell and the solvent, $\rho_{shell} - \rho_{solv}$ enter the expression as well.

The SANS curves of the diblock copolymers solutions in regimes I and II were analyzed using the following model function:

$$I(q) = I_{agg}(q) + I_{solv}(q) + I_{bkg} \tag{6.2}$$

The first term, $I_{agg}(q)$, is used to describe the low-q scattering due to large aggregates. $I_{solv}(q)$ is the so-called solvation term (Eq. 5.42-44), which is used to describe the high-q scattering, and I_{bkg} is the incoherent background. In many cases, $I_{\mathrm{agg}}(q)$ was approximated by a modified Porod term (Eq. 5.40). In some cases, the Guinier approximation could be used for $I_{\mathrm{agg}}(q)$, enabling the determination of the radius of gyration of the aggregates, R_{g} (Eq. 5.41). These are described in detail in chapter 5.

The incoherent background was fixed at 0.06 cm^{-1}. The scattering length density (SLD) of D_2O for neutrons, $\rho_{D_2O} = 6.3 \times 10^{-4}$ nm^{-2}, was taken from the literature.[217] The SLD value of the 0.004 M NaBr solution in D_2O was calculated as 6.2×10^{-4} nm^{-2}. The SLD values of the components of our systems were calculated using the mass densities, assuming 1.1 g cm^{-3} for PNIPMAM (estimated from the known density of PNIPAM, i.e. 1.1 g cm^{-3}) and 1.0 g cm^{-3} for PSPP (estimated from the constituent elements and assuming a density of 1.0 g cm^{-3}, typical for organic polymers). The following values were obtained: $\rho_{PNIPAM} = 8.1 \times 10^{-5}$ nm^{-2}, $\rho_{PNIPMAM} = 6.8 \times 10^{-5}$ nm^{-2} and $\rho_{PSPP} \approx 7.9 \times 10^{-5}$ nm^{-2}. According to the similarity of the SLD values for PNIPAM/PNIPMAM and PSPP and the penetration of D_2O into the micellar shells, the SLD values of the sphere ρ_{sphere} were kept in the range (0.79-1.35) $\times 10^{-4}$ nm^{-2} for $PSPP_{430}$-*b*-$PNIPAM_{200}$ and in the range (0.68-1.29) $\times 10^{-4}$ nm^{-2} for $PSPP_{498}$-*b*-

$PNIPMAM_{144}$. In the case of core-shell structures, a concentration gradient from the surface to the central part of the micelles may be present. Together with the above described reasons, the SLD values were kept in the order $\rho_{core} < \rho_{shell} < \rho_{D_2O}$, namely (0.8-1.5) × 10^{-4} nm^{-2} for ρ_{core}, (1.5-5.0) × 10^{-4} nm^{-2} for ρ_{shell} for $PSPP_{430}$-*b*-$PNIPAM_{200}$, and (0.7-1.4) × 10^{-4} nm^{-2} for ρ_{core}, (1.4-5.0) × 10^{-4} nm^{-2} for ρ_{shell} for $PSPP_{498}$-*b*-$PNIPMAM_{144}$ (obtained manually during fitting) and 6.3 × 10^{-4} nm^{-2} for ρ_{D_2O}.

The SANS curves were modeled using the SANS Data Reduction and Analysis software provided by the NIST Center for Neutron Research within the IGOR Pro software environment.[218]

6.2. Phase behavior

The present chapter is based on ref. [219,220].

The cloud points of 50 g L^{-1} solutions of the homopolymers $PSPP_{430}$, $PSPP_{498}$ and $PNIPMAM_{195}$ were determined using turbidimetry in salt-free D_2O during cooling and heating runs (not shown): CP_{UCST} ($PSPP_{430}$) = 29.6 ± 0.5 ºC, CP_{UCST}($PSPP_{498}$) = 31.3 ± 0.5 ºC and CP_{LCST}($PNIPMAM_{195}$) = 38.0 ± 0.5 ºC. The cloud point of PNIPAM in D_2O is known from literature to be about 32 ºC.[107,111] The measured value of CP_{LCST}($PNIPMAM_{195}$) is significantly lower than 44 °C mostly reported in the literature for PNIPMAM with molar masses in the range of 40,000 - 400,000 g mol^{-1}.[107-110] We attribute low value of CP_{LCST}($PNIPMAM_{195}$) to the hydrophobic fluorescence tag (see paragraph 4.5) in analogy to similar findings for PNIPAM labeled with the same fluorophore.[221] A temperature window between CP_{UCST} and CP_{LCST} is expected to be small in solution of $PSPP_{432}$-*b*-$PNIPAM_{200}$, and large in $PSPP_{498}$-*b*-$PNIPMAM_{144}$ solution, as intended.

Representative light transmission curves of $PSPP_{430}$-*b*-$PNIPAM_{200}$ and $PSPP_{498}$-*b*-$PNIPMAM_{144}$ in salt-free D_2O at 10 g L^{-1} are shown in Figure 6.1a,b. Figure 6.1c,d shows the concentration dependence of the cloud points in salt-free D_2O and in solutions with salt: $PSPP_{432}$-*b*-$PNIPAM_{200}$ in 0.004 M NaBr in D_2O and $PSPP_{498}$-*b*-$PNIPMAM_{144}$ in 0.006 M NaCl in D_2O.

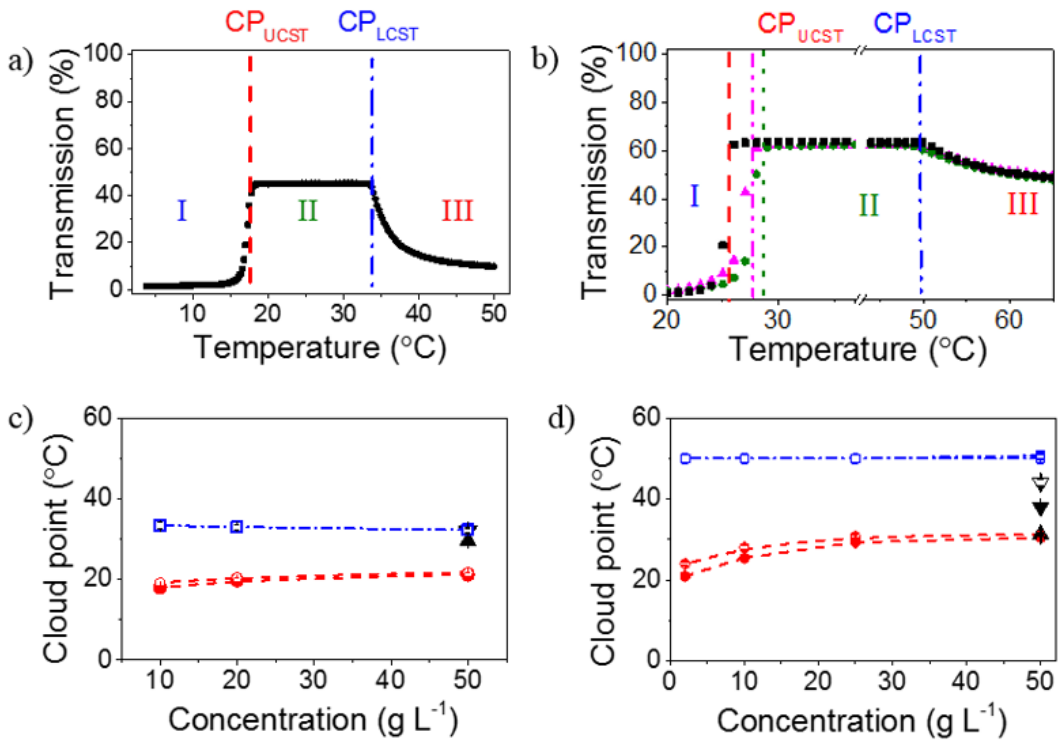

Figure 6.1: Light transmission of 10 g L^{-1} solutions of $PSPP_{430}$-*b*-$PNIPAM_{200}$ (a) and $PSPP_{498}$-*b*-$PNIPMAM_{144}$ (b) in salt-free D_2O (■), in 0.006 M NaCl (▲), and in 0.004 M NaBr (●). The lines show CP_{UCST} in salt-free solution (– –), 0.006 M NaCl (-·-), and 0.004 M NaBr in D_2O (·····), as well as CP_{LCST} in all solutions (-··-). I, II and III indicate the three regimes identified. Concentration dependence of the cloud points of $PSPP_{430}$-*b*-$PNIPAM_{200}$ (c) in salt-free D_2O (closed symbols) and in 0.004 M NaBr (open symbols) and of $PSPP_{498}$-*b*-$PNIPMAM_{144}$ (d) in salt-free D_2O (closed symbols) and in 0.006 M NaCl (open symbols): (●, ○) CP_{UCST}, (■, □) CP_{LCST}. For comparison, on (c): (▲) CP_{UCST} of $PSPP_{430}$ in salt-free D_2O, 50 g L^{-1}, (▼) the literature value of PNIPAM;[107,111] on (d): (▲) CP_{UCST} of $PSPP_{438}$, (▼) CP_{LCST} of $PNIPMAM_{195}$ homopolymers (both in salt-free D_2O, 50 g L^{-1}), (▽) cloud point for PNIPMAM from the literature are given as well.[107-110] The lines are guides to the eye.

Three regimes are distinguished in the transmission curves (Fig. 6.1a, b) indicated as I, II and III. In the regimes I and III, the diblock copolymers solutions are turbid. However, in regime III, some light is still transmitted (around 5 % and 45 % in the $PSPP_{430}$-*b*-$PNIPAM_{200}$ and $PSPP_{498}$-*b*-$PNIPMAM_{144}$ solutions, respectively), while in regime I, the transmission of light is blocked. Moreover, the transmission decreases sharply below CP_{UCST}, but only gradually above CP_{LCST}. This difference suggests the presence of different self-assembled structures in the regimes I and III. In regime II, where the solvent conditions are good for both blocks, and

where the polymer chains are expected to form a homogeneous, transparent solution, the transmission is significantly lower than 100 %, i.e. around 45 % and 60 % in the $PSPP_{430}$-*b*-$PNIPAM_{200}$ and $PSPP_{498}$-*b*-$PNIPMAM_{144}$ solutions, respectively, pointing to concentration fluctuations.

Turbidimetry results reveal interesting differences between the cloud points of the 50 g L^{-1} solutions of the diblock copolymers and the corresponding homopolymers (Figure 6.1c,d). The CP_{UCST} and CP_{LCST} of $PSPP_{430}$-*b*-$PNIPAM_{200}$ are found at 21.2 ± 0.5 ºC and 32.3 ± 0.5 ºC, respectively. The CP_{UCST} is markedly decreased (by about 8 ºC) compared to the one of the homopolymer $PSPP_{430}$ solution, while the CP_{LCST} is equal to the literature value of CP_{LCST} of PNIPAM. Thus, the CP_{UCST} of PSPP depends on the polymeric architecture and is altered by the presence of the PNIPAM block, whereas the CP_{LCST} of PNIPAM is unaffected by the second block.

In the $PSPP_{498}$-*b*-$PNIPMAM_{144}$ solution, the comparison of the cloud points reveals reverse dependency: The CP_{UCST} is 29.5 ± 0.5 ºC, thus about 2 °C lower than the one of the homopolymer $PSPP_{498}$ solution, which is a marginal reduction. The CP_{LCST} of the diblock copolymer is 49.5 ± 0.5 ºC, i.e. about 12 °C higher than the one of the homopolymer $PNIPMAM_{195}$ solution. One possible reason for the marked increase of CP_{LCST} of PNIPMAM is the position of the dye-labeled end group, which differs in the homopolymer and the diblock copolymer: in the latter, the label group is at the end of the PSPP block (Figure 4.4a), whereas in the homopolymer, it is attached at the end of PNIPMAM. Thus, the increased CP_{LCST} in $PSPP_{498}$-*b*-$PNIPMAM_{144}$ may be due to the larger spacing between the PNIPMAM block and the label group. Still, when comparing the literature values of CP_{LCST} of PNIPMAM (44 °C)[107-110] with the one found for the diblock copolymer (49.5 °C), the difference amounts to about 5 °C. Thus, CP_{LCST} of PNIPMAM is also altered by the presence of the PSPP block, i.e. it depends on the polymeric architecture and/or the environment, whereas CP_{UCST} of PSPP is almost unaffected by the presence of the PNIPMAM block.

The CP_{UCST} and CP_{LCST} values of the diblock copolymers in dependence on polymer concentration in salt-free D_2O are shown in Figure 6.1c,d. Both cloud points of $PSPP_{430}$-*b*-$PNIPAM_{200}$ depend on the polymer concentration (Figure 6.1c): CP_{UCST} increases from 18.0 ± 0.5 ºC at 10 g L^{-1} to 21.2 ± 0.5 ºC at 50 g L^{-1}, whereas CP_{LCST} slightly decreases from 33.4 ± 0.5 ºC to 32.3 ± 0.5 ºC in the same concentration range. In the $PSPP_{498}$-*b*-$PNIPMAM_{144}$ solution (Figure 6.1d), only CP_{UCST} exhibits concentration dependence: CP_{UCST} increases

from 21.0 ± 0.5 ºC at 2 g L^{-1} to 29.5 ± 0.5 ºC at 50 g L^{-1} with the increase being more pronounced below ca. 25 g L^{-1}. For all concentrations, the value of CP_{LCST} stays constant at 49.5 ± 0.5 °C within the precision of the measurements.

To summarize, CP_{UCST} of PSPP is sensitive to the polymer concentration, changes by the attachment to the PNIPAM block and only little to the PNIPMAM block. CP_{LCST} of PNIPAM is neither concentration-dependent nor not sensitive to the presence of the PSPP block. CP_{LCST} of PNIPMAM is not concentration-dependent as well, but markedly affected by neighboring groups, i.e. by the presence of the PSPP block or by the fluorescent tag.

6.2.1. Electrolyte effect on the phase behavior

The CP_{UCST} and CP_{LCST} values of $PSPP_{430}$-*b*-$PNIPAM_{200}$ and $PSPP_{498}$-*b*-$PNIPMAM_{144}$ in dependence on polymer concentration in 0.004 M NaBr in D_2O and in 0.006 M NaCl in D_2O, respectively, together with the values of the cloud points in salt-free D_2O are shown in Figure 6.1c,d. In solutions with salt, the values of CP_{UCST} are slightly higher than in salt-free D_2O, with the difference decreasing from 1.2 ± 0.5 ºC at 10 g L^{-1} to 0.6 ± 0.5 ºC at 50 g L^{-1} for $PSPP_{430}$-*b*-$PNIPAM_{200}$, and from 3.0 ± 0.5 °C at 2 g L^{-1} to 0.8 ± 0.5 °C at 50 g L^{-1} for $PSPP_{498}$-*b*-$PNIPMAM_{144}$. In contrast, CP_{LCST} of both PNIPAM and PNIPMAM stay constant. Thus, only CP_{UCST} of PSPP is sensitive to low concentrations of added low molar mass salts. Figure 6.1b presents the light transmission curves of 10 g L^{-1} solutions of $PSPP_{498}$-*b*-$PNIPMAM_{144}$ in salt-free D_2O, in 0.006 M NaCl, and in 0.004 M NaBr, illustrating the effect of the nature of the salt added. The CP_{UCST} value increases from 25.5 ± 0.5 ºC in salt-free D_2O to 27.5 ± 0.5 ºC in 0.006 M NaCl and to 28.8 ± 0.5 ºC in 0.004 M NaBr. Thus, NaBr has a stronger effect on the CP_{UCST} than NaCl, as expected from previous studies on PSPP homopolymers in aqueous solution, and in agreement with their positions in the Hofmeister series.[31] For 50 g L^{-1} solution of $PSPP_{498}$-*b*-$PNIPMAM_{144}$ in 0.004 M NaBr in D_2O, CP_{UCST} = 31.3 ± 0.5 ºC and CP_{LCST} = 49.5 ± 0.5 ºC were found (not shown). In the case of 50 g L^{-1} solution of $PSPP_{430}$-*b*-$PNIPAM_{200}$ in 0.004 M NaBr in D_2O, cloud points of CP_{UCST} = 21.8 ± 0.5 ºC, and CP_{LCST} = 32.3 ± 0.5 ºC are determined (not shown).

6.2.2. Comparison of the solution phase behavior of $PSPP_{432}$-*b*-$PNIPAM_{200}$ and $PSPP_{498}$-*b*-$PNIPMAM_{144}$

While the three regimes are present in both, $PSPP_{498}$-*b*-$PNIPMAM_{144}$ and of $PSPP_{432}$-*b*-$PNIPAM_{200}$, in D_2O, distinct differences are revealed in the phase behavior: the CP_{UCST} and CP_{LCST} values are ca. 9 ºC and 16 ºC higher respectively, in 50 g L^{-1} solutions of $PSPP_{498}$-*b*-$PNIPMAM_{144}$, and the width of regime II is thus considerably larger. We attribute this to two reasons: Firstly, the CP_{LCST} value of the $PNIPMAM_{195}$ is ca. 10 ºC higher than the one of PNIPAM. Secondly, the higher molar mass of the $PSPP_{498}$ block, compared to the $PSPP_{432}$ block, causes an increase of CP_{UCST},[31] which, in turn, enhances the increase of CP_{LCST} of the nonionic block in the $PSPP_{498}$-*b*-$PNIPMAM_{144}$. These observations differ markedly from the ones for $PSPP_{432}$-*b*-$PNIPAM_{200}$, for which CP_{USCT} of PSPP is reduced by 8 °C when the PNIPAM block is attached, while CP_{LCST} of PNIPAM is unaffected by the PSPP block. In consequence, the regime between the UCST and the LCST transitions is larger in the $PSPP_{498}$-*b*-$PNIPMAM_{144}$ solution, as we intended. In both diblock copolymers in D_2O, the turbidity is higher in regime I than in regime III, and whereas the transmittance decreases abruptly below CP_{UCST}, it decreases gradually above CP_{LCST}. The CP_{UCST} values increase upon addition of salt up tp a concentrations of ca. 0.006 M with CP_{LCST} being unchanged. The maximum transmittance in regime II of a 10 g L^{-1} $PSPP_{498}$-*b*-$PNIPMAM_{144}$ solution in salt-free D_2O (ca. 60 %) is higher than the one of the $PSPP_{432}$-*b*-$PNIPAM_{200}$ solution (ca. 45 %). Also, CP_{UCST} values of $PSPP_{498}$-*b*-$PNIPMAM_{144}$ increase slightly more in dilute NaBr and NaCl solution than for $PSPP_{432}$-*b*-$PNIPAM_{200}$, but still much less than for PSPP homopolymers (increase by about 10 °C).[31]

The three regimes are also reflected in temperature-resolved ^1H NMR spectra of the $PSPP_{498}$-*b*-$PNIPMAM_{144}$ block copolymer (10 g L^{-1} in D_2O) (for experimental details and results see the appendix, Figure A.1). Moreover, the broadening and attenuation of the NMR signals corroborates our view of temperature-controlled schizophrenic micellization of polymer $PSPP_{498}$-*b*-$PNIPMAM_{144}$, with the PSPP blocks forming the micellar core in regime I, and the PNIPMAM blocks in regime III.

6.3. Characterization of the unimers and aggregates using DLS

The present chapter is based on ref. [219,220].

To elucidate the changes in self-assembled mesoscopic structures upon heating from regime I to regime III, i.e. their changes at the UCST- and LCST-type transitions, the temperature-dependent self-assembly behavior of the $PSPP_{432}$-*b*-$PNIPAM_{200}$ and $PSPP_{498}$-*b*-$PNIPMAM_{144}$

diblock copolymers in D_2O was explored using temperature-resolved DLS measurements. DLS in backscattering geometry was applied in order to minimize the effects of multiple light scattering in the turbid solutions. Moreover, the concentration was set to 10 g L^{-1} to minimize multiple scattering.

The autocorrelation curves of both diblock copolymers show very slow decays in regime I, fast decays in regime II and intermediate decays in regime III (Figure 6.2a,b). Thus, temperature markedly affects the aggregation behavior.

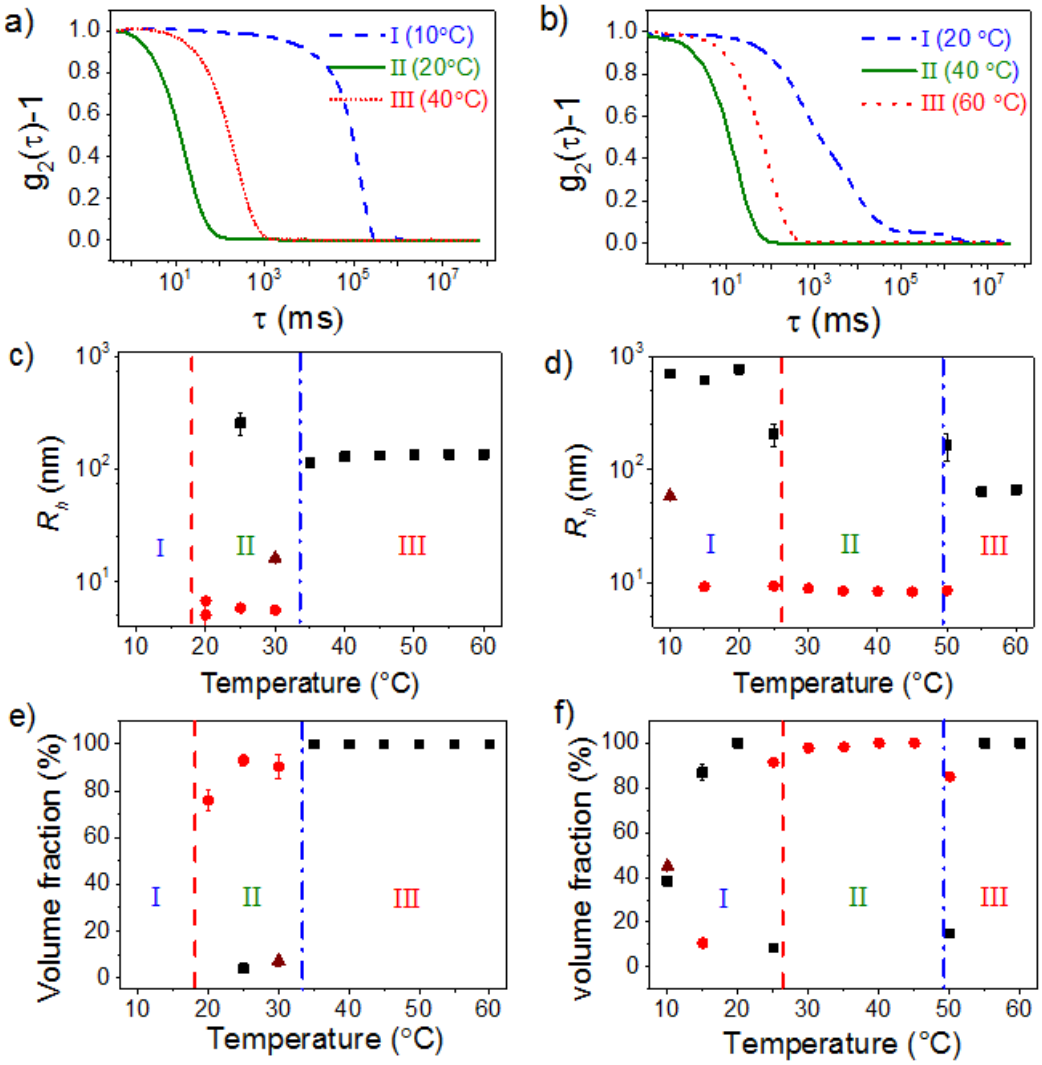

Figure 6.2: Results from DLS on salt-free solutions of $PSPP_{400}$-*b*-$PNIPAM_{200}$ (a, c, e) and $PSPP_{498}$-*b*-$PNIPMAM_{144}$ (b, d, f) in D_2O at 10 g L^{-1}, obtained in a heating runs. (a, b) Normalized intensity autocorrelation functions. Temperatures are indicated in the graphs. (c, d) Hydrodynamic radii and (e, f) volume fractions of the large aggregates (■), micelles (▲) and unimers (●) in dependence on temperature. The lines in (b - f) indicate the CP_{UCST} (- -) and CP_{LCST} (-·-) values from turbidity, respectively. The regimes I, II and III are indicated.

Analysis of the curves of the $PSPP_{432}$-*b*-$PNIPAM_{200}$ solution reveals the presence of 2 types of aggregates in regime II, but only 1 type in regime III. Whereas, 2 types of aggregates were found in regime I of the $PSPP_{498}$-*b*-$PNIPMAM_{144}$ solution, but only 1 type in regimes II and III. The hydrodynamic radii of aggregates and volume fractions are shown in Figure 6.2c-f.

In the $PSPP_{430}$-*b*-$PNIPAM_{200}$ solution, at temperatures below 19 ºC, the size of the large aggregates in regime I could not be quantified because they are larger than the resolution. Thus, we assume the formation of very large aggregates with an average hydrodynamic radius R_h > 1000 nm. Between 20 and 35 °C, i.e. in regime II, R_h of the majority component (volume fraction 90-96%) is 5.5 ± 0.2 nm, which presumably corresponds to unimers; the minority component (remaining 4-10 %) are particles with R_h = 260 ± 60 nm at 25 ºC and R_h = 16.2 ± 0.2 nm at 30 ºC (Figure 6.2c,e). The latter may tentatively be ascribed to micelles. Above 30 °C in regime III, only one component with R_h = 133 ± 8 nm is observed.

In the $PSPP_{498}$-*b*-$PNIPMAM_{144}$ solution, up to 25 °C, i.e. in regime I, aggregates with an average hydrodynamic radius, R_h, of 700 ± 5 nm, prevail (Figure 6.2d,f). Between 10 and 25 °C, the volume fraction of these large aggregates increases from 39 to 100 %. At 10 and 15 ºC, micelles are found as well with R_h = 59 ± 1 nm and 9.0 ± 0.4 nm and volume fractions of 45 and 11 %, respectively. Very large particles, having R_h > 1000 nm, constitute the remaining volume fraction. Between 25 and 50 °C, i.e. in regime II, R_h of the majority component (volume fraction 98-100 %) is 8.3 ± 0.1 nm, which presumably corresponds to unimers; the minority component (remaining 0-2 %) are very large particles with R_h > 1000 nm. At temperatures close to CP_{UCST} and CP_{LCST}, both unimers and aggregates are present, namely at 25 ºC, where 92 % unimers with R_h = 9.3 ± 0.2 nm and 8 % aggregates with R_h = 205 ± 43 nm are found, and at 50 ºC, where 85 % unimers with R_h = 8.5 ± 0.1 nm and 15% aggregates with R_h = 164 ± 44 nm are present. Above 50 °C, i.e. in regime III, R_h is 65 ± 3 nm with a volume fraction of 100 %.

The three regimes identified in turbidimetry are thus recovered in both systems. The magnitudes of the R_h values in the three regimes are consistent with the very low, the high and the intermediate light transmission (Figure 6.1a,b). The aggregates formed in regime I are much larger than those in regime III. Moreover, the absence of large aggregates in regime III confirms the absence of correlations between the micelles observed in SANS.

6.3.1. Comparison of the DLS results obtained for $PSPP_{432}$-*b*-$PNIPAM_{200}$ and $PSPP_{498}$-*b*-$PNIPMAM_{144}$

When comparing the DLS results obtained for the two systems, the following differences are revealed: In regime I, both solutions are turbid with very large aggregates, R_h > 700 nm and > 1000 nm for $PSPP_{498}$-*b*-$PNIPMAM_{144}$ and $PSPP_{432}$-*b*-$PNIPAM_{200}$, respectively. Moreover, in the solution of $PSPP_{498}$-*b*-$PNIPMAM_{144}$ the volume fraction of large aggregates increases with temperature, and the remaining volume fraction consist of small micelles and very large aggregates. In regime II, both solutions are semitransparent with unimers with R_h < 10 nm. Nevertheless, in the solution of $PSPP_{432}$-*b*-$PNIPAM_{200}$, 4 -10 % of the volume fraction consists of micelles with ca. 2 or even 50 times larger R_h, compared to the one of unimers. In regime III, the solution is "semi-turbid" with 100 % of aggregates having R_h values of ca. 65 nm and 133 nm for $PSPP_{498}$-*b*-$PNIPMAM_{144}$ and $PSPP_{432}$-*b*-$PNIPAM_{200}$, respectively.

6.4. Structural investigations using SANS

The present chapter is based on ref. [219,220].

The turbidimetry, ^{1}NMR and DLS results reveal differences in the phase behaviors of $PSPP_{432}$-*b*-$PNIPAM_{200}$ and $PSPP_{498}$-*b*-$PNIPMAM_{144}$ in salt-free D_2O, which may be assigned to the different composition and to the different chemical nature of the nonionic thermoresponsive block. It is known that, both PNIPMAM and PNIPAM are hydrated flexible coils in aqueous solution below the LCST, but the conformation of PNIPMAM is stiffer and the chains are more expanded due to the presence of a methyl group attached to the α-carbon of the repeat unit on the backbone on the backbone (see paragraph 4.2).[110,160]

6.4.1. Self-assembled structures in a PNIPMAM solution

To have a closer look at the structural behavior of the $PNIPMAM_{195}$ homopolymer, it is investigated with temperature-resolved SANS in salt-free D_2O. The relatively high polymer concentration of 50 g L^{-1} is chosen to enhance the scattering intensity, while the use of fully deuterated water ensures maximum contrast between the polymer and the solvent.

Figure 6.3a shows the SANS curves during a heating run from 22 °C to 49 °C. At 22 and 29 ºC, two smooth intensity decays are seen, which level off at q values above ca. 2.5 nm^{-1}. At 39 °C, the decay in intensity at low q values is more pronounced, while it dominates at 49 °C.

These SANS curves of $PNIPMAM_{195}$ differ strongly from the ones obtained from PNIPAM homopolymers.[137]

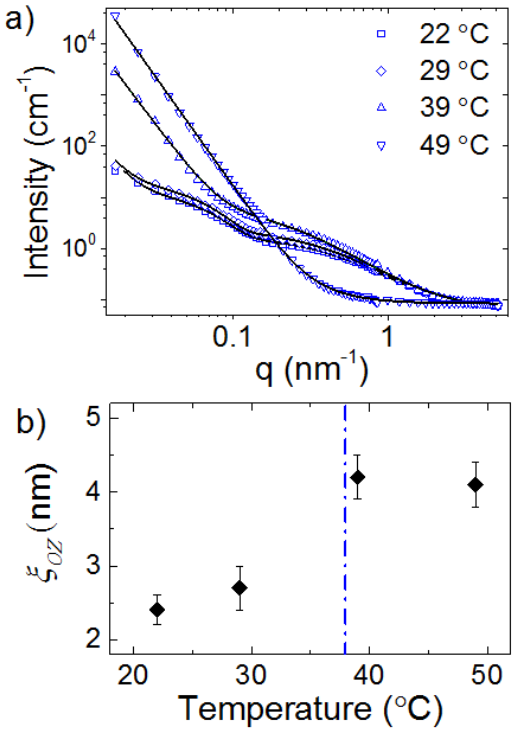

Figure 6.3: SANS curves from a 50 g L^{-1} $PNIPMAM_{195}$ solution in D_2O (symbols), where only every second point is shown for clarity, together with the fitting curves (—) (a). (b) Resulting temperature dependence of the correlation length, ξ_{OZ}. (-·-·-) CP_{LCST} from turbidimetry.

To analyze the structures, the SANS curves were fitted using the model described in Eq. 6.1. At 22 and 29 °C, i.e. below CP_{LCST}, in addition to the expected Ornstein-Zernike (OZ) term, describing concentration fluctuations, giving rise to the decay at 0.1-2.5 nm^{-1}, the scattering from polydisperse, homogeneous spherical particles ($P_{sphere}(q)$) had to be taken into account as well as scattering due to large aggregates, described by the Porod term. The contributions from spherical particles vanish at 39 and 49 °C, i.e. above the CP_{LCST}, and only the sum of the OZ and Porod terms are used for the analysis. At all temperatures, no hard-sphere structure factor is needed and therefore it is set to one. For all temperatures, the achieved fits agree well with the data (best fit parameters are compiled in Table A.1 in the appendix A).

The OZ structure factor could be applied at all investigated temperatures. ξ_{OZ} increases from ca. 2.4 nm at 22 ºC to ca. 4.1 nm at 39 ºC (Figure 6.3b), and I_{OZ} increases as well, reflecting critical behavior prior to the phase separation, as observed previously in PNIPAM solutions

as well.[137] At 49 °C, ξ_{OZ} is the same as at 39 ºC, but I_{OZ} decreases abruptly, indicating that the contributions from single chain scattering are reduced. The scaling factor I_0 of the decay at 0.01-2.5 nm^{-1} (describing spherical particles) slightly increases between 22 and 29 °C, indicating an increase of the volume fraction of the spherical particles close to the phase transition. At 22 and 29 °C, these particles have an average sphere radius r_{avg} = 25 ± 4 nm with a polydispersity p = 0.21 ± 0.03. Thus, the $PNIPMAM_{195}$ solution is not homogenous on length scales larger than a few nm, but, unexpectedly, reveals particles at larger length scales, which collapse at CP_{LCST}. At 22 and 29 °C, i.e. below CP_{LCST}, their SLD value varies in the range of (0.8-1.0) × 10^{-4} nm^{-2}, indicating penetration of D_2O into these particles. The forward scattering at low q values is described by the Porod law with the exponent α growing from 3.0 ± 0.1 at 22 °C and 29 ºC to 4.0 ± 0.2 at 39 °C and 49 ºC. This confirms the presence of very large, compact aggregates with rough surfaces below the CP_{LCST}, and with smooth surfaces above. The Porod scaling factor I_P slightly decreases between 29 and 39 °C. This reflects the decrease of the specific surface of these large aggregates above the CP_{LCST}, i.e. their increase in size.

To summarize, the $PNIPMAM_{195}$ homopolymer at 50 g L^{-1} in D_2O forms a solution with a correlation length ξ_{OZ} = 2.4-4.2 nm, and, in addition, polydisperse spherical particles with radii of around 25 nm below CP_{LCST}, which form large aggregates with rough surfaces. Above CP_{LCST}, the spherical particles collapse and form very large aggregates with smooth surfaces. Thus, the behavior of the $PNIPMAM_{195}$ solution differs from the one of PNIPAM.[137,222,223]

In a solution of PNIPAM with a similar molar mass (M_w = 25,000 g mol^{-1}) in D_2O at a concentration of 130 g L^{-1}, SANS revealed dissolved individual chains below CP_{LCST}, whereas above the cloud point scattering from large aggregates dominates.[137] In contrast, PNIPMAM forms larger particles and even large aggregates already below the cloud point. We assume two main reasons: (i) Despite the increased CP_{LCST} that is attributed to the stiff conformation of the PNIPMAM chains in solution, the additional methyl group on the backbone may favor hydrophobic interactions between the macromolecules already below the cloud point. (ii) The hydrophobic dye-labeled end group, which lowers the CP_{LCST} of the homopolymer, may promote aggregation already below the cloud point. However, this effect is not expected to play a significant role in the diblock copolymer, where the label is separated from the PNIPMAM block by the long zwitterionic block.

These effects may enforce the difference in the phase behavior and the structural changes in $PSPP_{498}$-*b*-$PNIPMAM_{144}$ and $PSPP_{432}$-*b*-$PNIPAM_{200}$ solutions upon temperature variation.

6.4.2. Self-assembled structures in solutions of the diblock copolymers

A detailed structural characterization of 50 g L^{-1} solutions of $PSPP_{432}$-*b*-$PNIPAM_{200}$ and $PSPP_{498}$-*b*-$PNIPMAM_{144}$ in salt-free D_2O was carried out using temperature-resolved SANS. Figure 6.4 presents the SANS curves of the diblock copolymers solutions during heating.

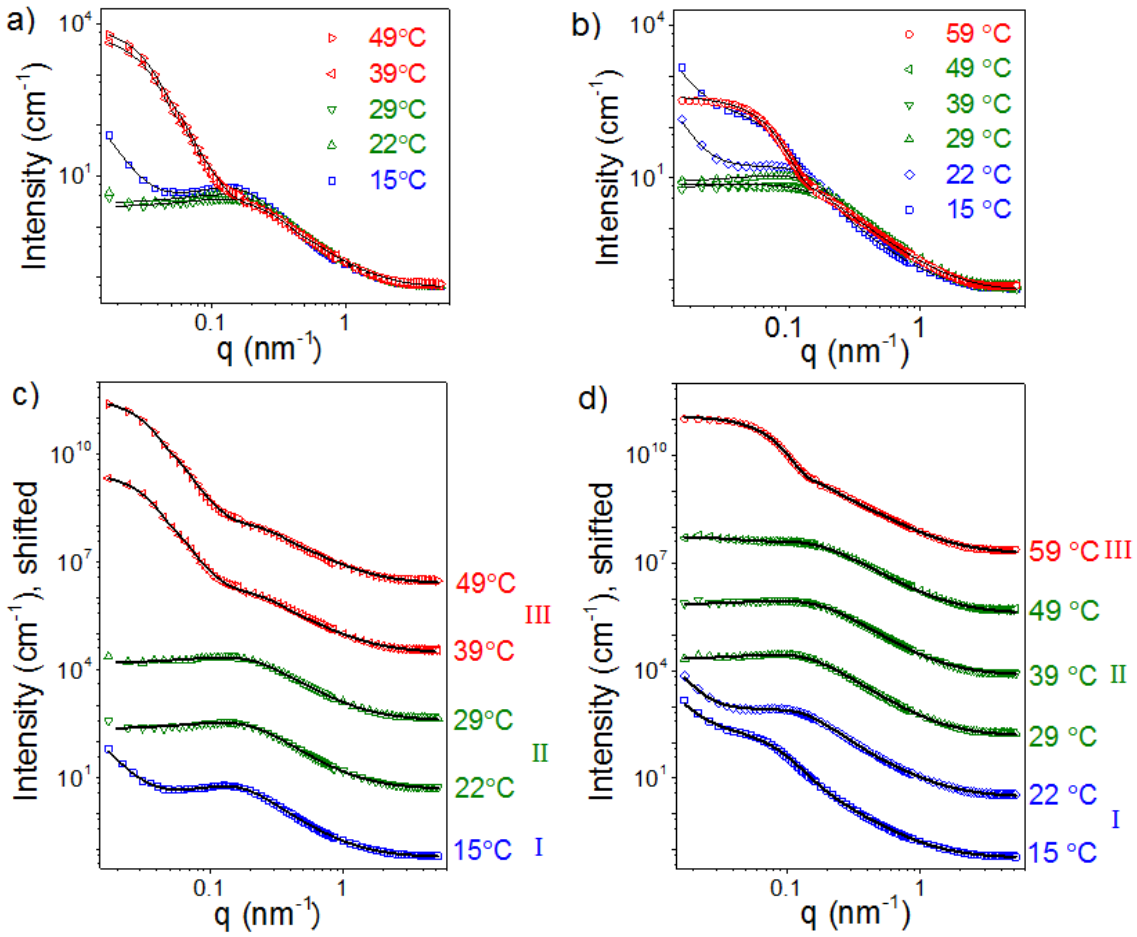

Figure 6.4: SANS curves from a 50 g L^{-1} salt-free solutions of $PSPP_{432}$-*b*-$PNIPAM_{200}$ (a, c) and $PSPP_{498}$-*b*-$PNIPMAM_{144}$ (b, d) in D_2O (symbols), where every third point is shown for clarity, together with the fitting curves (—) obtained using Eq. 6.1 in regimes I and III and Eq. 6.2 in regime II, see details below. In (c) and (d) the curves are shifted in intensity by a factor of 50 with respect to each other for better visibility. Regimes I, II and III are indicated by the blue, green and red color, respectively.

The three regimes already distinguished by turbidimetry and DLS are also reflected in the shapes of the SANS curves for both systems. For $PSPP_{430}$-*b*-$PNIPAM_{200}$, the SANS curve in

regime I (blue) features a smooth decay starting at the lowest *q* values with a shallow maximum at 0.16 nm^{-1} and becomes flat above ca. 3 nm^{-1}. In regime II (green), the curves shape is similar, except the decay at low-*q* values, which is not present any longer. In regime III (red) the curves decay steeply with a shallow second maximum at ca. 0.15 nm^{-1}, before leveling off at ca. 3 nm^{-1}.

In regime I of the $PSPP_{498}$-*b*-$PNIPMAM_{144}$ solution (blue), the SANS curves feature a smooth decay starting at the lowest *q* values with a shallow maximum, which moves from 0.06 nm^{-1} at 15 ºC to 0.1 nm^{-1} at 22 ºC. The curves become flat above ca. 3 nm^{-1}. In regime II (green), the curves look like the one at 22 ºC in regime I, except the decay at low-*q* values is not present. The curve in regime III (red) is flat up to ca. 0.06 nm^{-1}, then decays steeply with a shallow second maximum at ca. 0.15 nm^{-1}, before leveling off at ca. 3 nm^{-1}. The changes in the curves for both diblock copolymers are observed at the values of CP_{UCST} and CP_{LCST} obtained with turbidimetry (Figure 6.1a,b).

The SANS data were fitted using the models described in paragraph 6.1 (see Figure 6.4). Details for examples of the best fits to the scattering curves of the $PSPP_{432}$-*b*-$PNIPAM_{200}$ and $PSPP_{498}$-*b*-$PNIPMAM_{144}$ solutions are shown in Figures A.2 and A.3 in the appendix A. The fits, which are good in all regimes for both diblock copolymers, reveal substantial structural changes when CP_{UCST} and CP_{LCST} are crossed. The results of the fits using Eq. 6.2, applied in regimes I and II, as well as the ones using Eq. 6.1, applied in regimes I (as an alternative) and III, are summarized in Tables A.2-5 in the appendix A.

Results of the analysis of the SANS curves of $PSPP_{432}$-b-$PNIPAM_{200}$. According to the scenario described in chapter 3 (Figure 3.2), in the diblock copolymer solution in regime II molecularly dissolved polymers are expected. For unimers in dilute solution, single chain scattering, described by the Debye form factor, would be expected or, for more concentrated solutions, scattering of the Ornstein-Zernike type. However, as tested by fitting of these models, none of these behaviors is observed in the experiments. Instead, the SANS curves display a peak at a rather high *q*-value (Figure 6.4a,c), which is typical of polyelectrolytes in salt-free solution and describes the spatial distribution of the chains.[224] A maximum of the peak at q_0, corresponds to an average distance $d_0=2\pi/q_0$ between the charged domains.[225] Thus, we analyze the SANS curves of $PSPP_{432}$-*b*-$PNIPAM_{200}$ in regime II using such model described in Eq. 6.2, where the solvation term is used to describe the correlation peak and scattering at high *q* values, whereas the Porod term is not needed since no forward scattering

is observed (Figure A.2b in the appendix A). The solvation term reveals that the correlation length, ξ_{solv}, which can be regarded as the distance between the neighboring entanglement points, decreases from 6.5 ± 0.2 nm at 22 °C to 6.0 ± 0.1 nm at 29 °C (Table A.2 in the appendix A). This decrease of ξ_{solv} may be due to the different properties of the two blocks: polymer-polymer intermolecular interactions dominate over the interactions with water molecules for the PSPP block at 22 ºC, which is very close to its CP_{UCST}, whereas for the PNIPAM block, both types of interactions are equal in strength, and PNIPAM may form a hydrophilic shell around PSPP, which is at the origin of the higher ξ_{solv} value. In contrast, at 29 ºC, both blocks are in theta solvent conditions, and ξ_{solv} reflects the molecular conformation of the entire polymer. The solvation Porod exponent, m, is 2.00 ± 0.03 and 1.93 ± 0.02 at 22 °C and 29 °C, respectively, indicating that the system is close to theta solvent conditions with the higher value at 22 ºC again being related to the shell. The scaling factor of the solvation term, C, decreases from 4.2 ± 0.1 at 22 °C to 3.5 ± 0.1 at 29 °C. As expected, the value increases as CP_{UCST} is approached. The average distance between the charged domains, d_0, is 52 ± 3 and 50 ± 3 nm at 22 ° and 29 °C, respectively. At this large length scale the system is rather unaffected by the proximity of CP_{UCST}. The heterogeneities observed in regime II are at the origin of the reduced transmission (significantly below 100 %) in this regime (Figure 6.1a).

The shape of the curve from $PSPP_{432}$-*b*-$PNIPAM_{200}$ solution in regime I at high q values is similar to those in regime II, but the overall scattering intensity is higher (Figure 6.4a), which may be due to higher contrast caused by aggregation. Moreover, the scattering curves differ strongly at low q values, where large aggregates cause an increased forward scattering. The curve in regime I can be fitted using the same model as in regime II (Eq. 6.2), but now the Porod term is needed to describe the strong forward scattering at low q values (Figure A.2a in the appendix A). The correlation length ξ_{solv} = 8.6 ± 0.3 nm (Table A.2 in the appendix A). Analogous to ξ_{solv} in regime II at 22 ºC, it describes the correlation in the hydrophilic PNIPAM shell, surrounding the collapsed PSPP in the core, and it is larger than at higher temperatures. The solvation Porod exponent is m = 1.94, indicating that the solvent is still close to a theta solvent for the PNIPAM block. The scaling factor is C = 5.8 ± 0.1, which is 1.4-1.7 times higher than in regime II, which is an indication of the onset of phase separation.[213] d_0 is 48 nm, i.e. similar to the values obtained in regime II. The size of the very large aggregates cannot be resolved, but the upturn at q values below 0.08 nm^{-1} can be

approximated by the Porod law, $I_P(q)$. The Porod exponent is $\alpha = 4.1 \pm 0.1$, which indicates the presence of compact aggregates with smooth surfaces.

The scenario for the system depicted in chapter 3 (Figure 3.2) presumes micelle formation at temperatures below the CP_{UCST}, i.e. in regime I. Therefore, the curve from $PSPP_{432}$-*b*-$PNIPAM_{200}$ solution in regime I (at 15 °C) has been additionally fitted using the model described in Eq. 6.1, based on spheres correlated by a hard-sphere structure factor, plus an Ornstein-Zernike (OZ) term describing the concentration fluctuations in the non-compact shell and Porod scattering due to very large aggregates (Figure A.2c in the appendix A). The fitting curve fits the data equally well and allows gaining additional structural information. The spherical particles at 15 °C have an average sphere radius $r_{avg} = 4.4 \pm 0.1$ nm with a polydispersity $p = 0.48 \pm 0.03$ (the polydispersity can be enhanced due to aggregation) (Table A.3 in the appendix A, Figure 6.5A). The hard-sphere radius (or half the interparticle distance) is $R_{HS} = 18 \pm 2$ nm, which is slightly smaller than $d_0/2 = 24$ nm obtained by the solvation model. The hard-sphere volume fraction of correlated micelles, η, is about 0.12, the correlation between the spherical particles is thus very weak. The decay of the scattering intensity at high *q*-values is described by the OZ structure factor, which reveals $\xi_{OZ} = 4.0 \pm 0.3$ nm, which is half as large as ξ_{solv} from the solvation model and may comprise both, the inner part and the shell of the particles. The best SLD value of the spherical particles was found at $(8.0 \pm 0.3) \times 10^{-5}$ nm^{-2}, which corresponds to the range of SLD values of the PSPP and PNIPAM blocks. Thus, the spherical particles presumably do not contain D_2O. The Porod exponent $\alpha = 4.1 \pm 0.2$, which confirms the presence of compact aggregates with smooth surfaces. Altogether, in regime I, large aggregates seem to form, which consist of small correlated spheres with a highly polydisperse radius and an inner correlation length of a few nm.

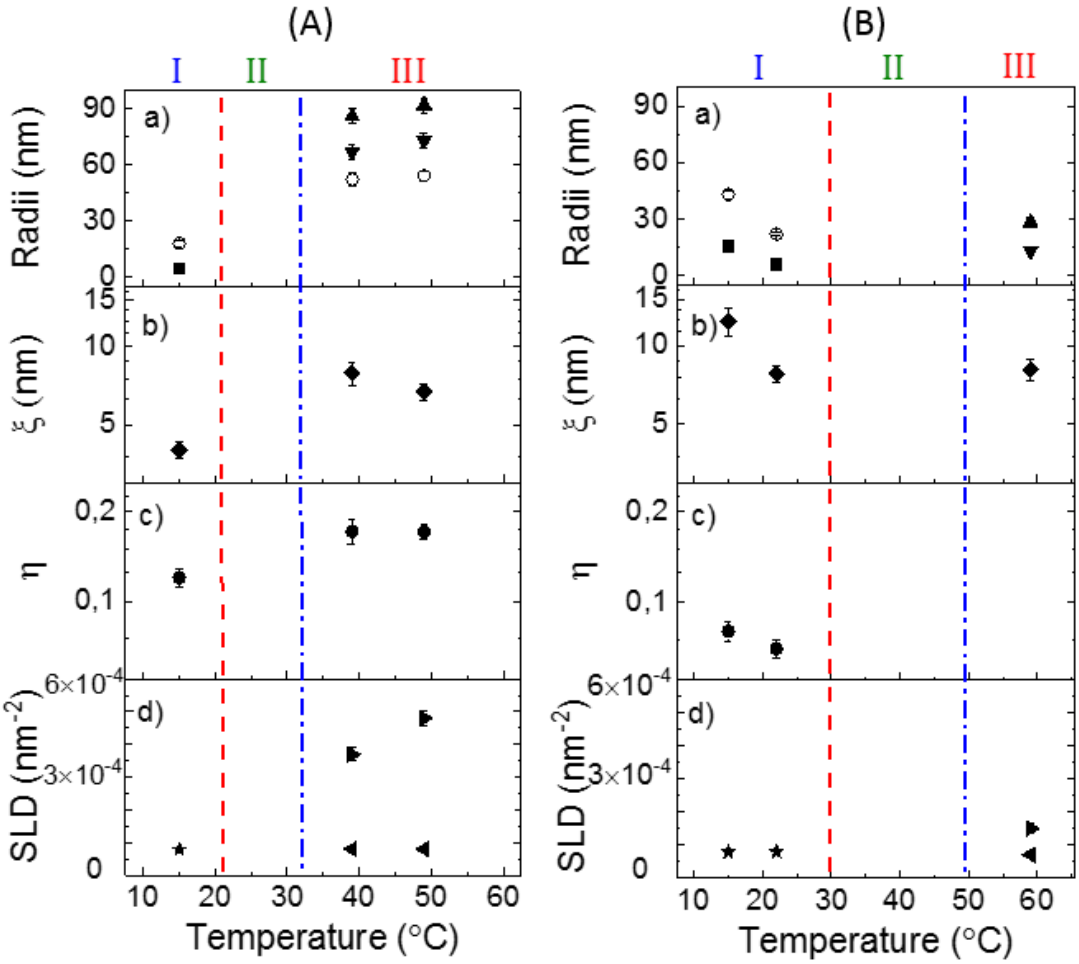

Figure 6.5: Results from fitting of the model in Eq. 6.1 to the SANS curves from $PSPP_{432}$-*b*-$PNIPAM_{200}$ and $PSPP_{498}$-*b*-$PNIPMAM_{144}$ solutions in regimes I and III (Figure 6.4). Temperature dependence of the sphere radius, r_{avg}, (■), the micellar radius of the core-shell structure, r_{mic} (▲), and the core radius, r_{core} (▼), the hard-sphere radius, R_{HS} (○) (a); of the correlation length, ξ_{OZ} (b), of the hard-sphere volume fraction, η (c), and of the SLD values of the polymer spheres (★) and the core (◀) and the shell (▶) of the core-shell micelles (d). In (b) and (c), a logarithmic axis is used. In some cases, the symbol size is larger than the error bar. (▬) and (▬): CP_{UCST} and CP_{LCST} values from turbidimetry. Regimes I, II and III are indicated on top of the graph.

The characteristic correlation peak of the polyelectrolyte systems is not present any longer in regime III, i.e. at temperatures far above the CP_{UCST} (Figure 6.4a,c). The scattering observed up to 0.1 nm^{-1} points to self-assembly of the diblock copolymers on length scales not higher than hundred nm. The model described in Eq. 6.1 is more applicable in regime III, where the form factor for core-shell spheres with a polydisperse core together with the hard-sphere and the OZ structure factors were used, while the Porod term was not needed (Figure A.2d in the

appendix A). The average core radius of the spheres is 67 ± 4 nm and 73 ± 4 nm at 39 and 49 ºC, respectively, with a moderate polydispersity p_{core} = 0.26 ± 0.03 and the shell thickness t = 19 ± 1 nm (Table A.3 in the appendix A, Figure 6.5A). Thus, the micellar radii are r_{mic} = 86 ± 4 nm at 39 ºC and 92 ± 4 nm at 49 ºC. Half the distance between the correlated micelles R_{HS} is 52 ± 3 nm at 39 ºC and 54 ± 3 nm at 49 ºC. The hard-sphere volume fraction, η, is slightly higher than the one in regime I, namely about 0.17. In contrast to the findings in regime I, R_{HS} is smaller than the spherical micelle radius, but follows the same trend. This may be attributed to different species being present at the micellar surface in regimes I and III. The PSPP block is about 3 times longer than PNIPAM block, and in regime III, the strong attractive interactions in the PNIPAM block lead to the formation of a hydrophobic core and allow interpenetration of the hydrophilic PSPP shells. The SLD value of the core varies in the range of (7.9-8.2) × 10^{-5} nm^{-2}, which is again comparable to the values of PSPP and PNIPAM, whereas the SLD of the shell is in the range (3.5-5.0) × 10^{-4} nm^{-2} (obtained manually during fitting), indicating a high amount of D_2O in the hydrophilic shell of the micelles, namely 54-74 % of D_2O. The correlation length ξ_{OZ} in regime III is 7.9 ± 0.7 nm at 39 ºC and 6.7 ± 0.5 nm at 49 ºC, thus slightly higher than in regimes I and II. In regime III, ξ_{OZ} describes the correlation in the hydrophilic PSPP shell. The slight increase of ξ_{OZ} at CP_{LCST} indicates a decrease of the osmotic compressibility and hence the shrinkage of the core due to the reinforced repulsive interaction in the PSPP shell. No forward scattering is observed in the SANS curves in regime III, which is in agreement with the results from turbidimetry, namely, the solution is not completely turbid.

Results of the analysis of the SANS curves of $PSPP_{498}$-b-$PNIPMAM_{144}$. The scattering curves of the $PSPP_{498}$-*b*-$PNIPMAM_{144}$ solution are slightly different from those of the $PSPP_{432}$-*b*-$PNIPAM_{200}$ solution (see above), but the same fitting models are applicable in all regimes.

In good agreement with the findings for the $PSPP_{432}$-*b*-$PNIPAM_{200}$ solution, single chain scattering models are not applicable to the SANS curves in regime II of the $PSPP_{498}$-*b*-$PNIPMAM_{144}$ solution (Figure 6.4b,d). The analysis of the curves is carried out using the model described in Eq. 6.2 (Figure A.3c,d in the appendix A), where the solvation term is used to describe the shallow maximum and scattering at a rather high q values, and the weak forward scattering observed at 49 ºC was fitted with the Guinier term. The correlation length from the solvation term, ξ_{solv}, decreases from 8.5 ± 0.6 nm at 29 °C to 6.2 ± 0.4 nm at 49 °C (Table A.4 in the appendix A). This decrease of the ξ_{solv}, may be due to the different properties of the two blocks accordingly: At 29 ºC, which is just above CP_{UCST}, the relatively

high ξ_{solv} value reflects mainly the correlation in the hydrophilic PNIPMAM shell surrounding the collapsed PSPP in the core. At 39 and 49 ºC, ξ_{solv} reflects the molecular conformation of the entire polymer. At 29-49 °C, the solvation Porod exponent, *m*, is 2.0 ± 0.1, indicating that the solvent is a theta solvent for the PNIPMAM shell at 29 ºC and for the entire polymer at 39 and 49 ºC. The scaling factor of the solvation term, *C*, decreases from 11.1 ± 0.9 cm^{-1} at 29 °C to 6.1 ± 0.5 cm^{-1} at 49 °C, i.e. close to CP_{UCST} the value is maximum. The average distance between the charged domains, d_0, is 75 ± 9 nm at 29-49 °C, which is quite large. Most probably, this is due to the expanded state of both blocks in regime II. This results from (i) the ionic attraction in the PSPP block which is weak above CP_{UCST}, and (ii) the stiff chain conformation of PNIPMAM below CP_{LCST}. At 49 ºC, additional aggregates with an average radius of gyration R_g = 32 ± 3 nm are detected. R_g is slightly smaller than the half of the distance between the charged domains, $d_0/2 \approx 38$ nm and may reflect the scattering from these domains.

In regime I, the scattering intensity at *q* values below 0.2 nm^{-1} is higher than in regime II (Figure 6.4b), which may be again due to higher contrast caused by aggregation. The shape of the curves is similar to those in regime II, but the maximum, which may be caused by ionic interactions in the PSPP block, is shifted to lower *q* values than in regime II. The difference at low q values is caused by an increased forward scattering due to formation of large aggregates. The curves in regime I are fitted using the same model as in regime II (Eq. 6.2), but with the Porod term (Figure A.3b in the appendix A). The solvation term reveals that ξ_{solv} increases from 12 ± 1 nm at 22 ºC to 38 ± 3 nm at 15 ºC (Table A.4 in the appendix A). Analogous to the correlation length in regime II at 29 ºC, it describes mainly the correlation in the hydrophilic PNIPMAM shell. Thus, ξ_{solv} increases with the strengthening of the attractive polymer-polymer interaction in the PSPP block forming the micellar core. The solvation Porod exponent *m* is 2.0 ± 0.1, indicating that the PNIPMAM block, which keep the system in the solvated state, is in theta conditions. The scaling factor increases steeply from *C* = 17 ± 2 cm^{-1} at 22 ºC to 137 ± 14 cm^{-1} at 15 ºC, indicating enhanced phase separation below CP_{UCST}.[213] d_0 increases from 78 ± 8 nm at 22 ºC to 118 ± 11 nm at 15 ºC, i.e. increases steeply due to the increasing polymer-polymer interactions in the PSPP block, causing formation of larger inhomogeneities at larger distance from each other. The Porod exponent is α = 4.0 ± 0.4, which indicates the presence of compact aggregates with smooth surfaces.

Due to the same reasons as for the above-described $PSPP_{430}$-*b*-$PNIPAM_{200}$, model described in Eq. 6.1 is additionally used for the curves fitting in regime I of the $PSPP_{498}$-*b*-

$PNIPMAM_{144}$ solution (Figure A.3a in the appendix A). The model describes formation of correlated spheres with a polydisperse radius. The fits are equally good and give additional structural information. The average radius of the polydisperse spherical particles increases from r_{avg} = 6.1 ± 0.5 at 22 °C to r_{avg} = 15 ± 2 nm at 15 °C (Table A.5 in the appendix A, Figure 6.5B), and the polydispersity is rather high (p = 0.47 ± 0.09), pointing to aggregation. R_{HS}, increases as well, namely from 22 ± 2 nm at 22 °C to 43 ± 3 nm at 15 °C. R_{HS} is larger than r_{avg} and follows the same trend, i.e. the spherical particles are spaced. The R_{HS} value is smaller than $d_0/2$, which is around 40 nm and 60 nm at 22 and 15 °C, respectively, but the trend is the same. The hard-sphere volume fraction, η, is about 0.08, indicating very weak correlation between the spherical particles. The OZ term reveals that ξ_{OZ} increases from 7.7 ± 0.3 nm at 22 °C to 12.3 ± 0.9 nm at 15 °C. These ξ_{OZ} values are comparable with r_{avg}, i.e. the presumed PNIPMAM shells are very loosely packed. ξ_{OZ} and ξ_{solv} cannot be compared directly but their values follow the same trend at low temperatures. The large values may be due to the stiff chain conformation of the PNIPMAM blocks, due to steric hindrance. The best SLD value was found at (7.3 ± 0.5) × 10^{-5} nm^{-2}, which corresponds to the SLD values of pure PSPP and PNIPMAM, i.e. the spherical particles presumably do not contain D_2O. The presence of compact aggregates with smooth surfaces confirmed by the Porod exponent α = 4.1 ± 0.3. Altogether, in regime I small polydisperse spheres are present, which become larger upon cooling. The surface of the spheres is covered by the expanded, hydrated PNIPMAM blocks. Nevertheless, the spheres are weakly correlated and form large aggregates.

In regime III, the SANS curve does not feature the characteristic correlation peak of the polyelectrolyte systems (Figure 6.4b,d) and the model of spherical core-shell particles with a polydisperse core (Eq. 6.2) is applicable, with the same contributions as for $PSPP_{432}$-*b*-$PNIPAM_{200}$, except the hard-sphere structure factor (Figure A.3e in the appendix A). The core radius is r_{core} = 13 ± 1 nm with a polydispersity p_{core} = 0.44 ± 0.04, and the shell thickness is t = 15 ± 2 nm, resulting in the micellar radius is r_{mic} = 28 ± 3 nm (Table A.5 in the appendix A). The SLD value of the core is (7.0 ± 0.2) ×10^{-5} nm^{-2}, whereas the SLD of the shell is (1.5 ± 0.2) × 10^{-4} nm^{-2} (obtained manually during fitting), indicating a small amount of ca. 12 % of D_2O in the hydrophilic shell of the micelles. ξ_{OZ} is 8.1 ± 0.8 nm, which describes the correlations in the PSPP shell around the collapsed PNIPMAM core. No forward scattering is observed in the SANS curves in regime III, which is in agreement with the results from turbidimetry, namely, that the solution is not completely turbid.

The SANS measurements are in good agreement with turbidimetry and DLS for both diblock copolymers. The stability in heating/cooling cycles was investigated using small-angle X-ray scattering (SAXS) at the example of a 150 g L^{-1} $PSPP_{498}$-*b*-$PNIPMAM_{144}$ solution in D_2O (for experimental details and results see the appendix A). The same equilibration times as in the SANS experiments were applied. No difference between heating and cooling was found.

6.4.2.1. Comparison of the self-assembled structures in salt-free solutions of $PSPP_{432}$-*b*-$PNIPAM_{200}$ and $PSPP_{498}$-*b*-$PNIPMAM_{144}$

The structures in the three regimes of the $PSPP_{432}$-*b*-$PNIPAM_{200}$ and $PSPP_{498}$-*b*-$PNIPMAM_{144}$ solutions, according to SANS and expectations relating to the (aggregated) behavior, are depicted in Figure 6.6.

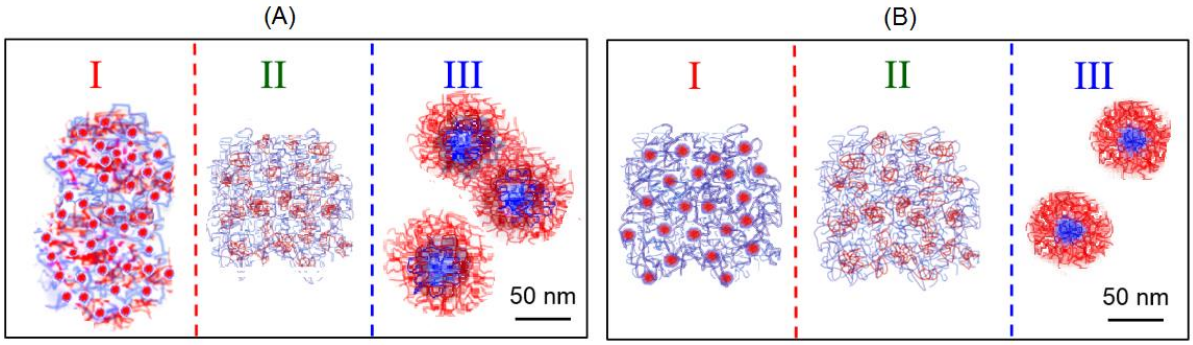

Figure 6.6: Schematic representation of the micelles/polymer coils in the three regimes of the $PSPP_{432}$-*b*-$PNIPAM_{200}$ (A) and $PSPP_{498}$-*b*-$PNIPMAM_{144}$ (B) solutions as indicated. Red: PSPP block, blue: PNIPAM/PNIPMAM block. (**--**) and (**-·-**): CP_{UCST} and CP_{LCST}.

In regime II, both blocks are soluble, and the solubility of the PSPP block is driven by the ionic interactions between water and the charged polymer chains, resulting in concentration fluctuations. In regimes I and III, the diblock copolymers are amphiphilic, but with reversed hydrophilic and hydrophobic blocks, and form micelles: In regime I, small spherical domain (5 nm and 6-15 nm in the solutions of $PSPP_{432}$-*b*-$PNIPAM_{200}$ and $PSPP_{498}$-*b*-$PNIPMAM_{144}$, respectively), presumably consisting of both, PSPP and PNIPAM/PNIPMAM, are immersed in a PNIPAM/PNIPMAM-rich matrix, are correlated and form very large aggregates. The expected core-shell structure of the micelles in regime I is not observed, probably because the PSPP and PNIPMAM blocks interact with each other. In contrast, in regime III, the micellar radius is much larger (90 nm and 28 nm in the solutions of $PSPP_{432}$-*b*-$PNIPAM_{200}$ and $PSPP_{498}$-*b*-$PNIPMAM_{144}$, respectively), and a core-shell structure is evident. Neither a

correlation of the micelles nor aggregation on larger length scales are observed, which may be due to the thick hydrophilic PSPP shell, keeping the micelles in the solvated state. The difference in the micellar radii in regimes I and III of both systems may be assigned to the block properties and the architecture of the diblock copolymers: The PSPP block, which is water-insoluble in regime I, is ca. 2/3 times longer than the PNIPAM/PNIPMAM block, which is water-insoluble in regime III.

The different chemical nature of the shells of the particles in regime I and in regime III of the solutions of both diblock copolymers indicated by several parameters: The hard-sphere structure factor describing the spatial correlations between the particles in the $PSPP_{498}$-*b*-$PNIPMAM_{144}$ solution applies only below CP_{UCST}, whereas no correlations were evident above CP_{LCST}. Half the interparticle distance in the $PSPP_{432}$-*b*-$PNIPAM_{200}$ solution is ca. 3 times larger above CP_{LCST} than below. The values of the correlation length ξ_{OZ} from the OZ structure factor in regime I and III for both diblock copolymers are different. Moreover, the different characters of the microphase-separated domains in regimes I and III are qualitatively corroborated by the temperature-dependent fluorescence characteristics of the solvatochromic end-group label at the example of the block copolymer $PSPP_{498}$-*b*-$PNIPMAM_{144}$ (for experimental details and results see the appendix A).

When comparing the SANS results from the $PSPP_{498}$-*b*-$PNIPMAM_{144}$ and the $PSPP_{432}$-*b*-$PNIPAM_{200}$ solutions in salt-free D_2O, three factors have to be considered: (i) The overall molar mass of $PSPP_{432}$-*b*-$PNIPAM_{200}$ is slightly lower. (ii) The block lengths and, accordingly, the composition of the diblock copolymers are different: In $PSPP_{432}$-*b*-$PNIPAM_{200}$, the PSPP block is 1.2 times shorter, whereas the nonionic block is 1.4 times longer, i.e. the fraction of PSPP is lower. (iii) PNIPMAM homopolymers forms aggregates in solution already below the cloud point, which is not the case in PNIPAM solutions. SANS curves from both diblock copolymers in regimes I-III are compiled in Figure A.4 in the appendix A.

In regime I, the overall scattering intensity is higher for $PSPP_{498}$-*b*-$PNIPMAM_{144}$. This is mainly due to the significantly higher forward scattering due to very large aggregates, and the mesoscopic length scales are larger, e.g. the radii of the spherical particles are a factor 1.3-3.4 times larger. One reason may be the higher block length of PSPP, which is at the origin of structure formation in this regime, i.e. below its CP_{UCST}. Another reason may be the tendency of PNIPMAM to expand below CP_{LCST}, as evidenced by our SANS measurements on

$PNIPMAM_{192}$, even though the CP_{LCST} is further away than it is in $PSPP_{432}$-*b*-$PNIPAM_{200}$. This effect may also promote the formation of very large aggregates in the $PSPP_{498}$-*b*-$PNIPMAM_{144}$ solution.

In regime II, the scattering intensity of the $PSPP_{498}$-*b*-$PNIPMAM_{144}$ solution is also higher, the polyelectrolyte peak is shifted to lower *q*-values and the length scales are larger: The average distance between the charged domains, d_0, is 1.5 times larger, which is presumably due to the expanded conformations of PNIPMAM block. The tendency to aggregation of the PNIPMAM block close to its CP_{LCST} is corroborated by the appearance of inhomogeneities on a length scale of around 30 nm just below CP_{LCST} in the $PSPP_{498}$-*b*-$PNIPMAM_{144}$ solution.

The largest differences between the two diblock copolymers are observed in regime III. In this regime, the overall scattering intensity of the $PSPP_{498}$-*b*-$PNIPMAM_{144}$ solution is lower, especially at low *q*-values, and the core radius is significantly smaller (13 nm vs. 73 nm). The core is formed by PNIPMAM which is smaller in size than the PNIPAM block, but this effect alone cannot explain this huge difference (using ideal chain statistics, the core radius should only differ by a factor $(200/144)^{1/2} = 1.18$). The core radius of 13 nm is rather close to the expected value of the end-to-end distance of PNIPMAM, which may be roughly estimated using the end-to-end distance of poly(methyl methacrylate) of a molar mass of 29,000 g mol^{-1} (value from end group analysis, Table 4.1),[226] namely 11 nm. Since the core radius of 73 nm found for $PSPP_{432}$-*b*-$PNIPAM_{200}$, is significantly larger, we suspect that for this diblock copolymer clusters of micelles are formed, whereas they are separated from each other for $PSPP_{498}$-*b*-$PNIPMAM_{144}$. This is confirmed by the absence of the spatial correlations between the particles in the $PSPP_{498}$-*b*-$PNIPMAM_{144}$ solution. This may be due to both, the longer PSPP block and the stronger tendency to aggregation of PNIPMAM .block. The micellar shell formed by PSPP that has a thickness of 15 nm for $PSPP_{498}$-*b*-$PNIPMAM_{144}$, is smaller than the one of $PSPP_{432}$-*b*-$PNIPAM_{200}$ (19 nm), and contains about 5 times less D_2O. Thus, the PSPP shell is more compact in the solution, which may point to its interaction with PNIPMAM.

6.4.3. Electrolyte effect

Turbidimetry reveals changes of the CP_{UCST} cloud points of the diblock copolymers in D_2O upon addition of low molar mass electrolytes (Figure 6.1b-d). The CP_{UCST} is found to increase in a 50 g L^{-1} solution of $PSPP_{430}$-*b*-$PNIPAM_{200}$ in 0.004 M NaBr in D_2O by about

0.6 °C, and by about 0.8 °C and 1.8 °C in a 50 g L^{-1} solution of $PSPP_{498}$-*b*-$PNIPMAM_{144}$ in 0.006 M NaCl and in 0.004 M NaBr in D_2O, respectively, compared to those in salt-free D_2O. To gain information about the structural changes caused by electrolyte addition, temperature-dependent SANS measurements of 50 g L^{-1} solutions of $PSPP_{430}$-*b*-$PNIPAM_{200}$ and $PSPP_{498}$-*b*-$PNIPMAM_{144}$ were performed in 0.004 M NaBr in D_2O (Figure 6.7). Zooms of the low *q* region of the SANS curves for both systems in regime I at 15 ºC, in regime II at 22/29 ºC and 49 ºC and in regime III at 49/59 ºC are shown in Figure A.6 in the appendix A.

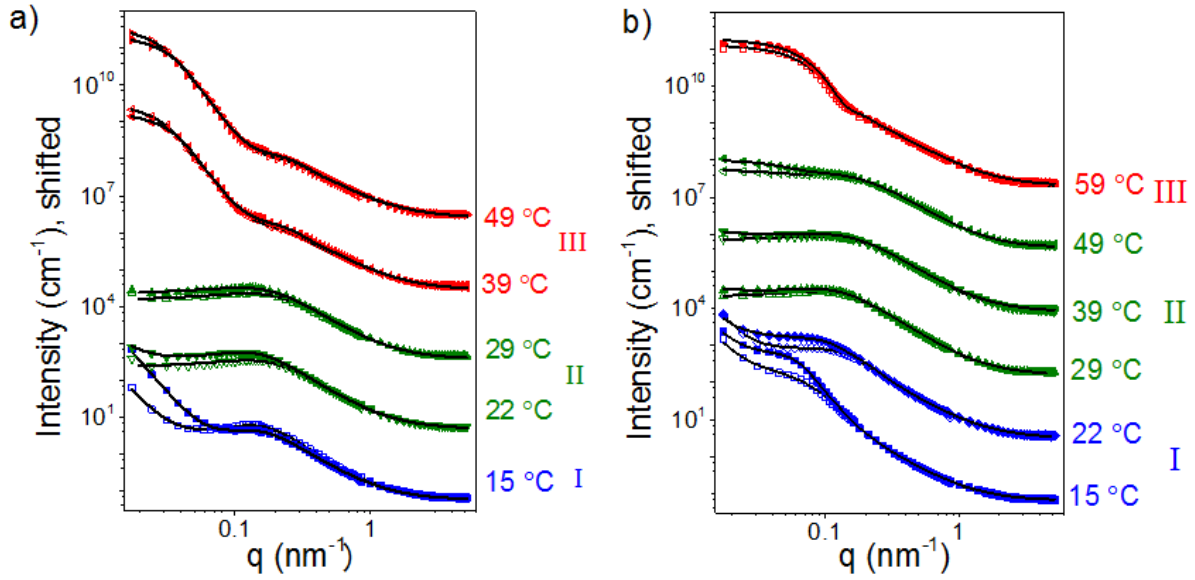

Figure 6.7: SANS curves from 50 g L^{-1} solutions of $PSPP_{430}$-*b*-$PNIPAM_{200}$ (a) and $PSPP_{498}$-*b*-$PNIPMAM_{144}$ (b) in salt-free D_2O (open symbols, from Figure 6.4) and in 0.004 M NaBr in D_2O (closed symbols), where only every third point is shown for clarity, together with the fitting curves (—) obtained using Eq. 6.1 in regimes I and III and Eq. 6.2 in regime II. The curves are shifted in intensity as in Figures 6.4 (c,d).

The SANS curves of $PSPP_{430}$-*b*-$PNIPAM_{200}$ in 0.004 M NaBr in D_2O (Figure 6.7a) feature significantly increased forward scattering at *q* values below ca 0.07 nm^{-1} in regime I (blue) (Figure A.6a in the appendix A) and weakly increased forward scattering in regime II (green) below ca 0.16 nm^{-1} (Figure A.6b in the appendix A). Above these *q* values, the curves stay virtually unchanged. The shape of the curves in regime III (red) remains unchanged over the entire *q* range, and only at *q* values below 0.03 nm^{-1}, the intensity is 1.5 times lower compared to the one in salt-free solution (Figure A.6c in the appendix A).

Slightly different changes were observed in the SANS curves of $PSPP_{498}$-*b*-$PNIPMAM_{144}$ in 0.004 M NaBr in D_2O (Figure 6.7b): In regime I (blue), the SANS curves feature

significantly increased forward scattering at q values below ca 0.09 nm^{-1} as well as a shift of the shallow maximum to lower q values (Figure A.6d in the appendix A). In regime II (green), the forward scattering below 0.04 nm^{-1} at 29 and 39 ºC, and below 0.06 nm^{-1} at 49 ºC is slightly increased (Figure A.6e,f in the appendix A). The shape of the curves in regime III (red) remain unchanged over the q range above 0.09 nm^{-1}, but at lower q values, the intensity is 1.5 times higher than in salt-free solution (Figure A.6g in the appendix A).

The same fitting models are used as for the curves from salt-free solutions, and the resulting parameters are compiled in Tables A.6 and A.8 (using Eq. 6.2) and Tables A.7 and A.9 (using Eq. 6.1) in the appendix A. The results of the latter are shown in Figure 6.8.

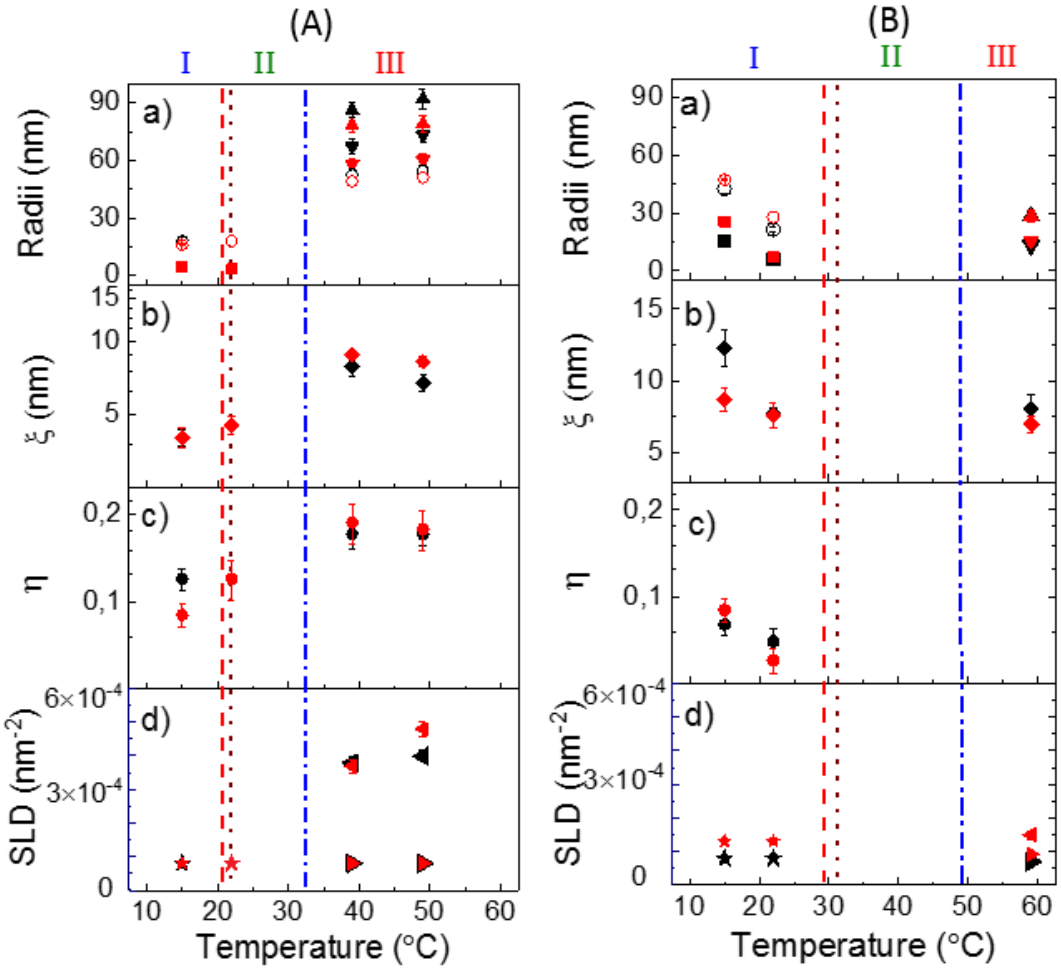

Figure 6.8: Results from model fitting to the SANS curves in Figures 6.4 and 6.7 from $PSPP_{430}$-*b*-$PNIPAM_{200}$ (A) and $PSPP_{498}$-*b*-$PNIPMAM_{144}$ (B) in salt-free D_2O (black symbols) and in 0.004 M NaBr in D_2O (red symbols), respectively. Same designations as in Figure 6.5. CP_{UCST} in salt-free D_2O (▬) and in 0.004 M NaBr in D_2O (┅), CP_{LCST} value (┅), all determined by turbidimetry.

Results of the analysis of the SANS curves of $PSPP_{432}$-b-$PNIPAM_{200}$ in 0.004 M NaBr in D_2O.
In regime II, the solvation term displays ξ_{solv} decreasing from 8.3 ± 0.3 nm at 22 °C to 6.5 ± 0.2 nm at 29 °C (Table A.6 in the appendix A). As in salt-free conditions, ξ_{solv} describes the correlations in the hydrophilic PNIPAM shell. At 22 °C, ξ_{solv} is about 2 nm higher compared to the one in salt-free solution, due to the stronger attractive interactions in the PSPP block. Its decrease at 29 ºC indicates a weakening of the interactions between the PSPP segments. The solvation Porod exponent, *m*, is around 2.0, indicating good solvent quality. The scaling factor *C* decreases from 7.7 ± 0.2 at 22 °C to 5.5 ± 0.1 at 29 °C, indicating the onset of phase separation at 22 ºC, which is shifted to a higher temperature than in salt-free D_2O due to the presence of NaBr. The average distance between the charged domains, d_0, is 55 ± 3 at 22 °C and 59 ± 4 nm at 29 °C, i.e. on average about 6 nm higher than in salt-free polymer solution. Thus, in regime II, the salt screening effect causes larger distances between the inhomogeneities. In contrast to the salt-free polymer solution, the Porod law has to be applied at 22 ºC to describe the increased forward scattering. The Porod exponent α = 3.1 ± 0.1 indicates the presence of aggregates with rough surfaces. The Porod amplitude is more than ten times lower than in regime I, meaning that only few aggregates are formed.

Since the solution starts to phase separate at 22 ºC, the SANS model described in Eq. 6.1 can be applied as well. The fitting results are compared to the ones obtained in salt-free solution at 15 ºC, i.e. in regime I. The spherical particles about 1.2 nm smaller in radii and have a higher polydispersity p = 0.64 ± 0.07 (Table A.7 in the appendix A, Figure 6.8A). The other parameters reveal no or only minor changes. The Porod law has to be applied to describe increased forward scattering, and it reveals the same parameters as when using the solvation model (Eq. 6.2).

Comparison of the resulting fitting parameters in regime I using Eq. 6.2, with and without NaBr addition, reveals the following changes (Table A.6 in the appendix A): With NaBr, the solvation term displays a slightly increased ξ_{solv} value (on average about 0.4 nm higher). The solvation Porod exponent, *m*, is 1.86, indicating a decline of the solvent quality. The scaling factor is lower (C = 4.8 ± 0.1), which is consistent with the shift of the phase separation to regime II to a higher temperature. d_0 is about 3 nm higher. The Porod exponent, α, is 4.3 ± 0.1 with its amplitude being about 2 times higher than the one in salt-free solution. Comparison of the resulting fitting parameters in regime I with and without NaBr addition when using Eq. 6.1 reveals following changes: r_{avg} is only 0.2 nm higher with a similar

polydispersity, p = 0.45 ± 0.04 (Table A.7 in the appendix A, Figure 6.8A). $2R_{HS}$ is 4 nm lower, indicating more closely spaced spheres, but which have a lower volume fraction η = 0.09 ± 0.1. The correlation length ξ_{OZ} is unchanged. The Porod law reveals α = 4.4 ± 0.2 with the amplitude being about 4 times higher than the one in salt-free solution, indicating stronger aggregation, possibly due to the screening effect. The SLD values are again unchanged.

In regime III, the core-shell micelles are smaller than in salt-free solution and characterized by a more stable size within this temperature range: r_{core} = 58 ± 3 nm, and the core polydispersity stays unchanged within the error, p_{core} = 0.28 ± 0.03, the shell thickness is t = 20 ± 1 nm and thus r_{mic} = 79 ± 4 nm (Table A.7 in the appendix A, Figure 6.8A). The micelles are correlated as well, $2R_{HS}$ is 100 ± 10 nm, and the volume fraction is about 0.19. Thus, the interparticle interactions are stronger, and the core-shell micelles are smaller in the presence of electrolyte. The SLD value of the core stays in the range of (0.77 - 0.83) × 10^{-4} nm^{-2}, whereas the SLD of the shell is in the range (3.6 - 4.2) × 10^{-4} nm^{-2}, indicating 55 - 59 % of D_2O, which is less compared to the salt-free conditions. The correlation length ξ_{OZ} in regime III is 8.8 ± 0.3 nm at 39 ºC and 8.2 ± 0.4 nm at 49 ºC, thus comparably higher than in salt-free conditions. In this regime, ξ_{OZ} describes the correlation in the hydrophilic PSPP shell and may be increased because of the screening effect. Again, no forward scattering is observed. Thus, at low salt concentrations and in the region where the aggregation is induced by the thermoresponsive block, salt addition causes a reduction of the micellar size due to the shrinkage of the hydrophilic PSPP shell which contains charges.

Results of the analysis of the SANS curves of $PSPP_{498}$-b-$PNIPMAM_{144}$ in 0.004 M NaBr in D_2O. In regime II, the correlation length ξ_{solv} (describing the correlation in the hydrophilic PNIPMAM shell) decreasing from 8.8 ± 0.9 nm at 29 °C to 5.8 ± 0.5 nm at 49 °C (Table A.8 in the appendix A). This indicates weakening of the attractive interactions between the PSPP segments. ξ_{solv} is unaffected by the presence of NaBr within the precision of the measurements. The solvation Porod exponent, m, is unchanged, i.e. around 2. The scaling factor C decreases from 13.4 ± 1.2 cm^{-1} at 29 °C to 7.1 ± 0.7 cm^{-1} at 49 °C. These values are slightly higher compared to the ones obtained in salt-free solution; thus, interpolymer interactions are strengthened due to the screening effect of the salt, in agreement with the upwards shift of CP_{UCST}. The average distance between the charged domains, d_0, is 83 ± 11 nm at 29 °C and at 39 °C and 103 ± 10 nm at 49 ºC. d_0 is on average 8 nm larger than in salt-

free solution, which is due to the electrostatic screening, and the difference is most pronounced close to CP_{LCST}. In contrast to the salt-free polymer solution, the Guinier approximation has to be applied to describe the observed upturn at low q values at all temperatures in regime II. Aggregates with radii of gyration R_g decreasing from about 91 nm at 29 ºC, to 60 nm at 39 ºC and further to 36 nm at 49 ºC are formed. The Guinier scaling factor decreases from 29 ºC to 39 ºC from about 6 to 2 cm^{-1}, indicating a decrease of the fraction of the aggregates above the UCST-type transition. It increases to 10 cm^{-1} at 49 ºC, which is 3 times higher compared to the one in salt-free solution. Screening by salt thus breaks up the larger aggregates/more homogeneous large-scale structure observed in salt-free solution, and the scattering of the aggregates moves into the accessible q-range.

In regime I, fitting Eq. 6.2 reveals a similar trend for all parameters as in salt-free solution, however, with the following differences (Table A.9 in the appendix A, Figure 6.8): The correlation length ξ_{solv} increases by a factor of about 1.4. Thus, the screening of ionic interactions causes the formation of spherical particles with a less compact (presumed) PNIPMAM shell. The solvation Porod exponent m is slightly higher (by 0.05 and by 0.21 at 22 and 15 ºC, respectively), indicating that the solvent quality of the shell improves at lower temperatures. The scaling factor C is 2 and 4 times higher at 22 and 15 ºC, respectively, due to the incipient phase separation, which already starts in regime II. Moreover, d_0 is on average about 20 nm larger. The Porod exponent and amplitude are unchanged.

The following differences are revealed when comparing the fitting parameters using Eq. 6.1 with and without NaBr addition: The sphere radius r_{avg} is only 1.3 nm larger at 22 ºC, but 11 nm larger at 15 ºC with a lower polydispersity at 15 °C: $p = 0.49 \pm 0.06$ at 22 ºC and $p = 0.34 \pm 0.02$ at 15 ºC (Table A.9 in the appendix A, Figure 6.8B). R_{HS} is on average 8 nm larger, indicating an increase in the space between the (larger) spheres. ξ_{OZ} differs only at 15 ºC, where it is around 4 nm smaller than in salt-free conditions. Most probably, the salt screening effect promotes the formation of more compact spherical particles at low temperatures and, at 15 ºC, the correlation length may also include contributions from the inner part of the sphere. The Porod law reveals $\alpha = 4.1 \pm 0.3$ with nearly the same amplitude as in salt-free solution, indicating a similar rate of aggregation. The SLD values are unchanged as well.

In regime III, the core-shell micelles are still uncorrelated and, within the uncertainties, unchanged from the salt-free solution, but have a slightly larger core: $r_{core} = 15 \pm 2$ nm (Table

A.9 in the appendix A, Figure 6.8B). The SLD value of the core is $(7.0 \pm 0.2) \times 10^{-5}$ nm^{-2}, whereas the SLD of the shell is $(9.2 \pm 0.8) \times 10^{-5}$ nm^{-2}, indicating around 5 % of D_2O in the shell, which is much less compared to the salt-free conditions. The correlation length ξ_{OZ} in regime III, describing the correlation in the hydrophilic PSPP-rich shell, is 7.0 ± 0.6 nm, thus slightly lower than in salt-free conditions. ξ_{OZ} may be decreased because of the screening effect. Again, no forward scattering is observed. Therefore, in regime III, where micelles with a PNIPMAM-rich core and a PSPP-rich shell are formed, the addition of a small amount of salt causes the formation of the micelles with a slightly larger core and a slightly thinner shell than in salt-free conditions.

6.4.3.1. Comparison of effect of salt in solutions of PSPP$_{498}$-*b*-PNIPMAM$_{144}$ and PSPP$_{432}$-*b*-PNIPAM$_{200}$

While the structural changes found in 0.004 M NaBr solutions of PSPP$_{432}$-*b*-PNIPAM$_{200}$ and PSPP$_{498}$-*b*-PNIPMAM$_{144}$ are only minor and follow the same trend, we nevertheless observe some specific differences.

In regime I, the enhanced interpolymer interactions caused by the salt screening effect lead to a slight increase of the dimensions of the small spherical particles and an enhanced aggregation. These changes are more pronounced in the solution of PSPP$_{498}$-*b*-PNIPMAM$_{144}$, compared to those in solution of PSPP$_{432}$-*b*-PNIPAM$_{200}$.

In accordance with the shift of CP_{UCST} to higher temperatures, large aggregates appear in both systems upon salt addition, and the solvation scaling factor increases in both systems. Nevertheless, in regime II of both diblock copolymer solutions, the screening of the charges does not make the polyelectrolyte peak to disappear. The concentration of NaBr, 0.004 M, is too low to alter the general behavior. In regime II, it only causes an enhancement of the attractive interpolymer interactions, and hence, the distance between the charged domains increases. These enhanced attractive interactions cause the formation of a small fraction of aggregates (with radii decreasing from ca. 90 nm to ca. 40 nm during heating, i.e. larger close to CP_{UCST}) in regime II of the PSPP$_{498}$-*b*-PNIPMAM$_{144}$ solution, and formation of large aggregates with smooth surface at temperatures slightly above CP_{UCST} in the PSPP$_{432}$-*b*-PNIPAM$_{200}$ solution.

The changes of the core-shell micelles formed in regime III upon addition of electrolyte are only minor in PSPP$_{498}$-*b*-PNIPMAM$_{144}$, where the micelles are uncorrelated. In contrast, in

$PSPP_{432}$-*b*-$PNIPAM_{200}$, the micelles presumably form clusters and become more compact. Accordingly, the decrease of solvent content in the micellar shell in $PSPP_{498}$-*b*-$PNIPMAM_{144}$ solution is around twice as large as in $PSPP_{432}$-*b*-$PNIPAM_{200}$ solution. This may be because the PSPP shell is not only sensitive to the presence of salt, but also to the interaction with the PNIPMAM block. The latter is characterized by a stronger tendency for aggregation due to the additional methyl group that increases its hydrophobicity.

6.5. Conclusions

This chapter presented a study of the influence of the architecture and the chemical nature of the individual blocks on the solution phase behavior for a doubly thermoresponsive diblock copolymers in D_2O consisting of a zwitterionic (PSPP) block and a nonionic thermoresponsive (PNIPAM or PNIPMAM) block, which exhibit UCST and LCST behavior, respectively. We compare the "schizophrenic" responsive aggregation behavior of $PSPP_{498}$-*b*-$PNIPMAM_{144}$ and $PSPP_{498}$-*b*-$PNIPMAM_{144}$ in D_2O. For both systems, CP_{UCST} is lower than CP_{LCST}, so that the zwitterionic and the nonionic blocks are hydrophilic at intermediate temperatures, and the diblock copolymers are water-soluble in the entire temperature range studied (10-65 °C). Their aggregation behavior can be controlled by two stimuli, namely temperature to which both blocks respond effectively though in opposite ways, and to added low molar mass electrolytes, which is particular to the zwitterionic block.

By means of turbidimetry, we elucidated the cloud points (CP_{UCST} and CP_{LCST}) in semidilute solutions of the diblock copolymers and the corresponding homopolymers in D_2O. Turbidimetric results show for both diblock copolymers the same general pattern, revealing three regimes of association and self-assembly. At low and high temperatures, namely below the UCST-type and above the LCST-type phase transitions of the blocks, the solutions are turbid indicating the formation of aggregates, while at intermediate temperatures, solutions are translucent. While the overall behavior of the systems is very similar, the cloud points are altered from the ones in the respective homopolymers in a different way: In $PSPP_{432}$-*b*-$PNIPAM_{200}$, the CP_{UCST} value markedly decreases as compared to the $PSPP_{430}$ homopolymer while CP_{LCST} is unchanged. In contrast, for $PSPP_{498}$-*b*-$PNIPMAM_{144}$, the CP_{LCST} value markedly increases compared to the $PNIPMAM_{195}$ homopolymer while CP_{UCST} remains unchanged. This qualitative difference may be assigned to the steric hindrance in PNIPMAM due to the additional methyl group, resulting in a higher sensitivity to the environment, including the PSPP block and the dye-labeled end group attached.

Temperature-resolved SANS measurements of the diblock copolymers in D_2O give structural information in the three regimes. Both $PSPP_{432}$-*b*-$PNIPAM_{200}$ and $PSPP_{498}$-*b*-$PNIPMAM_{144}$ exhibit behavior similar to polyelectrolytes in solution, due to the ionic interactions between the PSPP chains. The difference in block lengths, the PSPP block being two/three times as large as the PNIPAM/PNIPMAM block, and their individual properties, such as dominating ionic interpolymer interactions versus hydrogen bonding with water, yield the marked differences of the aggregation behavior below CP_{UCST} and above CP_{LCST}, respectively: Below CP_{UCST}, the turbid solutions are characterized by very large aggregates with a smooth surface. These are formed by correlated, small and homogeneous spherical particles, which are larger in the $PSPP_{498}$-*b*-$PNIPMAM_{144}$ solution than in the $PSPP_{432}$-*b*-$PNIPAM_{200}$ solution. In the intermediate temperature range, between the UCST- and LCST-type transitions, the solutions are optically not completely clear, but remains hazy. This is related to the concentration fluctuations due to the polyelectrolytic nature of the PSPP block. Above the LCST-type transition, the partially turbid solutions contain correlated spherical core-shell micelles with a polydisperse core in the solution of $PSPP_{432}$-*b*-$PNIPAM_{200}$ and uncorrelated ones in the solution of $PSPP_{498}$-*b*-$PNIPMAM_{144}$, the micelles are larger in the $PSPP_{432}$-*b*-$PNIPAM_{200}$ solution. DLS in backscattering geometry confirmed the overall behavior of the systems. In addition, no differences are observed in SAXS measurements taken during heating and cooling runs, as shown at the example of $PSPP_{498}$-*b*-$PNIPMAM_{144}$.

Thus, the aggregation behavior of $PSPP_{430}$-*b*-$PNIPAM_{200}$ and $PSPP_{498}$-*b*-$PNIPMAM_{144}$ seems to be generic, but with larger spheres below CP_{UCST} and smaller aggregates above CP_{LCST} in $PSPP_{498}$-*b*-$PNIPMAM_{144}$. This may be partially due to the different ratio of the lengths of the zwitterionic to the nonionic blocks. A more important reason may be the chemical difference between the PNIPMAM and PNIPAM nonionic blocks which may favor the formation of associated structures of PNIPMAM below its CP_{LCST}, and stronger hydrophobic aggregation of the polymer chains above. An additional reason may be interactions of the PNIPMAM block with the PSPP block, both disposing of the same polymer backbone, which do not occur for PNIPAM.

According to the observations in the solutions of both diblock copolymers, the use of the LCST transition for the controlled core-shell formation and release of hydrophobic active substances, is more favorable than the use of the UCST transition. This conclusion is supported by the temperature-dependent fluorescence characteristics of hydrophobic dye

labels attached to the polymer ends at the example of $PSPP_{498}$-*b*-$PNIPMAM_{144}$. While the dye partitions preferentially into the microphase-separated domains of the nonionic block above its LCST-type coil-to-collapse transition, it does not incorporate into the microphase-separated domains of the zwitterionic block provided below the UCST-type transition.

As the CP_{UCST} of PSPP is known to be sensitive to added electrolytes, salt effects on the aggregation behavior of the diblock copolymers in 0.004 M NaBr in D_2O were also investigated by means of turbidimetry and SANS. Turbidimetry results reveal a salt-induced shift of CP_{UCST} in solutions of $PSPP_{432}$-*b*-$PNIPAM_{200}$ and $PSPP_{498}$-*b*-$PNIPMAM_{144}$ to the higher temperature by about 1 °C and 2 °C, respectively, while CP_{LCST} remains virtually unchanged. Although the salt concentration (0.004 M NaBr) is too low to alter the general behavior of the polymer, slight structural changes were found in all regimes for both systems: enhanced aggregation and increased radii of the small spheres in regime I, an increased distance between the charged domains in regime II, and in regime III, decreased micellar dimensions in the $PSPP_{432}$-*b*-$PNIPAM_{200}$ solution and increased micellar core dimensions in the $PSPP_{498}$-*b*-$PNIPMAM_{144}$ solution. We explain this by screening of the ionic interactions between the polymer attached charged groups.

Thus, the UCST- and LCST-type transition temperatures can be controlled by the selection of the nonionic thermoresponsive block as well as by the lengths of both blocks. Moreover, the UCST-type transition can be altered by addition of low molar mass electrolytes, without affecting the LCST-type transition.

7. “Schizophrenic” behavior - substitution of the polysulfobetaine block

In the previous chapter, we investigated the influence of the architecture and the nonionic block substitution on the self-assembly in aqueous solutions of the block copolymers consisting of a zwitterionic polysulfobetaine PSPP block and a nonionic thermoresponsive PNIPMAM or PNIPAM block. In the present chapter, we will study the aggregation behavior in aqueous solution of twofold thermoresponsive diblock copolymers consisting of a zwitterionic polysulfobetaine PSBP block and a PNIPMAM or PNIPMAM nonionic block, namely $PSBP_{78}$-*b*-$PNIPAM_{100}$ and $PSBP_{78}$-*b*-$PNIPMAM_{115}$, and compare their behavior to those of $PSPP_{430}$-*b*-$PNIPAM_{200}$ and $PSPP_{498}$-*b*-$PNIPAM_{144}$, described in chapter 6. This way, we address the question how the nature of polysulfobetaine monomer influences the behavior of the diblock copolymers with PNIPAM and PNIPMAM blocks. PSBP has a spacer group extended by one methylene group and a higher CP_{UCST} compared to PSPP (see paragraph 4.3). Thus, in the solutions of the diblock copolymers with a PSBP block, the CP_{UCST} is expected to be higher than CP_{LCST}, i.e. regime II’ may be encountered (Figure 3.2). This allows us to study the aggregation behavior at each phase transition, maximizing the impact of the other block properties, in contrast to the previous study of the systems with a PSPP block (chapter 6) where the impact was minimum.

The CP_{UCST} of the ionic-strength sensitive PSBP has previously been found to decrease monotonously with increasing salt (sodium halide) concentration,[32] in contrast to PSPP, where CP_{UCST} has nonlinear behavior.[31] Therefore, in the systems with PSBP the salting-in effect upon NaBr addition might result in a decrese of CP_{UCST}, and hence, in the change of the regime II’ on regime II (Figure 3.2).

The strategy of the study is similar to the one presented in chapter 6, with the only difference that DLS measurements was not performed. We will discuss the results of the turbidimetric investigations of phase behavior of the homo- and diblock copolymers and the detailed structural studies of the diblock copolymers explored by SANS measurements in salt-free solution and in the presence of electrolyte (NaBr at concentration 0.004 M). The details of sample preparation can be found in paragraph 4.5.1.

7.1. Experimental set-up

Turbidimetry. Cloud points were determined by means of turbidimetry following the procedure described in chapter 6 with the only difference that measurements of the $PSBP_{78}$-*b*-$PNIPAM_{100}$ and $PSBP_{78}$-*b*-$PNIPMAM_{115}$ solutions were performed during heating form 35 ºC to 65 ºC and cooling from 35 ºC to 15 °C.

Small-angle neutron scattering (SANS). SANS experiments were performed at the instrument KWS-1 at the JCNS outstation at MLZ in Garching, Germany. The incident neutrons had a wavelength $\lambda = 0.45$ nm with a spread of 10 %. A *q*-range from 0.03 to 4.7 nm^{-1} was covered. Samples were mounted in quartz glass cells from Hellma Analytics with a neutron path of 1 mm. Boron carbide was used for measurement of the dark current, poly(methyl methacrylate) for the detector sensitivity and calibration of the intensity. The sample transmission was measured. The scattered intensity curves were azimuthally averaged and corrected for background scattering from the solvent-filled cell and parasitic scattering, taking into account transmissions with the software package QtiKWS provided by JCNS.

The diblock copolymers $PSBP_{78}$-*b*-$PNIPAM_{100}$ and $PSBP_{78}$-*b*-$PNIPMAM_{115}$ were measured in pure D_2O and $PSBP_{78}$-*b*-$PNIPMAM_{115}$ additionally in 0.004 M NaBr in D_2O. Measurements of the $PSBP_{78}$-*b*-$PNIPAM_{100}$ solution were performed while heating from 10 °C to 50 °C in steps of 10 °C. The $PSBP_{78}$-*b*-$PNIPMAM_{115}$ solution was heated from 20 °C to 65 °C in steps of 5 °C. In both cases, a copper sample holder and an inner flow circuit connected to a thermostat were used. After each temperature change, a thermal equilibration time of 15 min was applied. The measuring times were 30 min, 15 min and 5 min at the sample-detector distances (SDDs) of 20.00 m, 7.99 m and 1.99 m, respectively.

Modeling of the SANS curves. To describe the SANS curves of the $PSBP_{78}$-*b*-$PNIPAM_{100}$ and $PSBP_{78}$-*b*-$PNIPMAM_{115}$ solutions in regimes I and III, the model function described in chapter 6 in Eq. 6.1, was used. For the curves in regime I, the form factor of polydisperse, homogeneous spheres (Eqs. 5.19-21) was applied. It reveals the average radius r_{avg} with the polydispersity *p* modeled by the Schulz distribution, taking into account the difference in scattering length densities (SLD) of the sphere, ρ_{sphere}, and the solvent, $\rho_{solvent}$, (values used see below). In regime III, the form factor of flexible cylinders with polydisperse radius $P_{cyl}(q)$ is more applicable (Eqs. 5.24-32). $P_{cyl}(q)$ reveals the average cylinder radius R_{cyl}

with the polydispersity *p* modeled by the Schulz distribution, the contour length *L* and Kuhn length *b*, taking into account the differences in SLDs of the cylinder, ρ_{cyl}, and the solvent, ρ_{solv}. The scattering curves of the $PSBP_{78}$-*b*-$PNIPMAM_{115}$ solution in 0.004 M NaBr in D_2O at 35-45 °C, i.e. in regime II, were additionally analyzed using the solvation model described in chapter 6 in Eq. 6.2.

The incoherent background was fixed at 0.6 nm^{-1}. The SLD value of PSBP was calculated using the mass density, assuming 1.0 g cm^{-3} for PSBP (estimated from the constituent elements and assuming a density of 1.0 g cm^{-3}, typical for organic polymers), $\rho_{PSBP} \approx 7.3 \times 10^{-5}$ nm^{-2}. $\rho_{D_2O} = 6.3 \times 10^{-4}$ nm^{-2}, $\rho_{PNIPAM} = 8.1 \times 10^{-5}$ nm^{-2}, $\rho_{PNIPMAM} = 6.8 \times 10^{-5}$ nm^{-2} (for details see chapter 6). According to the similarity of the SLD values for PNIPAM/PNIPMAM and PSBP, the SLD values of the spherical or cylindrical particles ($\rho_{cylinder}$ or ρ_{sphere}) in regimes I and III, respectively, were kept in the range (7.3-8.1) × 10^{-5} nm^{-2} for $PSBP_{78}$-*b*-$PNIPMAM_{100}$, or at (6.8-7.3) × 10^{-5} nm^{-2} for $PSBP_{78}$-*b*-$PNIPMAM_{115}$, which correspond to an average of the SLD values of pure PSBP and PNIPAM or PNIPMAM, respectively. Thus, we assumed that the micelles do not contain D_2O.

7.2. Phase behavior

Using turbidimetry, the cloud point of a 50 g L^{-1} solution of the homopolymer $PSBP_{78}$ in salt-free D_2O was determined during a cooling run (not shown), CP_{UCST} ($PSBP_{78}$) = 78.2 ± 0.5 ºC. The cloud points of PNIPAM and PNIPMAM are known from literature to be about 32 ºC and 44 ºC.[107-111] In solutions of both $PSBP_{78}$-*b*-$PNIPAM_{100}$ and $PSBP_{78}$-*b*-$PNIPMAM_{115}$ the UCST-type transition is expected to be above the LCST-type transition. The overlap of the cloud points is expected to be stronger in the solution of $PSBP_{78}$-*b*-$PNIPAM_{100}$.

Figure 7.1a shows representative light transmission curves of 50 g L^{-1} solutions of $PSBP_{78}$-*b*-$PNIPAM_{100}$ in salt-free D_2O and in 0.004 M NaBr in D_2O. In salt-free solution, only ca. 2.8 % of light is transmitted, thus the transmission of light is virtually blocked in the entire temperature range investigated. An increase of the light transmission caused by macroscopic precipitation in the case when CP_{UCST} is higher than CP_{LCST} or when the chains are dissolved in the case of the reverse order of the cloud points, was not observed. This may be due to very close values of the CP_{UCST} and CP_{LCST}. Addition of NaBr causes a slight increase of the

light transmission in the range of 27-34 °C, due to a shift of CP_{UCST} of the PSBP block to lower temperatures. However, the increase amounts only to 1.2 %. This may be due to the very gradual transmission increase below the UCST-type transition; the LCST-type transition occurs before the attractive interactions in the PSBP block get sufficiently weak. Therefore, the three regimes distinguished in the transmission curves of the diblock copolymer in 0.004 M NaBr in D_2O may be indicated as I, II and III, according to the scenario described in chapter 3 (Figure 3.2): In regimes I and III, the transmission of light is low due to the micelle formation with reversed core-shell structure. In regime II, the light transmission is enhanced due to the incipient weakening of the polymer-polymer interactions in the PSBP block.

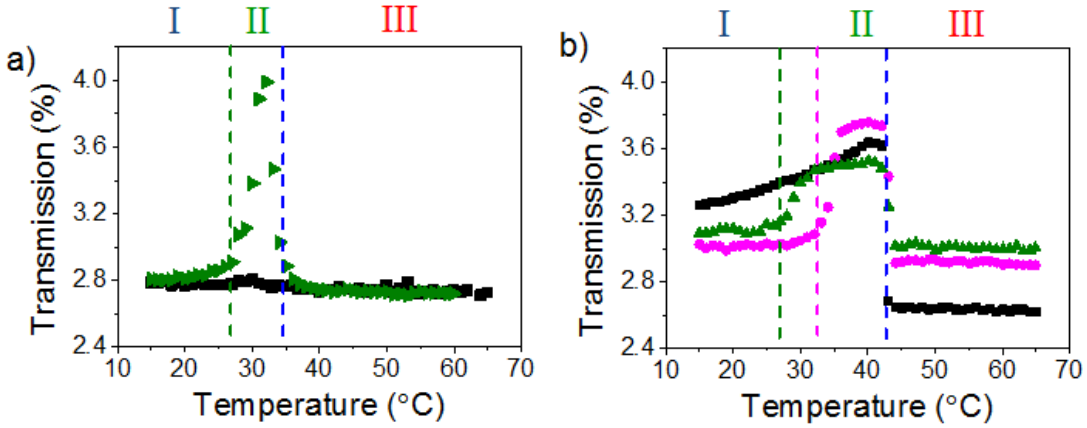

Figure 7.1: Light transmission curves of 50 g L^{-1} solutions of $PSBP_{78}$-*b*-$PNIPAM_{100}$ (a) and $PSBP_{78}$-*b*-$PNIPMAM_{115}$ (b) in salt-free D_2O (■), in 0.002 M NaBr (●), and in 0.004 M NaBr (▲) in D_2O. The lines show the onset of CP_{UCST} in 0.002 M NaBr (--) and 0.004 M NaBr in D_2O (--), as well as CP_{LCST} in all solutions (--).

A notably higher LCST transition of PNIPMAM compared to the one of PNIPAM could result in the enlarged temperature window between the onset of CP_{UCST} and CP_{LCST} in the solution of $PSBP_{78}$-*b*-$PNIPMAM_{115}$ compared to the one in the solution of $PSBP_{78}$-*b*-$PNIPAM_{100}$. Representative light transmission curves of 50 g L^{-1} solutions of $PSBP_{78}$-*b*-$PNIPMAM_{115}$ in salt-free D_2O, in 0.002 M and 0.004 M NaBr in D_2O are shown in Figure 7.1b. In salt-free conditions, the light transmission increases smoothly from ca. 3.2 % to 3.7 % during heating from 15 ºC to 43 ºC. The sharp decrease of the light transmission at 43 ºC indicates a phase transition. Above this temperature, the transmission of light is virtually blocked, only ca. 2.6 % of light is transmitted. One of the possible reasons of the slightly higher light transmission below 43 ºC is the very gradual transmission increase below the UCST-type transmission of the PSBP block. Another reason may lie in the properties of

PNIPMAM block: its increased hydrophobicity, compared to PNIPAM, due to the additional methyl group, may enforce aggregation already below CP_{LCST} (for details see paragraph 6.4.1). The light transmission increases in the solutions of $PSBP_{78}$-*b*-$PNIPMAM_{115}$ in 0.002 M and 0.004 M NaBr in D_2O in the ranges of 33–43 °C and 27–43 °C, respectively. The transition at 43 °C, which is unchanged in both salt-free solution and solutions with salt, is assigned to the CP_{LCST} of PNIPMAM, which is not expected to be susceptible to low molar mass salts, especially at low concentrations. Similar to the observations in the solution of $PSBP_{78}$-*b*-$PNIPAM_{100}$ in 0.004 M NaBr in D_2O, the lower transition may be assigned to the onset of the UCST-type transition. This onset decreases with an increase of the concentration of NaBr, confirming sensitivity of the PSBP block to low concentrations of added salt. Three regimes are distinguished in the transmission curves indicated as I, II and III (Figure 7.1b). In regimes I and III, the transmission of light is blocked. In regime II, only ca. 3.8 % of light is still transmitted, i.e. only 0.4-1.0 % higher than in regimes I and III. Thus, the attractive interactions between PSBP segments are only slightly affected by the low concentration of NaBr. The light transmission in regime III (above 43 °C) is slightly higher in solutions with NaBr, compared to the one in salt-free conditions. This may be due to the salt screening effect and ion sensitivity of the zwitterionic PSBP, which presumably compose a shell surrounding the PNIPMAM-rich core in regime III. This indicates that attractive interactions in PSBP are present even above the LCST-type transition.

The values of the CP_{LCST} determined in the solutions of $PSBP_{78}$-*b*-$PNIPAM_{100}$ and $PSBP_{78}$-*b*-$PNIPMAM_{115}$, namely 34 and 43 °C, respectively, are close to those known from the literature for PNIPAM (32 °C) and PNIPMAM (44 °C). Thus, the CP_{LCST} values in the solutions of both diblock copolymers are not susceptible to the presence of salt and to the polymer architecture, namely presence of the PSBP block. The CP_{UCST} values could not be precisely determined due to the proximity of the CP_{LCST}. Only the onset of the UCST-type transitions is observed below or close to the LCST-type transitions in the salt-free solution of $PSBP_{78}$-*b*-$PNIPMAM_{115}$ and in solutions with NaBr of both diblock copolymers. Nevertheless, we may conclude that the CP_{UCST} in the diblock copolymers solutions has significantly decreased, compared to the one of the homopolymer $PSBP_{78}$. Thus, the CP_{UCST} of PSBP is altered by the coupling to the PNIPAM/PNIPMAM block and by low concentrations of added low molar mass, i.e., it depends on the polymer architecture and the environment.

When comparing the values of the cloud points in the 50 g L^{-1} solutions of $PSBP_{78}$-*b*-$PNIPAM_{100}$ and $PSBP_{78}$-*b*-$PNIPMAM_{115}$ in 0.004 M NaBr in D_2O, a difference is revealed in the CP_{LCST} value, while the onset of CP_{UCST} is identical. The CP_{LCST} value of $PSPP_{432}$-*b*-$PNIPAM_{200}$ is ca. 8 ºC lower, which is in agreement with the fact that the CP_{LCST} value of the PNIPAM homopolymer is ca. 10 ºC lower than the one of PNIPMAM. Thus, the gap between the onset of the UCST-type transition and the LCST-type transition is maximum in the solution of $PSBP_{78}$-*b*-$PNIPMAM_{115}$ in 0.004 M NaBr, as intended.

7.3. Structural investigations using SANS

To identify the structural changes, being at the origin of the observed phase behavior of the diblock copolymers $PSBP_{78}$-*b*-$PNIPAM_{100}$ and $PSBP_{78}$-*b*-$PNIPMAM_{115}$, temperature-resolved SANS measurements of a 50 g L^{-1} solution were carried out.

7.3.1. Self-assembled structures in solutions of the diblock copolymers

Figure 7.2 presents the SANS curves of the salt-free solutions of $PSBP_{78}$-*b*-$PNIPAM_{100}$ and $PSBP_{78}$-*b*-$PNIPMAM_{115}$ in D_2O during heating. Only two regimes are clearly discernible by the curve shapes, presumably indicated as regimes I and III according to the turbidimetric measurements. The SANS curves of the $PSBP_{78}$-*b*-$PNIPAM_{100}$ solution in regime I (blue) feature a smooth decay starting at the lowest *q* values with a shallow maximum at ca. 0.1 nm^{-1}, which become flat above ca. 2 nm^{-1}. The curves in regime III (red) decays up to ca. 0.09 nm^{-1}, then feature three peaks at 0.16, 0.28 and 0.43 nm^{-1} at 50 °C and at 0.17, 0.32 and 0.46 nm^{-1} at 40 °C. The curve leveling off at ca. 2 nm^{-1}. The curves of the $PSBP_{78}$-*b*-$PNIPMAM_{115}$ solution are very similar to those of $PSBP_{78}$-*b*-$PNIPAM_{100}$, with some differences in regimes I and III: The overall intensity and the intensity of shallow maximum decrease during heating up to 45 °C. The curves in regime III (red) decay up to ca. 0.07 nm^{-1}, then only two peaks are observed at 0.14 and 0.4 nm^{-1}, and the second peak is less pronounced at 50 °C.

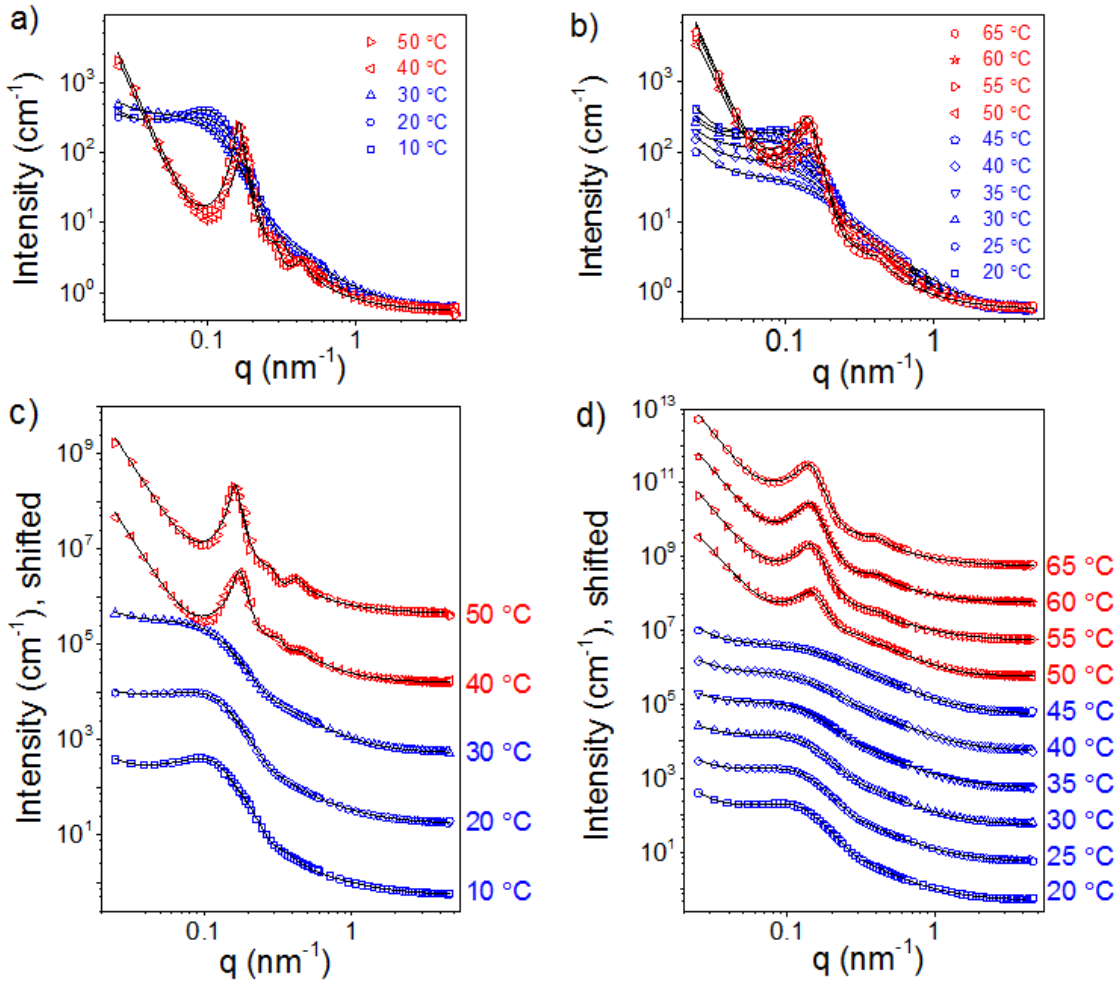

Figure 7.2: SANS curves from a 50 g L^{-1} salt-free solution of $PSBP_{78}$-*b*-$PNIPAM_{100}$ (a, c) and $PSBP_{78}$-*b*-$PNIPMAM_{115}$ (b, d) in D_2O (symbols), where every third point is shown for clarity, together with the fitting curves (—) obtained using Eq. 6.1, see details below. In (c) and (d) the curves are shifted in intensity by a factor of 50 with respect to each other for better visibility. Regimes I and III are indicated by the blue and red color, respectively.

The dramatic changes in the curves of $PSBP_{78}$-*b*-$PNIPAM_{100}$ are observed at 30-40 °C, which is in agreement with the CP_{LCST} value (ca. 34 °C) found in the turbidimetric measurements. In contrast, the changes in the curves of $PSBP_{78}$-*b*-$PNIPMAM_{115}$ are observed at 45-50 °C, but the CP_{LCST} was found at 43 °C. Most probably this is due to the difference in the measurement protocols: Prior turbidimetry measurements, the sample solution was equilibrated at 35 °C, after which heating and cooling runs were measured. During SANS measurements, the sample was measured during a heating run starting at 20 °C, and equilibration of 15 min at each temperature may have been too short. At 45 °C, the proximity of the CP_{UCST} and CP_{LCST} may result in competition of the attractive interactions in the PSBP

and PNIPMAM blocks and cause a delay. The delay is observed only in solution of $PSBP_{78}$-*b*-$PNIPMAM_{115}$, which was measured in steps of 5 °C, whereas for the solution of $PSBP_{78}$-*b*-$PNIPAM_{100}$ the step width was 10 °C, and no delay was detected.

To analyze the structures, model fits were carried out. Figure B.1 in the appendix B shows two examples of the best fits to the scattering curves for both solutions of $PSBP_{78}$-*b*-$PNIPAM_{100}$ (Figure B.1a,c) and $PSBP_{78}$-*b*-$PNIPMAM_{115}$ (Figure B.1b,d) using the model function described above (chapter 6, Eq. 6.1). The fits are good in both regimes and reveal substantial structural changes during heating from regime I to regime III. The results of the fits for $PSBP_{78}$-*b*-$PNIPAM_{100}$ are summarized in Tables B.1 and B.2 in the appendix B and for $PSBP_{78}$-*b*-$PNIPMAM_{115}$ in Tables B.3 and B.4 in the appendix B.

Results of the analysis of the SANS curves of $PSBP_{78}$-b-$PNIPAM_{100}$. In regime I of $PSBP_{78}$-*b*-$PNIPAM_{100}$, micelle formation is expected (Figure 3.2). The SANS curves were decently fitted using the model described in Eq. 6.1, based on spheres correlated by a hard-sphere structure factor, plus an Ornstein-Zernike structure factor and a Porod term to describe intensity fluctuations at high and low q values, respectively (Figure B.1a in the appendix B). The polydisperse spherical particles have an average sphere radius r_{avg} = 14 ± 2 nm with a polydispersity slightly increasing from p = 0.22 ± 0.02 at 10 °C to p = 0.28 ± 0.03 at 30 °C (Table B.1 in the appendix B, Figure 7.3A). The average hard-sphere radius is R_{HS} = 25 ± 4 nm, which is almost twice the average radius. The volume fraction of correlated micelles, η, decreases from ca. 0.15 at 10 ºC to ca. 0.04 at 30 ºC. This indicates a weak correlation between the spherical particles, which becomes even weaker during heating. Ornstein-Zernike (OZ) structure factor reveals that ξ_{OZ} increases from 1.5 ± 0.2 nm at 10 °C to 3.6 ± 0.3 nm at 30 °C. ξ_{OZ} is much lower than the spherical radius. The low ξ_{OZ} may comprise the concentration fluctuations in the inner part and the shell, its increase indicates that the spheres (or their shells particularly) are getting more loose during heating to CP_{UCST}. The Porod exponent α = 4.0 ± 0.3 indicates formation of large compact aggregates with smooth surfaces. However, the contribution of a Porod term is weak, indicating a low fraction of the aggregates. Altogether, in regime I, small correlated spheres seem to form with a polydisperse radius. These spheres form a low fraction of large aggregates with smooth surfaces.

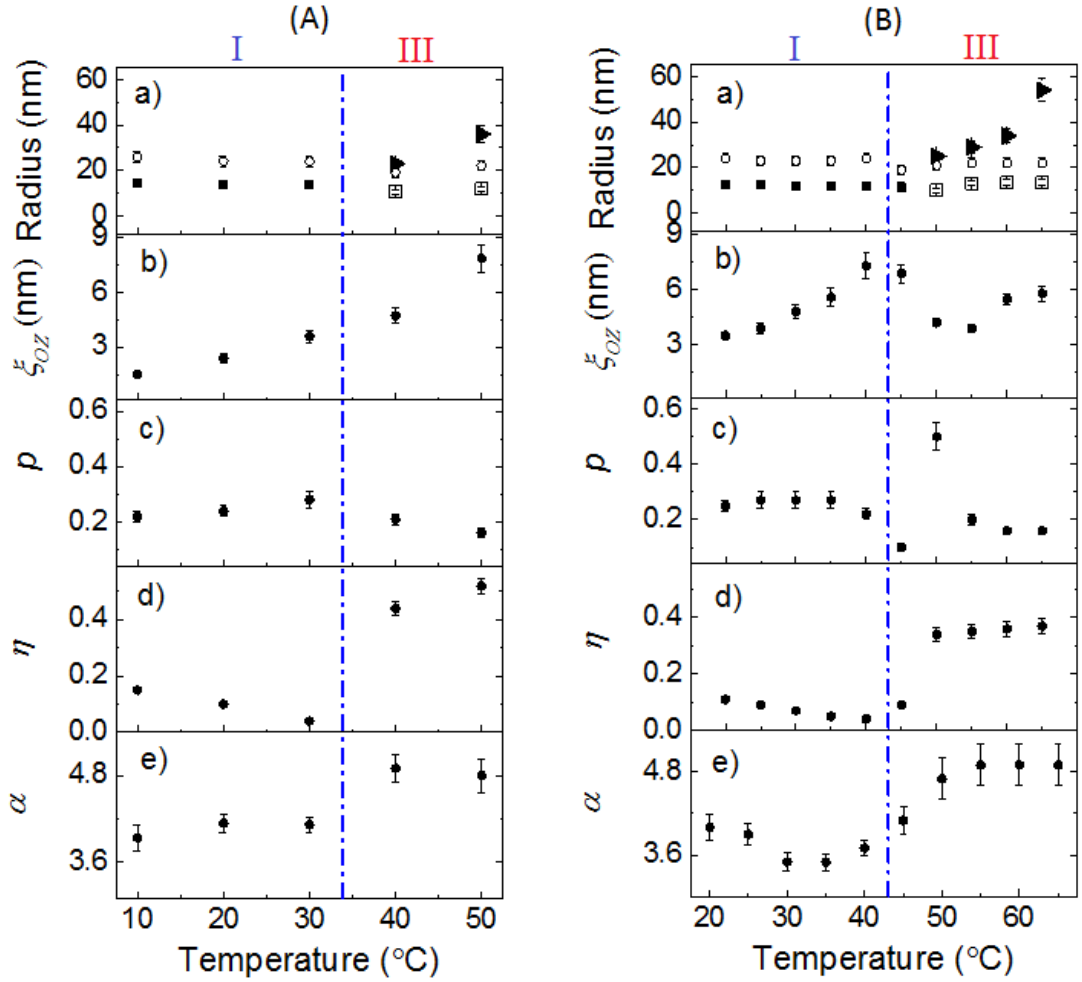

Figure 7.3: Results from fitting using Eq. 6.1 to the SANS curves of (A) $PSBP_{78}$-*b*-$PNIPAM_{100}$ and (B) $PSBP_{78}$-*b*-$PNIPMAM_{115}$ in Figure 7.2. Temperature dependence of the micellar radius, r_{avg}, (■), r_{cyl}, (□), contour cylinder length, l, (▶), the hard-sphere radius, R_{HS} (○) (a); of the correlation length, ξ_{OZ} (b), of the polydispersity of the micellar radius, p (c), of the hard-sphere volume fraction, η (d), and of the Porod exponent α values (e). In some cases, the symbol size is larger than the error bar. (---): CP_{LCST} values from turbidimetry. Regimes I and III are indicated on top of the graph.

The complex shape of the curves in regime III is very different from those in regime I. The best fits were achieved using the model (Eq. 6.1) based on flexible cylinders correlated by a hard-sphere structure factor, plus a solvation term, which is used to describe the correlation peak at a rather high q-value, which is typical of polyelectrolytes in salt-free solution,[224] together with the Porod term (Figure B.1c in the appendix B). Thus, in regime III, flexible cylindrical particles with a polydisperse core are formed, accompanied at small length scales by concentration fluctuations typical for polyelectrolytes in salt-free solution. The average

cylindrical core radius R_{avg} slightly increases from 10.6 ± 1.0 nm at 40 ºC to 11.9 ± 1.2 nm at 50 ºC, with a moderate polydispersity, which, in turn, decreases during heating from p = 0.21 ± 0.02 at 40 ºC to 0.16 ± 0.02 at 50 ºC (Table B.2 in the appendix B, Figure 8.3A). The average contour length of the cylinders increases during heating from L = 23 ± 2 nm at 40 ºC to 36 ± 4 nm at 50 ºC, along with the increase of the average Kuhn length from b = 10 ± 1 nm at 40 ºC and 16 ± 2 nm at 50 ºC. Kuhn length describes the length of hypothetical segments that can be considered as freely joined, i.e. the local stiffness of the chain. The increase of the Kuhn length and the contour length during heating indicates that there is no change in the stiffness of the cylinders, as the ratio L/b is identical at 40 and 50 °C, namely 2.3. We assume, that in regime III, the strong attractive interactions in both PNIPAM and PSBP blocks lead to the formation of cylinders with a PNIPAM-rich core presumably covered by a PSBP-rich shell. The cylinders aggregate apparently by attaching to each other's ends, thus forming longer cylinders with a minor increase in the core radius during heating. The hard-sphere structure factor reveals the correlation between the micelles with distance $2R_{HS}$ increasing from 38 ± 4 nm at 40 ºC to 44 ± 6 nm at 50 ºC. R_{HS} is larger than the micelle radius, but smaller than the contour length and follows the same trend as both these parameters. The hard-sphere volume fraction of correlated cylindrical micelles, η, is about 0.48 ± 0.07, i.e. much stronger than in regime I. The solvation term reveals ξ_{solv} increasing from 4.7 ± 0.4 nm at 40 ºC to 7.9 ± 0.8 nm at 50 ºC. We assume that ξ_{solv} describes the correlation in the PSBP-rich shell surrounding PNIPAM-rich core. The increase of ξ_{solv} may be assigned to the weakening of the interactions between PSBP segments. The solvation Porod exponent decreasing from m = 1.36 ± 0.12 at 40 °C to 0.94 ± 0.10 at 50 °C, indicating a decline of the solvent conditions for the entire polymer and continuous aggregation. The scaling factor decreased slightly from C = 1.7 ± 0.1 cm^{-1} at 40 °C to 1.5 ± 0.1 at 50 °C cm^{-1}, the value is slightly higher closer to the cloud points. d_0 is around 15 ± 2 nm, which is a moderate value, most probably due to the strong polymer-polymer interactions in the entire diblock copolymer. The d_0 value is smaller than $2R_{HS}$, which is around 41 ± 9 nm, but the trend is the same. The Porod law indicates the presence of compact aggregates with very smooth surfaces, α = 4.8 ± 0.3. Moreover, the contribution of a Porod term in regime III is much more pronounced than in regime I, indicating much higher fraction of large aggregates. Altogether, in regime III, cylinders seem to form with a polydisperse radius and a correlation length of a few nm. These cylinders are correlated; moreover, they form large aggregates with very smooth surface.

Results of the analysis of the SANS curves of $PSBP_{78}$-b-$PNIPMAM_{115}$. For the fitting of the curves of $PSBP_{78}$-*b*-$PNIPMAM_{115}$ in regime I and III the model described in Eq. 6.1 with the same contributions as for $PSBP_{78}$-*b*-$PNIPAM_{100}$ was used (Figure B.1b,d in the appendix B). In regime I, the polydisperse spherical particles have an average sphere radius r_{avg} = 12.0 ± 1.3 nm with a moderate polydispersity decreasing from p = 0.27 ± 0.04 at 20-35 °C to 0.22 ± 0.02 at 40 °C and 0.10 ± 0.01 at 45 °C (Table B.3 in the appendix B, Figure 7.3B). The average hard-sphere radius decreasing from R_{HS} = 23 ± 3 nm at 10-40 °C to 19 ± 2 at 45 °C. R_{HS} is twice larger than the micelle radius, i.e. the spheres are spaced. The hard-sphere volume fraction of spherical micelles, η, decreases from ca. 0.11 at 20 ºC to ca. 0.04 at 40 ºC with a subsequent increase back to 0.09 at 45 °C. The very weak correlation of the spherical particles becomes even weaker at 40 °C and slightly enhances at 45 °C. The Ornstein-Zernike term reveals ξ_{OZ} increasing from 3.5 ± 0.2 nm at 20 °C to 7.3 ± 0.8 nm at 40 °C and decreasing to 6.9 ± 0.5 nm at 45 °C, indicating that the shell of the particles is getting less compact during heating and slightly back at 45 °C. The Porod exponent decreases from α = 4.0 ± 0.2 at 20 °C to 3.5 ± 0.1 at 35 °C with a subsequent increase to 4.1 ± 0.2 at 45 °C, which confirms the presence of compact aggregates with smooth surfaces which are getting more rough during heating to 35 °C and become smooth again at 45 °C. The minor changes of parameters observed at 40 °C compared to those at lower temperatures, may be due to the improvement of the solvent conditions for the PSBP block close to its CP_{UCST} and the changes at 45 °C due to the proximity of the CP_{LCST} of the PNIPMAM block.

In regime III, the average core radius of flexible cylindrical particles increases from 10.1 ± 1.1 nm at 50 ºC to 13.5 ± 1.2 nm at 65 ºC, respectively, with a polydispersity decreasing during heating from p = 0.50 ± 0.05 at 50 ºC to 0.16 ± 0.01 at 55-65 ºC (Table B.4 in the appendix B, Figure 7.3B). The average contour length of the cylinders grows rapidly from L = 25 ± 2 nm at 50 ºC to 54 ± 5 nm at 65 ºC, with the average Kuhn length increasing from b = 16 ± 2 nm at 50 ºC to 18 ± 2 nm at 55-65 ºC. The ratio L/b increases during heating from 1.7 on average at 50-60 °C to 3 at 65 °C, indicating a decrease of the stiffness of the cylinders above 60 °C. One of the possible reasons is the weakening of the attractive interactions in the PSBP block. The hard-sphere structure factor reveals the correlation between the micelles with half the interparticle distance $2R_{HS}$ = 44 ± 6 nm. $2R_{HS}$ is larger than the micelle radius and the contour length at 50-60 ºC, but smaller than the contour length at 65 °C. The hard-sphere volume fraction of correlated cylindrical micelles η = 0.36 ± 0.04 is much higher than the one of correlated spheres in regime I. The solvation term reveals ξ_{solv} increasing from 4.2

± 0.2 nm at 50 ºC to 5.8 ± 0.4 nm at 65 ºC. ξ_{solv} describes the correlations in the micellar PSBP-rich shell, its increase during heating is related to the continuous aggregation of the PNIPMAM block and the weakening of the attractive ionic interactions between the PSBP segments. The solvation Porod exponent decreases from m = 1.59 ± 0.21 nm at 50 ºC to 1.16 ± 0.11 nm at 65 ºC, indicating that the polymer is in bad solvent conditions, which are getting worse during heating. The scaling factor decreases from C = 3.2 ± 0.2 cm^{-1} at 50 ºC to 1.6 ± 0.2 cm^{-1} at 65 ºC, which is an indication of the phase separation at 50 °C. d_0 decreases from 17 ± 2 nm at 50 ºC to 14 ± 3 nm at 55-65 ºC, due to the strengthening of polymer-polymer interactions in the diblock copolymer during heating related to the PNIPMAM aggregation. The d_0 value is much smaller than $2R_{HS}$, which is around 44 ± 4 nm. The forward scattering at low q values is again described by the Porod law with an exponent increasing from α = 4.7 ± 0.3 at 50 ºC to 4.9 ± 0.3 at 65 ºC, which confirms the presence of compact aggregates with very smooth surface. Similar to the observations in the solution of $PSBP_{78}$-*b*-$PNIPAM_{100}$, the contribution of a Porod term in regime III is more pronounced than in regime I, indicating higher fraction of large aggregates.

7.3.1.1. Comparison of the self-assembled structures in salt-free solutions of $PSBP_{78}$-*b*-$PNIPAM_{100}$ and $PSBP_{78}$-*b*-$PNIPMAM_{115}$

Figure 7.4 shows the structures in the three regimes, according to SANS and expectations relating to the (aggregated) behavior. The overall behavior of $PSBP_{78}$-*b*-$PNIPAM_{100}$ and $PSBP_{78}$-*b*-$PNIPMAM_{115}$ in salt-free solution is similar. No intermediate regime II was observed neither from the view of the SANS curves of both diblock copolymers, nor from results of their fitting. In regimes I and III of both diblock copolymers, spherical and cylindrical micelles are formed, respectively. Besides the different shape, the micelles in regime III are more strongly correlated compared to those in regime I and cause stronger aggregation. This results in the formation of higher fraction of large aggregates in regime III. The difference may be attributed to strong attractive polymer-polymer interactions in both blocks in regime III, while in regime I, the aggregation mainly caused by the interactions in the PSBP block. The concentration fluctuations in the shell of the particles in regime III, described by a solvation term, prove the strong interaction between PSBP segments due to the proximity of the CP_{UCST} to CP_{LCST}.

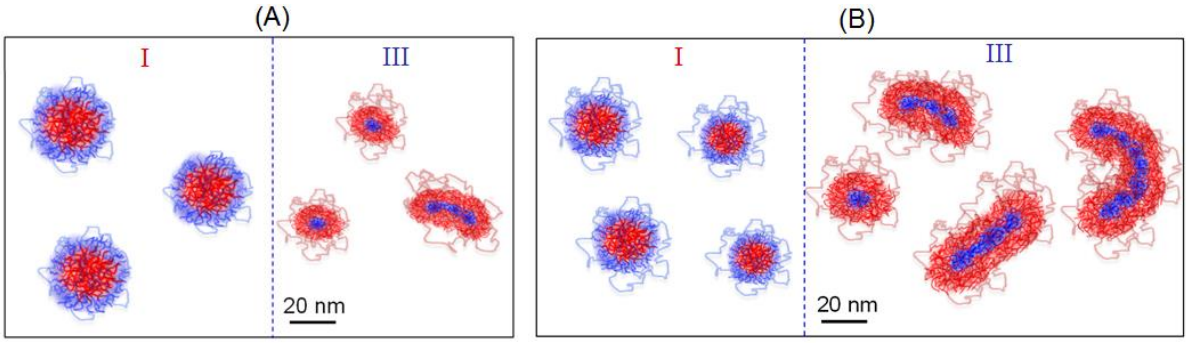

Figure 7.4: Schematic representation of the micelles in 50 g L^{-1} salt-free solutions of (A) $PSBP_{78}$-*b*-$PNIPMAM_{115}$ and (B) $PSBP_{78}$-*b*-$PNIPMAM_{115}$ in the two regimes as indicated. Red: PSBP block, blue: PNIPMAM block. Approximate value position of CP_{LCST} (---).

Two factors have to be considered when comparing the SANS results from the $PSBP_{78}$-*b*-$PNIPAM_{100}$ and $PSBP_{78}$-*b*-$PNIPMAM_{115}$ solutions in salt-free D_2O: (i) The lengths of the nonionic blocks and, accordingly, the composition of the diblock copolymers are slightly different: in $PSBP_{78}$-*b*-$PNIPAM_{100}$, the PNIPAM block is 1.3 times longer than PSBP, whereas in $PSBP_{78}$-*b*-$PNIPMAM_{115}$ the PNIPMAM block is 1.5 times longer than PSBP. (ii) PNIPMAM forms aggregates already below the cloud point which is not the case in PNIPAM solutions (see paragraph 6.4.1).

In regime I, the overall scattering intensity is similar at low temperatures, but during heating it decreases for the $PSBP_{78}$-*b*-$PNIPMAM_{115}$ solution, which is mainly due to the decrease of the forward scattering. This is related to an increase of the roughness of the aggregates surfaces, and, on mesoscopic length scales, to the pronounced increase of the correlation length, which describes mainly the correlation in the hydrophilic PNIPMAM shell surrounding the collapsed PSBP in the core, in the $PSBP_{78}$-*b*-$PNIPMAM_{115}$ solution. A possible reason may be start of disengagement of the overlapped PSBP coils in accordance with turbidimetry measurements results, which reveal a very gradual increase of the transmission below the UCST-type transition. Nevertheless, the average radius of small spherical particles is stable during heating and is about 13 ± 1 nm in both $PSBP_{78}$-*b*-$PNIPAM_{100}$ and $PSBP_{78}$-*b*-$PNIPMAM_{115}$ solutions.

In regime III, the overall scattering intensity in $PSBP_{78}$-*b*-$PNIPAM_{100}$ is lower, especially at *q*-values below 0.2 nm^{-1}, which is due to the lower PNIPAM block length, compared to PNIPMAM. Very large aggregates in regime III are formed from cylindrical micelles with the comparable micellar radius in the solutions of $PSBP_{78}$-*b*-$PNIPAM_{100}$ (about 11 nm) and

$PSBP_{78}$-*b*-$PNIPMAM_{115}$ (about 13). The contour length increases during heating from 23 nm at 40 °C to 36 nm at 50 °C in the solution of $PSBP_{78}$-*b*-$PNIPAM_{100}$ and from 25 nm at 50 °C to 54 nm at 65 °C in the solution of $PSBP_{78}$-*b*-$PNIPMAM_{115}$. Thus, the dimensions of the cylindrical particles are slightly larger in the $PSBP_{78}$-*b*-$PNIPMAM_{115}$ solution, moreover, the micelles are more correlated. We suspect that, in the $PSBP_{78}$-*b*-$PNIPMAM_{115}$ solution, aggregation of the cylindrical micelles proceeds more easily compared to the one in $PSBP_{78}$-*b*-$PNIPAM_{100}$ due to both, the lover fraction of PSBP and hence the comparably smaller impact of the polyelectrolyte properties of the PSBP block, and the stronger tendency to aggregation of PNIPMAM. The stiffness of the cylinders is unchanged in the solution of $PSBP_{78}$-*b*-$PNIPAM_{100}$, while in the solution of $PSBP_{78}$-*b*-$PNIPMAM_{115}$ it is decreased at 65 °C, which may be caused by changes in the interactions in PSBP, namely achievement of the CP_{UCST}.

The core-shell structure of the micelles expected in regimes I and III could not be resolved, which may be due to the fact that the aggregation is governed by ionic interactions in the PSBP block in regime I, and by interactions in the PNIPAM/PNIPMAM block in regime III, which are, in turn, complicated by the interactions with PSBP block due to the proximity of the values of CP_{UCST} and CP_{LCST}. Thus, in both regimes, homogeneous micelle-like associates are formed instead of distinct core-shell micelles.

7.3.2. Electrolyte effect

Turbidimetry results reveals a marginal increase of the light transmission in the intermediate temperature ranges, from 27 °C to 35 °C and from 27 °C to 43 °C for the $PSBP_{78}$-*b*-$PNIPAM_{100}$ and $PSBP_{78}$-*b*-$PNIPMAM_{115}$ solutions, respectively (Figure 7.1). Temperature-dependent SANS measurements were performed at the example of a 50 g L^{-1} solution of $PSBP_{78}$-*b*-$PNIPMAM_{115}$ in 0.004 M NaBr in D_2O in order to gain information about the structural changes caused by electrolyte addition (Figure 7.5). The onset of CP_{UCST} of $PSBP_{78}$-*b*-$PNIPMAM_{115}$ is found to decrease by about 6 °C in 0.004 M NaBr in D_2O, compared to the one in 0.002 M NaBr in D_2O. From these we assume that the decrease of the CP_{UCST} is more than 6 °C compared to the value in salt-free D_2O, which cannot be resolved precisely (see above).

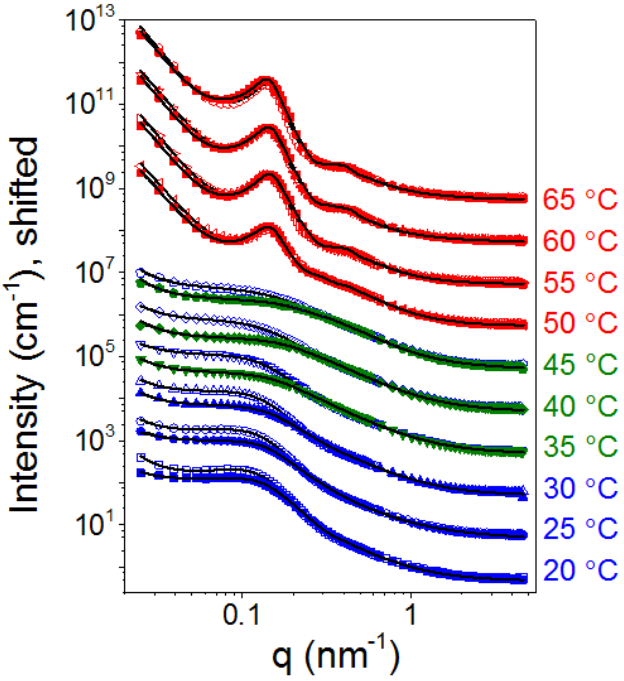

Figure 7.5: SANS curves from a 50 g L^{-1} solution of $PSBP_{78}$-*b*-$PNIPMAM_{115}$ in salt-free D_2O (open symbols, from Figure 7.2d) and in 0.004 M NaBr in D_2O (closed symbols), where every third point is shown for clarity, together with the fitting curves (—) obtained using Eq. 6. The curves are shifted in intensity as in Figure 7.2. Regimes I, II and III are indicated by the blue, green and red color, respectively.

At 20-45 °C, i.e. below CP_{LCST}, the SANS curves of $PSBP_{78}$-*b*-$PNIPMAM_{115}$ in 0.004 M NaBr in D_2O feature significantly decreased forward scattering at q values below ca 0.2 nm^{-1} as well as a shift of the peak to lower q values, compared to the ones in salt-free D_2O (Figure 7.2d). The shape of the curves at 45-65 °C, i.e. in regime III (red), remains unchanged in the q range above 0.08 nm^{-1}; at lower q values, the intensity is slightly lower compared to the one in salt-free conditions. The same fitting model with the same contributions as for the curves from salt-free solution was used in regimes I, II (Figure B.2a in the appendix B) and III. The scattering curves at 35-45 °C, were additionally analyzed using the model described in Eq. 6.2 (Figure B.2b in the appendix B). The resulting parameters for regimes I, II and III are compiled in Tables B.5-7 in the appendix B.

Comparison of the fitting parameters at 20-45 °C, i.e. with regime I of the salt-free polymer solution, using Eq. 6.1 with and without NaBr addition reveals the following changes: In the solution with NaBr, the sphere radius r_{avg} continuously decreasing during heating from 12 to 10 nm at 20-30 ºC, i.e. around 1-2 nm lower than in salt-free conditions, and from 3 to 2 nm 35-45 ºC, i.e. around 9 nm lower on average (Table B.5 in the appendix B, Figure 7.6). The

polydispersity of the radius is unchanged at 20-30 ºC, by ca. 0.6 higher at 35-40 ºC and by ca. 0.4 higher at 45 ºC. R_{HS} is by ca. 3 nm smaller at 20-30 °C and by ca. 6 nm at 35-45 °C, indicating a decrease in the distance between the (larger) spheres at 20-30 °C and an increase in the distance between the (smaller) spheres at 35-45 °C, where R_{HS} is almost 6 times larger than r_{avg}. The hard-sphere volume fraction is unchanged at 20-30 °C, and slightly higher at 35-45 °C (ca. 0.03). The correlation length ξ_{OZ} at 20-30 ºC is around 2-3 nm higher than in salt-free conditions, at 35 ºC, it is nearly equal (ca. 5.7 nm) and at 40-45 ºC, it is around 2 nm lower. The overall trend of ξ_{OZ} during heating is different: while in salt-free conditions it is increases during heating, in 0.004 M NaBr in D_2O, it increases up to 30 °C with a subsequent decrease. Most probably, at 20-30 °C, ξ_{OZ} describes the correlation length in the PNIPMAM-rich shell of the spherical particles, while above 30 °C, the correlation length may also include contributions from the inner part of the sphere. The Porod term reveals $\alpha = 3.9 \pm 0.3$ at 20-35 °C, which decreases to 3.3 ± 0.3 at 40-45 °C with slightly lower amplitude than in salt-free solution, indicating a lower rate of aggregation and change of the aggregates surfaces from smooth to rough above 30 °C. Similar to the salt-free solution, the Porod amplitude increases at 45 °C, together with the changes in other parameters (decrease of *p*, increase of η) mentioned above this indicate an increase in aggregation due to the proximity of the LCST-type transition. Altogether, small correlated spherical micelles seem to form in $PSBP_{78}$-*b*-$PNIPMAM_{115}$ in 0.004 M NaBr in D_2O at 20-45 °C, with decreasing radius and increasing polydispersity at 35-45 °C. These micelles form large aggregates having surface changing from smooth to rough at 35 °C. Thus, the temperature range at 35-45 °C may be identified as regime II, where the attractive interactions in the PSBP block are weakened, and the range at 20-30 °C may be assigned to regime I, respectively. However, according to the turbidimetry measurements, regime II appears in solution of $PSBP_{78}$-*b*-$PNIPMAM_{115}$ in 0.004 M NaBr in D_2O at 27-43 °C, i.e. expected to be detected during SANS measurement at 30-40 °C, i.e. at temperature on ca. 3 °C lower. The possible reason of the difference in the cloud points measured by turbidimetry and SANS may be related to the difference in the protocol and described above at the example of the curves obtained in salt-free solution.

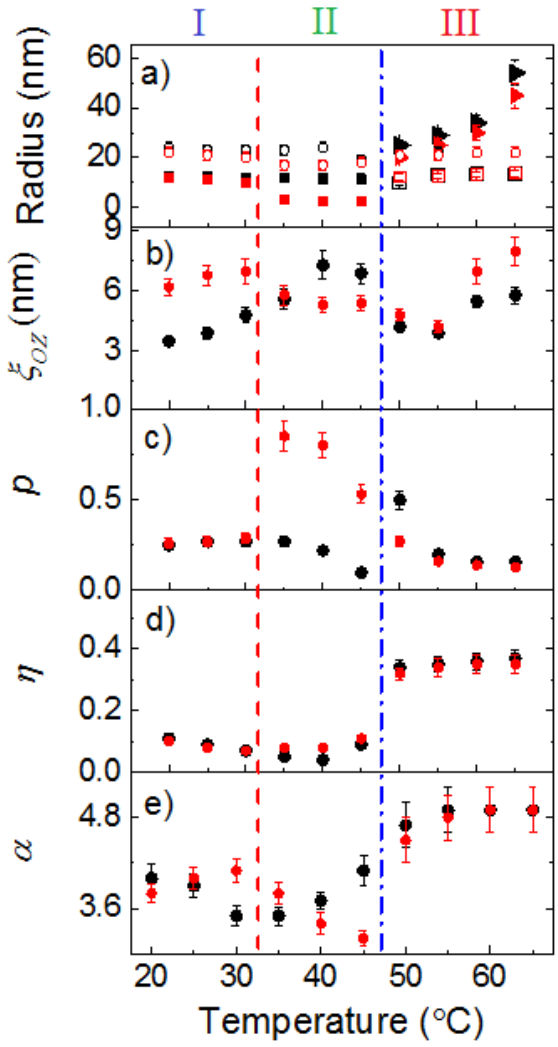

Figure 7.6: Results from model fitting using Eq. 6.1 to the SANS curves in Figure 7.2 and 7.5 from $PSBP_{78}$-*b*-$PNIPMAM_{115}$ in salt-free D_2O (black symbols) and in 0.004 M NaBr in D_2O (red symbols), respectively. Same designations as in Figure 7.3. (**--**) and (**-·-**): the approximate onset of CP_{UCST} and CP_{LCST} values. Regimes I, II and III are indicated on top of the graph.

According to the previous observation for the diblock copolymers with PSPP block (see chapter 6), namely $PSPP_{432}$-*b*-$PNIPAM_{200}$ and $PSPP_{498}$-*b*-$PNIPMAM_{144}$, in regime II was used the model (Eq. 6.2) describing the concentration fluctuations caused by the polyelectrolytic nature of the PSPP block. Therefore, the SANS curves at 35-45 °C were additionally fitted using this model (Eq. 6.2), were the solvation and a Porod terms are used to describe the correlation peak at rather high q-values and forward scattering at low q values, respectively. The equally well curves fit allows gaining additional structural information. The correlation length from the solvation term, ξ_{solv}, decreases from 8.6 ± 0.6 nm at 35 °C to 5.1 ±

0.3 nm at 45 °C (Table B.6 in the appendix B). At 35 ºC, ξ_{solv} most probably describes mainly the correlations in the hydrophilic PNIPMAM-rich shell surrounding the collapsed PSBP-rich core, while at 45 °C ξ_{solv} reflects the molecular conformation of the entire polymer. The average solvation Porod exponent m = 2.0 ± 0.2, indicating tetha solvent conditions. The scaling factor of the solvation term, C, decreases from 40 ± 3 cm^{-1} at 35 °C to 22 ± 2 cm^{-1} at 45 °C, i.e. the value increases close to the onset of the gradual CP_{UCST}. The average distance between the charged domains is quite large and increases from d_0 = 85 ± 7 nm at 35 °C to 105 ± 10 nm at 45 °C, indicating an expanded state of both blocks in regime II. This is the result of (i) the ionic attraction in the PSPP block which weakens above the onset of CP_{UCST}, and (ii) the stiff chain conformation of PNIPMAM below CP_{LCST}. The Porod law reveals α decreasing from 3.3 ± 0.1 at 35 °C to 2.8 ± 0.1 at 45 °C, with slightly lower amplitude than in salt-free solution, indicating a lower rate of aggregation and change of the aggregates surface from smooth to rough.

In regime III, the average radius of the flexible cylinders is unchanged, only close to CP_{LCST}, namely at 50 °C, a slightly larger radius compared to the one in salt-free conditions was found (ca. 2 nm larger). The average contour length of the cylinders is decreased by ca. 5 nm at 50-60 °C and by ca. 9 nm at 65 °C and follow the same trend; the average Kuhn length is 6 nm smaller at 50 ºC and ca. 1 nm at 55-65 ºC. Thus, besides the core radius, the cylindrical dimensions are decreased upon addition of NaBr at low concentration. The hard-sphere structure is unchanged, as well as the hard-sphere volume fraction, η. The correlation length ξ_{solv} in regime III increases from 4.8 ± 0.3 nm at 50 °C to 8.0 ± 0.7 nm at 65 °C, thus it is slightly larger than in salt-free conditions. In regime III, ξ_{solv} presumably describes the correlation in the PSBP-rich shell and may be increased because of the weakening of the attractive interactions in PSBP block due to the salt-screening effect. The other parameters, including the solvation Porod exponent m, the scaling factor C and the distance between the charged domains d_0 are nearly unchanged within the error. Thus, in the regime where cylindrical micelles with a PNIPMAM-rich core and a PSBP-rich shell are formed, the addition of a small amount of salt causes the formation of the micelles with a slightly larger core and smaller length than in salt-free solution.

7.4. Influence of the zwitterionic block nature on the aggregation behavior

To answer the question how the nature of the zwitterionic block may influence the aggregation behavior of the diblock copolymers with PNIPAM and PNIPMAM blocks, we

compare the turbidimetry and SANS results for the diblock copolymers with PSBP and PSPP blocks, namely $PSBP_{78}$-*b*-$PNIPAM_{100}$ and $PSBP_{78}$-*b*-$PNIPMAM_{115}$ with $PSPP_{432}$-*b*-$PNIPAM_{200}$ and $PSPP_{498}$-*b*-$PNIPMAM_{144}$. Several factors have to be considered when comparing the behavior of the polymer solutions in salt-free D_2O: (i) The overall molar mass of the $PSPP_{432}$-*b*-$PNIPAM_{200}$ is about 4 times higher compared to $PSBP_{78}$-*b*-$PNIPAM_{100}$ as well as the overall molar mass of the $PSPP_{498}$-*b*-$PNIPMAM_{144}$ compared to $PSBP_{78}$-*b*-$PNIPMAM_{115}$ (i) The composition of the diblock copolymers is different: in $PSPP_{432}$-*b*-$PNIPAM_{200}$ and $PSPP_{498}$-*b*-$PNIPMAM_{144}$, the zwitterionic PSPP block lengths are 2 or 3 times longer than nonionic PNIPAM or PNIPMAM block lengths, respectively. Whereas, the block lengths in $PSBP_{78}$-*b*-$PNIPAM_{100}$ and $PSBP_{78}$-*b*-$PNIPMAM_{115}$ differ only slightly, and the fraction of zwitterionic block is slightly lower: PNIPAM and PNIPMAM are 1.3 and 1.5 times longer than PSBP. (ii) PSBP is more hydrophobic and reveals much higher cloud points than analogous PSPP of identical molar mass and even higher.

7.4.1. Phase behavior of the systems with PSBP and PSPP

The overall behavior of the diblock copolymers with PSBP as the ionic-strength sensitive block differs strongly from the one with PSPP blocks: In salt-free conditions, solutions of the diblock copolymers with PSPP exhibit three different regimes, which are not distinguished in solutions of the diblock copolymers with PSBP. The maximum change of the light transmission of the $PSPP_{432}$-*b*-$PNIPAM_{200}$ and $PSPP_{498}$-*b*-$PNIPMAM_{144}$ solutions is about 40 and 60 % in regime II, respectively. In addition, the light transmission in the solutions of both diblock copolymers with PSPP block in regime III is higher than in regime I, while in the solutions of the diblock copolymers with PSBP block, it is equally low for $PSBP_{78}$-*b*-$PNIPAM_{100}$, and for $PSBP_{78}$-*b*-$PNIPMAM_{115}$ few percentage higher in regime I than in regime III. We attribute this difference to the stronger attractive interactions between the PSBP segments compared to PSPP, which result in close position of the cloud points. Therefore, the attractive interactions in the PSBP block are still strong in a certain temperature range in regime III, i.e. above the CP_{LCST}, and result in enhanced aggregation, which cause high turbidity. In the $PSBP_{78}$-*b*-$PNIPMAM_{115}$ solution, the light transmission starts to increase when approaching the onset of the gradual UCST-type transition, but the LCST-type transition occurs before the clearing point is reached.

In both $PSBP_{78}$-*b*-$PNIPAM_{100}$ and $PSBP_{78}$-*b*-$PNIPMAM_{115}$ solutions, the cloud points are altered from the ones of the respective homopolymers in a similar way: the values of CP_{UCST}

are decreased due to the presence of PNIPAM or PNIPMAM block, respectively, compared to those obtained for $PSBP_{78}$ homopolymer solution. The values of CP_{LCST} stay unaffected. In contrast, the cloud points in $PSPP_{432}$-*b*-$PNIPAM_{200}$ and $PSPP_{498}$-*b*-$PNIPMAM_{144}$ solutions are altered from the ones of the respective homopolymers in a different way: Whereas in $PSPP_{432}$-*b*-$PNIPAM_{200}$, CP_{UCST} decreases strongly compared to the one of $PSPP_{430}$ homopolymer, but CP_{LCST} is unchanged; in $PSPP_{498}$-*b*-$PNIPMAM_{144}$, CP_{LCST} increases strongly compared to the one of $PNIPMAM_{195}$ homopolymer, and CP_{UCST} is unaffected. The increase of the CP_{LCST} in $PSPP_{498}$-*b*-$PNIPMAM_{144}$, assigned to a higher sensitivity of PNIPMAM to the environment, including the PSPP block and the dye-labeled end group attached, compared to PNIPAM (see chapter 6), was not observed in $PSBP_{78}$-*b*-$PNIPMAM_{115}$. This may be ascribed to the difference in the properties of PSBP and PSPP and their interactions with PNIPMAM.

7.4.2. Self-assembled structures in solutions of the polymers with PSBP and PSPP

Besides the difference in the phase behavior described above, the structures formed in the systems with PSPP and PSBP blocks in regimes I and III are variant. The comparison of the SANS results is presented below according to the nonionic blocks of the diblock copolymers with PSBP and PSPP, namely PNIPAM and PNIPMAM. In addition, the SANS results set only two regimes (I and III) in the $PSBP_{78}$-*b*-$PNIPAM_{100}$ and $PSBP_{78}$-*b*-$PNIPMAM_{115}$ solutions, which thus will be compared.

Comparison of the self-assembled structures in the solutions of $PSBP_{78}$-b-$PNIPAM_{100}$ and $PSPP_{430}$-b-$PNIPAM_{200}$. In regime I, the SANS curves look similar, but by virtue of the higher forward scattering and higher intensity of the shallow maximum, which is shifted to the lower *q* values, the overall scattering intensity is higher for the $PSBP_{78}$-*b*-$PNIPAM_{100}$ solution compared to the one for the $PSPP_{430}$-*b*-$PNIPAM_{200}$ solution. This is due to the formation of larger aggregates with smoother surfaces composed from the spheres with radius ca. 3 times larger compared to those in solution of $PSPP_{430}$-*b*-$PNIPAM_{200}$, even though $PSBP_{78}$-*b*-$PNIPAM_{100}$ has the lower molar mass and the fraction of zwitterionic block, which is at the origin of structure formation in regime I, compared to $PSPP_{430}$-*b*-$PNIPAM_{200}$. Moreover, the small spheres in solution of $PSPP_{430}$-*b*-$PNIPAM_{200}$ are more polydisperse and less correlated with each other. A reason for the structural difference in regime I of the $PSBP_{78}$-*b*-$PNIPAM_{100}$ and $PSPP_{430}$-*b*-$PNIPAM_{200}$ solutions may lie in the stronger tendency of PSBP to

aggregation, which is consistent with the ca. 50 °C higher CP_{UCST} of the $PSBP_{78}$ compared to the CP_{UCST} of the $PSPP_{430}$.

In regime III, the shape of the SANS curves from the solutions of $PSBP_{78}$-*b*-$PNIPAM_{100}$ and $PSPP_{430}$-*b*-$PNIPAM_{200}$ is completely different at q values below 1 nm^{-1}, as well as the resolved structures. In contrast to the structures found in the $PSPP_{430}$-*b*-$PNIPAM_{200}$ solution, namely spherical micelles having a core-shell structure, in the solution of $PSBP_{78}$-*b*-$PNIPAM_{100}$, cylindrical micelles without a detectable core-shell structure were determined. The dimensions of the spherical micelles formed in the $PSPP_{430}$-*b*-$PNIPAM_{200}$ solution are higher compared to the cylindrical micelles formed in the $PSBP_{78}$-*b*-$PNIPAM_{100}$ solution, which is consistent with the higher molar mass of $PSPP_{430}$-*b*-$PNIPAM_{200}$. Cylindrical micelles, in turn, form large aggregates with smooth surfaces, which were not observed in the $PSPP_{430}$-*b*-$PNIPAM_{200}$ solution. In addition, the volume fraction of the correlated cylinders is ca. 2.8 times higher than the one of the correlated core-shell spheres. The possible reasons of stronger tendency to aggregation in the $PSBP_{78}$-*b*-$PNIPAM_{100}$ solution may be (i) the higher fraction of PNIPMAM, which is at the origin of micelle formation in regime III, compared to $PSPP_{430}$-*b*-$PNIPAM_{200}$, and (ii) still strong attractive interactions in the PSBP block close to its CP_{UCST}, which presumably forms a shell surrounding the PNIPAM-rich core.

Comparison of the self-assembled structures in the solutions of $PSBP_{78}$-b-$PNIPMAM_{115}$ and $PSPP_{498}$-b-$PNIPMAM_{144}$. The shape of the SANS curves in regime I is similar, but the curves from the $PSPP_{498}$-*b*-$PNIPMAM_{144}$ solution display a shallow maximum at lower and higher q values at 15 °C and 22 °C, respectively; and higher scattering intensity at high q values at 22 °C. This is confirmed by the ca. 1.3 times larger radius of the spherical particles found in the $PSPP_{430}$-*b*-$PNIPAM_{200}$ solution at 15 °C, and ca. 2 times smaller radius at 22 °C, compared to the spherical particles found in the $PSBP_{78}$-*b*-$PNIPMAM_{115}$ solution. The higher radius at 15 °C is consistent with the higher molar mass of $PSPP_{498}$-*b*-$PNIPMAM_{144}$, the smaller radius at 22 °C is due to the weakening of the attractive interactions in the PSPP block close to its CP_{UCST}. Again, the particles in the solution of $PSPP_{430}$-*b*-$PNIPAM_{200}$ are more polydisperse and less correlated, than in the solution of $PSBP_{78}$-*b*-$PNIPMAM_{115}$, where the aggregation is governed by stronger interactions in the PSBP block. Nevertheless, the large aggregates in the solution of $PSPP_{430}$-*b*-$PNIPAM_{200}$ have smooth surfaces at all temperatures below the CP_{UCST}, while in the solution of $PSBP_{78}$-*b*-$PNIPMAM_{115}$, the aggregates surfaces change from smooth to rough during heating due to the gradual weakening of the attractive

interactions between the PSBP chains at the onset of the gradual CP_{UCST} which occur above the CP_{LCST}.

In regime III, the shape of the SANS curves from the solutions of $PSBP_{78}$-*b*-$PNIPMAM_{115}$ and $PSPP_{498}$-*b*-$PNIPMAM_{144}$ is different as well, especially at *q* values below 1 nm^{-1}. Different structures are found in the systems, namely spherical micelles having a core-shell structure in the $PSPP_{498}$-*b*-$PNIPMAM_{144}$ solution and cylindrical micelles without a detectable core-shell structure in the $PSBP_{78}$-*b*-$PNIPMAM_{115}$ solution. In contrast to the systems with PNIPAM, the dimensions of the cylindrical micelles formed in $PSBP_{78}$-*b*-$PNIPMAM_{115}$ solution are higher compared to spherical micelles formed the $PSPP_{498}$-*b*-$PNIPMAM_{144}$ solution. Moreover, the cylindrical micelles are correaleted and form large aggregates with smooth surfaces, in contrast to uncorrelated core-shell spherical mielles in the $PSPP_{498}$-*b*-$PNIPMAM_{144}$ solution. Which is assigned to the higher fraction of PNIPMAM and presence of attractive interactions in both PNIPMAM and PSBP in regime III due to the proximity of CP_{UCST} to CP_{LCST}.

7.5. Conclusions

In this chapter of the thesis, we have studied the aggregation behavior of doubly thermoresponsive diblock copolymers consisting of zwitterionic PSBP block and a nonionic PNIPAM or PNIPMAM block, exhibiting both UCST and LCST behavior, respectively. We studied the "schizophrenic" responsive aggregation behavior of $PSBP_{78}$-*b*-$PNIPAM_{100}$ and $PSBP_{78}$-*b*-$PNIPMAM_{115}$ in D_2O and compared with the behavior of $PSPP_{432}$-*b*-$PNIPAM_{200}$ and $PSPP_{498}$-*b*-$PNIPMAM_{144}$ described in Chapter 6, in order to investigate the influence of the zwitterionic block nature on the phase behavior of the diblock copolymers with PNIPAM and PNIPMAM blocks.

The phase behavior of the diblock copolymers and the corresponding PSBP homopolymer in D_2O is investigated using turbidimetry. The high value of the CP_{UCST} found in the solution of the PSBP homopolymer (ca. 80 °C) is expected to lead to more than 30 °C and 40 °C higher CP_{UCST} than the CP_{LCST} in the corresponding block copolymers with PNIPMAM and PNIPAM, respectively. Against the expectations, in the entire temperature range studied, the $PSBP_{78}$-*b*-$PNIPAM_{100}$ solution is turbid indicating the formation of aggregates. In the $PSBP_{78}$-*b*-$PNIPMAM_{115}$ solution a marginal, gradual increase of the light transmission up to 43 °C with following decrease, indicate a phase transition, which could not be identified as a

LCST- or an UCST-type. We assume that the presence of the nonionic block causes a decrease of CP_{UCST} of the PSBP block, which then become close to CP_{LCST} of the PNIPAM/PNIPMAM block. The difference in the light transmission of the solutions of the diblock copolymers may be due to the higher CP_{LCST} of PNIPMAM compared to PNIPAM. The increase of the light transmission detected in the $PSBP_{78}$-*b*-$PNIPMAM_{115}$ solution is assigned to the onset of the gradual CP_{UCST}.

The CP_{UCST} of the PSBP block has been previously found to decrease by ca. 13 °C in 0.004 M NaBr solution in H_2O.[32] The electrolyte effect on the phase behavior of the diblock copolymers solutions in 0.004 M NaBr in D_2O was investigated by means of turbidimetry. Upon addition of small amount of NaBr in the diblock copolymers solutions an intermediate temperature range has been derived, which allows to estimate the values of the cloud points. Turbidimetry results reveal a salt-induced shift of the onset of CP_{UCST} in both solutions of $PSBP_{78}$-*b*-$PNIPAM_{100}$ and $PSBP_{78}$-*b*-$PNIPMAM_{115}$ to the lower temperature by about 10 and 20 °C (when compared to the CP_{LCST} assuming its proximity with CP_{UCST} in salt-free solution), respectively, while CP_{LCST} remains virtually unchanged. Thus, the distance between CP_{UCST} and CP_{LCST} in 0.004 M NaBr in D_2O is larger in the solution of $PSBP_{78}$-*b*-$PNIPMAM_{115}$, as intended.

Temperature-resolved SANS measurements of the solutions of $PSBP_{78}$-*b*-$PNIPAM_{100}$ and $PSBP_{78}$-*b*-$PNIPMAM_{115}$ in D_2O reveal only two regimes in dependence of temperature, indicated as I and III. This is due to close positions of the cloud points, which is in agreement with the results from turbidimetry. The transition from regime I to regime III was observed at 30-40 °C and 45-50 °C, i.e. at CP_{LCST} determined by turbidimetry, in solutions of $PSBP_{78}$-*b*-$PNIPAM_{100}$ and $PSBP_{78}$-*b*-$PNIPMAM_{115}$, respectively. The individual properties of the blocks, such as dominating ionic interpolymer interactions versus hydrogen bonding with water, yield the marked differences of the aggregation behavior in regime I and III, respectively: In regime I, i.e. below the UCST-type transition, where PSBP block is at the origin of structure formation, SANS reveals formation of small homogeneous spherical particles with a polydisperse radius of about 14 nm in the $PSBP_{78}$-*b*-$PNIPAM_{100}$ solution and about 12 nm in the $PSBP_{78}$-*b*-$PNIPMAM_{115}$ solution, which are correlated and form small fraction of very large aggregates. The surface of the large aggregates in the $PSBP_{78}$-*b*-$PNIPMAM_{115}$ solution changes from smooth to rough during heating. A reason for this may lie in the gradual weakening of the attractive interactions between PSBP segments below CP_{UCST}, which presumably occur later than the CP_{LCST}. In regime III, i.e. above the LCST-

type transition, PNIPAM/PNIPMAM block is at the origin of structure formation, but attractive interactions in PSBP are still string due to the close positions of CP_{UCST} and CP_{LCST}. This lead to the formation of very large aggregates, but in a larger fraction than in regime I. The aggregates are formed by correlated flexible cylinders with a polydisperse radius and a contour length increasing during heating. The radius of cylindrical micelles is about 11 nm and 13 nm in solutions of $PSBP_{78}$-*b*-$PNIPAM_{100}$ and $PSBP_{78}$-*b*-$PNIPMAM_{115}$, respectively. The contour length is larger than the radius of the cylinders by factor which increases during heating from 2 to 3 in the $PSBP_{78}$-*b*-$PNIPAM_{100}$ solution and from 2 to 4 in the $PSBP_{78}$-*b*-$PNIPMAM_{115}$ solution.

Thus, the difference in the architecture affects the conformation of the diblock copolymers in solution: larger spheres below CP_{UCST} and smaller cylinders above CP_{LCST} are formed in the $PSBP_{78}$-*b*-$PNIPAM_{100}$ solution. This may be partially due to the slightly different ratio of the lengths of the zwitterionic to the nonionic blocks and partially due to the chemical difference between the PNIPMAM and PNIPAM nonionic blocks: In regime I, PNIPMAM may prevent continuous aggregation of PSBP due to the formation of stiff conformations below its CP_{LCST}. In regime III of the $PSBP_{78}$-*b*-$PNIPMAM_{115}$ solution, the stronger tendency to aggregation of PNIPMAM compared to PNIPAM and the smaller impact of the polyelectrolyte properties due to the smaller fraction of PSBP compared to $PSBP_{78}$-*b*-$PNIPAM_{100}$ promote slightly stronger aggregation.

The electrolyte effect on the self-assembled structure formation was investigated at the example of the $PSBP_{78}$-*b*-$PNIPMAM_{115}$ solution in 0.004 M NaBr in D_2O by means of SANS. Structural changes caused by the screening of the ionic interactions were found in both regimes I and III: lower rate of aggregation and decrease of the small spheres radius in regime I and a decrease of the length of the cylinders in regime III. Moreover, regime II was identified in good agreement with the turbidimetry measurements. In regime II, the system exhibit behavior similar to polyelectrolytes in solution, due to the ionic interactions between the PSBP chains. The interactions are strong enough to cause formation of low fraction of large aggregates with rough surfaces.

The CP_{UCST} of the homopolymer $PSBP_{78}$ is ca. 50 °C higher compared to the CP_{UCST} of the homopolymers $PSPP_{430}$ and $PSPP_{498}$ described in chapter 6, even though the molar mass of $PSBP_{78}$ is ca. 4.3 and ca. 5 times lower than the one of $PSPP_{430}$ and $PSPP_{498}$, respectively. This is due to the higher hydrophobicity of the PSBP block, which spacer group is extended

by one methylene group between the charged groups, compared to PSPP. The difference in the properties of the zwitterionic blocks enforces the difference in the phase behavior and the structural changes in solutions of the corresponding diblock copolymers with PNIPAM/PNIPMAM block upon temperature variation. We observe the following difference in the phase behavior of the diblock copolymers with PSPP or PSBP zwitterionic block and a PNIPAM/PNIPMAM nonionic block: Whereas the light transmission in salt-free solutions of the systems with PSBP block is virtually blocked, the transmission is varied in solutions of the diblock copolymers with PSPP block, namely assigned to three regimes where the solution is turbid, semi-transparent and semi-turbid. For both systems with PSPP, CP_{UCST} is lower than CP_{LCST}, so that the zwitterionic and the nonionic blocks are hydrophilic at intermediate temperatures, while no intermediate temperature range was observed in the systems with PSBP due to the close positions of CP_{UCST} and CP_{LCST}.

The SANS results reveal two regimes in solutions of the diblock copolymers with PSBP and PNIPAM/PNIPMAM blocks, indicated as I and III. The structures formed in regimes I and III of the systems with PSPP and PSBP block are accordingly different: In regime I, large aggregates formed by small homogeneous spheres are detected in both systems, but the dimensions are different: Despite the lower molar mass of $PSBP_{78}$-*b*-$PNIPAM_{100}$ and lower fraction of zwitterionic block, which is at the origin of micelle formation in regime I, compared to $PSPP_{430}$-*b*-$PNIPAM_{200}$, the high tendency to aggregation of PSBP results and in higher dimensions in the $PSBP_{78}$-*b*-$PNIPAM_{100}$ solution. Whereas the aggregation is less favored in the $PSBP_{78}$-*b*-$PNIPMAM_{115}$ solution compared to $PSPP_{498}$-*b*-$PNIPMAM_{144}$, which is consistent with the higher molar mass of $PSPP_{498}$-*b*-$PNIPMAM_{144}$ and lower fraction of zwitterionic block, but mainly due to the gradual weakening of the attractive interactions in PSBP at the onset of the gradual CP_{UCST}. In regime III, the determined structures are different: spherical micelles having a core-shell structure in solutions of the diblock copolymers with PSPP and PNIPAM/PNIPMAM blocks, and large aggregates formed by flexible cylinders in solution of the diblock copolymers with PSBP and PNIPAM/PNIPMAM blocks. Formation of large aggregates indicates higher tendency to aggregation in both solutions of the diblock copolymers with PSBP zwitterionic block, where the attractive interactions in both zwitterionic and nonionic block are present due to the close positions of CP_{UCST} and CP_{LCST} and properties of PSBP. The mesoscopic length scales are larger in the $PSPP_{430}$-*b*-$PNIPAM_{200}$ solution, i.e. the dimensions of core-shell micelles are higher compared to the cylindrical particles in the $PSBP_{78}$-*b*-$PNIPAM_{100}$ solution. This tendency is

reversed in the systems with PNIPMAM, the dimensions of the cylindrical micelles formed in $PSBP_{78}$-*b*-$PNIPMAM_{115}$ solution are higher compared to spherical micelles formed the $PSPP_{498}$-*b*-$PNIPMAM_{144}$ solution. This qualitative difference in the mesoscopic structures may be due to the higher tendency to aggregation of the PNIPMAM compared to PNIPAM above CP_{LCST} (see chapter 6).

Thus, the UCST- and LCST-type transition temperatures can be controlled by the selection of both zwitterionic and nonionic thermoresponsive blocks as well as their molar masses. Addition of low molar mass electrolytes to the polymer solution may cause changes of the UCST-type transition without affecting the LCST-type transition, and the effect depends on the nature of the zwitterionic block.

8. “Schizophrenic” behavior - variation of the block lengths

In the previous chapters 6 and 7, we investigated the influence of the nature of a nonionic thermoresponsive block (PNIPAM or PNIPMAM) and a zwitterionic polysulfobetaine block (PSPP or PSBP) on the self-assembly in aqueous solution of the corresponding twofold thermoresponsive diblock copolymers of different architecture. In the present chapter, we aim to study the influence of the composition of the diblock copolymers, namely the relative lengths of the zwitterionic and nonionic blocks, on the aggregation behavior at the example of the diblock copolymers with a PSBP and a PNIPMAM block. In other words, we will investigate the systems in which the impact of the properties of the zwitterionic block prevail over those of the nonionic block and vice versa. To this end, we will investigate the aggregation behavior in aqueous solution of the diblock copolymers $PSBP_{51}$-*b*-$PNIPMAM_{156}$ and $PSBP_{243}$-*b*-$PNIPMAM_{103}$, with ca. 3 times lower or ca. 2.5 times higher block lengths of PSBP than those of PNIPMAM, respectively. We will compare their behaviors to the one of $PSBP_{78}$-*b*-$PNIPMAM_{115}$, described in chapter 7, where the block length of PSBP is only 1.5 times lower than the one of PNIPMAM. According to the previously described observations of the behavior of $PSBP_{78}$-*b*-$PNIPMAM_{115}$ in salt-free solution, which is characterized by the close position of the CP_{UCST} and CP_{LCST}, due to a reduction of the CP_{UCST} caused by the presence of PNIPMAM block, in salt-free solutions of $PSBP_{51}$-*b*-$PNIPMAM_{156}$ and $PSBP_{243}$-*b*-$PNIPMAM_{103}$, the CP_{UCST} is expected to be lower and higher than CP_{LCST}, respectively. Thus, the transition from the core-shell micelles of one type to the opposite one via a molecularly dissolved state in the $PSBP_{51}$-*b*-$PNIPMAM_{156}$ solution and via precipitation in the $PSBP_{243}$-*b*-$PNIPMAM_{103}$ solution is expected. Therefore, with these systems, regimes II and II’ indicated in Figure 3.2 may be encountered.

In this part of the work, we discuss the results of the turbidimetric investigations of phase behavior of the corresponding homopolymers and the detailed structural studies of the diblock copolymers by SANS measurements in salt-free solution. The details of sample preparation can be found in in paragraph 4.5.1.

8.1. Experimental set-up

Turbidimetry. The cloud points of the homopolymers $PSBP_{51}$ and $PSBP_{243}$ were determined following the procedure described in chapter 6.

Small-angle neutron scattering (SANS). SANS experiments were performed following the procedure described in chapter 7. The diblock copolymers $PSPP_{51}$-*b*-$PNIPMAM_{156}$ and $PSPP_{243}$-*b*-$PNIPMAM_{103}$ were measured in salt-free D_2O. Measurements were performed while heating from 20 °C to 60 °C in steps of 10 °C.

Modeling of the SANS curves. To describe the SANS curves of the $PSBP_{51}$-*b*-$PNIPMAM_{156}$ and $PSBP_{243}$-*b*-$PNIPMAM_{103}$ solutions in regimes I and III, the model function described in chapter 6 in Eq. 6.1, based on polydisperse spheres or flexible cylinders, was used. For the SANS curves of the $PSBP_{51}$-*b*-$PNIPMAM_{156}$ solution, the form factors of polydisperse, homogeneous spheres (Eqs. 5.19-21) and the form factor of flexible cylinders with polydisperse radius (Eqs. 5.24-32) were applied in regimes I and III, respectively. For the SANS curves of the $PSBP_{243}$-*b*-$PNIPMAM_{103}$ solution, the form factor of polydisperse, homogeneous spheres was applied in both regimes I and III. The form factors of polydisperse spheres and of flexible cylinders take into account the difference in scattering length densities (SLD) of the particles (ρ_{sphere} or $\rho_{cylinder}$) and the solvent, $\rho_{solvent}$ (values used see in paragraph 7.1). Additionally, the scattering curves of $PSBP_{51}$-*b*-$PNIPMAM_{156}$ at 30 °C (regime I) and 40 °C (regime II), were analyzed using the solvation model described in chapter 6 in Eq. 6.2. The incoherent background was fixed at 0.6 nm^{-1}.

8.2. Phase behavior of the homopolymers

The cloud points, $CP_{UCST,}$ of 50 g L^{-1} solutions of the homopolymers $PSBP_{51}$ and $PSBP_{243}$ in salt-free D_2O were determined *via* turbidimetry during cooling runs (not shown): CP_{UCST} ($PSBP_{51}$) = 75.6 ± 0.5 ºC and CP_{UCST} ($PSBP_{243}$) > 100 ºC. The cloud point of PNIPMAM is about 44 ºC.[107-110] In the $PSPP_{51}$-*b*-$PNIPAM_{156}$ solution, the UCST-type transition is expected to be close to or below than the LCST-type transition, which is due to the expected reduction of the CP_{UCST} caused by the presence of PNIPMAM block, in accordance with our previous observation of the aggregation behavior of $PSBP_{78}$-*b*-$PNIPMAM_{115}$ in D_2O, as mentioned above. In solutions of $PSPP_{243}$-*b*-$PNIPMAM_{103}$, the UCST-type transition is expected to be above the LCST-type transition.

8.3. Structural investigations using SANS

In order to get insight into the structural changes of $PSBP_{51}$-*b*-$PNIPMAM_{156}$ and $PSBP_{243}$-*b*-$PNIPMAM_{103}$ in salt-free D_2O during temperature variation, temperature-resolved SANS measurements of 50 g L^{-1} solutions of the diblock copolymers were carried out. Figure 8.1 presents the SANS curves of the salt-free solutions of $PSBP_{51}$-*b*-$PNIPMAM_{156}$ and $PSBP_{243}$-*b*-$PNIPMAM_{103}$ in D_2O during heating.

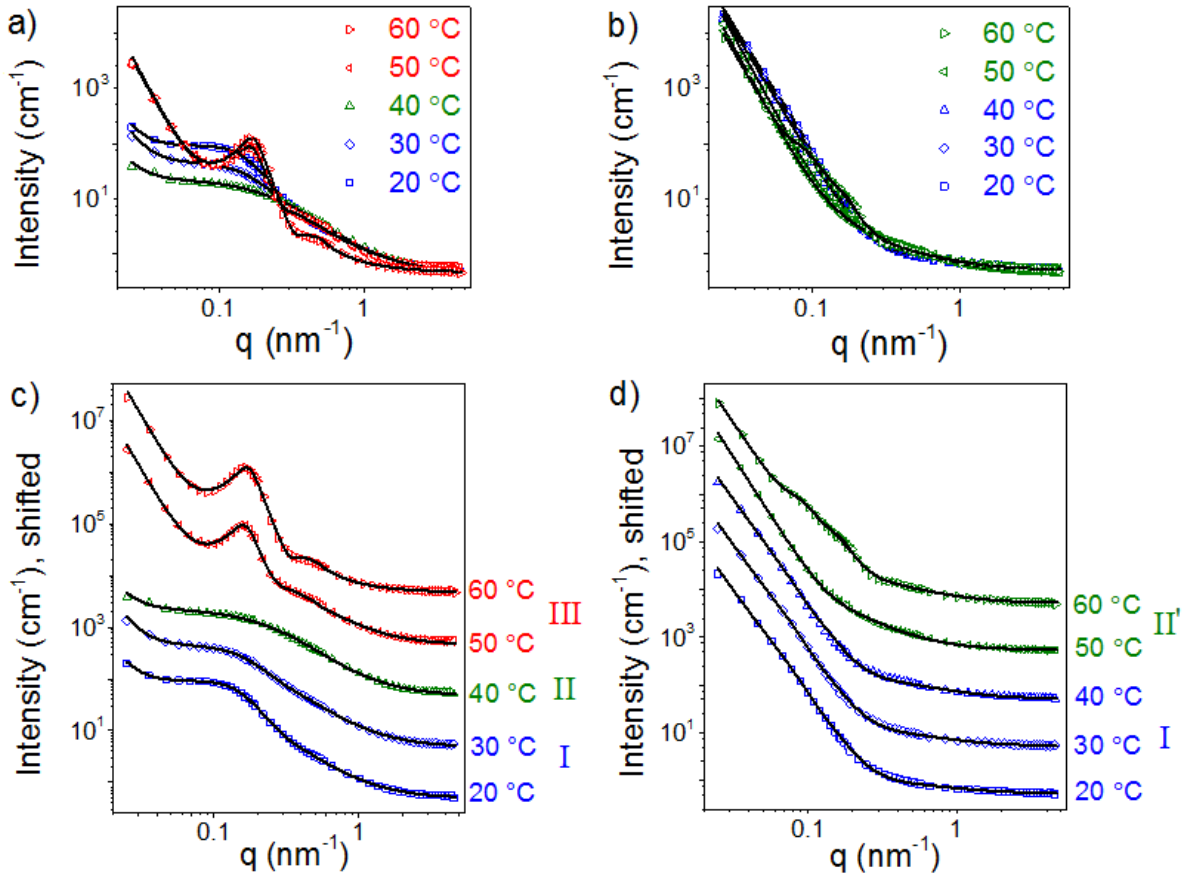

Figure 8.1: SANS curves from 50 g L^{-1} salt-free solutions of $PSBP_{51}$-*b*-$PNIPMAM_{156}$ (a, c) and $PSBP_{243}$-*b*-$PNIPMAM_{103}$ (b, d) in D_2O (symbols), where every third point is shown for clarity, together with the models fits (—) obtained using Eq. 6.1 in regimes I and III and Eq. 6.2 in regime II of the $PSBP_{51}$-*b*-$PNIPMAM_{156}$ solution, and using Eq. 6.1 at all temperatures for $PSBP_{243}$-*b*-$PNIPMAM_{103}$, see details below. In (c) and (d) the curves are shifted in intensity by a factor of 50 with respect to each other for better visibility. Regimes I, II and III are indicated by the blue, green and red color, respectively.

Three regimes are discernible by the curve shapes of the $PSBP_{51}$-*b*-$PNIPMAM_{156}$ solution, indicated as regimes I, II and III (Figure 8.1a). The SANS curves in regime I (blue) feature a

smooth decay starting at the lowest *q* values with a shallow maximum at ca. 0.1 nm^{-1}. The curves level off at ca. 2 nm^{-1}. In regime II (green), the curve looks similar to those in regime I, except the weaker decay at low *q* values. The curves in regime III (red) decay up to ca. 0.09 nm^{-1}, then two peaks are observed at 0.16 and 0.43 nm^{-1}. The curves become flat above ca. 2 nm^{-1}. The SANS curves from the $PSBP_{243}$-*b*-$PNIPMAM_{103}$ solution look very different from those of $PSBP_{51}$-*b*-$PNIPMAM_{156}$, as well as from those of $PSBP_{78}$-*b*-$PNIPMAM_{115}$ (see Figure 7.2). Moreover, the shape of the SANS curves from the $PSBP_{243}$-*b*-$PNIPMAM_{103}$ solution at different temperatures is very similar to each other, due to the very strong forward scattering, Therefore, the regimes could not be distinguished by the curve shapes. At 20-40 °C, the SANS curves feature a pronounced decay up to ca. 0.3 nm^{-1} and become flat above ca. 1 nm^{-1}. Above this temperature range, the SANS curves exhibit slightly different features: At 50 °C, the decay is pronounced up to ca. 0.2 nm^{-1}, then the curve decays steeply up to 0.5 nm^{-1}. At 60 °C, the curve decays starting at the lowest *q* values with three shallow maxima at ca. 0.09, 0.17 and 0.39 nm^{-1}. The curves become flat at ca. 1 nm^{-1}.

To analyze the structures, the SANS data were fitted using the model functions described in chapter 6. The best fits to the scattering curves of the $PSBP_{51}$-*b*-$PNIPMAM_{156}$ solution in regime II using model functions described in Eq. 6.1 and 6.2 are shown in Figure C.1 in the appendix C. The ones of the $PSBP_{51}$-*b*-$PNIPMAM_{156}$ and $PSBP_{243}$-*b*-$PNIPMAM_{103}$ solutions using the model function described in Eq. 6.1 are presented in Figure C.2 in the appendix C. The fits reveal substantial structural changes during heating in the three different regimes of the $PSBP_{51}$-*b*-$PNIPMAM_{156}$ solution. The results of the fits for $PSBP_{51}$-*b*-$PNIPMAM_{156}$ in regime II and in regime I at 30 °C (additionally) using Eq. 6.2 are summarized in Table C.1 in the appendix C, and in regimes I, II (additionally) and III using Eq. 6.1 are summarized in in Table C.2 in the appendix C. The results of the fits of the SANS curves of the $PSBP_{243}$-*b*-$PNIPMAM_{103}$ solution using Eq. 6.1 are summarized in Table C.3 in the appendix C.

Results of the analysis of the SANS curves of $PSBP_{51}$-b-$PNIPMAM_{156}$. According to the findings for the solutions of $PSPP_{430}$-*b*-$PNIPAM_{200}$ and $PSPP_{498}$-*b*-$PNIPMAM_{144}$, where regime II was discernible as well (see chapter 6 for details), the analysis of the SANS curves of the $PSBP_{51}$-*b*-$PNIPMAM_{156}$ solution in regime II was carried out using the model described in Eq. 6.2. The shallow maximum observed at a rather high *q*-value is typical for polyelectrolyte systems in salt-free solution and described with the solvation term (Figure C.1 in the appendix C). The forward scattering at low *q* values is fitted with a Porod term. The

solvation Porod exponent is m = 2.01 ± 0.02 (Table C.1 in the appendix C), indicating that the solvent is a theta solvent. The scaling factor is C = 19 ± 2 cm^{-1}. The average distance between the charged domains is d_0 = 15 ± 2 nm, which is a moderate value. The moderate value of d_0 may be the result of the strong polymer-polymer interactions in the entire diblock copolymer. The correlation length is ξ_{solv} = 4.8 ± 0.2 nm, it may reflect the molecular conformation of the entire polymer. The Porod term reveals the exponent α = 3.3 ± 0.2, which indicates the presence of compact aggregates with rough surfaces.

The shape of the curve at 30 °C in regime I is similar to those in regime II with some differences (Figure 8.1a): The overall scattering intensity is higher than in regime II, which may be due to a higher contrast caused by aggregation. The scattering intensity is also higher at low q values, where large aggregates cause an increased forward scattering. The shallow maximum is shifted to lower q values. Nevertheless, the curve at 30 °C can be fitted using the same model as in regime II (Eq. 6.2). The fitting results reveal the following changes, compared to those in regime II (Table C.1 in the appendix C): The solvation Porod exponent m = 1.82 ± 0.2, indicating a decline of the solvent conditions. The scaling factor increases up to C = 42 ± 4 cm^{-1}, indicating progressive phase separation. d_0 decreases to 8 ± 1 nm, i.e. it decreases strongly due to strengthening of the attractive polymer-polymer interaction in the PSBP block. ξ_{solv} is almost twice higher, namely 9.9 ± 0.3 nm, and describes mainly the correlation in the hydrophilic, presumably PNIPMAM-rich shell surrounding the collapsed PSBP in the core. Its increase is caused by the attractive interactions between the PSBP segments. The Porod exponent is α = 3.8 ± 0.2, which indicates the presence of compact aggregates with smooth surfaces.

In accordance with the previously described observations on the analogously designed copolymers with a PSBP block (chapter 7), which suggests the formation of spherical micelles below CP_{UCST}, the curves in regime I were fitted using the model described in Eq. 6.1, based on correlated and homogeneous spheres with polydisperse core. The model includes an Ornstein-Zernike (OZ) term describing the concentration fluctuations and Porod scattering due to very large aggregates (Figure C.2a in the appendix C), The fitting curves fit the data equally well and allow gaining additional structural information. The spherical particles have an average sphere radius r_{avg} = 11 ± 1 with a moderate polydispersity p = 0.25 ± 0.04 (Figure 8.2, Table C.2 in the appendix C). Half the interparticle distance R_{HS} = 20 ± 3 nm. R_{HS} is larger than r_{avg} and, at 30 °C, it is much larger than $d_0/2$, which is around 4 nm. The volume fraction of correlated spheres, η, is about 0.08, indicating very weak correlation.

The OZ term reveals that ξ_{OZ} increases from 5.4 ± 0.5 nm at 20 °C to 6.5 ± 0.6 nm at 30 °C. These values are half as large as the average sphere radii, which means that the presumed PNIPMAM-rich shell is loosely packed. The large values of ξ_{OZ} may reflect the stiff chain conformation of the PNIPMAM blocks, due to steric hindrance (see chapter 6 for details). The Porod exponent is α = 4.5 ± 0.3, confirming the presence of compact aggregates with smooth surfaces.

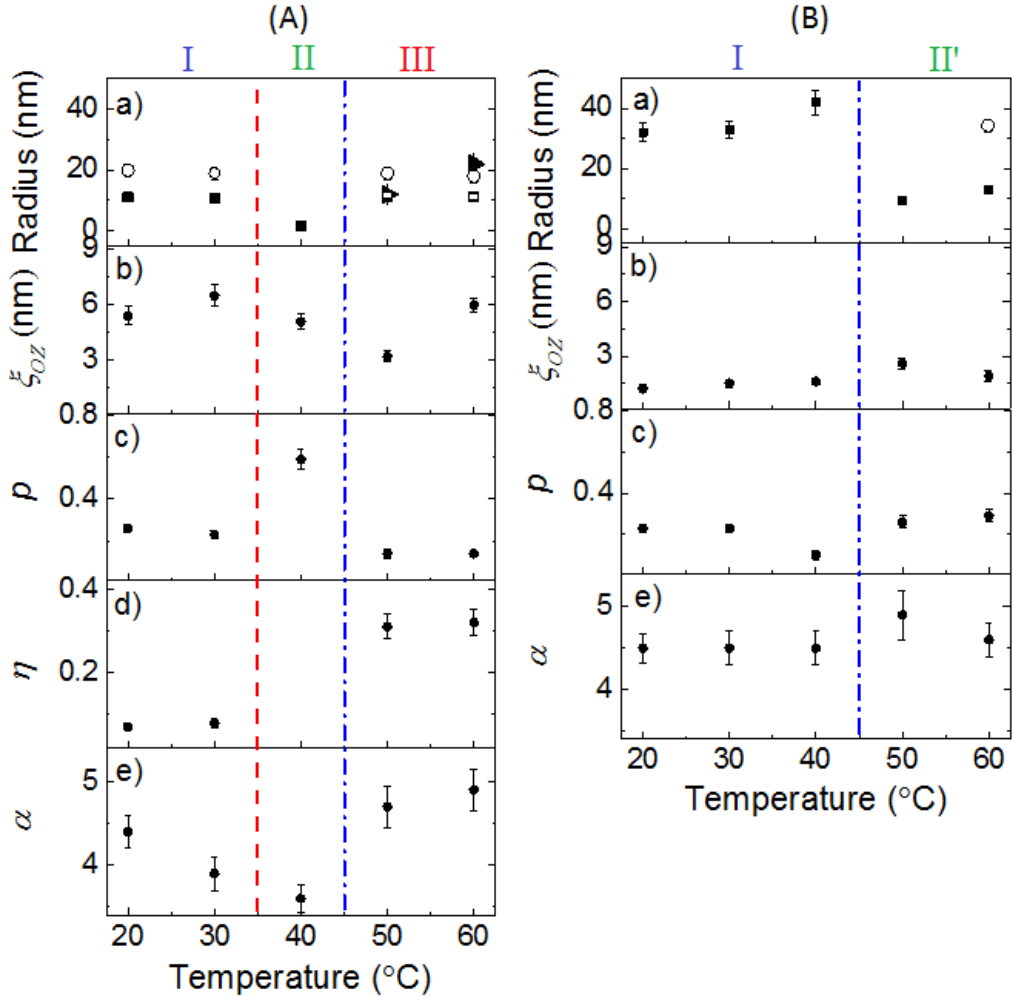

Figure 8.2: Results from model fitting using Eq. 6.1 to the SANS curves of (A) $PSBP_{51}$-*b*-$PNIPMAM_{156}$ and (B) $PSBP_{243}$-*b*-$PNIPMAM_{103}$ solutions in Figure 8.1. Temperature dependence of the micellar radius, r_{avg}, (■), r_{cyl}, (□), contour cylinder length, *l*, (▶), the hard-sphere radius, R_{HS} (○) (a); of the correlation length, ξ_{OZ} (b), of the polydispersity of the micellar radius, *p* (c), of the hard-sphere volume fraction, η (d), and of the Porod exponent α values (e). In some cases, the symbol size is larger than the error bar. (--) and (-·-): approximate values of CP_{UCST} and CP_{LCST}. Regimes I, II or II' and III are indicated on top of the graph.

The model based on polydisperse spheres, can be applied to the curve in regime II as well, but this time a hard-sphere structure factor is not needed (Figure C.1b in the appendix C). The fits are equally good, and the fitting results reveal the following changes compared to regime I (Table C.2 in the appendix C, Figure 8.2A): r_{avg} is decreased to 1.7 ± 0.2 nm with twice higher polydispersity, p = 0.59 ± 0.05, which can be enhanced due to the weakening of the interpolymer interactions in the PSBP block above CP_{UCST}. ξ_{OZ} = 5.1 ± 0.5 nm, which is about 1.4 nm lower than at 30 °C. In regime II, ξ_{OZ} may reflect the molecular conformation of the entire polymer. The Porod exponent α = 3.6 ± 0.2, confirming the presence of compact aggregates with rough surfaces. Nevertheless, on the mesoscopic level the spheres are not correlated.

The overall shape of the curves in regime III is different from those in regimes I and II, but similar to those in regime III of the $PSBP_{78}$-*b*-$PNIPAM_{100}$ and $PSBP_{78}$-*b*-$PNIPMAM_{115}$ solutions described in chapter 7. By parity of reasoning the curves are fitted using the model described in Eq. 6.1, based on the flexible cylinders correlated by a hard-sphere structure factor, plus a solvation and a Porod term (Figure C.2c in the appendix C). Thus, in regime III, flexible cylindrical particles with a polydisperse core are formed. The average cylindrical core radius is 11 ± 1 nm, with a narrow polydispersity p = 0.14 ± 0.01 (Table C.2 in the appendix C, Figure 8.2A). The average contour length of the cylinders increases during heating from L = 12 ± 1 nm at 50 ºC to 22 ± 2 nm at 60 ºC, along with an increase of the average Kuhn length, describing the local stiffness of the chain, from b = 3.3 ± 0.2 nm at 40 ºC to 10 ± 1 nm at 50 ºC. The ratio L/b increases during heating from 4 to 5, indicating a decrease in the stiffness of the cylinders. Analogously to the findings for $PSBP_{78}$-*b*-$PNIPAM_{100}$ and $PSBP_{78}$-*b*-$PNIPMAM_{115}$, we assume, that the cylinders in regime III of the $PSBP_{51}$-*b*-$PNIPMAM_{156}$ solution aggregate by attaching to each other’s ends, thus forming longer cylinders during heating. The hard-sphere structure factor reveals R_{HS} = 19 ± 3 nm, i.e. almost twice as large as the micelle radius. The volume fraction of correlated cylindrical micelles is η = 0.32 ± 0.03, which is much higher than the one of correlated spheres in regime I (ca. 0.08). Thus, apart from the different shape, the particles in regime III are more strongly correlated with each other compared to those in regime I. The solvation correlation length ξ_{solv} increases from 3.2 ± 0.3 nm at 50 ºC to 6.0 ± 0.5 nm at 60 ºC. This increase may be assigned to the continuous aggregation of the PNIPMAM block forming a core and weakening of the attractive interactions in the PSBP-rich shell between the PSBP segments, which may still present in regime III. The solvation Porod exponent decreases from m = 1.67

± 0.15 at 50 °C to 1.13 ± 0.10 at 60 °C, which may indicate a decline of the solvent conditions for a fraction of PSBP involved in the core due to the strengthening of the polymer-polymer interactions in the PNIPMAM block against the backdrop of still strong interactions in the PSBP block. The scaling factor C is higher at 50 ºC (2.0 ± 0.2 cm^{-1}) than at 60 ºC (0.8 ± 0.1 cm^{-1}), which is due to progressive phase separation right above CP_{LCST}. d_0 decreases from about 16 nm at 50 ºC to about 11 nm at 60 ºC, which is due to the strengthening of the polymer-polymer interactions in the PNIPMAM block. The Porod exponent α = 4.8 ± 0.3, which confirms the presence of compact aggregates with smooth surfaces.

To summarize, the micelles formed in the $PSBP_{51}$-*b*-$PNIPMAM_{156}$ solution feature change of the shape upon heating from spherical in regime I, to cylindrical in regime III, through an intermediate state, where the block copolymer exhibits behavior similar to polyelectrolytes in solution, due to the ionic interactions between the PSBP chains. The average spherical radius in regime I is comparable to that of the cylinders in regime III, i.e. ca. 11 nm. But the length of the cylinders increases from 12 to 22 nm during heating from 50 to 60 °C. ξ_{OZ} and ξ_{solv} cannot be compared directly, but the trend of their values indicates changes, which reflects rearrangement of the core and shell during heating. Apart from the difference in the shape, the micelles in regime III are more correlated compared to those in regime I. The difference may be assigned to the block properties and the block copolymer architecture: The PSBP block, which is water-insoluble in regime I, is shorter than the PNIPMAM block, which is water-insoluble in regime III. The particles form large aggregates in all regimes, but the aggregates have smooth surfaces in regimes I and III, while in regime II the aggregates surfaces change to rough. Thus, attractive interactions between the PSBP segments dominate over the interactions of the PSBP with water molecules even in regime II according to the presence of large aggregates. These interactions in the PSBP block may cause an additional impact on the formation of large aggregates in regime III as well.

According to the SANS results for $PSBP_{51}$-*b*-$PNIPMAM_{156}$ we assume that the CP_{UCST} value is in the range of 30-40 °C and the CP_{LCST} is in the range of 40-50 °C. The CP_{UCST} of the diblock copolymer is much lower than the CP_{UCST} of the corresponding homopolymer $PSBP_{51}$ (ca. 76 °C), while the values of CP_{LCST} of PNIPMAM and the diblock copolymer are in the same range. Thus, the CP_{UCST} is altered by the presence of PNIPMAM, whereas the CP_{LCST} may be unaffected by the presence of the second block or shifted for a few degrees only.

Results of the analysis of the SANS curves of $PSBP_{243}$-b-$PNIPMAM_{103}$. As mentioned above, the SANS curves of the $PSBP_{243}$-*b*-$PNIPMAM_{103}$ solution reveal very strong forward scattering in in the entire temperature range studied. The curves were fitted using the model described in Eq. 6.1, based on polydisperse spheres plus an Ornstein-Zernike and a Porod terms, the contribution of the latter term is dominant; a hard-sphere structure factor is needed at 60 °C only (Figure C.2b,d in the appendix C). The spherical particles have an average sphere radius increasing from r_{avg} = 32 ± 2 at 20-30 °C to 42 ± 4 at 40 °C, then decreasing to 9 ± 1 nm at 50 °C with following increase to 13 ± 1 nm at 60 °C (Table C.3 in the appendix C, Figure 8.2B). The polydispersity of the radius is moderate and decreases from p = 0.23 ± 0.02 at 20-30 °C to 0.10 ± 0.01 at 40 °C with a subsequent increase to 0.28 ± 0.05 at 50-60 °C. The spheres are correlated only at 60 °C, and half the interparticle distance is R_{HS} = 35 ± 3 nm, which is almost 5 times larger than the average micellar radius, indicating weak correlation. The hard-sphere volume fraction of correlated micelles, η, is about 0.22. ξ_{OZ} increases from 1.2 ± 0.1 nm at 20 °C to 2.6 ± 0.2 nm at 50 °C with a subsequent decrease to 1.9 ± 0.2 nm at 60 °C. ξ_{OZ} at 60 °C is ca. 0.3 nm higher than ξ_{OZ} at 40 °C, but ca. 0.7 nm smaller than the one at 50 °C. The Porod exponent α = 4.6 ± 0.6 indicates formation of compact aggregates with very smooth surfaces.

Altogether, in the solution of $PSBP_{243}$-*b*-$PNIPMAM_{103}$, large aggregates with smooth surfaces seem to form at all investigated temperatures. The aggregates, in turn, are formed by spherical particles with a polydisperse radius. Formation of the spheres below 50 °C, having radius 3 times as large as the radius of the spheres formed at higer temperatures, may be assigned to the attractive interactions between the PSBP chains below its CP_{UCST}. An increase of the radius at 40 °C may be due to the tendency to aggregation of the PNIPMAM block close to its CP_{LCST}, which occurs below the CP_{UCST}. We assume that the sudden decrease of the radius of the spherical particles at 50 °C with following increase at 60 °C, as well as the increase of the polydispersity of the radius and the increase of the correlation length at 50 °C with following decrease at 60 °C, indicating shrinkage of PNIPMAM above its CP_{LCST} and following continuous aggregation. In accordance with this stronger aggregation, the particles are correlated at 60 °C. At 50 °C ξ_{OZ} may describe the formed PSBP-rich shell around the collapsed PNIPMAM right above its CP_{LCST}. ξ_{OZ} is smaller than the average sphere radii, which mean that the particles are closely packed. Thus, the SANS curves at 50-60 °C may belong to regime II’ according to the scenario depicted in Figure 3.2

in chapter 3, where the formation of macroscopic precipitates is expected between CP_{LCST} and CP_{UCST}. The curves at 20-40 °C are ascribed to regime I, respectively.

From the SANS results for the $PSBP_{243}$-*b*-$PNIPMAM_{103}$ solution, we assume that CP_{LCST} is below CP_{UCST} and that its value is in the range of 40-50 °C, which is consistent with CP_{LCST} of PNIPMAM. The CP_{UCST} of the diblock copolymer could not be discerned, as it is apparently above 60 °C, which does not contradict to the value of the CP_{LCST} of the corresponding homopolymer $PSBP_{243}$ (>100 °C).

8.4. Influence of the zwitterionic and nonionic blocks ratio on the aggregation behavior

To answer the question how the ratio of the molar masses or the lengths of the zwitterionic and nonionic blocks may influence the aggregation behavior of the diblock copolymers, we compare the SANS results from the $PSBP_{51}$-*b*-$PNIPMAM_{156}$, $PSBP_{78}$-*b*-$PNIPMAM_{115}$ (for details see chapter 7) and the $PSBP_{243}$-*b*-$PNIPMAM_{103}$ solutions in salt-free D_2O. Two factors have to be considered: (i) The overall molar mass of $PSBP_{243}$-*b*-$PNIPMAM_{103}$ is about two times higher, than those of $PSBP_{51}$-*b*-$PNIPMAM_{156}$ and $PSBP_{78}$-*b*-$PNIPMAM_{115}$, which are almost equal. (ii) The composition of the diblock copolymers is different: in $PSBP_{51}$-*b*-$PNIPMAM_{156}$, the PNIPMAM block is 3 times longer than the PSBP block; in $PSBP_{78}$-*b*-$PNIPMAM_{115}$, the PNIPMAM block is 1.5 times longer than the PSBP block, i.e. the values of the block lengths are closer to each other, and in $PSBP_{243}$-*b*-$PNIPMAM_{103}$, the PNIPMAM block is 2.4 times shorter than the PSBP block.

The structures, according to the SANS results from the $PSBP_{51}$-*b*-$PNIPMAM_{156}$ and $PSBP_{243}$-*b*-$PNIPMAM_{103}$ solutions and expectations relating to the (aggregated) behavior, are depicted in Figure 8.3. An analogous schematic representation of the structures in the $PSBP_{78}$-*b*-$PNIPMAM_{115}$ is shown in Figure 7.4.

Hereinafter, the $PSBP_{51}$-*b*-$PNIPMAM_{156}$, $PSBP_{78}$-*b*-$PNIPMAM_{115}$ and $PSBP_{243}$-*b*-$PNIPMAM_{103}$ solutions for convenience will be abbreviated as BC1 (BC denotes block copolymer), BC2 and BC3, respectively.

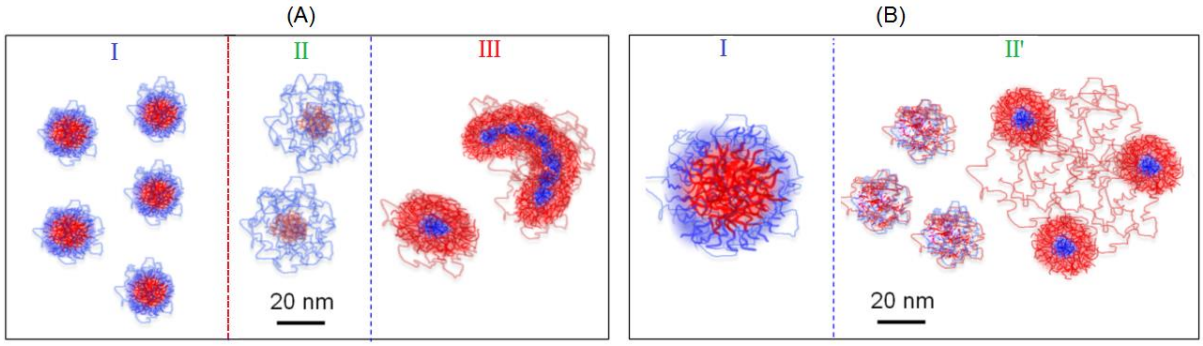

Figure 8.3: Schematic representation of the micelles in (A) $PSBP_{51}$-*b*-$PNIPMAM_{156}$ and (B) $PSBP_{243}$-*b*-$PNIPMAM_{103}$ solutions in the three/two regimes as indicated. Red: PSPP block, blue: PNIPMAM block. (**--**) and (**-·-**): approximate values positions of CP_{UCST} and CP_{LCST}.

The cloud point/points in BC1 and BC3 are assumed from the SANS results. The step of the SANS measurements of 10 °C allows to assume only the range of the values of the cloud points. The difference in the cloud points determined in BC2 by means of SANS, compared to those determined by means of turbidimetry (see chapter 7), namely the delay of ca. 2 °C during heating, may indicate that the systems with PSBP block need longer equilibration time than used in SANS experiments (15 min) and cause a minimum deviation of 2 °C. Moreover, only the onset of CP_{UCST} could be observed in BC1 and BC2, due to very gradual transition of PSBP. Nevertheless, we may conclude that in these two systems the value of CP_{UCST} is sensitive to the polymer architecture, namely to the presence of the PNIPMAM block: CP_{UCST} in BC1 and BC2 is shifted to lower values by more than 10 °C when comparing with the cloud points of the corresponding homopolymers. In BC3, the CP_{UCST} could not be determined, because its value is higher than the maximum measuring temperature, namely 60 °C. CP_{LCST} in all three systems under investigation is found to be in the range of 40-50 °C, which does not contradict the value of CP_{LCST} of PNIPMAM, but does not allow to conclude about its susceptibility to the presence of PSBP block due to the large temperature range.

In regime I, the overall scattering intensity in BC3 is much higher compared to the one in BC1 and BC2 due to the strong forward scattering originating from very large aggregates, which make the shape of its SANS curves very different. The scattering intensity for BC2 in regime I is higher than for BC1, while the shape of the SANS curves for these two systems is very similar. At the mesoscopic length scales, formation of spherical particles with polydisperse radius was found for all three systems, but the overall behavior in BC3 is very different, compared to BC1 and BC2. The radius of the spherical particles is stable during

heating in BC1 and BC2, while it increases in BC3. The average radius of the spherical particles in BC3 is ca. 3 times larger than in BC1 and BC2. This is in agreement with the higher overall molar mass of BC3 compared to BC1 and BC2 and the higher fraction of PSBP, which is at the origin of the structure formation in regime I. The radius of the spheres in BC1 is only ca. 1 nm smaller than in BC2, due to the smaller molar mass of BC1 and the smaller fraction of PSBP in this system. The polydispersity of the radius is comparable in all three systems. The correlation length increases during heating in all three systems, indicating that the packing density of the presumably PNIPMAM-rich micellar shells is decreases. The values of the correlation length are comparable for the systems BC1 and BC2 and ca. 3 times smaller in BC3, which may be due to the higher fraction of PSBP and smaller fraction of PNIPMAM in BC3, resulting in the formation of larger particles with thinner shell. A weak correlation of the spheres is detected only in BC1 and BC2. On the large scales, the aggregates' surfaces changes from smooth to rough in BC2 during heating, due to the onset of the gradual CP_{UCST}, while in BC1 and BC3, the aggregates surfaces are smooth at all temperatures.

As intendent, regime II, in which a diblock copolymer exhibits behavior similar to polyelectrolytes in solution, due to the ionic interactions between the PSBP chains, was found in BC1. Nevertheless, the attractive interactions between the PSBP segments are strong enough to cause formation of small fraction of large aggregates with rough surfaces. Regime II', with macroscopic precipitates formed due to attractive polymer-polymer interactions in both PSBP and PNIPMAM, was detected in BC3. In regime II' of BC3, very large aggregates are formed by polydisperse spherical particles with radius about 10 nm. We may conclude that the absolute molar mass of the PNIPMAM block should be at least 1.3 times higher than PSBP in order to obtain a system, in which CP_{UCST} would be lower than CP_{LCST}, and about 6 times lower to obtain a system with reverse position of the cloud points.

Regime III will be compared only for the systems, in which it was observed, namely BC1 and BC2. The shape of the SANS curves for these two systems is similar. Results of the SANS curves fitting reveal the formation of large aggregates with smooth surfaces composed by the cylindrical micelles with polydisperse radius. The average radius of the cylinders formed in BC2 increases from 10 to 14 during heating, while for BC1 it is stable and is about 11 nm. The polydispersity of the radius is higher in BC2. The contour length of the cylinders increases during heating and in BC2 it is almost twice as high as in BC1, despite the fact that,

in BC2, the fraction of PNIPMAM, which is at the origin of the micelle formation in regime III, is smaller than in BC1. This indicates that the attractive interactions in PSBP block, the fraction of which is higher in BC2, play an important role in the formation of the cylinders. Thus, in BC2, the longer cylinders are formed due to longer block length of PSBP, i.e. higher fraction of PSBP, and hence comparably higher impact of the ionic attractive interactions in PSBP. The correlation of the cylinders is alike, while the volume fraction of correlated cylinders is slightly higher in BC2. The other parameters are similar.

For all described above systems, the expected core-shell structure of the micelles in regimes I and III (when applicable) could not be resolved due to the similarity of the SLD values of the PSBP and PNIPMAM blocks (see paragraph 7.3).

8.5. Conclusions

This part of the thesis is devoted to studies of the influence of the architecture and particularly the blocks lengths on the self-assembly in aqueous solution of the doubly thermoresponsive diblock copolymers consisting of a zwitterionic PSBP block and a nonionic PNIPMAM block. We investigated the "schizophrenic" responsive aggregation behavior of $PSBP_{51}$-*b*-$PNIPMAM_{156}$ and $PSBP_{243}$-*b*-$PNIPMAM_{103}$ in D_2O using temperature-resolved SANS. For completeness, we compare the results with the observations described in chapter 7 on the analogous copolymer $PSBP_{78}$-*b*-$PNIPMAM_{115}$.

The length of the PSBP and PNIPMAM blocks and their ratio play an important role in the self-assembly of the diblock copolymers in aqueous solution. The architecture of these three diblock copolymers lead to three possible options for the positions of the cloud points in dependence on temperature, as depicted in Figure 3.2 in chapter 3: the diblock copolymers are amphiphilic and form micelles in solution below UCST- and above LCST-type transitions, but with reversed hydrophilic and hydrophobic blocks. The transition from the presumably core-shell micelles of one type to the opposite one, i.e. from regime I to regime III, proceeds via precipitation in the $PSBP_{243}$-*b*-$PNIPMAM_{103}$ solution (regime II’), via the regime where the polymer chains are in expanded state in the $PSBP_{51}$-*b*-$PNIPMAM_{156}$ solution (regime II) and without an intermediate state in the $PSBP_{78}$-*b*-$PNIPMAM_{115}$ solution, due to close positions of the cloud points. We note, that in the $PSBP_{243}$-*b*-$PNIPMAM_{103}$ solution, the regime III was not identified, due to the very high value of CP_{UCST} and an insufficient number of measurements at high temperature.

Similar to the observations for the diblock copolymers with PSPP blocks (described in chapter 6), the diblock copolymers with PSBP block exhibit behavior similar to polyelectrolytes in solution, due to the ionic interactions between the PSBP chains. In all three systems with PSBP and PNIPMAM blocks below CP_{UCST}, the attractive interactions between the PSBP chains lead to the formation of very large aggregates with smooth surfaces by correlated, small and homogeneous spherical particles, resulting in a turbid solution. The dimensions of the structures formed in the $PSBP_{51}$-*b*-$PNIPMAM_{156}$ and $PSBP_{78}$-*b*-$PNIPMAM_{115}$ solutions are similar and lower than in the $PSBP_{243}$-*b*-$PNIPMAM_{103}$ solution. We assume that the higher overall molar mass of the diblock copolymer, together with the higher fraction of PSBP lead to an enhanced aggregation in the $PSBP_{243}$-*b*-$PNIPMAM_{103}$ solution. In regime II of the $PSBP_{51}$-*b*-$PNIPMAM_{156}$ solution, high number of ionic groups bound to the PSBP block cause the formation of a small fraction of large aggregates and concentration fluctuations. In regime II' of the $PSBP_{243}$-*b*-$PNIPMAM_{103}$ solution, a high fraction of large aggregates with smooth surfaces formed by small spherical particles is formed due to the attractive interactions in both PSBP and PNIPMAM blocks. The individual properties of the blocks, such as dominating ionic interpolymer interactions versus hydrogen bonding with water, yield the marked differences of the aggregation behavior below CP_{UCST} and above CP_{LCST}, respectively. In regime III, the $PSBP_{51}$-*b*-$PNIPMAM_{156}$ and $PSBP_{78}$-*b*-$PNIPMAM_{115}$ solutions contain correlated flexible cylinders with a polydisperse radius and increasing contour length during heating. The dimensions of the cylinders are larger in the $PSBP_{78}$-*b*-$PNIPMAM_{115}$ solution, which is contradictory to the higher fraction of PNIPMAM in $PSBP_{51}$-*b*-$PNIPMAM_{156}$, which is at the origin of the micelle formation in regime III. Thus, the structure formation in regime III is governed by the attractive interactions in both PSBP and PNIPMAM.

Thus, a double switchable system (Figure 3.2) where the transition from the core-shell micelles of one type to the opposite one may proceed depending on temperature via precipitation, or via the molecularly dissolved state, or directly, can be obtained by variation of the polymer architecture, namely the blocks lengths. Moreover, the structure of the micelles depends strongly on the lengths of the blocks of different nature, which predict the impact of the block features in the self-assembly of the block copolymers. In addition, as it is shown at the example of the $PSBP_{78}$-*b*-$PNIPMAM_{115}$ solutions, the cloud points and hence the behavior of the diblock copolymer in aqueous solution may be additionally controlled by the concentration of added low molar mass electrolytes.

9. Summary and conclusion

This dissertation discussed the "schizophrenic" self-organization in aqueous solution of twofold thermoresponsive diblock copolymers consisting of a zwitterionic polysulfobetaine block and a nonionic thermoresponsive block, exhibiting UCST and LCST behavior, respectively.

In the first part, we focused on the influence of the architecture and the chemical nature of the individual blocks on the aggregation behavior of the diblock copolymers consisting of a zwitterionic PSPP block and a nonionic thermoresponsive PNIPAM of PNIPMAM block, namely $PSPP_{432}$-*b*-$PNIPAM_{200}$ and $PSPP_{498}$-*b*-$PNIPMAM_{144}$, in D_2O. For both systems, CP_{UCST} is lower than CP_{LCST}, so that the diblock copolymers are water-soluble in the entire temperature range studied (10 - 65 °C). Turbidimetry, DLS, and temperature-resolved SANS show for the diblock copolymers the same general pattern, revealing three regimes of association and self-assembly in solution. Between CP_{UCST} and CP_{LCST}, the polymer solutions are translucent due to concentration fluctuations caused by ionic interactions between the PSPP chains. At low temperatures, namely below CP_{UCST}, the polyelectrolyte nature of the PSPP block induce formation of very large aggregates with smooth surfaces by correlated, small and homogeneous spherical particles, which result in a high turbidity of the polymer solutions. At high temperatures, namely above CP_{LCST}, the solutions are partially turbid due to the attractive interactions in the nonionic PNIPAM/PNIPMAM blocks, which do not lead to the formation of large aggregates as below CP_{UCST}, but to the formation of spherical core-shell micelles with a polydisperse core. The core-shell structure of the micelles expected below CP_{UCST} could not be resolved, which may be due to the fact that the aggregation is governed by ionic interactions in the PSPP block and due to the interactions between the PSPP and PNIPAM/PNIPMAM blocks. The marked differences of the aggregation behavior below CP_{UCST} and above CP_{LCST} may be assigned to the difference in block lengths and their individual properties, such as dominating ionic interpolymer interactions versus hydrogen bonding with water, respectively.

The aggregation behavior of $PSPP_{432}$-*b*-$PNIPAM_{200}$ and $PSPP_{498}$-*b*-$PNIPMAM_{144}$ in solution seems to be generic, yet, the cloud points are different: higher values of CP_{UCST} and CP_{LCST} as well as a larger temperature range between the cloud points was observed in the $PSPP_{498}$-*b*-$PNIPMAM_{144}$ solution, compared to $PSPP_{432}$-*b*-$PNIPAM_{200}$. Moreover, the cloud points are altered in the copolymers from the ones in the respective homopolymers in a different way,

partially due to the different ratio of the lengths of the zwitterionic to the nonionic blocks and partially due to the chemical difference between the nonionic PNIPMAM and PNIPAM blocks. The choice of PNIPMAM as nonionic thermoresponsive block increases not only the width of the intermediate temperature regime by increasing CP_{LCST}. The apparently small molecular change by adding one methyl group to the repeat unit modulates markedly the interaction of the nonionic block with adjacent zwitterionic and hydrophobic segments in the block copolymer, quite differently from PNIPAM. In addition, SANS revealed the formation of larger spheres below CP_{UCST} and smaller core-shell micelles above CP_{LCST} in the $PSPP_{498}$-*b*-$PNIPMAM_{144}$ solution compared to $PSPP_{430}$-*b*-$PNIPAM_{200}$. The reasons for the findings seem complex, suggesting a certain extent of hydrophobic interaction between PNIPMAM chains already below the phase transition, as well as interactions with the zwitterionic block, and a stronger hydrophobic aggregation of the polymer chains above CP_{LCST}.

The sensitivity of PSPP to the addition of low molar mass salts was investigated by means of turbidimetry and SANS. Presence of an electrolyte, namely NaBr at a concentration of 0.004 M, results in a salt-induced increase of the CP_{UCST} in both systems, due to screening of the ionic interactions between the charged groups, while CP_{LCST} stays unaffected. The shift of the CP_{UCST} is smaller than the temperature range between the CP_{UCST} and CP_{LCST}, and the general pattern of the systems is unchanged. Although, the salt concentration is very low, it causes minor structural changes in the entire investigated temperature range.

The second part of the thesis was devoted to the influence of the nature of the zwitterionic polysulfobetaine block (PSPP or PSBP) on the self-assembly in aqueous solution of the corresponding twofold thermoresponsive diblock copolymers with a nonionic PNIPAM/PNIPMAM block. We investigated the aggregation behavior of the $PSBP_{78}$-*b*-$PNIPAM_{100}$ and $PSBP_{78}$-*b*-$PNIPMAM_{115}$ diblock copolymers in D_2O by means of turbidimetry and SANS and compared their behavior to those of $PSPP_{430}$-*b*-$PNIPAM_{200}$ and $PSPP_{498}$-*b*-$PNIPMAM_{144}$. Similar to the diblock copolymers with PSPP, the diblock copolymers with the PSBP block reveal water-solubility in the entire temperature range studied (10-65 °C). The spacer group in PSBP which is extended by one methylene group between the charged groups compared to the one in PSPP results in stronger ionic interactions between the PSBP chains and a much higher CP_{UCST}. The presence of the nonionic PNIPAM/PNIPMAM block causes a decrease of CP_{UCST} of the PSBP block, compared to the respective homopolymer, so that CP_{UCST} is close to CP_{LCST} for both systems. SANS revealed a generic pattern of the aggregation behavior and only two different regimes

in the solutions of $PSBP_{78}$-*b*-$PNIPAM_{100}$ and $PSBP_{78}$-*b*-$PNIPMAM_{115}$ in dependence on temperature, i.e. below CP_{UCST} and above CP_{LCST}. The transitions from one regime to another one occur close to the CP_{LCST} values of the PNIPAM and PNIPMAM homopolymers, accordingly. CP_{UCST} seems to be very gradual and presumably lies above the CP_{LCST} in both systems. Both at low and high temperatures, namely below CP_{UCST} and above CP_{LCST}, strong ionic interactions in the PSBP block cause the formation of rather micelle-like associates than distinct core-shell micelles. Below CP_{UCST}, formation of very large aggregates with smooth surfaces by correlated, small and homogeneous spherical particles was found, similar to the findings in the solutions of the diblock copolymers with the zwitterionic PSPP block. The spherical particles are less polydisperse, more correlated and larger in size, compared to those in solutions of the diblock copolymers with PSPP. Above CP_{LCST}, still strong ionic interactions between the PSBP chains together with the polymer-polymer interactions in the nonionic PNIPAM/PNIPMAM block lead to the formation of large aggregates, which was not found in the systems with the PSPP block. Moreover, the aggregates are formed by correlated cylindrical particles with a polydisperse radius and a contour length increasing during heating.

Distinct differences of the properties of the nonionic PNIPAM and PNIPMAM blocks cause structural differences also in the diblock copolymers solutions with the PSBP block. In the $PSBP_{78}$-*b*-$PNIPMAM_{115}$ solution, which features a higher CP_{LCST} compared to $PSBP_{78}$-*b*-$PNIPAM_{100}$, weakening of the attractive interactions between the PSBP chains, due to the onset of the gradual CP_{UCST}, are detected already below CP_{LCST}: The surface of the aggregates changes from smooth to rough which goes along with the decrease of the radius of the small spheres during heating, resulting in very low and gradual increase of the light transmission. In contrast, in the $PSBP_{78}$-*b*-$PNIPAM_{100}$ solution, neither changes in the light transmission nor structural changes are observed below CP_{LCST}. In addition, SANS revealed the formation of larger spheres below CP_{UCST} and smaller cylindrical micelles above CP_{LCST} $PSBP_{78}$-*b*-$PNIPAM_{100}$ solution, compared to $PSBP_{78}$-*b*-$PNIPMAM_{115}$. This may be partially due to the difference in the lengths of both blocks as well as different nature the nonionic blocks and their interactions with PSBP.

Addition of NaBr at a concentration of 0.004 M causes a shift of the CP_{UCST} in both solutions of $PSBP_{78}$-*b*-$PNIPAM_{100}$ and $PSBP_{78}$-*b*-$PNIPMAM_{115}$ to lower temperatures, in contrast to the diblock copolymers with the PSPP block where a salt-induced increase of CP_{UCST} was detected; and CP_{LCST} remains virtually unchanged, as intended. This way, an intermediate

temperature range between CP_{UCST} and CP_{LCST} has been derived, which is larger in the solution of $PSBP_{78}$-*b*-$PNIPMAM_{115}$, accordingly. The intermediate range is again characterized by the concentration fluctuations due to the polyelectrolyte nature of the PSPP block, as found at the example of the $PSBP_{78}$-*b*-$PNIPMAM_{115}$ solution by means of SANS. Again, minor salt-induced structural changes were found both below CP_{USCT} and above CP_{LCST}.

In the last part of the work, we focused on the architecture of diblock copolymers consisting of a zwitterionic PSBP block and a nonionic thermoresponsive PNIPMAM block in D_2O, namely the relative lengths of the constituting blocks. By means of SANS, we studied the aggregation behavior in aqueous solution of $PSBP_{51}$-*b*-$PNIPMAM_{156}$ and $PSBP_{243}$-*b*-$PNIPMAM_{103}$, with ca. 3 times lower or ca. 2.5 times higher block lengths of PSBP than those of PNIPMAM, respectively. Additionally, we compared their behavior to the behavior of $PSBP_{78}$-*b*-$PNIPMAM_{115}$, where the block length of PSBP is only 1.5 times lower than the one of PNIPMAM. Below CP_{UCST}, ionic interactions between the PSBP chains cause the formation of very large aggregates with smooth surfaces in all three systems. The largest aggregates are found in the solution of $PSBP_{243}$-*b*-$PNIPMAM_{103}$, which has the highest molar mass, together with the highest block length of PSBP, which is at the origin of aggregation at low temperatures. An intermediate temperature range, between CP_{UCST} and CP_{LCST}, was detected only in the $PSBP_{51}$-*b*-$PNIPMAM_{156}$ and $PSBP_{243}$-*b*-$PNIPMAM_{103}$ solutions. In the $PSBP_{51}$-*b*-$PNIPMAM_{156}$ solution, where CP_{UCST} is below CP_{LCST}, a high number of ionic groups bound to the PSBP block cause the formation of a small fraction of large aggregates and concentration fluctuations. In the $PSBP_{243}$-*b*-$PNIPMAM_{103}$ solution, where CP_{UCST} is above CP_{LCST}, a high fraction of large aggregates with smooth surfaces are formed due to the attractive interactions in both PSBP and PNIPMAM blocks. Above CP_{LCST}, correlated cylinders with a polydisperse radius and increasing contour length during heating were found in the $PSBP_{51}$-*b*-$PNIPMAM_{156}$ and $PSBP_{78}$-*b*-$PNIPMAM_{115}$ solutions. The dimensions of the cylinders are larger in the $PSBP_{78}$-*b*-$PNIPMAM_{115}$ solution, although the fraction of PNIPMAM, which is at the origin of the micelle formation above CP_{LCST}, is higher in $PSBP_{51}$-*b*-$PNIPMAM_{156}$. Thus, the structure formation above CP_{LCST} is governed by the attractive interactions in both PSBP and PNIPMAM. We note, that in the $PSBP_{243}$-*b*-$PNIPMAM_{103}$ solution, the CP_{UCST} value as well as the structures above CP_{UCST} was not identified, due to and an insufficient number of measurements at high temperatures and further investigation is needed.

Thus, the variation of the relative lengths of the zwitterionic PSBP and the nonionic PNIPMAM blocks, allows to obtain a double switchable systems which exhibits a switch from micelles with a non-ionic shell and a polysulfobetaine core at low temperatures to the reverse micelles at high temperatures in three different ways: via precipitation, when CP_{UCST} is above CP_{LCST}, as in the $PSBP_{243}$-*b*-$PNIPMAM_{103}$ solution; via a molecularly dissolved state of the polymer chains with concentration fluctuations, when CP_{UCST} is below CP_{LCST}, as in the $PSBP_{51}$-*b*-$PNIPMAM_{156}$ solution; and directly, when the cloud points are close to each other, as in the $PSBP_{78}$-*b*-$PNIPMAM_{115}$ solution. The structure of the micelles depends strongly on the precise molecular structure of the diblock copolymers.

Summarizing the above mentioned results, we conclude that a proper selection of the diblock copolymer's architecture, namely the chemical structures of the zwitterionic and nonionic thermoresponsive blocks as well as their molar masses, allows to control the UCST- and LCST-type transition temperatures and determines the detailed responsive self-assembly. Moreover, addition of low molar mass salt to the polymer solution may cause changes of the UCST-type transition without affecting the LCST-type transition, giving rise to an orthogonal switch from the system with molecularly dissolved polymers in the intermediate state to the system with large aggregates, or vice versa, depending on the zwitterionic block properties and the initial intermediate state.

The diblock copolymers investigated in the present work showed a “smart” behavior in aqueous solution, as the reversible formation and disruption of the micelles, as well as an intermediate stage, which can be controlled by the architecture of the diblock copolymers and triggered by tuning the temperature and, due to the ion sensitivity of the polysulfobetaine block, by the ionic strength of the solution. Such materials might have a great potential for several applications, e.g. in the biomedical field and in the development of switchable surfaces and thermo-optical devices.[81]

The usefulness of these materials for encapsulation of a hydrophobic substances in the core of the micelle was demonstrated at the example of $PSPP_{144}$-*b*-$PNIPMAM_{498}$. The results of the temperature-dependent fluorescence characteristics of hydrophobic dye labels attached to the polymer ends show the dye partitions into the microphase-separated domains, but preferentially of the nonionic block above its LCST-type transition. Accordingly, the use of the LCST-type transition is more favorable than the use of the UCST-type transition for the

transport and release of hydrophobic active substances. Moreover, above the LCST-type transition in the diblock copolymers with the PSPP and PNIPAM or PNIPMAM blocks, a core-shell structure was detected, whereas below the UCST-transition, structure formation is much less pronounced. This is attributed to the different types of interactions, namely hydrophobic and ionic ones, dominating in the different regimes. For the systems with PSBP and PNIPAM/PNIPMAM blocks, where the strong ionic interactions between the PSBP chains affect the micelle formation below the UCST-type transition as well as above LCST-type transition, further investigations of its capability to transfer hydrophobic substances are needed.

Of course, other questions concerning the structure formation in the solutions of the diblock copolymers remain, and further experiments will certainly add significant information to the ongoing discussion. For instance, the detection of core-shell structure, which is of great interest for further application, using SANS is complicated because of the similarity of the SLD values of the zwitterionic and nonionic blocks of the investigated diblock copolymers. Further experiments with the deuteration of one of the blocks, which will allow to follow the block in the formation of the core or shell, will certainly add significant information to the ongoing discussion. Another interesting aspect for all potential applications in biological or environmental systems that inherently contain low molar mass electrolytes is the sensitivity of the investigated diblock copolymers to different environments.

Appendix A. Supporting information for chapter 6

The present appendix is based on ref. [219,220].

In the appendix, will be presented:

- ^{1}H NMR results from PSPP$_{498}$-*b*-PNIPMAM$_{144}$ in D_2O obtained in heating/cooling cycles
- Best fit parameters for the SANS data of a 50 g L^{-1} solutions of PNIPMAM$_{195}$.
- Fits to the SANS curves from a 50 g L^{-1} solutions of PSPP$_{430}$-*b*-PNIPAM$_{200}$, and PSPP$_{498}$-*b*-PNIPMAM$_{144}$ and best fit parameters for the SANS data.
- Comparison of the SANS curves from PSPP$_{498}$-*b*-PNIPMAM$_{144}$ and PSPP$_{430}$-*b*-PNIPAM$_{200}$ solutions in salt-free D_2O.
- Temperature-dependent fluorescence characteristics of the solvatochromic end-group.
- SAXS results from PSPP$_{498}$-*b*-PNIPMAM$_{144}$ in D_2O obtained in heating/cooling cycles.
- Comparison of the low *q* region in the fits to the SANS curves from PSPP$_{498}$-*b*-PNIPMAM$_{144}$ and PSPP$_{430}$-*b*-PNIPAM$_{200}$ solutions in salt-free D_2O and in 0.004 M NaBr in D_2O.
- Best fit parameters for the SANS data of a 50 g L^{-1} solutions of PSPP$_{430}$-*b*-PNIPAM$_{200}$ and PSPP$_{498}$-*b*-PNIPMAM$_{144}$ in 0.004 M NaBr in D_2O.

Characterization of the $PSPP_{498}$-*b*-$PNIPMAM_{144}$ solution using ^1H nuclear magnetic resonance (NMR)

The present paragraph is based on ref. [220].

Temperature-resolved ^1H NMR of 10 g L^{-1} solutions of $PSPP_{498}$-*b*-$PNIPMAM_{144}$ in D_2O were carried out using a Bruker Avance 500 spectrometer (500 MHz). The measurements were performed during heating and cooling starting at 40 °C, respectively, in intervals of 5 °C. Samples were equilibrated at each temperature 30 min before measurement.

Results from ^1H NMR

The temperature-dependent solution phase behavior of the $PSPP_{498}$-*b*-$PNIPMAM_{144}$ diblock copolymer in D_2O was explored using temperature-resolved ^1H NMR measurements. The three regimes in the $PSPP_{498}$-*b*-$PNIPMAM_{144}$ solution determined by turbidimetry are also reflected in temperature-resolved ^1H NMR spectra of the block copolymer (10 g L^{-1} in D_2O) (Figure A.1). In regime II, at 35-45 °C, the proton signals of both the PSPP and PNIPMAM blocks are well visible, relatively narrow, and the values of their integrals agree with the copolymer composition. In regime I, however, the signals characteristic for the PSPP block (e.g. at ~2.0, ~2.25, and 2.8-3.6 ppm)[31] broaden increasingly and loose much of their intensity with decreasing temperature, while the signal characteristic for the PNIPMAM block at ca. 3.9 ppm remains virtually unchanged. Also, the intensity of the signal centered at ~0.95 ppm, which is characteristic for the methyl group on the polymer backbone is markedly reduced, as the PSPP block is considerably longer than the PNIPMAM block. In comparison, the intensity of the signal centered at ~1.15 ppm, which has contributions from the methylene protons of the backbone, but is in large parts due to the methyl groups of the isopropyl moiety of PNIPMAM, becomes much less attenuated when lowering the temperature. The scenario of regime I is reversed in regime III, when heating above 45 °C. Whereas the signals characteristic for the PSPP block remain nearly unchanged, the signal at 3.9 ppm of the PNIPMAM block continuously decreases with heating. Further, the intensity of the mixed signal group at 1.15 ppm is increasingly reduced in comparison to the mixed signal centered at 0.95 ppm, in agreement with the relative contributions of the two blocks to these signals (see above). The broadening and attenuation of the NMR signals is explained by aggregation and desolvatation of the individual PSPP and PNIPMAM blocks below CP_{UCST} or above CP_{LCST}, respectively. This behavior corroborates our view of temperature-controlled

schizophrenic micellization of polymer $PSPP_{498}$-*b*-$PNIPMAM_{144}$, with the PSPP blocks forming the micellar core in regime I, and the PNIPMAM blocks in regime III. Nevertheless, we note that these changes do not take place abruptly, but rather gradually. Even at 10 °C, i.e., well below CP_{UCST}, the signals of the PSPP block are still well visible, implying an appreciable residual hydration of the collapsed PSSP chains. The same remark holds true for the PNIPMAM signal at 3.9 ppm, which even at 70 °C, i.e., well above CP_{LCST}, has not completely vanished.

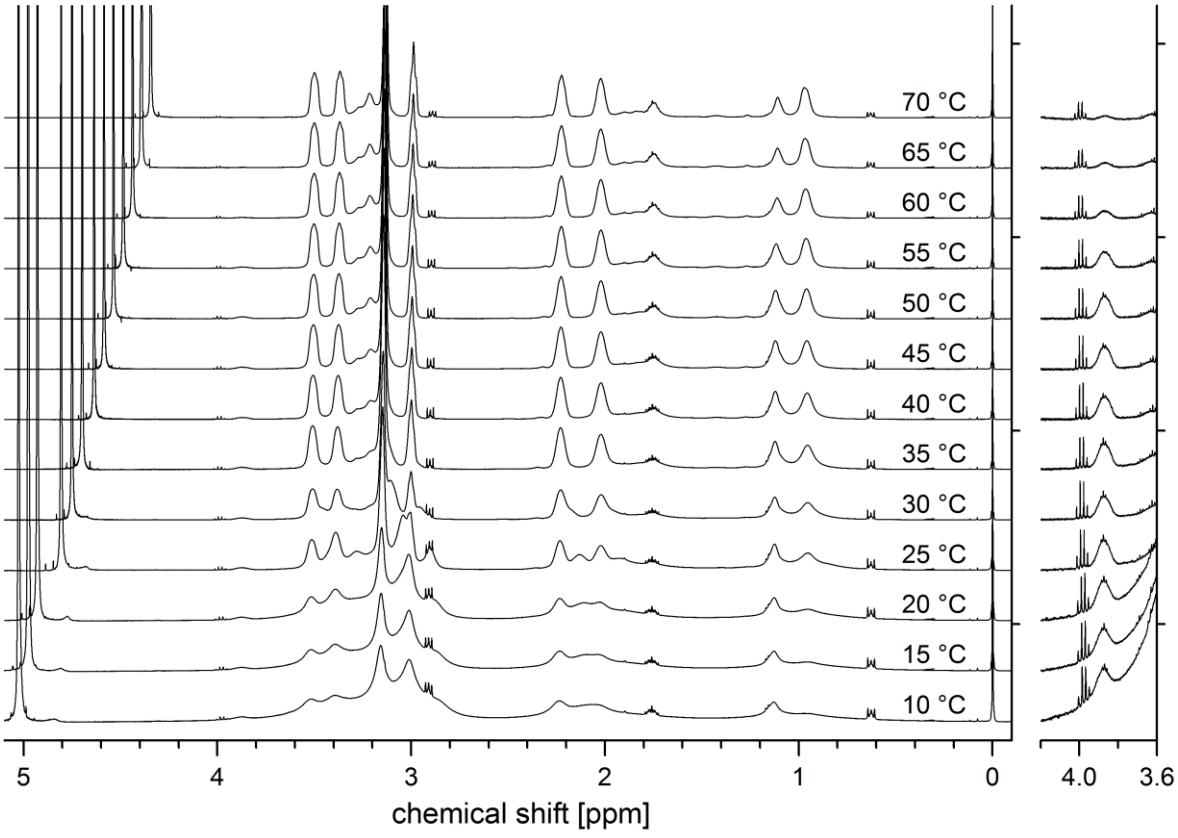

Figure A.1: Temperature dependent ^{1}H NMR spectra of $PSPP_{498}$-*b*-$PNIPMAM_{144}$ in D_2O. Temperature decreases from 70 °C (top curve) to 10 °C (bottom curve) in steps of 5 °C. Left: full spectra. Right: section between 4.2 and 3.6 ppm, with signal intensities magnified by a factor of 12.5. The weak highly resolved signals originate from incomplete deuteration of the internal reference 3-trimethylsilylpropanesulfonic acid–d_6 sodium salt.

Table A.1. Best fit parameters of Eq. 6.1 for the SANS data of a 50 g L^{-1} $PNIPMAM_{195}$ solution in D_2O at different temperatures.

	22 ºC	29 ºC	39 ºC	49 ºC
I_0 [cm^{-1}]	$(2.9 \pm 0.1)\times10^{-3}$	$(3.5 \pm 0.1)\times10^{-3}$		
r_{avg} [nm]	25 ± 3	26 ± 3		
p	0.20 ± 0.02	0.22 ± 0.02		
I_P	$(1.3 \pm 0.1) \times 10^{-5}$	$(8.0 \pm 0.1) \times 10^{-6}$	$(2.3 \pm 0.1) \times 10^{-6}$	$(5.0 \pm 0.4) \times 10^{-6}$
α	3.0 ± 0.2	3.1 ± 0.2	4.0 ± 0.3	4.3 ± 0.3
Ioz [cm^{-1}]	1.4 ± 0.1	1.9 ± 0.2	4.8 ± 0.4	0.18 ± 0.02
ξ_{OZ} [nm]	2.4 ± 0.2	2.7 ± 0.2	4.2 ± 0.3	4.1 ± 0.3
SLD sphere [nm^{-2}]	$(9.0\pm 1.0) \times 10^{-4}$	$(9.0\pm 1.0) \times 10^{-4}$		

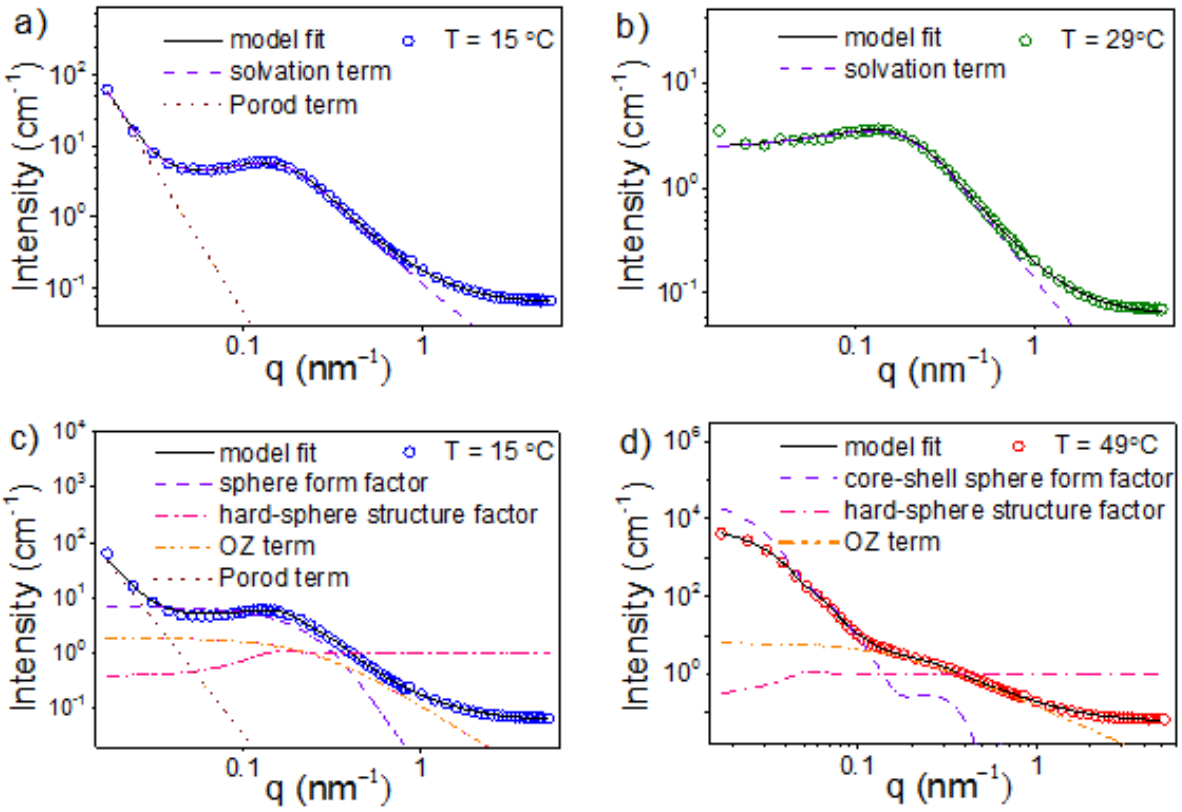

Figure A.2: Representative SANS curves from a 50 g L^{-1} $PSPP_{430}$-*b*-$PNIPAM_{200}$ solution in D_2O, where only every third data point is shown for clarity, together with the model fits (—) obtained using Eq. 6.1 in regimes I and III and Eq. 6.2 in regime II, see details in the chapter 6 in the main text. The symbols show the experimental data at 15 °C (regime I, a, c), 29 °C (regime II, b) and 49 °C (regime III, d), respectively. The other lines represent the contributions to the models as described in the graphs.

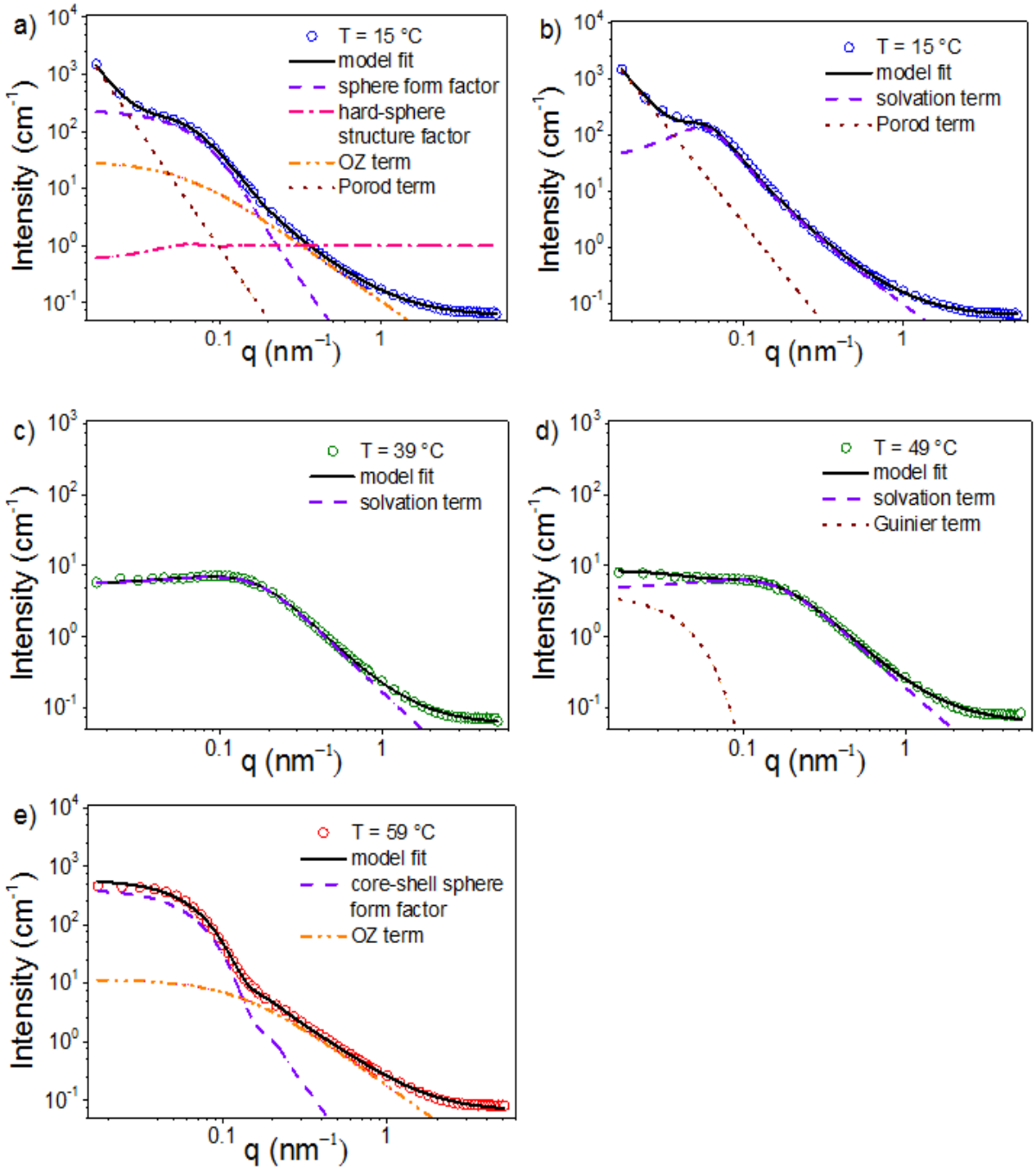

Figure A.3: Representative SANS curves from a 50 g L^{-1} $PSPP_{498}$-*b*-$PNIPMAM_{144}$ solution in D_2O, where every third point is shown for clarity, together with the model fits (**—**) obtained using Eq. 6.1 in regimes I and III and Eq. 6.2 in regime II, see details in the chapter 7 in the main text. The symbols show the experimental data (a,b) at 15 °C (regime I), (c) 39 °C (regime II), (d) 49 °C (regime II) and (e) 59 °C (regime III), respectively. The other lines represent the contributions to the models as described in the graphs.

Table A.2. Best fit parameters of Eq. 6.2 for the SANS data of a 50 g L^{-1} $PSPP_{430}$-*b*-$PNIPAM_{200}$ solution in D_2O in regimes I and II.

	Regime I	Regime II	
	15 °C	22 °C	29 °C
I_P	$(3.2 \pm 0.1)\times10^{-10}$	-	-
α	4.1 ± 0.1	-	-
C [cm^{-1}]	5.8 ± 0.1	4.2 ± 0.1	3.5 ± 0.1
ξ_{solv} [nm]	8.6 ± 0.2	6.5 ± 0.2	6.0 ± 0.1
m	1.94 ± 0.03	2.00 ± 0.03	1.93 ± 0.02
d_0 [nm]	48 ± 2	52 ± 3	50 ± 3

Table A.3. Best fit parameters of Eq. 6.1 for the SANS data of a 50 g L^{-1} $PSPP_{430}$-*b*-$PNIPAM_{200}$ solution in D_2O in regimes I and III.

	Regime I	Regime III	
	15 ºC	39 ºC	49 ºC
r_{avg} [nm]	4.4 ± 0.1	-	-
p	0.48 ± 0.03	-	-
r_{mic} [nm]	-	86 ± 4	92 ± 4
r_{core} [nm]	-	67 ± 4	73 ± 4
p_{core}	-	0.26 ± 0.02	0.26 ± 0.03
R_{HS} [nm]	18 ± 2	52 ± 3	54 ± 3
η	0.12 ± 0.01	0.17 ± 0.02	0.17 ± 0.01
I_P	$(1.5 \pm 0.5) \times 10^{-10}$	-	-
α	4.1 ± 0.2	-	-
Ioz [cm^{-1}]	1.9 ± 0.2	8.6 ± 0.7	6.2 ± 0.5
ξ_{OZ} [nm]	4.0 ± 0.3	7.9 ± 0.9	6.7 ± 0.5
SLD sphere/core [nm^{-2}]	$(8.0 \pm 0.3) \times 10^{-5}$	$(8.0 \pm 0.2) \times 10^{-5}$	$(8.0 \pm 0.2) \times 10^{-5}$
SLD shell [nm^{-2}]	-	$(3.7 \pm 0.2) \times 10^{-4}$	$(4.8 \pm 0.2) \times 10^{-4}$

Table A.4. Best fit parameters of Eq. 6.2 for the SANS data of a 50 g L^{-1} $PSPP_{498}$-*b*-$PNIPMAM_{144}$ solution in D_2O in regimes I and II.

	Regime I		Regime II		
	15 °C	22 °C	29 °C	39 °C	49 °C
I_P	$(2.1 \pm 0.1)\times10^{-6}$	$(2.4 \pm 0.2)\times10^{-6}$			
α	4.0 ± 0.2	3.5 ± 0.2			
I_G [cm^{-1}]					2.8 ± 0.3
R_g [nm]					32 ± 3
C [cm^{-1}]	137 ± 14	17 ± 2	11.1 ± 0.9	7.0 ± 0.6	6.1 ± 0.5
ξ_{solv} [nm]	38 ± 3	12 ± 1	8.5 ± 0.6	6.8 ± 0.5	6.2 ± 0.4
m	2.01 ± 0.10	1.96 ± 0.09	2.03 ± 0.08	2.03 ± 0.09	2.00 ± 0.11
d_0 [nm]	118 ± 11	78 ± 8	77 ± 7	72 ± 8	75 ± 7

Table A.5. Best fit parameters of Eq. 6.1 for the SANS data of a 50 g L^{-1} $PSPP_{498}$-*b*-$PNIPMAM_{144}$ solution in D_2O in regimes I and III.

	Regime I		Regime III
	15 ºC	22 ºC	59 ºC
r_{avg} [nm]	15 ± 2	6.1 ± 0.5	-
p	0.45 ± 0.03	0.49 ± 0.07	-
r_{mic} [nm]	-	-	28 ± 3
r_{core} [nm]	-	-	13 ± 1
p_{core}	-	-	0.44 ± 0.04
R_{HS} [nm]	43 ± 3	22 ± 2	-
η	0.08 ± 0.01	0.07 ± 0.01	-
I_P	$(7.6 \pm 0.3) \times 10^{-7}$	$(6.1 \pm 0.6) \times 10^{-8}$	-
α	4.1 ± 0.3	4.1 ± 0.2	-
Ioz [cm^{-1}]	16.3 ± 0.9	9.1 ± 0.2	11.6 ± 0.9
ξ_{OZ} [nm]	12.3 ± 0.9	7.7 ± 0.3	8.1 ± 0.8
SLD sphere/core [nm^{-2}]	$(7.3 \pm 0.5) \times 10^{-5}$	$(7.3 \pm 0.5) \times 10^{-5}$	$(7.3 \pm 0.2) \times 10^{-5}$
SLD shell [nm^{-2}]	-	-	$(1.5 \pm 0.2) \times 10^{-4}$

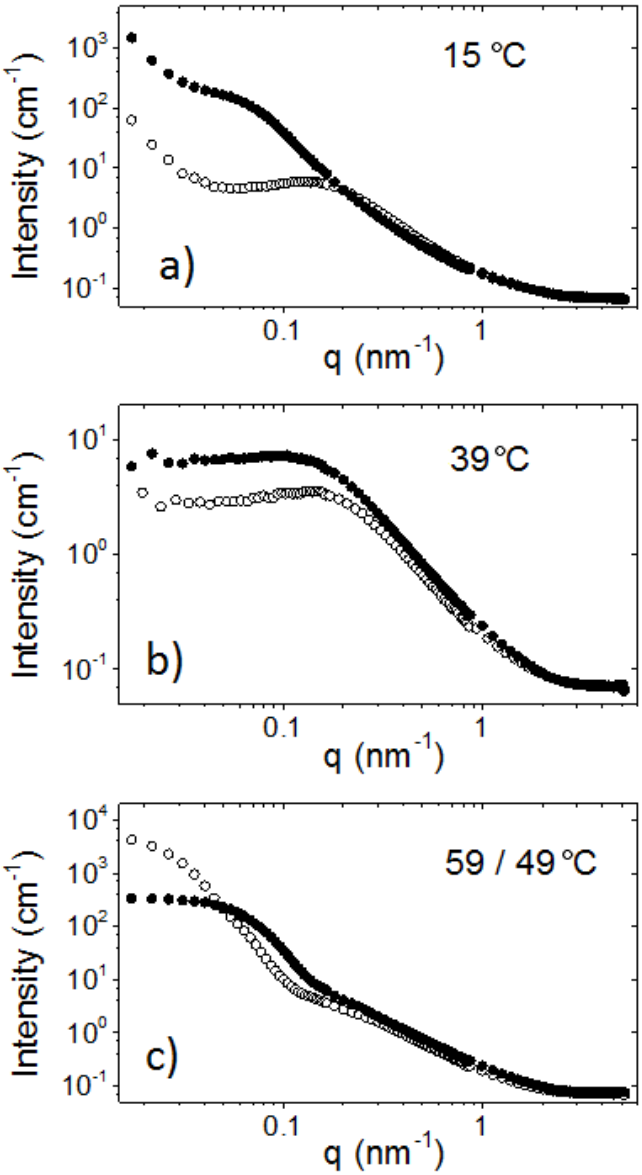

Figure A.4: Comparison of the SANS curves from a 50 g L^{-1} $PSPP_{498}$-*b*-$PNIPMAM_{144}$ (closed symbols) and $PSPP_{430}$-*b*-$PNIPAM_{200}$ (open symbols) solutions in salt-free D_2O at (a) 15 ºC (regime I), (b) 39 °C (regime II) and (c) 59 °C ($PSPP_{498}$-*b*-$PNIPMAM_{144}$) and 49 ºC ($PSPP_{432}$-*b*-$PNIPAM_{200}$) (regime III). Only every second point is shown for clarity.

Temperature-dependent fluorescence characteristics of the solvatochromic end-group label

The present paragraph is based on ref. [220].

The fluorescence behavior of the $PSPP_{498}$ and $PNIPMAM_{195}$ homopolymers and the block copolymer $PSPP_{498}$-*b*-$PNIPMAM_{144}$ was investigated. Fluorescence spectra were recorded by a Perkin Elmer Luminescence Spectrometer LS 50 B.

In the case of homopolymer $PNIPMAM_{195}$, the emission maximum of the fluorophore shifts in dilute solution from 546 nm below CP_{LCST} to 536 nm above CP_{LCST}, which goes in parallel with a strong increase of the fluorescence intensity. This indicates a less polar environment of the fluorophore above the coil-to globule phase transition, quite similar to the behavior of analogously labeled PNIPAM.[221] Accordingly, the hydrophobic dye partitions preferentially into the PNIPMAM-rich microphase. In contrast, in the case of $PSPP_{498}$, the emission maximum of the fluorophore stays at 544 nm independently of the temperature and of the coil-to globule phase transition, while the fluorescence intensity is always weak. Accordingly, the collapsed zwitterionic block does not accommodate the polar, but hydrophobic dye. The fluorescence behavior of the block copolymer $PSPP_{498}$-*b*-$PNIPMAM_{144}$, in which the solvatochromic label is attached to the zwitterionic block, corresponds to the one of the PSPP homopolymer. Below CP_{UCST}, at ambient temperature, and above CP_{LCST}, the emission maximum is always found at about 543 nm, supporting the view that the microphase separated domains of PSPP formed below CP_{UCST} are much less hydrophobic than the domains formed by PNIPAM above CP_{LCST}. This would account for the reduced disposition of the block copolymer to produce well-defined core-shell aggregate structures below CP_{UCST}.

Small-Angle X-ray Scattering (SAXS)

The present paragraph is based on ref. [220].

SAXS measurements were performed using a SAXS GANESHA 300XL instrument. The X-ray wavelength was λ = 1.54 Å and the sample-detector distance (SDD) 1.08 m, resulting in a q-range of 0.06 – 2.1 nm^{-1}. Two-dimensional scattering patterns were recorded on a Pilatus 300K detector with a pixel size of 172 µm × 172 µm. The scattering data were analyzed using the Fit2d software.[227] The 2D images were normalized to the intensity of the incident beam, azimuthally averaged and corrected for background scattering from the quartz capillary and for electronic noise. Samples were loaded in 1 mm quartz capillaries in a heatable sample holder. A 150 g L^{-1} $PSPP_{498}$-*b*-$PNIPMAM_{144}$ solution in D_2O was prepared at room temperature and was stirred for 2 days in a thermo-shaker at 40 °C. Measurements were performed according to the following protocols: (i) heating from 40 °C to 60 °C and subsequent cooling back in steps of 5 °C; (ii) cooling from 40 °C to 20 °C and subsequent heating back in steps of 4 °C. At each step, the equilibration time was 15 min. The exposure time at each temperature was 30 min.

To model the SAXS curves, the two level Beaucage model was used:[228-230]

$$I_B(q) = G\exp\left(\frac{-q^2 R_g^2}{3}\right) + \frac{C}{q^d} erf\left[\left(\frac{qR_g}{6^{1/2}}\right)\right]^{3d}, \quad \text{(A1)}$$

G and C are the scaling factors of the Guinier and the Porod prefactor, R_g the radius of gyration and d the Porod exponent. The error $erf[x]^{3d}$ ensures a smooth transition between the two terms. C reads:

$$C = \frac{Gd}{R_g^d}\left[\left(\frac{6d^2}{(2+d)(2+2d)}\right)\right]^{d/2} \Gamma(x), \quad \text{(A2)}$$

where $\Gamma(x)$ is the gamma function.

The SANS curves were modeled using the SANS Data Reduction and Analysis software provided by the NIST Center for Neutron Research within the IGOR Pro software environment.[218]

Results from SAXS

Temperature-resolved SAXS measurements of a 150 g L^{-1} $PSPP_{498}$-*b*-$PNIPMAM_{144}$ solution in D_2O were performed in order to get additional information on the structural changes and to detect a possible influence of the thermal history. Figure A.5a presents the SAXS curves from a heating/cooling run between 40 °C and 60 °C and from a cooling/heating run between 40 °C and 20 °C. They are characterized by one or two smooth decays and become flat above ca. 2.5 nm^{-1}.

Since the *q* range of the SAXS measurement is limited, we refrain from fitting the more detailed models used for the SANS curves which are described in the main text. Moreover, a higher polymer concentration was chosen for SAXS to increase the scattering signal. Therefore, we use a two-level Beaucage model (Eqs. A1 and A2) to detect and quantify possible differences according to the protocol.

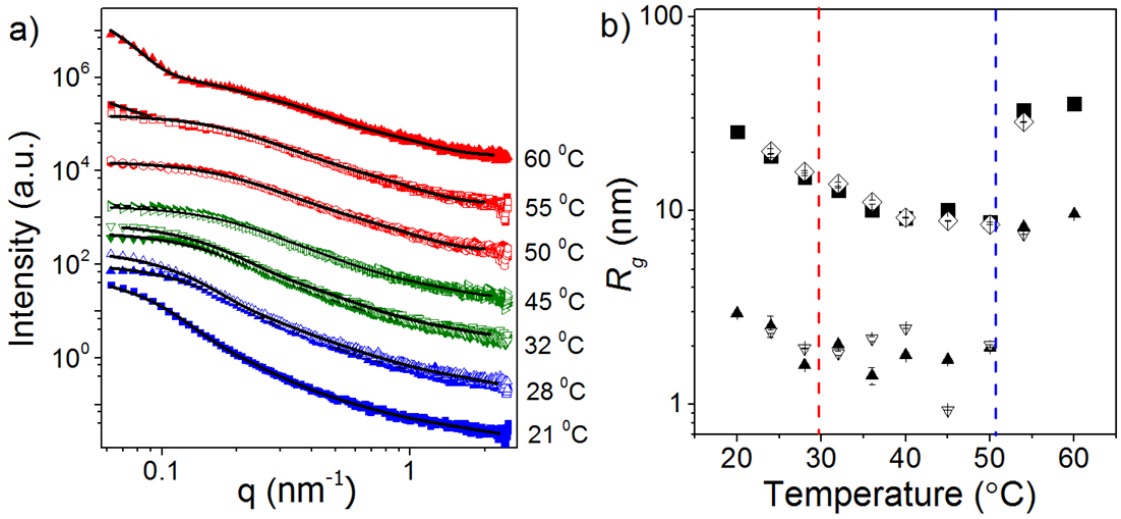

Figure A.5: (a) Representative SAXS-curves from a 150 g L^{-1} $PSPP_{498}$-*b*-$PNIPMAM_{144}$ solution in D_2O together with the model fits (—) during heating from 40 °C to 60 °C and during cooling from 40 °C to 20 °C (closed symbols) and during the subsequent cooling back and heating back runs (open symbols). The curves are shifted vertically by a factor of 10. The colors blue, green and red indicate the three regimes I, II and III as determined by turbidimetry at 50 g L^{-1}. (b) Resulting radii of gyration. Symbols correspond to the two types of particles: smaller (up and down triangles) and larger ones (black squares and diamonds). Red and blue dashed lines indicate CP_{UCST} and CP_{LCST}, respectively, as determined by turbidimetry at 50 g L^{-1}.

Figure A.5b presents the results from model fitting. Two kinds of length scales are identified. The smaller ones correspond to a radius of gyration of ca. 1-3 nm in regimes I and II and of ca. 10 nm in regime III. This contribution may be due to the concentration fluctuations in the micellar shell, i.e. the ξ values. Moreover, larger particles are observed whose radius of gyration decreases from 26 nm at 20 °C to 10 nm at 45 °C, i.e. in regimes I and II, and which is 30 nm and 36 nm at 54 °C and 60 °C, i.e. in regime III. These may correspond to the micelles observed by SANS in regimes I and III and to the large-scale concentration fluctuations in regime II. Upon cooling, very similar values are obtained in the entire temperature range. (The minor changes in the SAXS data seen in Figure S4a give rise to minor changes in the other fitting parameters, but not in the radii of gyration.) We conclude that there is no hysteresis between heating and cooling and that the sample is in equilibrium at all temperatures.

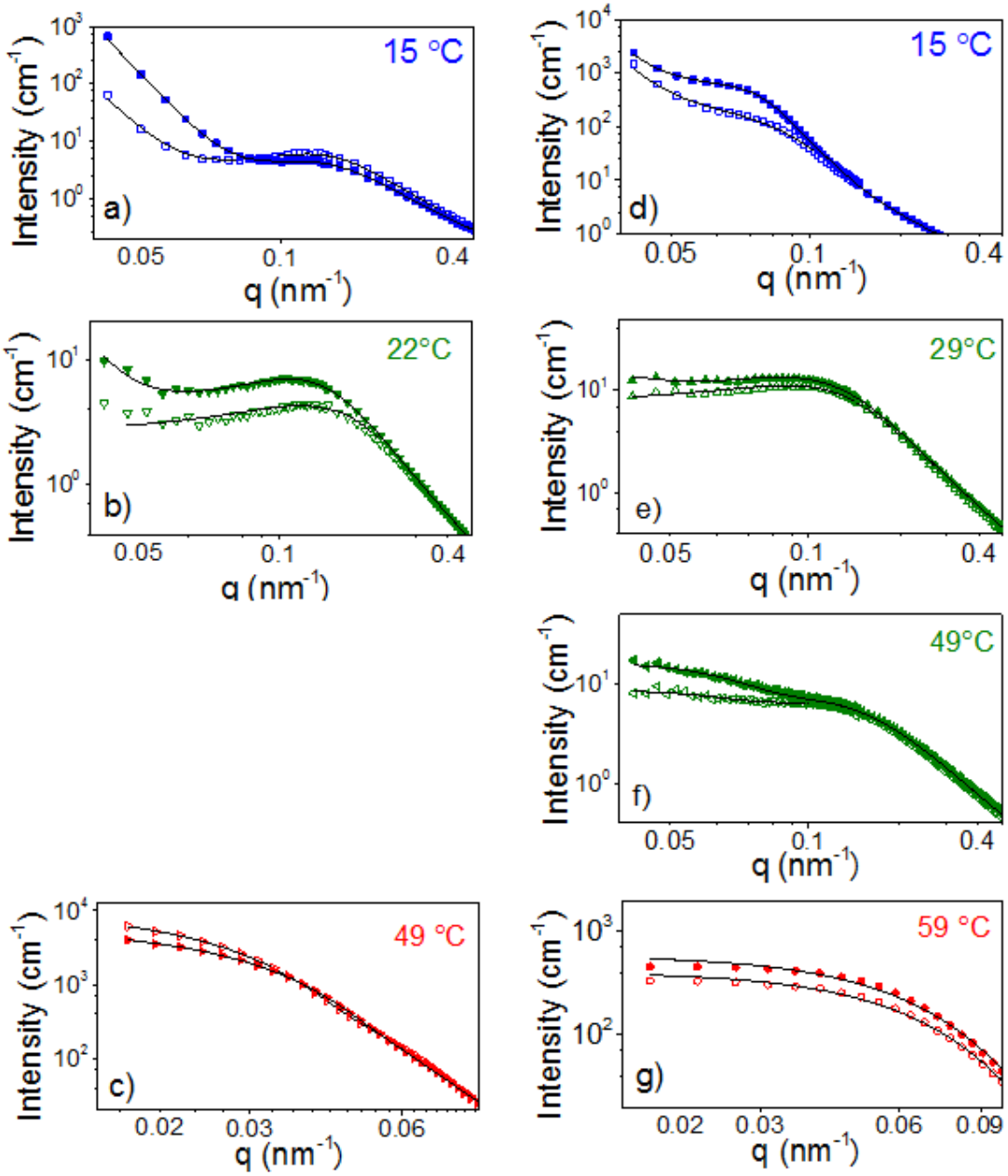

Figure A.6: Zooms of the low *q* region of the SANS curves from 50 g L^{-1} solutions of $PSPP_{430}$-*b*-$PNIPAM_{200}$ (a-c) and $PSPP_{498}$-*b*-$PNIPMAM_{144}$ (d-g) in salt-free D_2O (open symbols, from Figures 6.4 in the main text) and in 0.004 M NaBr in D_2O (closed symbols), where only every third point is shown for clarity, together with the fitting curves (—) obtained using Eq. 6.1 in regimes I and III and Eq. 6.2 in regime II, see details in the chapter 6 in the main text. Curves in regime I at 15 ºC (a, d), in regime II at 22/29 ºC (b, e) and 49 ºC (f) and in regime III at 49/59 ºC (c, d), where every second point is shown for clarity.

Table A.6. Best fit parameters of Eq. 6.2 to the SANS data of a 50 g L^{-1} $PSPP_{430}$-*b*-$PNIPAM_{200}$ solution in 0.004 M NaBr in D_2O in regimes I and II.

	Regime I	Regime II	
	15 °C	22 °C	29 °C
I_P	$(7.4 \pm 0.3) \times 10^{-10}$	$(2.1 \pm 0.1) \times 10^{-8}$	
α	4.3 ± 0.1	3.1 ± 0.1	
C [cm^{-1}]	4.8 ± 0.1	7.7 ± 0.2	5.5 ± 0.1
ξ_{solv} [nm]	8.2 ± 0.3	8.3 ± 0.3	6.5 ± 0.2
m	1.86 ± 0.03	1.95 ± 0.04	2.00 ± 0.03
d_0 [nm]	51 ± 3	55 ± 3	59 ± 4

Table A.7. Best fit parameters of Eq. 6.1 for the SANS data of a 50 g L^{-1} $PSPP_{430}$-*b*-$PNIPAM_{200}$ solution in 0.004 M NaBr in D_2O in regimes I, II and III.

	Regime I	Regime II	Regime III	Regime III
	15 ºC	22 ºC	39 ºC	49 ºC
r_{avg} [nm]	4.6 ± 0.1	3.3 ± 0.1	-	-
p	0.45 ± 0.04	0.64 ± 0.07	-	-
r_{mic} [nm]	-	-	78 ± 3	79 ± 4
r_{core} [nm]	-	-	58 ± 3	60 ± 3
p_{core}	-	-	0.28 ± 0.02	0.28 ± 0.03
R_{HS} [nm]	16 ± 2	18 ± 2	49 ± 3	51 ± 3
η	0.09 ± 0.01	0.12 ± 0.02	0.19 ± 0.03	0.18 ± 0.03
I_P	$(6.0 \pm 0.3) \times 10^{-10}$	$(2.1 \pm 0.2) \times 10^{-8}$	-	-
α	4.4 ± 0.2	3.1 ± 0.3	-	-
Ioz [cm^{-1}]	1.9 ± 0.2	3.0 ± 0.4	12.6 ± 1.1	11.5 ± 0.9
ξ_{OZ} [nm]	4.0 ± 0.4	4.5 ± 0.4	8.8 ± 0.3	8.2 ± 0.4
SLD sphere/core [nm^{-2}]	$(8.0 \pm 0.3) \times 10^{-5}$	$(8.0 \pm 0.3) \times 10^{-5}$	$(8.0 \pm 0.2) \times 10^{-5}$	$(8.0 \pm 0.2) \times 10^{-5}$
SLD shell [nm^{-2}]	-	-	$(3.8 \pm 0.2) \times 10^{-4}$	$(4.0 \pm 0.2) \times 10^{-4}$

Table A.8. Best fit parameters of the model in Eq. 6.2 for the SANS data of a 50 g L^{-1} $PSPP_{498}$-*b*-$PNIPMAM_{144}$ solution in 0.004 M NaBr in D_2O in regimes I and II.

	Regime I		Regime II		
	15 °C	22 °C	29 °C	39 °C	49 °C
$I_P \times 10^{-6}$	(2.6 ± 0.6)	(3.9 ± 0.4)			
α	4.0 ± 0.2	3.8 ± 0.3			
I_G [cm^{-1}]			6.0 ± 0.6	2.0 ± 0.2	9.8 ± 0.9
R_g [nm]			91 ± 9	60 ± 6	36 ± 4
C [cm^{-1}]	550 ± 20	33 ± 3	13.4 ± 1.2	8.1 ± 0.8	7.1 ± 0.7
ξ_{solv} [nm]	54 ± 5	15 ± 1	8.8 ± 0.9	6.8 ± 0.5	5.8 ± 0.5
m	2.24 ± 0.12	2.01 ± 0.08	2.05± 0.07	2.03 ± 0.05	2.03 ± 0.13
d_0 [nm]	140 ± 12	94 ± 9	85 ± 8	80 ± 9	103 ± 10

Table A.9. Best fit parameters of the model in Eq. 6.1 for the SANS data of a 50 g L^{-1} $PSPP_{498}$-*b*-$PNIPMAM_{144}$ solution in 0.004 M NaBr in D_2O in regimes I and III.

	Regime I		Regime III
	15 ºC	22 ºC	59 ºC
r_{avg} [nm]	26 ± 3	7.4 ± 0.6	-
p	0.34 ± 0.02	0.49 ± 0.06	-
r_{mic} [nm]	-	-	29 ± 3
r_{core} [nm]	-	-	15 ± 2
p_{core}	-	-	0.41 ± 0.04
R_{HS} [nm]	47 ± 5	28 ± 3	-
η	0.09 ± 0.01	0.06 ± 0.01	-
I_P	(6.9 ± 0.4) × 10^{-7}	(8.5 ± 0.9) × 10^{-8}	-
α	4.1 ± 0.3	4.0 ± 0.3	-
Ioz [cm^{-1}]	8.1 ± 0.6	9.7 ± 0.9	9.5 ± 1.0
ξ_{OZ} [nm]	8.7 ± 0.8	7.6 ± 0.5	7.0 ± 0.6
SLD sphere/core [nm^{-2}]	(7.3 ± 0.5) × 10^{-5}	(7.3 ± 0.5) × 10^{-5}	(7.0 ± 0.2) × 10^{-5}
SLD shell [nm^{-2}]	-	-	(9.2 ± 0.8) × 10^{-5}

Appendix B. Supporting information for chapter 7

In this appendix, will be presented:

- Fits to the SANS curves from 50 g L^{-1} solutions of $PSBP_{78}$-*b*-$PNIPAM_{100}$ in D_2O and $PSBP_{78}$-*b*-$PNIPMAM_{115}$ in D_2O and in 0.004 M NaBr (at 40 °C).
- Best fit parameters for the SANS data of a 50 g L^{-1} solutions of $PSBP_{78}$-*b*-$PNIPAM_{100}$ and $PSBP_{78}$-*b*-$PNIPMAM_{115}$ in D_2O and in 0.004 M NaBr in D_2O.

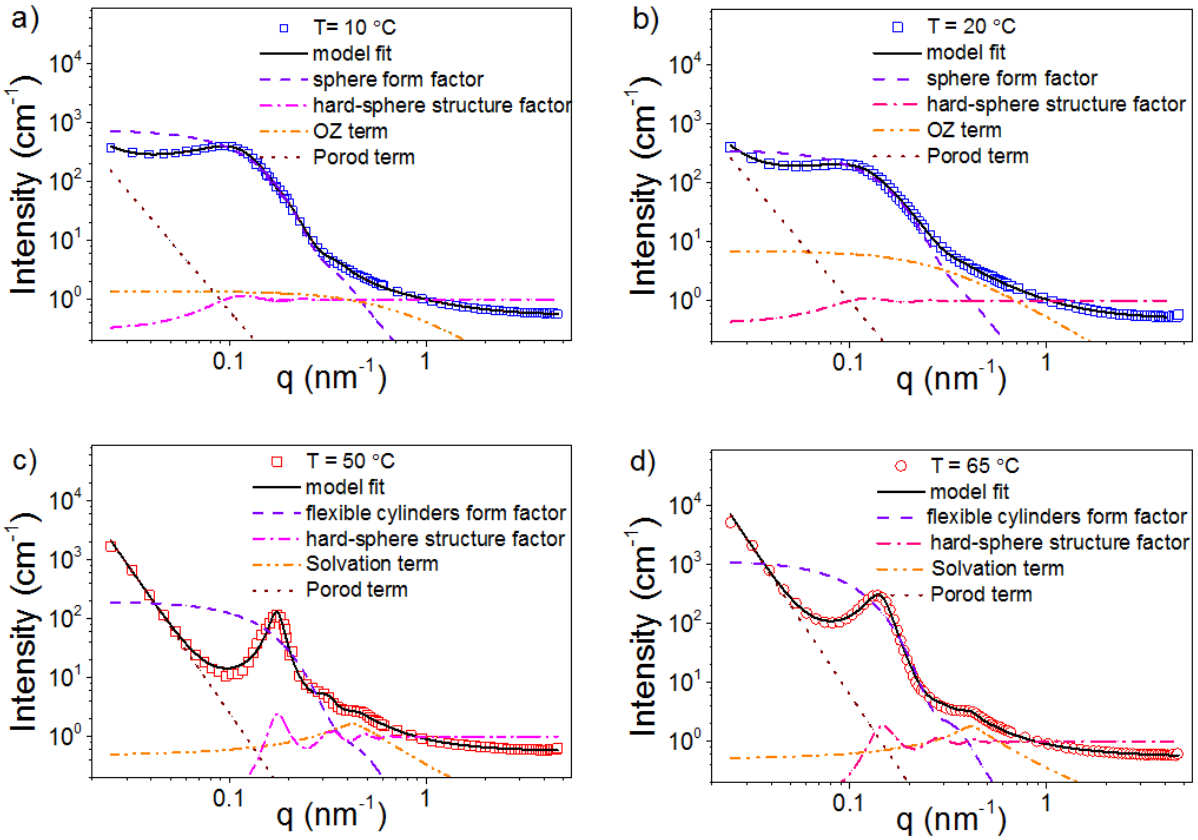

Figure B.1: Representative SANS curves from a 50 g L^{-1} $PSBP_{78}$-*b*-$PNIPAM_{100}$ (a, c) and $PSBP_{78}$-*b*-$PNIPMAM_{115}$ (b, d) solutions in D_2O, where every second point is shown for clarity, together with the model fits (—) obtained using Eq. 6.1, see details in the chapters 6-7 in the main text. The symbols show the experimental data from a 50 g L^{-1} $PSBP_{78}$-*b*-$PNIPAM_{100}$ solution in D_2O at 10 °C (regime I, a) and 50 °C (regime III, c) and data from a 50 g L^{-1} $PSBP_{78}$-*b*-$PNIPAM_{100}$ solution in D_2O at 20 °C (regime I, b) and 65 °C (regime III, d). The other lines represent the contributions to the models as described in the graphs.

Table B.1. Best fit parameters of Eq. 6.1 for the SANS data of a 50 g L^{-1} $PSBP_{78}$-*b*-$PNIPAM_{100}$ solution in D_2O in regimes I.

	10 ºC	20 ºC	30 ºC
r_{avg} [nm]	14.4 ± 1.4	13.8 ± 1.3	13.8 ± 1.3
p	0.22 ± 0.02	0.24 ± 0.02	0.28 ± 0.03
R_{HS} [nm]	26 ± 3	24 ± 2	24 ± 2
η	0.15 ± 0.01	0.10 ± 0.01	0.04 ± 0.01
I_P	$(8.6 \pm 0.8) \times 10^{-9}$	$(1.2 \pm 0.1) \times 10^{-9}$	$(3.2 \pm 0.3) \times 10^{-9}$
α	3.9 ± 0.2	4.1 ± 0.3	4.1 ± 0.3
I_{OZ} [cm^{-1}]	1.4 ± 0.1	3.4 ± 0.2	8.3 ± 0.7
ξ_{OZ} [nm]	1.5 ± 0.2	2.4 ± 0.2	3.6 ± 0.3
SLD sphere		$(7.7 \pm 0.4) \times 10^{-5}$	

Table B.2. Best fit parameters of Eq. 6.1 for the SANS data of a 50 g L^{-1} $PSBP_{78}$-*b*-$PNIPAM_{100}$ solution in D_2O in regime III.

	40 ºC	50 ºC
R_{avg} [nm]	10.6 ± 1.0	11.9 ± 1.2
L [nm]	23 ± 2	36 ± 4
b [nm]	10 ± 1	16 ± 2
p	0.21 ± 0.02	0.16 ± 0.02
R_{HS} [nm]	19 ± 2	22 ± 3
η	0.44 ± 0.02	0.52 ± 0.03
I_P	$(4.9 \pm 0.4) \times 10^{-10}$	$(7.0 \pm 0.6) \times 10^{-10}$
α	4.9 ± 0.3	4.8 ± 0.3
C [cm^{-1}]	1.7 ± 0.1	1.5 ± 0.1
ξ_{solv} [nm]	4.7 ± 0.4	7.9 ± 0.8
m	1.36 ± 0.12	0.94 ± 0.10
d_0 [nm]	15 ± 2	15 ± 2
SLD cylinder	$(7.7 \pm 0.4) \times 10^{-5}$	

Table B.3. Best fit parameters of equation 6.1 for the SANS data of a 50 g L^{-1} $PSBP_{78}$-*b*-$PNIPMAM_{115}$ solution in D_2O in regime I.

	20 ºC	25 ºC	30 ºC	35 ºC	40 ºC	45 ºC
r_{avg} [nm]	12.7 ± 1.3	12.3 ± 1.2	12.1 ± 1.2	11.7 ± 1.1	11.5 ± 1.2	11.5 ± 1.2
p	0.25 ± 0.02	0.27 ± 0.03	0.27 ± 0.03	0.27 ± 0.03	0.22 ± 0.02	0.10 ± 0.01
R_{HS} [nm]	24 ± 2	23 ± 2	23 ± 2	23 ± 2	24 ± 2	19 ± 2
η	0.11 ± 0.01	0.09 ± 0.01	0.07 ± 0.01	0.05 ± 0.01	0.04 ± 0.01	0.09 ± 0.01
$I_P \times 10^{-8}$	10.0 ± 1.0	1.3 ± 0.1	8.4 ± 0.9	8.6 ± 0.9	1.6 ± 0.2	14.7 ± 1.2
α	4.0 ± 0.2	3.9 ± 0.2	3.5 ± 0.1	3.5 ± 0.1	3.7 ± 0.1	4.1 ± 0.2
I_{OZ} [cm^{-1}]	7 ± 1	10 ± 1	17 ± 2	25 ± 2	46 ± 3	46 ± 3
ξ_{OZ} [nm]	3.5 ± 0.2	3.9 ± 0.3	4.8 ± 0.4	5.6 ± 0.5	7.3 ± 0.7	6.9 ± 0.5
SLDsphere	$(7.1 \pm 0.3) \times 10^{-5}$					

Table B.4. Best fit parameters of equation 6.1 for the SANS data of a 50 g L^{-1} $PSBP_{78}$-*b*-$PNIPMAM_{115}$ solution in D_2O in regime III.

	50 ºC	55 ºC	60 ºC	65 ºC
R_{avg} [nm]	10.1 ± 1.0	13.1 ± 1.1	13.5 ± 1.2	13.5 ± 1.2
L [nm]	25 ± 2	29 ± 3	34 ± 3	54 ± 5
b [nm]	16 ± 2	18 ± 2	18 ± 2	18 ± 2
p	0.50 ± 0.05	0.20 ± 0.02	0.16 ± 0.01	0.16 ± 0.2
R_{HS} [nm]	21 ± 2	22 ± 2	22 ± 2	22 ± 2
η	0.34 ± 0.02	0.35 ± 0.03	0.36 ± 0.03	0.37 ± 0.03
$I_P \times 10^{-9}$	2.2 ± 0.2	0.8 ± 0.1	0.9 ± 0.1	1.2 ± 0.1
α	4.7 ± 0.3	4.9 ± 0.3	4.9 ± 0.3	4.9 ± 0.3
C [cm^{-1}]	3.2 ± 0.2	1.6 ± 0.1	1.5 ± 0.1	1.6 ± 0.2
$\xi solv$ [nm]	4.2 ± 0.2	3.9 ± 0.2	5.5 ± 0.3	5.8 ± 0.4
m	1.59 ± 0.21	1.53 ± 0.13	1.13 ± 0.10	1.16 ± 0.11
d_0 [nm]	17 ± 2	15 ± 2	14 ± 1	14 ± 1
SLD cylinder	$(7.1 \pm 0.3) \times 10^{-5}$			

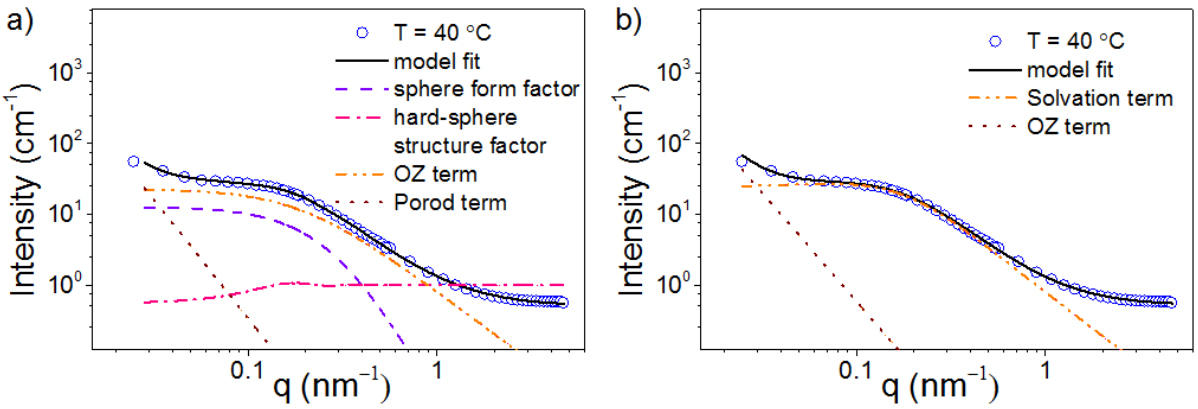

Figure B.2: Representative SANS curves from a 50 g L^{-1} PSBP$_{78}$-*b*-PNIPMAM$_{115}$ solution in 0.004 M NaBr in D_2O, together with the model fits obtained using Eqs. 6.1 (a) and 6.2 (b) (**—**). The symbols show the experimental data obtained at 40 °C (regime II). The other lines represent the contributions to the models as described in the graphs.

Table B.5. Best fit parameters of Eq. 6.1 for the SANS data of a 50 g L^{-1} PSBP$_{78}$-*b*-PNIPMAM$_{115}$ solution in 0.004 M NaBr in D_2O in regimes I and II.

	Regime I			Regime II		
	20 ºC	25 ºC	30 ºC	35 ºC	40 ºC	45 ºC
r_{avg} [nm]	11.8 ± 1.2	11.1 ± 1.0	10.0 ± 1.0	2.9 ± 0.3	2.3 ± 0.2	2.3 ± 0.2
p	0.26 ± 0.03	0.27 ± 0.03	0.29 ± 0.03	0.85 ± 0.08	0.80 ± 0.07	0.53 ± 0.05
R_{HS} [nm]	22 ± 2	21 ± 2	20 ± 2	17 ± 2	17 ± 2	18 ± 2
η	0.10 ± 0.01	0.08 ± 0.01	0.07 ± 0.01	0.08 ± 0.01	0.08 ± 0.01	0.11 ± 0.01
$I_P \times 10^{-9}$	11.1 ± 1.1	2.1 ± 0.2	1.4 ± 0.1	0.5 ± 0.1	62 ± 2	459 ± 57
α	3.8 ± 0.1	4.0 ± 0.1	4.1 ± 0.2	3.8 ± 0.2	3.4 ± 0.1	3.2 ± 0.1
I_{OZ} [cm^{-1}]	21 ± 21	31 ± 3	36 ± 4	26 ± 3	23 ± 3	23 ± 3
ξ_{OZ} [nm]	6.2 ± 0.4	6.8 ± 0.5	7.0 ± 0.6	5.8 ± 0.5	5.3 ± 0.4	5.4 ± 0.5
SLDsphere	(7.1 ± 0.3) × 10^{-5}					

Table B.6. Best fit parameters of Eq. 6.2 for the SANS data of a 50 g L^{-1} $PSBP_{78}$-*b*-$PNIPMAM_{115}$ solution in 0.004 M NaBr in D_2O in regime II.

	35 ºC	40 ºC	45 ºC
$I_P \times 10^{-7}$	1.8 ± 0.1	3.9 ± 0.2	19 ± 2
α	3.3 ± 0.1	3.1 ± 0.1	2.8 ± 0.1
C [cm^{-1}]	40 ± 3	27 ± 2	22 ± 2
$\xi solv$ [nm]	8.6 ± 0.6	6.2 ± 0.4	5.1 ± 0.3
m	1.93 ± 0.13	1.99 ± 0.13	2.05 ± 0.15
d_0 [nm]	85 ± 7	90 ± 8	105 ± 10

Table B.7. Best fit parameters of Eq. 6.1 for the SANS data of a 50 g L^{-1} $PSBP_{78}$-*b*-$PNIPMAM_{115}$ solution in 0.004 M NaBr in D_2O in regime III.

	50 ºC	55 ºC	60 ºC	65 ºC
R_{avg} [nm]	12.3 ± 1.2	12.6 ± 1.1	13.3 ± 1.2	13.8 ± 1.3
L [nm]	20 ± 21	25 ± 3	30 ± 37	45 ± 5
b [nm]	10 ± 1	17 ± 2	17 ± 2	19 ± 2
p	0.27 ± 0.02	0.16 ± 0.01	0.14 ± 0.01	0.13 ± 0.01
R_{HS} [nm]	21 ± 2	21 ± 3	22 ± 2	22 ± 2
η	0.32 ± 0.02	0.34 ± 0.03	0.35 ± 0.03	0.35 ± 0.03
$I_P \times 10^{-9}$	4.3 ± 0.2	0.7 ± 0.1	0.9 ± 0.1	0.7 ± 0.1
α	4.5 ± 0.3	4.8 ± 0.3	4.9 ± 0.3	4.9 ± 0.3
C [cm^{-1}]	3.8 ± 0.3	1.6 ± 0.1	1.5 ± 0.1	1.4 ± 0.2
$\xi solv$ [nm]	4.8 ± 0.3	4.2 ± 0.3	7.0 ± 0.61	8.0 ± 0.7
m	1.49 ± 0.13	1.50 ± 0.11	1.10 ± 0.11	1.13 ± 0.12
d_0 [nm]	17 ± 2	15 ± 2	13 ± 1	13 ± 1
SLD cylinder	$(7.1 \pm 0.3) \times 10^{-5}$			

Appendix C. Supporting information for chapter 8

In the present appendix, will be presented: Fits to the SANS curves from 50 g L^{-1} solutions of $PSBP_{51}$-*b*-$PNIPAM_{156}$ and $PSBP_{243}$-*b*-$PNIPMAM_{103}$ in D_2O and best fit parameters for the SANS data.

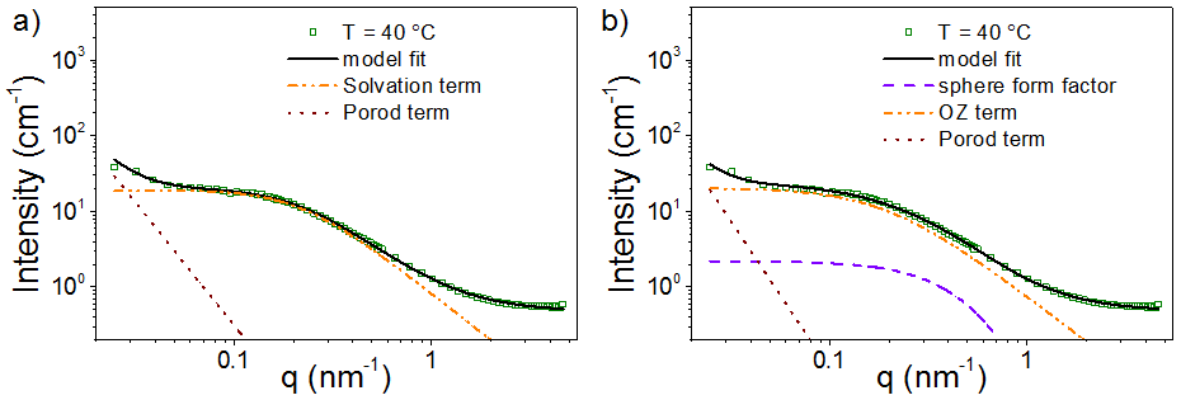

Figure C.1: Representative SANS curves from a 50 g L^{-1} PSBP$_{51}$-*b*-PNIPMAM$_{156}$ solution in D_2O, where every second point is shown for clarity, together with the model fits obtained using Eqs. 6.1 (a) and 6.2 (b) (—). The symbols show the experimental data obtained at 40 °C (regime II). The other lines represent the contributions to the models as described in the graphs.

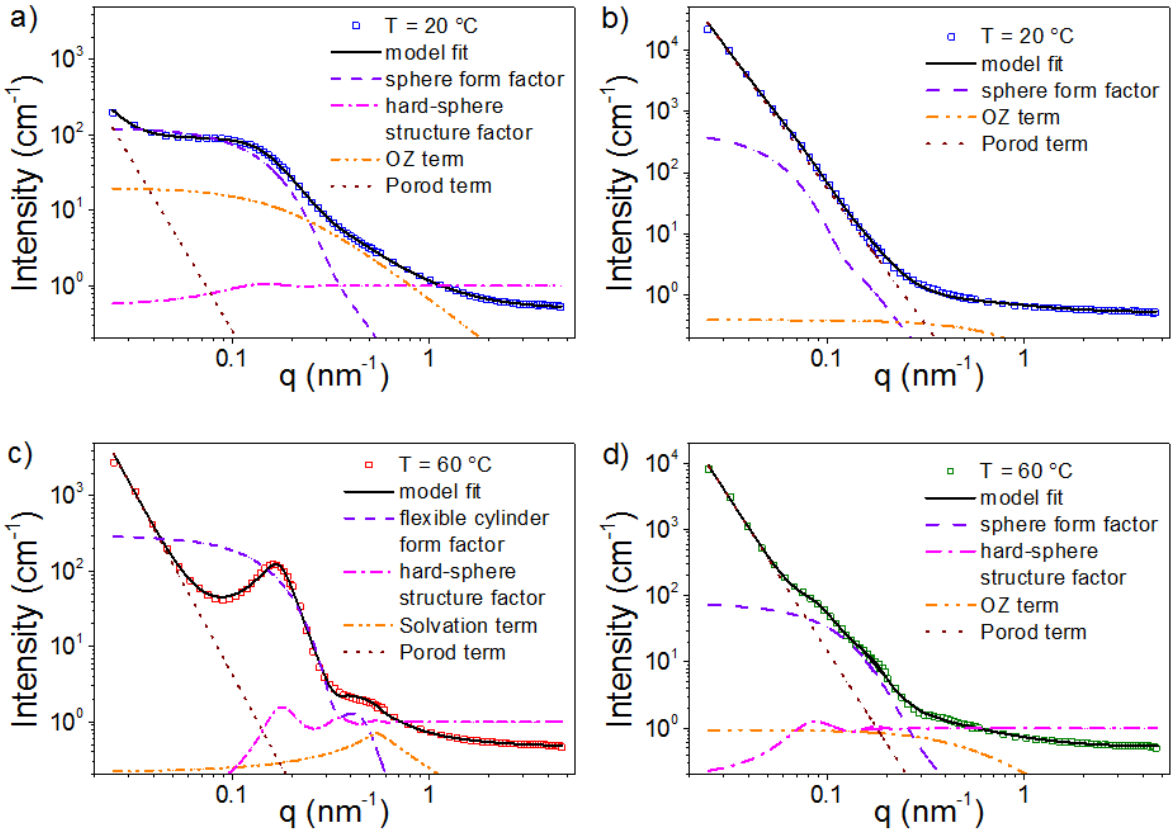

Figure C.2: Representative SANS curves from 50 g L^{-1} PSBP$_{51}$-*b*-PNIPMAM$_{156}$ (a, c) and PSBP$_{243}$-*b*-PNIPMAM$_{103}$ (b, d) solutions in D_2O in regimes I (a, b) and III (c, d), where every second point is shown for clarity, together with the model fits obtained using Eq. 6.1 (—). The symbols show the experimental data at 20 °C (regime I, a, b) and 60 °C (regime III, c, d). The other lines represent the contributions to the models as described in the graphs.

Table C.1. Best fit parameters of Eq. 6.2 for the SANS data of a 50 g L^{-1} $PSBP_{51}$-*b*-$PNIPMAM_{156}$ solution in D_2O in regime I at 30 °C and regime II.

	Regime I 30 °C	Regime II 40 ºC
I_P	$(1.4 \pm 0.1) \times 10^{-8}$	$(9.7 \pm 0.8) \times 10^{-8}$
α	3.8 ± 0.2	3.3 ± 0.2
C [cm^{-1}]	42 ± 4	19 ± 2
$\xi solv$ [nm]	9.9 ± 0.3	4.8 ± 0.2
m	1.82 ± 0.02	2.01 ± 0.02
d_0 [nm]	8 ± 1	15 ± 2

Table C.2. Best fit parameters of Eq. 6.1 for the SANS data of a 50 g L^{-1} $PSBP_{51}$-*b*-$PNIPMAM_{156}$ solution in D_2O in regimes I, II and III.

	Regime I		Regime II	Regime II	
	20 ºC	30 ºC	40 ºC	50 ºC	60 ºC
r_{avg} [nm]	11.1 ± 1.0	10.7 ± 1.1	1.7 ± 0.2		
R_{avg} [nm]				11.1 ± 1.1	11.1 ± 1.0
L [nm]				12 ± 1	22 ± 2
b [nm]				3.3 ± 0.2	10 ± 1
p	0.26 ± 0.03	0.23 ± 0.02	0.59 ± 0.05	0.14 ± 0.01	0.14 ± 0.01
R_{HS} [nm]	20 ± 2	19 ± 2		19 ± 2	18 ± 2
η	0.07 ± 0.01	0.08 ± 0.01		0.31 ± 0.02	0.32 ± 0.03
$I_P \times 10^{-9}$	3.5 ± 0.3	0.6 ± 0.1	0.8 ± 0.1	16 ± 1	53 ± 4
α	4.4 ± 0.2	3.9 ± 0.2	3.6 ± 0.2	4.7 ± 0.3	4.9 ± 0.3
I_{OZ} [cm^{-1}]	20 ± 2	33 ± 3	20 ± 2		
ξ_{OZ} [nm]	5.4 ± 0.5	6.5 ± 0.6	5.1 ± 0.4		
C [cm^{-1}]				2.0 ± 0.2	0.8 ± 0.1
$\xi solv$ [nm]				3.2 ± 0.3	6.0 ± 0.5
m				1.67 ± 0.15	1.13 ± 0.10
d_0 [nm]				16 ± 2	11 ± 1
SLDsphere	$(7.1 \pm 0.3) \times 10^{-5}$				

Table C.3. Best fit parameters of equation 6.1 for the SANS data of a 50 g L^{-1} $PSBP_{243}$-*b*-$PNIPMAM_{103}$ solution in D_2O.

	20 ºC	30 ºC	40 ºC	50 ºC	60 ºC
r_{avg} [nm]	32 ± 3	33 ± 3	42 ± 4	9 ± 1	13 ± 1
p	0.23 ± 0.02	0.23 ± 0.02	0.10 ± 0.01	0.26 ± 0.03	0.29 ± 0.03
R_{HS} [nm]					35 ± 3
η					0.22 ± 0.01
$I_P \times 10^{-8}$	7.1 ± 0.6	6.2 ± 0.1	5.7 ± 0.5	3.2 ± 0.2	7.7 ± 0.7
α	4.5 ± 0.2	4.5 ± 0.2	4.5 ± 0.1	4.9 ± 0.3	4.6 ± 0.2
I_{OZ} [cm^{-1}]	0.4 ± 0.1	0.6 ± 0.1	0.8 ± 0.2	1.6 ± 0.3	0.9 ± 0.2
ξ_{OZ} [nm]	1.2 ± 0.1	1.5 ± 0.1	1.6 ± 0.1	2.6 ± 0.2	1.9 ± 0.2
SLDsphere			$(7.1 \pm 0.3) \times 10^{-5}$		

Bibliography

[1] Harada, A.; Kataoka, K. *Prog. Polym. Sci.* **2006**, *31*, 949-982.

[2] Mai, Y.; Eisenberg, A. *Chem. Soc. Rev*. **2012**, *41*, 5969-5985.

[3] Raffa, P.; Wever, D. A. Z.; Picchioni, F.; Broekhuis, A. A. *Chem. Rev*. **2015**, *115*, 8504-8563.

[4] Nicolai, T.; Colombani, O.; Chassenieux, C. *Soft Matter* **2010**, *6*, 3111-3118.

[5] Schaeffel, D.; Kreyes, A.; Zhao, Y.; Landfester, K.; Butt, H.-J.; Crespy, D.; Koynov, K. *ACS Macro Lett.* **2014**, *3*, 428-432.

[6] Wright, D. B.; Patterson, J. P.; Pitto-Barry, A.; Cotanda, P.; Chassenieux, C.; Colombani, O.; O'Reilly, R. K. *Polym. Chem.* **2015**, *6*, 2761-2768.

[7] Dimitrov, I.; Trzebicka, B.; Müller, A. H. E.; Dworak, A.; Tsvetanov, C. B. *Prog. Polym. Sci*. **2007**, *32*, 1275-1343.

[8] Laschewsky, A. *SÖFW-Journal* **2011**, *137*, 34-40.

[9] Laschewsky, A.; Müller-Buschbaum, P.; Papadakis, C. M. *Progr. Colloid Polym. Sci.* **2013**, *140*, 15-34.

[10] Kelley, E. G.; Albert, J. N. L.; Sullivan, M. O.; Epps, T. H. *Chem. Soc. Rev*. **2013**, *42*, 7057-7071.

[11] Strandman, S.; Zhu, X. X. *Prog. Polym. Sci.* **2015**, *42*, 154-176.

[12] Yoshimitsu, H.; Korchagina, E.; Kanazawa, A.; Kanaoka, S.; Winnik, F. M.; Aoshima, S. *Polym. Chem.* **2016,** *7*, 2062-2068.

[13] Aseyev, V.; Tenhu, H.; Winnik, F. M. *Adv. Polym. Sci.* **2011**, *242*, 29–89.

[14] Roy, D.; Brooks, W. L. A.; Sumerlin, B. S. *Chem. Soc. Rev.*, **2013**, *47*, 7214–7243.

[15] Schulz, D. N.; Peiffer, D. G.; Agarwal, P. K.; Larabee, J.; Kaladas, J. J.; Soni, L.; Handwerker, B.; Garner, R. T. *Polymer* **1986,** *27*, 1734-1742.

[16] Köberle, P.; Laschewsky, A.; Lomax, T. D. *Makromol. Chem., Rapid Commun.* **1991,** *12*, 427- 433.

[17] Seuring, J.; Agarwal, S. *Macromol. Rapid Commun.* **2012**, *33*, 1898–1920.

[18] Seuring, J.; Agarwal, S. *ACS Macro Lett.* **2013**, *2*, 597–600.

[19] Bütün, V.; Liu, S.; Weaver, J. V. M.; Bories-Azeau, X.; Cai, Y.; Armes, S. P. *React. Funct. Polym*. **2006**, *66*, 157-165.

[20] Kotsuchibashi, Y.; Ebara, M.; Aoyagi, T.; Narain, R. *Polymers* **2016**, *8*, 1-25.

[21] Liu, S.; Billingham, N. C.; Armes, S. P. *Angew. Chem. Int. Ed.* **2001**, *40*, 2328-2331.

[22] Arotçaréna, M.; Heise, B.; Ishaya, S.; Laschewsky, A. *J. Am. Chem. Soc.* **2002**, *124*, 3787-3793.

[23] Virtanen, J.; Arotçaréna, M.; Heise, B.; Ishaya, S.; Laschewsky, A.; Tenhu, H. *Langmuir* **2002,** *18*, 5360-5365.

[24] Maeda, Y.; Mochiduki, H.; Ikeda, I. *Macromol. Rapid Commun.* **2004**, *25*, 1330–1334.

[25] Wang, D.; Wu, T.; Wan, X.; Wang, X.; Liu, S. *Langmuir* **2007**, *23*, 11866-11874.

[26] Shih, Y.-J.; Chang, Y.; Deratani, A.; Quemener, D. *Biomacromolecules* **2012**, *13*, 2849-2858.

[27] Zhang, Q.; Hong, J.-D.; Hoogenboom, R. *Polym. Chem.* **2013**, *4*, 4322-4325.

[28] Cummings, C.; Murata, H.; Koepsel, R.; Russell, A. J. *Biomacromolecules* **2014**, *15*, 763-771.

[29] Kelley, E. G.; Albert, J. N. L.; Sullivan, M. O.; Epps III, T. H. *Chem. Soc. Rev*. **2013**, *42*, 7057-7071.

[30] Mary, P.; Bendejacq, D. D.; Labeau, M.-P.; Dupuis, P. *J. Phys. Chem. B* **2007,** *111*, 7767-7777.

[31] Hildebrand, V.; Laschewsky, A.; Zehm, D. *J. Biomater. Sci., Polym. Ed.* **2014**, *25*, 1602-1618.

[32] Hildebrand, V.; Laschewsky, A.; Wischerhoff, E. *Polym. Chem.* **2016,** *7*, 731-740.

[33] Rubinstein, M., Colby R. H. *Polymer Physics*. Oxford University Press, 2003.

[34] Miller-Chou, B. A.; Koenig, J. L. *Prog. Polym. Sci*. **2003**, 28, 1223–1270.

[35] Flory, P.J. *J. Chem. Phys*. **1942**, *10*, 51-61.

[36] Gedde, U. W. *Polymer Physics*. Kluwe Academic Publishers, 2001.

[37] Burke, J. *The Book and Papaer Group Annual*, chapter Solubility Parameters: Theory and Application, 13–58, 1984.

[38] Twardowski, T. E**.** *Introduction to Nanocomposite Materials:* Properties**,** Processing, Characterization. Destech Publications, Inc., 2007.

[39] Teraoka, I. *Polymer solutions*. *An Introduction to Physical Properties.* Polytechnic University Brooklyn, New York, 2002.

[40] Flory, P. J. *J. Chem. Phys.* **1941**, *9*, 660; **1942**, *10*, 51; **1949**, *17*, 303.

[41] Huggins, M. L. *J. Chem Phys.* **1941**, *9*, 440; *J. Phys. Chem*. **1942**, *46*, 151; *J. Am. Chem. Soc.* **1942**, *64*, 1712.

[42] Grosberg, A. Y.; Khokhlov, A. R. *Statistical physics of macromolecules*. AIP Press, 1994.

[43] Yamakawa, H.; Abe, F.; Einaga, Y. *Macromolecules* **1994**, *27*, 5704–5712.

[44] Hoffman, A. S. *J. Controlled Release*, **1987**, *6*, 297-305.

[45] Gil, E. S.; Hudson, S. *Prog. Polym. Sci.* **2004**, *29*, 1173–1222.

[46] Wu, G.; Li, Y.; Han, M.; Liu, X. N. *J. Membr. Sci.* **2006**, *283*, 13–20.

[47] Kanazawa, H. *J. Sep. Sci*. **2007**, *30*, 1646–1656.

[48] Nagase, K.; Kobayashi, J.; Okano, T. *J. R. Soc. Interface* **2009**, *6*, S293-S309.

[49] Nath, N.; Chilkoti, A. *Adv. Mater*. **2002**, *14*, 1243–1247.

[50] Wischerhoff, E.; Badi, N.; Lutz, J.-F.; Laschewsky, A. *Soft Matter* **2010**, *6*, 705-713.

[51] Tang, Z.; Akiyama, Y.; Okano, T. *Polymers* **2012**, *4*, 1478-1498.

[52] Ward, M. A.; Georgiou, T. K. *Polymers* **2011**, *3*, 1215-1242.

[53] Hoffman, A. S. *Adv. Drug. Deliv. Rev.* **2013**, *65*, 10–16.

[54] Tang, Z.; Akiyama, Y.; Okano, T. *J. Polym. Sci., Part B: Polym. Phys.* **2014**, *52*, 917-926.

[55] Reineke, T. M. *ACS Macro Lett.* **2016**, *5*, 14-18.

[56] Honey, P. J.; Rijo, J.; Anju, A.; Anoop, K.R. *Acta Pharmaceut. Sin. B* **2014**, *4*, 120–127.

[57] Hocine, S.; Li. M. H. *Soft Matter* **2013**, *9*, 5839-5861.

[58] Wu, C.; Wang, X. *Phys. Rev. Lett.* **1998**, *80*, 4092–4094.

[59] Hoogenboom, R.; Rogers, S.; Can, A.; Becer, C. R.; Guerrero-Sanchez, C.; Wouters, D; Hoeppener, S.; Schubert, U. S. *Chem. Commun.* **2009**, *37*, 5582-5584.

[60] Glatzel, S.; Laschewsky, A.; Lutz, J.-F. *Macromolecule.***2011**, *44*, 413-415.

[61] Zhang, Q. L.; Schützling, P.; Theater, P.; Hoogenboom, R. *Polym. Chem*, **2012**, *3*, 1418–1426.

[62] Buscall, R.; Corner, T. *Eur. Polym. J.* **1982**, *18*, 967–974.

[63] Huglin, M. B.; Radwan, M. A. *Polym. Int.* **1991**, *26*, 97–104.

[64] Laschewsky, A. *Polymers* **2014**, *6*, 1544-1601.

[65] Aoki, T.; Nakamura, K.; Sanui, K.; Kikuchi, A.; Okano, T.; Sakurai, Y.; Ogata, N. *Polym. J.* **1999**, *31*, 1185–1188.

[66] Cai, X.; Zhong, L.; Su, Y.; Lin, S.; He, X. *Polym. Chem.* **2015**, *6*, 3875-3884.

[67] Alexandridis, P.; Lindman, B editors. *Amphiphilic Block Copolymers: Self-Assembly and Applications*. Elsevier, **2000**.

[68] O'Reilly, R. K.; Hawker, C. J.; Wooley, K. L. *Chem. Soc. Rev.* ***2006***, *35*, 1068–1083.

[69] Riess, G. *Prog Polym Sci* **2003**, 28, 1107–1170.

[70] Israelachvili, J. N.; Mitchel, D. J.; Ninham, B.W. *J. Chem. Soc. Faraday Trans. I* **1976,** *72*, 1525-1568.

[71] Blanazs, A.; Armes, S. P.; Ryan, A. J. *Macromol. Rapid Commun.*, **2009**, *30*, 267–277.

[72] Sugihara, S.; Kanaoka, S.; Aoshima, S. *J. Polym. Sci., Part A: Polym. Chem*. **2004**, *42*, 2601-2611.

[73] Mertoglu, M.; Garnier, S.; Laschewsky A.; Skrabania, K.; Storsberg, J. *Polymer* **2005**, *46*, 7726-7740.

[74] Xie, D.; Ye, X.; Ding, Y.; Zhang, G.; Zhao, N.; Wu, K.; Cao, Y.; Zhu, X. X. *Macromolecules* **2009**, *42*, 2715-2720.

[75] Weiss, J.; Laschewsky, A. *Macromolecules* **2012,** *45*, 4158-4165.

[76] Jaksch, S.; Schulz, A.; Kyriakos, k.; Zhang, J.; Grillo, I.; Pipich, V.; Jordan, R.; Papadakis, C. M. *Colloid Polym. Sci.* **2014**, *292*, 2413-2425.

[77] Bütün, V.; Billingham, N. C;.Armes, S. P. *J. Am. Chem. Soc.* **1998,** *120*, 11818–11819.

[78] Tian, H.-Y.; Yan, J.-J.; Wang, D.; Gu, C.; You, Y. Z.; Chen, X. S. *Macromol. Rapid Commun.* **2011**, *32*, 660-664.

[79] Kawauchi, Y.; Kouka, A.; Guragain, S.; Bastakoti, B. P.; Yusa, S.-i.; Nakashima. K. *Colloids and Surfaces A: Physicochemical and Engineering Aspects.* **2013**, *434*, 56-62.

[80] Zhang, Q.; Tosi, F.; Ügdüler , S.; Maji, S.; Hoogenboom, R. *Macromol. Rapid Commun.* **2015**, *36*, 633-639.

[81] Can, A.; Zhang, Q.; Rudolph, T.; Schacher, F. H.; Gohy, J.-F.; Schubert, S. U.; Hoogenboom, R. *Eur. Polym. J.* **2015**, *69*, 460-471.

[82] Tang, Y.-H.; Li, Z.; Li, X.; Deng, M.; Karniadakis, G. E. *Macromolecules.* **2016**, *49*, 2895-2903.

[83] Liu, S.; Armes, S. P. *Langmuir* **2003**, *19*, 4432–4438.

[84] Cai, Y.; Armes, S. P. *Macromolecules* **2005**, *38*, 271–279.

[85] Wang, D.; Yin, J.; Zhu, Z.; Ge, Z.; Liu, H.; Armes, S. P.; Liu, S. *Macromolecules* **2006**, *39*, 7378–7385.

[86] Longenecker, R.; Mu, T., Hanna, M., Burke, N. A. D., Stöver, H. D. H. *Macromolecules* **2011**, *44*, 8962-8971.

[87] Weaver, J. V. M.; Armes, S. P.; Bütün, V. *Chem. Commun.* **2002**, *124*, 3787-3793.

[88] Mori, H.; Kato, I.; Saito, S.; Endo, T. *Macromolecules* **2010**, *43*, 1289-1298.

[89] Sun, H., Chen, X., Han, X., Liu, H. *Langmuir* **2017**, *33*, 2646−2654.

[90] Lowe, A. B.; Torrex, M.; Wang, R. *J. Polym. Sci., Part A: Polym. Chem.* **2007**, 45, 5864–5871.

[91] Ge, Z.; Cai, Y.; Yin, J.; Zhu, Z.; Rao, J.; Liu. S. *Langmuir*. **2007**, *23*, 1114-1122.

[92] Jiang, X.; Zhang, G.; Narain, R.; Liu, S. *Langmuir* **2009**, 25, 2046–2054.

[93] Zhang, Y.; Liu, H.; Hu, J.; Li, C.; Liu, S. *Rapid Commun.* **2009**, 30, 941–947.

[94] Chang, C.; Wei, H.; Feng, J.; Wang, Z.-C.; Wu, X.-J.; Wu, D.-Q.; Cheng, S.-X.; Zhang, X.-Z.; Zhuo, R.-X. *Macromolecules* **2009**, *42*, 4838–4844.

[95] Roy, D.; Cambre, J. N.; Sumerlin, B. S. *Chem. Commun*, **2009**, 2106–2108.

[96] Zhang, H.; Tong, X.; Zhao, Y. *Langmuir*, **2014**, *30*, 11433-11441.

[97] Käfer, F.; Liu, F.; Stahlschmidt, U.; Jérôme, V.; Freitag, R.; Karg, M.; Agarwal, S. *Langmuir*, **2015**, *31*, 8940-8946.

[98] Huang, G.; Li, H.; Feng, S.; Li, X.; Tong, G.; Liu, J.; Quan, C.; Jiang, Q.; Zhang, C.; Li, Z. *Macromol. Chem. Phys.*, **2015**, *216*, 1014–1023.

[99] Mäkinen, L.; Varadharajan, D.; Tenhu, H.; Hietala, S. *Macromolecules* **2016**, *49*, 986-993.

[100] Schattling, P.; Jochum, F. D.; Theato, P. *Polym. Chem.* **2014**, *5* (1), 25−36.

[101] Smith, A. E.; Xu, X.; Kirkland-York, S. E.; Savin, D. A.; McCormick, C. L. *Macromolecules.* **2010**, *43*, 1210-1217.

[102] Zhu, Y.; Noy, J.-M.; Lowe, A. B.; Roth, P. J. *Polym. Chem.* **2015**, *6*, 5705-5718.

[103] Wang, X.; Qiu, X.; Wu, C. *Macromolecules* **1998**, *31*, 2972−2976.

[104] Maeda, Y.; Higuchi, T.; Ikeda, I. *Langmuir* **2000**, *16*, 7503–7509.

[105] Pamies, R.; Zhu, K.; Kjøniksen, A.-L.; Nyström**,** B. *Polym. Bull.* **2009**, *62*, 487-502.

[106] Halperin, A.; Kröger, M.; Winnik, F. M. *Angew. Chem. Int. Ed.* **2015,** *54*, 15342-15367.

[107] Fujishige, S.; Kubota, K.; Ando, I. *J. Phys. Chem*. **1989**, *93*, 3311−3313.

[108] Chytrý, V.; Netopilík, M.; Bohdanecký, M.; Ulbrich, K. *J. Biomater. Sci. Polym. Ed.* **1997**, *8*, 817-824.

[109] Duracher, D.; Elaissari, A.; Pichot, C. *Colloid. Polym. Sci.* **1999**, *277*, 905-913.

[110] Djokpe, E.; Vogt, W. *Macromol. Chem. Phys.* **2001**, *202*, 750-757.

[111] Schild, H. G. *Prog. Polym. Sci.* **1992**, *17*, 163–249.

[112] Heskins, M.; Guillet, J. E. *J. Macromol. Sci.: Part A – Chem.***1968**, *2*, 1441-1455.

[113] Afroze, F.; Nies, E.; Berghmans, H. *J. Mol. Struct*. **2000**, *554*, 55–68.

[114] Rebelo, L. P. N.; Visak, Z. P.; de Sousa, H. C.; Szydlowski, J.; de Azevedo, R. G.; Ramos, A. M.; Najdanovic-Visak, V.; Nunes da Ponte, M.; Klein, J. *Macromolecules* **2002**, *35*, 1887–1895.

[115] Okada, Y.; Tanaka, F. *Macromolecules* **2005**, *38*, 4465.

[116] Maeda, Y.; Nakamura, T.; Ikeda, I. *Macromolecules*, **2001**, *34*, 1391–1399.

[117] Katsumoto, Y.; Tanaka, T.; Sato, H.; Ozaki, Y. *J. Phys. Chem. A* **2002**, 106, 3429–3435.

[118] Abbott, L. J.; Tucker, A. K.; Stevens, M. J. *J. Phys. Chem. B*, **2015**, *119* (9), 3837–3845.

[119] Wu, C.; Wang X. *Physical Review Letters* **1998**, *80*, 4092–4094.

[120] Wang, X.; Qiu, X.; Wu, C. *Macromolecules* **1998**, *31*, 2972–2976.

[121] Zhou, K.; Lu, Y.; Li, J.; Shen, L.; Zhang, G.; Xie, Z.; Wu, C. *Macromolecules* **2008**, *41*, 8927−8931.

[122] Matsuyama, A.; Tanaka, F. *J. Chem. Phys.* **1991**, *94*, 781-786.

[123] Tanaka, F.; Koga, T.; Kaneda, I.; Winnik, F.M. *J. Phys.: Condens. Matter* **2011**, *23*, 28410.

[124] Tanaka, T. *Phys. Rev. Lett. 40* **1978**, 820-823.

[125] Kubota, K.; Fujishige, S.; Ando, I. *J. Phys. Chem.* **1990**, *94*, 5154-5158.

[126] Grosberg, A. Y.; Kuznetsov, D.V. *Macromolecules* **1993**, *26*, 4249-4251.

[127] Wu, C.; Zhou, S. *Macromolecules* **1995**, *28*, 5388-5390.

[128] Tanaka, F.; Koga, T. *PRL* **2008**, *101*, 028302.

[129] Tanaka, F.; Koga, T.; Kojima, H.; Xue, N.; Winnik, F.M. *Macromolecules* **2011**, *44*, 2978-2989.

[130] Kogure, H.; Nanami, S.; Masuda, Y.; Toyama, Y.; Kubota, K. *Colloid Polym. Sci.* **2005**, 283, 1163–1171.

[131] Kujawa, P.; Segui, F.; Shaban, S.; Diab, C.; Okada, Y.; Tanaka F.; Winnik, F. M. *Macromolecules* **2006**, *39*, 341−348.

[132] Satokawa, Y.; Shikata, T.; Tanaka, F.; Qiu, X.-P.; Winnik, F. M. *Macromolecules* **2009**, *42*, 1400−1403.

[133] Philipp, M.; Kyriakos, K.; Silvi, L.; Lohstroh,W.; Petry,W.; Krüger, J. K.; Papadakis, C. M.; Müller-Buschbaum, P. *J. Phys. Chem. B* **2014**, *118*, 4253–4260.

[134] Balu, C.; Delsanti, M.; Guenoun, P. *Langmuir* **2007,** *23*, 2404-2407.

[135] Gorelov, A.V.; Chesne, A. Du; Dawson. K. A. *Physica A* **1997**, *240*, 443 – 452.

[136] Aseyev, V.; Hietala, S.; Laukkanen, A.; Nuopponen, M.; Confortini, O.; Du Prez F. E.; Tenhu. H. *Polymer* **2005**, *46*, 7118–7131.

[137] Meier-Koll, A.; Pipich, V.; Busch, P.; Papadakis, C. M.; Müller-Buschbaum, P. *Langmuir* **2012**, *28*, 8791−8798.

[138] Cao, Z.; Liu, W.; Gao, P.; Yao, K.; Li, H.; Wang, G. *Polymer* **2005**, 46, 5268−5277.

[139] Rimmer, S.; Soutar, I.; Swanson, L. *Polym. Int*. **2009**, *58*, 273–278.

[140] Hiruta, Y.; Shimamura, M.; Matsuura, M.; Maekawa, Y.; Funatsu, T.; Suzuki, Y.; Ayano, E. Okano, T.; Kanazawa, H. *ACS Macro Lett. 3* **2014**, 281–285.

[141] Furyk, S.; Zhang, Y.; Ortiz-Acosta, D.; Cremer, P. S.; Bergbreiter, D. E. *J. Polym. Sci., Part A: Polym. Chem.* **2006**, 44, 1492−1501.

[142] Xia, Y.; Burke, N. A. D.; Stöver, H. D. H. *Macromolecules* **2006**, *39*, 2275–2283.

[143] Hiruta, Y.; Nagumo, Y.; Suzuki, Y.; Funatsu, T.; Ishikawa, Y.; Kanazawa, H. *Colloids Surf., B* **2015**, *132*, 299–304.

[144] Yamato, M.; Akiyama, Y.; Kobayashi, J.; Yang, J.; Kikuchi, A.; Okano, T. *Prog. Polym.Sci.* **2007**, *32*, 1123–1133.

[145] Wei, H.; Cheng, S.-X.; Zhang, X.-Z.; Zhuo, R.-X. *Prog. Polym. Sci.* **2009**, *34*, 893–910.

[146] Ayano, E., & Kanazawa, H. *Anal. Sci.* **2014**, *30*, 167-173.

[147] Du, H.; Wickramasinghe, R.; Qian, X. *J. Phys. Chem. B* **2010,** *114*, 16594–16604.

[148] Henderson, I. M.; Adams, P. G.; Monta˜no, G. A.; Paxton, W. F. *J. Polym. Sci. B: Polym.Phys.* **2014**, *52*, 507–516.

[149] Obiweluozor, F.O.; GhavamiNejad, A.; Hashmi, S.; Vatankhah-Varnoosfaderani, M.; Stadler, F.J. *Macromol. Chem. Phys.* **2014**, *215*, 1077–1091.

[150] Lo Nostro, P.; Ninham, B. W. *Chem. Rev.* **2012**, *112*, 2286-2322.

[151] Salis, A.; Ninham, B. W. *Chem. Soc. Rev.* **2014**, *43*, 7358-7377.

[152] Zhang, Y.; Furyk, S.; Bergbreiter, D.E.; Cremer, P.S. *J. Am. Chem. Soc.* **2005**, *127*, 14505–14510.

[153] Zhang, Y. J.; Cremer, P. S. *Curr. Opin. Chem. Biol.* **2006**, *10*, 658.

[154] Cho, Y. H.; Zhang, Y. J.; Christensen, T.; Sagle, L. B.; Chilkoti, A.; Cremer, P. S. *J. Phys. Chem. B* **2008**, *112*, 13765.

[155] Tiktopulo, E. I.; Uversky, V. N.; Lushchik, V. B.; Klenin, S. I.; Bychkova, V. E.; Ptitsyn, O. B. *Macromolecules*, **1995**, *28*, 7519- 7524.

[156] Sánchez, M. S.; Hanykova´, L. Ilavsky´, M.; Pradas, M. M. *Polymer* **2004**, *45*, 4087-4094.

[157] Starovoytova, L.; Spěváček, J.; Ilavsky´, M. *Polymer* **2005**, *46*, 677–683.

[158] Wu. Y.; Meersman, F.; Ozaki, Y. *Macromolecules* **2006**, *39*, 1182–8.

[159] Schmidt, P.; Dybal, J.; Trchova´, M. *Vib. Spectrosc*. **2006**, *42*, 278.

[160] Tang, Y; Ding, Y. W.; Zhang, G. Z. *J. Phys. Chem. B* **2008**, *112*, 8447-8451.

[161] Dybal, J.; Trchová, M.; Schmidt, P. *Vib. Spectrosc.* **2009**, *51*, 44–51.

[162] Kubota, K.; Hamano, K.; Kuwahara, N.; Fujishige, S.; Ando, I. *Polymer Journal* **1990**, *22*, 1051 - 1057.

[163] Starovoytova, L.; Spěváček, J.; Trchová, M. *Eur. Polym. J.* **2007**, *43*, 5001-5009.

[164] Spěváček, J.; Starovoytova, L.; Hanyková, L.; Kouřilová, H. *Macromol. Symp.* **2008**, *273*, 17–24.

[165] Luo, S.; Hu, X.; Ling, C.; Liu, X.; Chen, S. Han, M. *Polym. Int.* **2011**, *60*, 717–724.

[166] Jochum, F. D.; Roth, P. J.; Kessler, D.; Theato, P. *Biomacromolecules* **2010**, *11*, 2432-2439.

[167] Kudaibergenov, S.; Jaeger, W.; Laschewsky, A. *Adv. Polym. Sci.* **2006,** *201*, 157-224.

[168] Hildebrand, V. Twofold Switchable Block Copolymers Based on New Polyzwitterions PhD thesis, Mathematisch-Naturwissenschaftlichen Fakultät der Universität Potsdam, 2016.

[169] Lowe, A. B.; McCormick, C. L. *Polyelectrolytes and Polywitterions: Synthesis, Properites and Applications* **2006**, *937*, 65-78.

[170] Galin, J. C. *Polyzwitterions (Overview)*, CRC Press: Boca Raton, Vol. 9, 1996.

[171] Lowe, A. B.; McCormick. C. L. *Chem. Rev.* **2002**, *102*, 4177-4190.

[172] Singh, P. K.; Singh, V. K.; Singh, M. *E-Polym.* **2007**, *7*, 335–368.

[173] Tarannum, N.; Singh, M. *Rev. Adv. Sci. Eng.* **2013**, *2*, 1–22.

[174] Georgiev, G. S.; Karnenska, E. B.; Vassileva, E. D.; Kamenova, I. P.; Georgieva, V. T.; Iliev, S. B.; Ivanov, I. A. *Biomacromolecules* **2006,** *7*, 1329-1334.

[175] Woodfield, P. A.; Zhu, Y.; Pei, Y.; Roth, P. J. *Macromolecules.* **2014**, *47*, 750-762.

[176] Salamone, J. C.; Volksen, W.; Olson, A. P.; Israel, S. C. *Polymer.* **1978**, *19*, 1157-1162.

[177] Soto, V. M.; Galin. J. C. *Polymer.* **1984**, *25*, 254-262.

[178] Wielema, T. A.; Engberts. J. B. F. N. *Eur. Polym. J.* **1990**, *26*, 639-642.

[179] Chang, Y.; Chen, W.-Y.; Yandi, W.; Shih, Y.-J.; Chu, W.-L.; Liu, Y.-L.; Chu, C.-W.; Ruaan, R.-C.; Higuchi, A. *Biomacromolecule*s **2009**, *10*, 2092–2100.

[180] Zhao, Y., Bai, T., Shao, Q., Jiang, S., Shen, A. Q. *Polym. Chem.* **2015**, *6*, 1066-1077.

[181] Keddie, D. J.; Moad, G.; Rizzardo, E.; Thang, S. H. *Macromolecules* **2012,** *45*, 5321-5342.

[182] Lawler, D. M. Spectrophotometry: turbidimetry and nephelometry. In: Worsf, P.; Townshend, A.; Poole, C. (Eds.) Encyclopedia of Analytical Science, second ed. Elsevier, 2005, 343–351.

[183] Varian Cary® 50 UV-Vis Spectrophotometer (accessed May 2017). URL http://cn.agilent.com/cs/library/specifications/public/si-0821.pdf

[184] Berne, B. J. and Pecora, R. *Dynamic Light Scattering*. John Willey & Sons, Inc., 1976.

[185] Brown, W. *Dynamic Light Scattering*. Oxford Science Publications, 1993.

[186] Schärtl, W. *Light Scattering from Polymer Solutions and Nanoparticle Dispersions.* Springer-Verlag, 2007.

[187] Technical Note published by Malvern: Achieving high sensitivity at different scattering angles with different optical configurations. 2014. (accessed May 2017). URL http://www.cif.iastate.edu/sites/default/files/uploads/Other_Inst/Particle%20Size/Non-Invasive%20Backscatter%20(NIBS)%20Explained.pdf

[188] Schmitz, K. S. *Dynamic Light Scattering by Macromolecules*. Academic, New York, **1990**.

[189] Giannopoulou, A.; Aletras, A. J.; Pharmakakis, N.; Papatheodorou, G. N.; Yannopoulos, S. N. *J Chem Phys*. **2007**, *127*, 205101.

[190] Zetasizer Nano ZS Performance, simplicity, versatility. (accessed May 2017). URL http://www.malvern.com/en/products/product-range/zetasizer-range/zetasizer-nano-range/zetasizer-nano-zs/

[191] Hammouda, B. *A Tutorial on Small-Angle Neutron Scattering from Polymers.* National Institute of Standards and Technology Materials Science and Engineering Laboratory, Gaithersburg, MD 20899, June 1995.

[192] Pynn, R. Chapter 2: Neutron scattering - a nondestructive microscope for seeing inside matter. *Los Alamos Science*, **1990**, *19*, 1–31.

[193] Michael, C. R. Neutron Scattering in the Analysis of Polymers. In *Encyclopedia of Analytical Chemistry*, John Wiley & Sons, 2012.

[194] Grillo. I. *Soft-Matter Characterization*, chapter Small Angle Neutron Scattering and Application in Soft Condensed Matter, pages 707–759. Springer: Dordrecht, Netherlands, 2008.

[195] Spala, O. *Neutrons, X-rays and Light*: Scattering Methods Applied to Soft Condensed Matter, Editors: Lindner, P.; Zemb, Th. Amsterdam:Elsevier, 2002.

[196] A. J. Jackson. Introduction to small-angle neutron scattering and neutron reflectometry. NIST Center for Neutron Research, May 2008.

[197] Feoktystov, A.; Frielinghaus, H.; Di, D.; Jaksch, S.; Pipich, V.; Appavou, M.-S.; Babcock, E.; Hanslik, R.; Engels, R.; Kemmerling, G.; Kleines, H.; Ioffe, A.; Richterd, D.; Brückele, T. *J. Appl. Cryst.* **2015**, *48*, 61-70.

[198] Castelletto, V.; Hamley, I. W. *Fibre Diffraction Review* **2003**, *11*, 36-43.

[199] Kotlarchyk, M.; Chen, S-H. *J. Chem. Phys.* **1983**, *79*, 2461-2469.

[200] Schulz, G. V.; *Z. Phys. Chem.* **1935**, *43*, 25-46.

[201] Bartlett, P.; Ottewil, R. H. *J. Chem. Phys.* **1992**, *96*, 3306-3315.

[202] Guinier, A.; Fournet, G. *Small-Angle Scattering of X-Rays*; John Wiley and Sons Inc.: New York, 1955.

[203] Karayianni, M.; Pispas, S. Self-assembly of amphiphilic block copolymers in selective solvents. In *Fluorescence Studies of Polymer Containing Systems*, Prochazka, K., Ed.; Springer Series on Fluorescence 16, Springer International Publishing, Switzerland; 2016, Chapter 2, pp 27-63.

[204] Pedersen, J. S.; Schurtenberger, P. *Macromolecules* **1996**, *29*, 7602-7612.

[205] Chen, W.-R.; Butler, P. D.; Magid, L. J. *Langmuir* **2006**, *22*, 6539−6548.

[206] Cheng, C.Y.; Oh, H.; Wang, T.Y.; Raghavan, S.R.; Tung, S.H. *Langmuir* **2014**, *30*, 10221−10230.

[207] Percus, J. K.; Yevick, G. *J. Phys. Rev.* **1958**, *110*, 1-13.

[208] Ornstein, L.S.; Zernike, F. *Proc. Acad. Sci. Amsterdam* **1914**, *17*, 793-806.

[209] Koper, G. J. M; Bedeaux, D. *Physica A* **1992**, *187*, 489-502.

[210] Porod, G. *Kolloid-Zeitschrift* **1951**, *124*, 83–114.

[211] Koberstein, J. T.; Morra, B.; Stein, R. S. *J. Appl. Cryst.* **1980**, *13*, 34−45.

[212] Hammouda, B. *J. Appl. Cryst.* **2010**, *43*, 716–719.

[213] Horkay, F.; Hammouda, B. *Colloid. Polym. Sci.* **2008**, *286*, 611-620.

[214] Feuz, L.; Strunz, P.; Geue, T.; Textor, M.; Borisov, O. *Eur. Phys. J.* **2007**, *23*, 237–245.

[215] Shibayama, M.; Tanaka, T. *J. Chem. Phys.* **1992**, *97*, 6829-6841.

[216] LAMP, the Large Array Manipulation Program, (accessed May 2017). URL http://www.ill.eu/data_treat/lamp.

[217] Sears, V. F. *Neutron News* **1992**, *3*, 26-37.

[218] Kline, S. R. *J. Appl. Crystallogr*. **2006**, *39*, 895-900.

[219] Vishnevetskaya, N. S.; Hildebrand, V., Niebuur, B.-J., Grillo, I.; Filippov S. K.; Laschewsky, A.; Müller-Buschbaum, P.; Papadakis, C. M. *Macromolecules* **2016**, *49*, 6655-6668.

[220] Vishnevetskaya, N. S.; Hildebrand, V., Niebuur, B.-J., Grillo, I.; Filippov S. K.; Laschewsky, A.; Müller-Buschbaum, P.; Papadakis, C. M. *Macromolecules* **2017**, *doi:10.1021/acs.macromol.7b00356*.

[221] Inal, S.; Kölsch, J. D.; Chiappisi, L.; Janietz, D.; Gradzielski, M.; Laschewsky, A.; Neher, D. *J. Mater. Chem. C* **2013**, *1*, 6603-6612.

[222] Wu, C.; Li, W.; Zhu, X. X. *Macromolecules* **2004**, *37*, 4989-4992.

[223] Cheng, H.; Shen, L.; Wu, C. *Macromolecules* **2006**, *39*, 2325-2329.

[224] Bernstein-Levi, O.; Ochbaum, G.; Bitton, R2. *Colloids Surf. B Biointerfaces* **2016**, *137*, 214–220.

[225] Roe, R.J. *Methods of X-ray and Neutron Scattering in Polymer Science*; Oxford University Press: New York, 2000.

[226] Fetters, L. J.; Lohse, D. J. Colby, R. H. Chain Dimensions and Entanglement Spacings. In: *Physical Properties of Polymers Handbook*. 2nd ed., Mark, J.E., Ed.; Springer, 2007; Chapter 25, pp. 445-454.

[227] Hammersley, A. Fit 2d primer (accessed May 2017). URL http://www.esrf.eu/computing/scientific/FIT2D/.

[228] Beaucage, G. *J. Appl. Cryst.* **1995**, *28*, 717–728.

[229] Hammouda, B.. *J. Appl. Cryst*. **2010**, *43*, 1474–1478.

[230] Hammouda, B.; Jia, D.; Cheng, D. *J. of Sci. Technol.* **2015**, *3*, 1-8.

List of publications

Publications related to the dissertation

• Vishnevetskaya, N. S.; Hildebrand, V.; Niebuur, B.-J.; Grillo, I.; Filippov S. K.; Laschewsky, A.; Müller-Buschbaum, P.; Papadakis, C. M. Aggregation Behavior of Doubly Thermoresponsive Polysulfobetaine-*b*-poly(*N*-isopropylacrylamide) Diblock Copolymers. *Macromolecules* **2016**, *49*, 6665-6668.

• Vishnevetskaya, N. S.; Hildebrand, V.; Niebuur, B.-J.; Grillo, I.; Filippov S. K.; Laschewsky, A.; Müller-Buschbaum, P.; Papadakis, C. M. "Schizophrenic" Micelles from Doubly Thermoresponsive Polysulfobetaine-*b*-Poly(*N*-isopropylmethacrylamide) Diblock Copolymers. *Macromolecules* **2017**, doi: 10.1021/acs.macromol.7b00356.

Further publications

• Kyriakos, K.; Philipp, M.; Lin, C. H.; Dyakonova, M.; Vishnevetskaya, N.; Grillo, I.; Zaccone, A.; Miasnikova, A.; Laschewsky, A.; Müller-Buschbaum, P.; Papadakis, C. M. "Quantifying the interactions in the aggregation of thermoresponsive polymers: The effect of cononsolvency", *Macromolecular Rapid Communications* **2016**, *37*, 420-425.

• Dyakonova, M. A.; Gotzamanis, G.; Niebuur, B.-J.; Vishnevetskaya, N. S.; Raftopoulos, K. N.; Di, Z.; Filippov, S. K.; Tsitsilianis, C.; Papadakis, C. M. "pH Responsiveness of hydrogels formed by telechelic polyampholytes", *Soft Matter* **2017**, doi: 10.1039/c7sm0031

Scientific reports

• Vishnevetskaya, N.; Hildebrand, V.; Philipp, M.; Laschewsky, A.; Grillo, I.; Müller-Buschbaum, P.; Papadakis, C. M. "Aggregation behavior of doubly thermo-responsive poly(sulfobetaine-*b*-(*N*-isopropylmethacrylamide) diblock copolymers", Lehrstuhl für Funktionelle Materialien, Annual Report, 2014.

• Vishnevetskaya, N.; Hildebrand, V.; Philipp, M.; Laschewsky, A.; Grillo, I.; Müller-Buschbaum, P.; Papadakis, C. M. "Aggregation behavior of doubly thermo-responsive poly(sulfobetaine-*b*-(*N*-isopropylmethacrylamide) diblock copolymers", Lehrstuhl für Funktionelle Materialien, Annual Report, 2015.

• Vishnevetskaya, N.; Hildebrand, V.; Di, Z.; Laschewsky, A.; Müller-Buschbaum, P.; Papadakis, C. M. "Aggregation behavior of doubly thermoresponsive diblock copolymers consisting of poly(sulfobetaine) and poly(*N*-isopropylacrylamide) or poly(*N*-isopropylmethacrylamide)", Lehrstuhl für Funktionelle Materialien, Annual Report, 2016.

Conference talks

• **Vishnevetskaya**, **N.;** Hoang, V.; Laschewsky, A.; Papadakis, C. M. "Orthogonally switchable diblock copolymers", 12th European Summer School on Scattering Methods Applied to Soft Condensed Matter, Bombannes, France, 16 - 23 May 2014.

• **Vishnevetskaya**, **N.;** Hoang, V.; Laschewsky, A.; Papadakis, C. M. "Aggregation behavior of doubly thermo-responsive poly(sulfobetaine-*b*-(*N*-isopropylmethacrylamide) diblock copolymers", Polymer Days: Beyond Self-Assembly - Making Polymeric Materials More Versatile, Berlin, Germany, 30 Sept - 2 Oct 2014.

• **Vishnevetskaya**, **N.;** Hildebrand, V.; Philipp, M.; Laschewsky, A.; Müller-Buschbaum, P.; Papadakis, C. M. "Aggregation behavior of doubly thermo-responsive poly(sulfobetaine-*b*-(*N*-isopropylmethacrylamide) diblock copolymers", DPG-Frühjahrstagung, Berlin, Germany, 15 – 20 March 2015.

• **Vishnevetskaya**, **N.;** Hildebrand, V.; Philipp, M.; Laschewsky, A.; Müller-Buschbaum, P.; Papadakis, C. M. "Aggregation behavior of doubly thermo-responsive poly(sulfobetaine-*b*-(*N*-isopropylmethacrylamide) diblock copolymers", 2nd internal biennial science meeting of the MLZ, Grainau, Germany, 15 – 18 Jun 2015.

• **Vishnevetskaya**, **N.;** Hildebrand, V.; Philipp, M.; Grillo, I.; Laschewsky, A.; Müller-Buschbaum, P.; Papadakis, C. M. "Aggregation behavior of doubly thermo-responsive poly(sulfobetaine-*b*-(*N*-isopropylmethacrylamide) diblock copolymers", Greek-German Workshop 2015 'Structural investigation and molecular dynamics of nanostructured polymeric materials', Athens, Greece, 28 September – 1 October 2015.

• Laschewsky, A.; Hildebrand, V.; Nizardo, N. M.; Schönemann, E.; Wischerhoff, E.; Müller-Buschbaum, P.; Papadakis, C. M.; **Vishnevetskaya**, **N.** "New poly(sulfobetaine)s as versatile stimuli-responsive building blocks", Biennial Meeting of the GDCh Division of Macromolecular Chemistry and Satellite Meeting of the SFB Transregio 102, Halle, 11 – 14 Sep 2016.

Conference poster presentations

• **Vishnevetskaya**, **N.;** Hoang, V.; Laschewsky, A.; Papadakis, C. M. "Aggregation behavior of doubly thermo-responsive poly(sulfobetaine-*b*-(*N*-isopropylmethacrylamide) diblock copolymers", SNI2014: Deutsche Tagung für Forschung mit Synchrotronstrahlung, Neutronen und Ionenstrahlen an Großgeräten 2014, 21 – 23 Sep 2014.

• **Vishnevetskaya**, **N.;** Hoang, V.; Laschewsky, A.; Papadakis, C. M. "Aggregation behavior of doubly thermo-responsive poly(sulfobetaine-*b*-(*N*-isopropylmethacrylamide) diblock copolymers", DPG Frühjahrstagung, Dresden, 30 Mar – 4 Apr 2014.

• **Vishnevetskaya**, **N.;** Hoang, V.; Laschewsky, A.; Papadakis, C. M. "Orthogonally switchable block copolymers", German-Greek Workshop, Garching, Germany, 12 – 16 May 2014.

• **Vishnevetskaya**, **N.;** Hildebrand, V.; Philipp, M.; Laschewsky, A.; Müller-Buschbaum, P.; Papadakis, C. M. "Aggregation behavior of doubly thermo-responsive poly(sulfobetaine-*b*-(*N*-isopropylmethacrylamide) diblock copolymers", 15th Conference of the International Association of Colloid and Interface Scientists, Mainz, 24 – 29 May 2015.

• Hildebrand, V.; Laschewsky, A.; Müller-Buschbaum, P.; Papadakis, C. M.; **Vishnevetskaya**, **N.** "Twofold Switchable Zwitterionic Block Copolymers, and their "Schizophrenic" Micellar Self-organization Behavior", European Polymer Congress EPF – Dresden, 21 – 26 June 2015.

• Hildebrand, V.; Laschewsky, A.; Müller-Buschbaum, P.; Papadakis, C. M.; **Vishnevetskaya**, **N.** "Twofold Switchable Zwitterionic Block Copolymers, and their "Schizophrenic" Micellar Self-organization Behavior", 62. SEPAWA Congress and EDC – Fulda, 14 – 16 October 2015.

• Hildebrand, V.; Laschewsky, A.; Müller-Buschbaum, P.; Papadakis, C. M.; **Vishnevetskaya**, **N.** "Twofold Switchable Zwitterionic Block Copolymers as a Promising Drug Delivery System", Symposium: Transition Metal-Catalyzed Reactions with Organoboron Compounds – Potsdam, 7 March 2016.

• **Vishnevetskaya**, **N.;** Hildebrand, V.; Laschewsky, A.; Müller-Buschbaum, P.; Papadakis, C. M. "Aggregation behavior of doubly thermo-responsive poly(sulfobetaine-*b*-(*N*-isopropylmethacrylamide) diblock copolymers", DPG Frühjahrstagung, Regensburg, 6 - 11 March 2016.

Acknowledgments

I would like to acknowledge all the people who have provided me with various forms of help, advice, support and encouragement during the work on this project.

First of all, I would like to express my sincere gratitude to my supervisor Prof. Dr. Christine M. Papadakis, for giving me the opportunity of being part of her group and to work on this interesting and challenging project. Working under her supervision was a great chance for me to grow professionally and personally. Her great support, continuous guidance and professional help made the development of this study and completion of my PhD possible.

I would also like to extend my appreciation to Prof. Dr. André Laschewsky (University of Potsdam, Fraunhofer IAP) and Prof. Dr. Peter Müller-Buschbaum (Chair of Functional Materials) for the deep and interesting discussions within the framework of our common project, which were invaluably useful and informative for me.

I want to express my thanks to Dr. Viet Hildebrand (University of Potsdam) and Dr. Martine Philipp, with whom I had the opportunity to collaborate during our common project. Their knowledge and deep understanding of the subject made the development of this project successful. Moreover, this work was based on materials synthesized by Dr. Viet Hildebrand, therefore very special thanks for his efforts on preparing such high-quality polymers and great collaboration.

An important part of this work was based on the SANS measurements, which were conducted with the help of the beamline scientists Dr. Isabelle Grillo from the D11 SANS instrument (ILL, Grenoble, France) and Dr. Zhenyu Di from the KWS-1 SANS instrument (MLZ, Garching). I thank them for providing professional support and guidance during beam times.

Furthermore, I would like to thank Dr. Sergey K. Filippov (Institute of Macromolecular Chemistry (IMC) in Prague, Czech Republic) for giving me the opportunity to carry out DLS measurements. I would also like to thank A. Lieske and M. Walter (Fraunhofer IAP) for support with the SEC measurements and M. Heydenreich, A. Krtitschka, and D. Schanzenbach (University of Potsdam) for support with the temperature dependent ^{1}H NMR studies.

I would especially like to thank members of the Soft Matter Physics Group, current and former: Dr. Anatoly V. Berezkin, Dr. Konstantinos Kyriakos, Dr. Konstantinos Raftopoulos,

Acknowledgments

Dr. Margarita Dyakonova, M. Sc. Bart-Jan Niebuur, M. Sc. Christina Psylla, M. Sc. Florian Jung, M. Sc. Xiaohan Zhang, B. Sc. Kora-Lee Claude. Thank you for all your wonderful contributions during the work on this project, I am extremely fortunate to have you as colleagues.

Special thanks must go to all members of the Chair of Functional Materials for nice and friendly working-atmosphere and for the good moments we had together.

In addition, I would like to thank to the secretaries of our group, Susanna Fink and Marion Waletzki for their help with many bureaucratic challenges.

I would like to acknowledge the Deutsche Forschungsgemeinschaft (DFG) for the financial support of this project (Pa771/14-1, MU 1487/17-1, LA 611/11-1).

Many thanks go to my family for their constant support, love, trust, and for feeling so close despite being so far.